1214

Deep inelastic muon scattering on lithium, carbon and deuterium targets at 200 GeV

Alan Paić

Université de Neuchâtel Institut de Physique

Groupe de physique nucléaire et corpusculaire

Deep inelastic muon scattering on lithium, carbon and deuterium targets at 200 GeV

Rapport de thèse

presenté à la Faculté des Sciences de l'Université de Neuchâtel pour l'obtention du grade de docteur ès Sciences, mention physique

par

Alan Paić,
physicien diplômé de l'Université de Zagreb

IMPRIMATUR POUR LA THÈSE

Deep inelastic muon scattering on lithium, carbon and deuterium targets at 200 GeV

de Monsieur Alan Paic

UNIVERSITÉ DE NEUCHÂTEL

FACULTÉ DES SCIENCES

La Faculté des sciences de l'Université de Neuchâtel
sur le rapport des membres du jury,

Messieurs J.-L. Vuilleumier, M. Treichel,
M. Arneodo (Cosenza) et D. von Harrach
(Mayence)

autorise l'impression de la présente thèse.

Neuchâtel, le 27 mai 1994

Le doyen:

H.-H. Nägeli

Abstract

Structure function ratios F_2^{Li}/F_2^D and F_2^C/F_2^D have been measured in deep inelastic scattering of 200 GeV muons using the CERN SPS muon beam on fixed ^{2}H, ^{6}Li and ^{12}C targets. A broad kinematic range is covered: $10^{-4} < x_{Bj} < 0.7$ and $0.01 < Q^2 < 70$ GeV$^2/c^2$, extending more than an order of magnitude lower in x_{Bj} than earlier measurements of nuclear F_2 ratios by the New Muon Collaboration at CERN.

Confirming earlier observations, this measurement finds a depletion of the ratio with respect to unity, often referred to as shadowing for $x_{Bj} < 0.05$, a slight enhancement (or antishadowing) between $0.05 < x_{Bj} < 0.15$, and the subsequent fall of the ratio known as the EMC effect thereafter. However, a novel feature of these data is that both ratios show a certain leveling (or saturation) in the shadowing region, F_2^{Li}/F_2^D saturating at $0.890 \pm 0.010(stat.) \pm 0.021(syst.)$ and F_2^C/F_2^D at $0.851 \pm 0.014(stat.) \pm 0.029(syst.)$. This is found to agree with results for shadowing on photoabsorption experiments ($x_{Bj} = 0$). A comparison with existing theoretical models is given.

A preliminary result from a study of the jet topology of the events would suggest that the events with 1+2-jet topology are more shadowed than the ones with 1+1-jet topology in the carbon nucleus. This result would indicate that the gluon distribution is more shadowed than the quark one. A preliminary study of Bose-Einstein correlations of produced like-sign pions is presented.

Contents

List of Figures

List of Tables

Acknowledgements

I would like to thank my advisor, prof. Jean-Luc Vuilleumier for the opportunity to work on the New Muon Collaboration experiment, and for advice and support at crucial moments.

The data analyzed in this work were taken at the very beginning of my stay at CERN – I would like to thank the New Muon Collaboration as a whole for trusting me with these valuable data.

My understanding of the apparatus, especially during the alignment and calibration procedure, is largely due to discussions with drs. William Burger, Eva Kabuss and prof. Ewa Rondio. Sharing experience and knowledge about computer bugs with David Sanders and other graduate students (Matthias, Maarten, Reiner, Andreas, Anna, Peter, Ursula) during that period saved me a lot of effort.

At a later stage, useful advice and comments came from dr. Maarten de Jong.

Special gratitude goes to prof. Michele Arneodo for fruitful physics discussions in the final stage of analysis and his careful reading of this thesis. The radiative corrections and systematic errors due to them are entirely due to dr. Antje Brüll.

Our dear Liz was more than a secretary – cheerful and helpful, she was the sunshine of the corridor.

Merci à Yolande pour tout ce qui touche aux bandes et pour une partie de la production qu'elle a faite.

Un grand merci à Béatrice, qui a non seulement été un soutien constant, supportant un mari trop souvent absent, mais a aussi participé activement à la préparation de certaines illustrations.

Last, but not least, hvala tati, prof. G. Paić̀u, koji me doveo na CERN i učio zanatu fizičara od malih nogu pa do doktorata.

Introduction

This thesis bears on deep inelastic muon scattering on "nuclear" targets: deuterium, lithium and carbon. The subject is on the interface between particle and nuclear physics – the effect we want to measure is the modification of the quark distribution in nucleons when these are surrounded by a nuclear medium.

The present work is based on data taken during a 13-day period in December 1989 with the NMC spectrometer, in the CERN SPS M2 muon beam line.

After a brief overview of the experimental and theoretical knowledge about the subject in chapter 1, we shall describe the experimental apparatus in chapter 2. In chapter 3 the alignment, calibration and data reduction procedure shall be described, followed by a rendering of the structure function ratio analysis in chapter 4. The results of this analysis, showing nuclear effects on the F_2 structure function and their comparison to existing theoretical predictions, follow in chapter 5. A preliminary glimpse at hadron physics – jet topologies and pion interferometry is given in chapter 6. Conclusions are given in chapter 7.

Chapter 1

Deep inelastic scattering on nucleons and nuclei

1.1 Deep inelastic scattering

Curiosity has brought us first to divide the *indivisible* (the atom), then the nucleus, and now also the nucleons are found to possess an inner world of their own, with quarks and gluons of different colour and flavour. What an enchanting voyage!

How do we get to know all this? Nobody can possibly see inside an atom, let alone a nucleon! The ultimate microscope of the physicist is scattering. Scattering of alpha-particles was first used by Rutherford at the beginning of the century. The telltale scattering at very high angles was the first material evidence of the existence of a small, hard and massive nucleus.

Rutherford's success in describing the atom (almost) correctly after this simple experiment has put thousands of physicists on the same track, with the Olympic motto: *Citius, altius, fortius* (faster, higher, stronger). The faster the incident particle, the stronger (more deeply inelastic) the scattering, and the higher the resulting resolution, and the better our knowledge of the tiny and fascinating world of elementary(?) particles.

And just as Rutherford was rewarded by an understanding of the atom, late 1960's high energy experimentalists were rewarded by a similar result in deep inelastic *ep* scattering [1]. The cross section they measured showed no steep decrease at large four-momentum transfers as one would expect for elastic scattering off a uniform proton. This was the proof that was needed to support the already existing quark model as a valid description of the proton. In conclusion, the incident electrons were scattering no longer on a proton, but on the individual quarks themselves! Physicists were thus brought into the situation of a billiard player who suddenly realizes that the target billiards are no longer uniform: they are rather like rubber balls with three marbles trapped inside. So when you hit the billiard softly, it behaves as a whole, but if you hit it hard, the white billiard will bounce off one marble only. In order to make the analogy a bit more convincing, we would have to introduce an assumption as to how the marbles are kept together inside the billiard. If we imagine them being glued together, then it is clear that if we don't hit the billiard too hard, the three marbles and outer rubber shell will behave as one – we won't see a difference from a hard, uniform billiard. If we hit it harder though, the glue will break and the three marbles will fly apart. Or, more likely, the hit marble will separate from the other two, which are "spectators".

Here of course the analogy stops. Because nobody ever saw a single quark flying freely in a detector. We see jets of hadrons instead (see Chapter 6). Also, it is hard to imagine such a strong billiard player who would bring in enough energy to create marble-antimarble pairs. And this is what we do in deep inelastic scattering: we use a high-energy electron or muon ("white billiard") which is supposed structureless (in order not to complicate the interpretation of the end result) and scatter it off a complex object. This object then creates a complex final state, which we can choose to ignore or to study in terms of jet topologies, interferometry and such (see Chapter 6), but the initial lepton comes out unscathed. By measuring the incoming and outgoing lepton alone, we measure the *inclusive* deep inelastic scattering cross section. If we choose to ignore the final state of the target nucleon (nucleus), we have to correct the measured cross section for the "soft" (elastic) component of the scattering (see section 4.3.1 on radiative corrections). But to continue our story, we need a little formalism...

1.1.1 Kinematics and variables

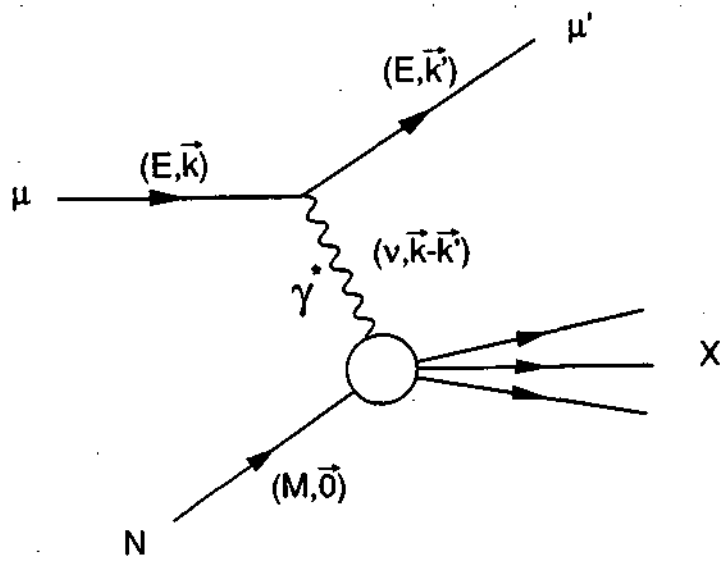

Figure 1.1: One-photon exchange diagram in deep inelastic muon scattering. A virtual (massive) photon is exchanged. The nucleon is initially at rest. The incoming and outgoing muons are measured, whereas for an inclusive cross section the hadronic final state remains unmeasured. Also the initial and final spin states are unmeasured and thus averaged over.

The Feynman graph of the one-photon exchange between the lepton probe and target nucleon is shown in Fig. 1.1. In the laboratory frame the incoming lepton has four-momentum

$$k = (E, \mathbf{k}),$$

the scattered lepton

$$k' = (E', \mathbf{k}'),$$

and the target nucleon

$$p = (M, \mathbf{0}).$$

Conservation of four-momenta at the lepton vertex gives for the virtual photon:

$$q = k - k' = (\nu, \mathbf{k} - \mathbf{k}'),$$

with $\nu = E - E'$, the energy transfer. We introduce the positive invariant mass squared of the photon (sometimes called the "virtuality"):

$$\begin{aligned} Q^2 = -q^2 = -(k-k')^2 &= 2(EE' - pp'\cos\theta) - 2m^2 \\ &\approx 4EE'\sin^2\frac{\theta}{2} \text{ (for large } Q^2), \end{aligned}$$

the Bjorken scaling variable

$$x_{Bj} = \frac{Q^2}{2pq} = \frac{Q^2}{2M\nu},$$

the transferred energy fraction

$$y_{Bj} = \frac{pq}{pk} = \frac{\nu}{E},$$

and the invariant mass squared of the nucleon – virtual photon system

$$W^2 = (p+q)^2 = M^2 + 2M\nu - Q^2.$$

All variables are first given in their Lorentz invariant form, then in the lab system, where the target nucleon is at rest.

Q^2 is a measure of the "resolving power" of the virtual photon (the wavelength of which is $\hbar c/Q$). At low Q^2 ($Q^2 \approx 0.01$ GeV$^2/c^2$) we get predominantly coherent scattering (the nucleus recoils as a whole, the wavelength is ≈ 2 fm). At $Q^2 \approx 0.04$ GeV$^2/c^2$, the wavelength equals the diameter of the nucleon so now the nucleons are resolved and as we go higher and higher in Q^2, we reveal the inner structure of the nucleons, especially above 0.5 GeV$^2/c^2$ where the nucleon and resonance form factors rapidly decrease.

Concerning the x_{Bj} variable for the moment let us just note that its physical interpretation in the quark parton model at sufficiently high values of Q^2 (typically over 0.5 GeV$^2/c^2$) is the fraction of the nucleon momentum carried by the struck parton. This is easily seen in the so-called Breit frame (or infinite momentum frame) defined as:

$$\mathbf{k}' = -\mathbf{k},$$

where transversal momentum components may be neglected and the energy transfer is zero - the struck parton behaves as if it bounced off a brick wall [2] (Fig. 1.2.).

Calculating the invariant mass of the system (quark + virtual γ) we have:

$$W^2 = (p_q + q)^2 = p_q^2 + q^2 + 2p_q q = m_q^2 - Q^2 + 2p_q q,$$

and after the scattering we have

$$W^2 = m_q^2$$

because a quark cannot be excited to a different state, so we are actually dealing with *elastic* scattering off a quark. Hence the condition for scattering:

$$\begin{aligned} Q^2 = 2p_q q &= x \cdot 2pq \\ \Rightarrow x &= \frac{Q^2}{2pq}, \end{aligned}$$

and we recognize the familiar expression for x_{Bj}. For coherent scattering, $x_{Bj} = A$, the atomic number (for the struck particle is the whole nucleus, carrying A times the average nucleon momentum), for quasielastic scattering $x_{Bj} = 1$ (the struck particle being the nucleon), and for deep inelastic scattering it lies between 0 and 1. Note that in Fig. 1.2 the angular momentum is conserved for spin 1/2 quarks. A spin 1 photon makes simply the spin of the quark flip over.

W^2 is especially useful for characterizing the resonance region, as resonances occur at $W^2 = m^2_{Resonance}$.

1.1.2 Deep inelastic cross section and structure functions

Most succinctly the *inclusive* double-differential cross section of the one-photon exchange of Fig. 1.1. can be written as a product of a lepton vertex term, a hadron vertex term and the square of the virtual photon propagator:

$$\frac{\mathrm{d}^2\sigma}{\mathrm{d}\Omega \mathrm{d}E'} = \frac{\alpha^2}{Q^4}\frac{E'}{E} L_{\mu\nu} W^{\mu\nu}, \tag{1.1}$$

where Ω is the solid angle, α the electromagnetic coupling constant, $L_{\mu\nu}$ the leptonic tensor described by QED, and $W^{\mu\nu}$ the hadronic tensor essentially parametrizing our ignorance about the hadron vertex. In particular it is a sum over all possible final states X and initial and final spin states. Taking the most general possible form of $W^{\mu\nu}$, assuming parity and current conservation, and omitting any antisymmetric parts which would anyway vanish in the product with a symmetric $L_{\mu\nu}$, one finds [3] that the cross section may be parametrized by two unknown scalar functions which we call "structure functions" $W_1(\nu, Q^2)$, $W_2(\nu, Q^2)$ as follows:

$$\frac{\mathrm{d}^2\sigma}{\mathrm{d}\Omega \mathrm{d}E'} = \frac{4\alpha^2 E'^2}{Q^4}\left(2W_1 \sin^2\frac{\theta}{2} + W_2 \cos^2\frac{\theta}{2}\right). \tag{1.2}$$

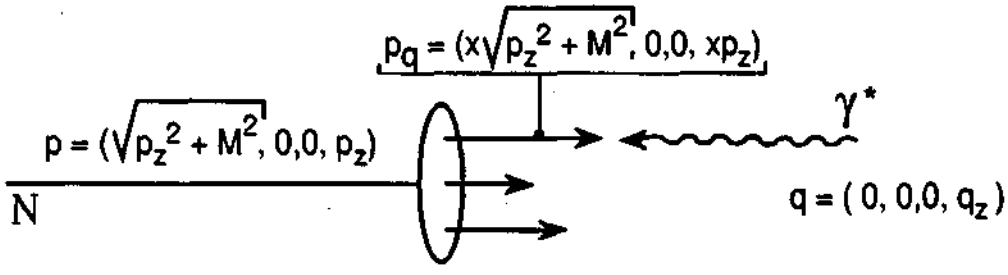

Figure 1.2: A nucleon in the infinite momentum frame. The struck quark carries four-momentum $p_q = xp$, a fraction x of the nucleon four-momentum p

Deep inelastic lepton scattering can be thought of simply as the scattering of a virtual photon off a nucleon, in that the lepton is only responsible for creating this virtual photon. A *virtual* photon is characterized by one additional degree of freedom with respect to a *real* one: it can have longitudinal polarization. This is why it is interesting to introduce the function $R(\nu, Q^2)$, the ratio of longitudinally to transversely polarized photon absorption cross sections:

$$R(\nu, Q^2) = \frac{\sigma_l}{\sigma_t} = \frac{W_2(\nu, Q^2)}{W_1(\nu, Q^2)} \left(1 + \frac{\nu^2}{Q^2}\right) - 1. \tag{1.3}$$

Simple theoretical reasoning [4] starting from the assumption that deep inelastic scattering off a nucleon is really only elastic scattering off a "free", pointlike parton in the limit:

$$\begin{aligned} Q^2 &\rightarrow \infty \\ \nu &\rightarrow \infty \\ \frac{Q^2}{\nu} &\quad \text{finite} \end{aligned}$$

leads to the concept of *Bjorken scaling.* That is to say, in the above mentioned limit (also called the Bjorken limit), the structure functions W_1 and W_2 no longer depend on both ν and Q^2, but only on their *ratio*, or on the earlier defined scaling variable x_{Bj}. So we can apply the following substitution:

$$\begin{aligned} MW_1(\nu, Q^2) &\longrightarrow F_1(x) = \frac{1}{2} \sum_i e_i^2 \left[q_i(x) + \overline{q_i}(x)\right] \\ \nu W_2(\nu, Q^2) &\longrightarrow F_2(x) = \sum_i x e_i^2 \left[q_i(x) + \overline{q_i}(x)\right], \end{aligned}$$

where we sum over all flavours i, e_i is the charge of quark of flavour i, and q_i is the probability for a quark of flavour i to have a momentum fraction x_{Bj} of the nucleon. This result follows if one calculates the cross section for the elastic scattering of a charged lepton off a pointlike, spin 1/2, charged particle (as in e.g. $\mu - e$ scattering), and then assumes that the total cross section (1.2) is just an incoherent sum of such elastic contributions from partons. In practice and beyond the naive quark parton model (where the nucleon simply consists of three uninteracting quarks) we have been using up to now, this scaling is violated because of the interactions between quarks at finite Q^2 ($\rightarrow QCD$, see below), so that F_1 and F_2 are slow functions of Q^2 as well. This gives for the cross section:

$$\frac{\mathrm{d}^2\sigma}{\mathrm{d}x\mathrm{d}Q^2} = \frac{4\pi\alpha^2}{Q^4} \left[\left(1 - y - \frac{Mxy}{2E}\right) \frac{F_2(x, Q^2)}{x} + y^2 F_1(x, Q^2) \right], \tag{1.4}$$

or equivalently, in terms of F_2 and R:

$$\frac{\mathrm{d}^2\sigma}{\mathrm{d}x\mathrm{d}Q^2} = \frac{4\pi\alpha^2}{Q^4} \frac{F_2(x, Q^2)}{x} \left[1 - y - \frac{Mxy}{2E} + \frac{y^2}{2} \frac{1 + 4M^2x^2/Q^2}{1 + R(x, Q^2)} \right]. \tag{1.5}$$

In the Bjorken limit for spin 1/2 partons, $R = 4M^2x^2/Q^2$, whereas for spin 0 partons $R = \infty$. Experimentally R is found to be above the first prediction, but does vanish at high Q^2 [5].

The most successful theory to date which can give some predictions about scale breaking, albeit only in the high-Q^2, i.e. short-wavelength domain, is Perturbative Quantum Chromodynamics (PQCD). We start from the concept of quarks as free, charged, spin 1/2 partons at $Q^2 \to \infty$, with a strong parton coupling that appears at finite Q^2:

$$\alpha_s(Q^2) = \frac{12\pi}{(33 - 2N_f)\ln(Q^2/\Lambda^2)},$$

where N_f is the number of quark flavors and Λ is the scale, a number determined from experiment and currently estimated at about 200 MeV, corresponding to a wavelength of $\sim 1fm$, the radius of the proton. QCD is then able to predict the evolution in Q^2 of the quark and gluon distributions, provided Q^2 stays sufficiently large (above ~ 1 GeV$^2/c^2$) so that α_s is sufficiently small for a perturbative calculation. This evolution in the leading $\ln(Q^2)$ approximation (and first order in α_S)is described by the Dokshitzer-Gribov-Lipatov-Altarelli-Parisi (DGLAP) evolution equations [1] [6]:

$$\frac{dq_i(x,Q^2)}{d(\ln Q^2/\mu^2)} = \frac{\alpha_S(Q^2)}{2\pi}\int_x^1 \frac{dz}{z}\left[q_i(z,Q^2)P_{qq}(x/z) + G(z,Q^2)P_{qG}(x/z)\right] \quad (1.6)$$

$$\frac{dG(x,Q^2)}{d(\ln Q^2/\mu^2)} = \frac{\alpha_S(Q^2)}{2\pi}\int_x^1 \frac{dz}{z}\left[\sum_j q_j(z,Q^2)P_{Gq}(x/z) + G(z,Q^2)P_{GG}(x/z)\right], \quad (1.7)$$

where the sum runs over all quark and antiquark flavours, $q_i(z,Q^2)$ ($G(z,Q^2)$) are the probabilities for a quark of flavour i (gluon) to be found with fraction z of the nucleon momentum, and $P_{ab}(x/z)$ are the *splitting* functions. More precisely, $P_{qq}(x/z) = P_{Gq}[(z-x)/z]$ describes the probability for a quark of momentum fraction z to radiate a gluon of momentum fraction $(z-x)$ and retain momentum fraction x. Similarly, $P_{qG}(x/z)$ is the probability for a gluon of momentum fraction z to create a quark-antiquark pair where the quark will carry momentum fraction x and the antiquark momentum fraction $(z-x)$ or vice-versa, whereas $P_{GG}(x/z)$ gives the probability for a gluon to radiate another gluon (the so-called "triple gluon vertex", distinct feature of QCD not existing in QED – a photon cannot radiate another photon). These equations essentially say that a parton with momentum fraction x_{Bj} can actually be a "daughter" parton "generated" by some "parent" parton at a higher momentum fraction z by some QCD process. The quantity μ^2 is an infrared cutoff scale for gluon radiation; for $Q^2 < \mu^2$ the nucleon appears as in the naive quark parton model: made up of three valence quarks.

A qualitative graphical representation of the Q^2 evolution (i.e. scale breaking) of F_2 in the perturbative *and* nonperturbative regimes is given in Fig. 1.3. An elementary proton at very low Q^2 carries the whole of its momentum. Resolving valence quarks and hitting only one of them means we hit a parton with 1/3 of the nucleon momentum. This is a naive QPM picture. Taking into account the interactions between quarks due to gluon exchange, the quark momentum is smeared. By the Heisenberg uncertainty principle we can understand this smearing as a consequence of valence quark confinement. However, the gluons now carry about half the momentum (see below), so the distribution is shifted down to a mean of about 1/6 [88]. Finally, arriving in the perturbative QCD regime, the gluons themselves fluctuate into Dirac sea quark-antiquark pairs. This makes it possible for the virtual photon to be "absorbed" by one of the sea quarks. This is how deep inelastic

[1] often referred to as Altarelli-Parisi equations

scattering is sensitive to the gluon distribution. Incidentally, it is impossible for a gluon itself to "absorb" a photon the way a quark does, because the gluon has no charge and thus does not couple to the virtual photon.

Increasing Q^2 further still brings about only a very slow (logarithmic) scale breaking described by the DGLAP evolution equations.

In this respect one should note that the integral of F_2 over the whole x range at a given value of Q^2 measures the total momentum fraction carried by the valence *and* sea quarks

$$\int_0^1 F_2(x,Q^2) = \int_0^1 \sum_f e_f^2 x q_f(x,Q^2) \mathrm{d}x, \tag{1.8}$$

measured to be about 0.127 ± 0.005, corresponding to a momentum fraction carried by quarks of 46% for a deuteron at $Q^2 = 15$ GeV$^2/c^2$ [7]. This means that more tban half the momentum of the nucleon is carried by glnons.

Experimentally, the F_2 structure function on the proton and deuteron has been measured by many experiments. Let us just mention some of the most recent and precise measurements:

- a series of experiments at the Stanford Linear Accelerator during the seventies and early eighties at intermediate and high x_{Bj} [8];
- the European Muon Collaboration (EMC) [9, 10] and
- the BCDMS collaboration [11, 12] in the CERN SPS muon beam in the early eigbties at somewhat lower values of x_{Bj};
- most recently by the New Muon Collaboration down to $x_{Bj} = 0.006$ [13] with more data currently being analysed eventually to extend even lower in x_{Bj}.

A longstanding discrepancy between the EMC and BCDMS measurements has been resolved by these newest NMC results which are found to be in agreement with BCDMS and disagree with EMC up to 20 % in the lowest x_{Bj} bins. The current experimental knowledge taken from three consistent data sets (leaving out EMC) is summarized in Fig. 1.4. Such detailed knowledge of the F_2 structure functions of the proton and the deuteron enabled us recently to extract quark and gluon distributions and α_S from a QCD analysis of the observed scale breaking [14] (Fig. 1.5.).

One must mention that all eyes are today turned towards the HERA experiments, H1 and ZEUS, which will be able to measure structure functions down to $x_{Bj} = 10^{-4}$. Some preliminary HERA results compared to NMC results as a function of x_{Bj} are shown in Fig. 1.6.

Apart from charged leptons, there is another "clean" probe one can use to probe the interior of nucleons – the neutrino (or antineutrino). The neutrino can react via neutral current or charged current, exchanging a neutral Z^0 or a charged W boson:

$$\begin{aligned}
\nu_\mu + N &\longrightarrow \nu_\mu + X \quad (\mathrm{Z}^0 \text{ exchanged}) \\
\overline{\nu_\mu} + N &\longrightarrow \overline{\nu_\mu} + X \quad (\mathrm{Z}^0 \text{ exchanged}) \\
\nu_\mu + N &\longrightarrow \mu^- + X \quad (W^+ \text{ excbanged}) \\
\overline{\nu_\mu} + N &\longrightarrow \mu^+ + X \quad (W^- \text{ exchanged})
\end{aligned} \tag{1.9}$$

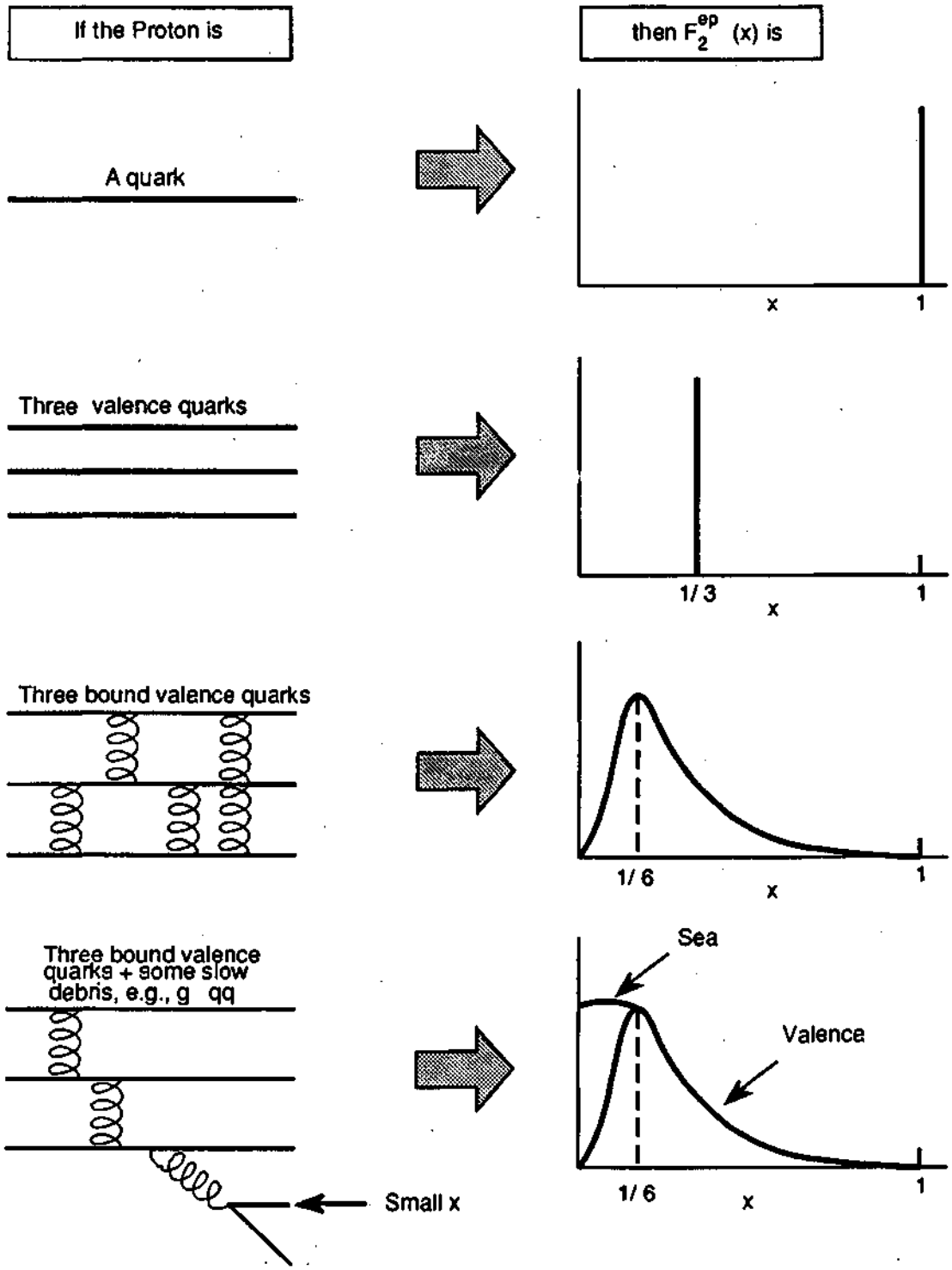

Figure 1.3: Increasing Q^2 of the virtual photon probe reveals more and more details of the proton structure (see text).

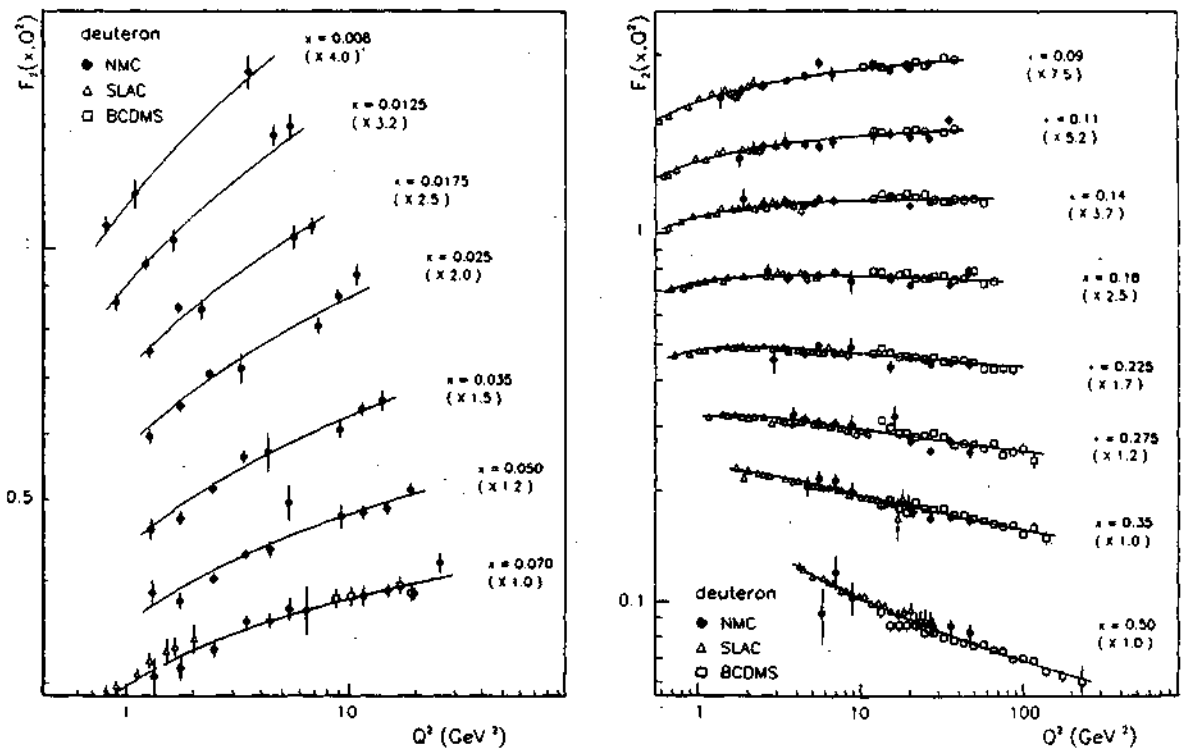

Figure 1.4: $F_2^D(x, Q^2)$ from NMC (black points), SLAC (triangles) and BCDMS (squares). The curve is a 15-parameter fit through all three data sets. Data points from different x bins have been multiplied by the factors in parentheses for clarity of presentation. From [13]

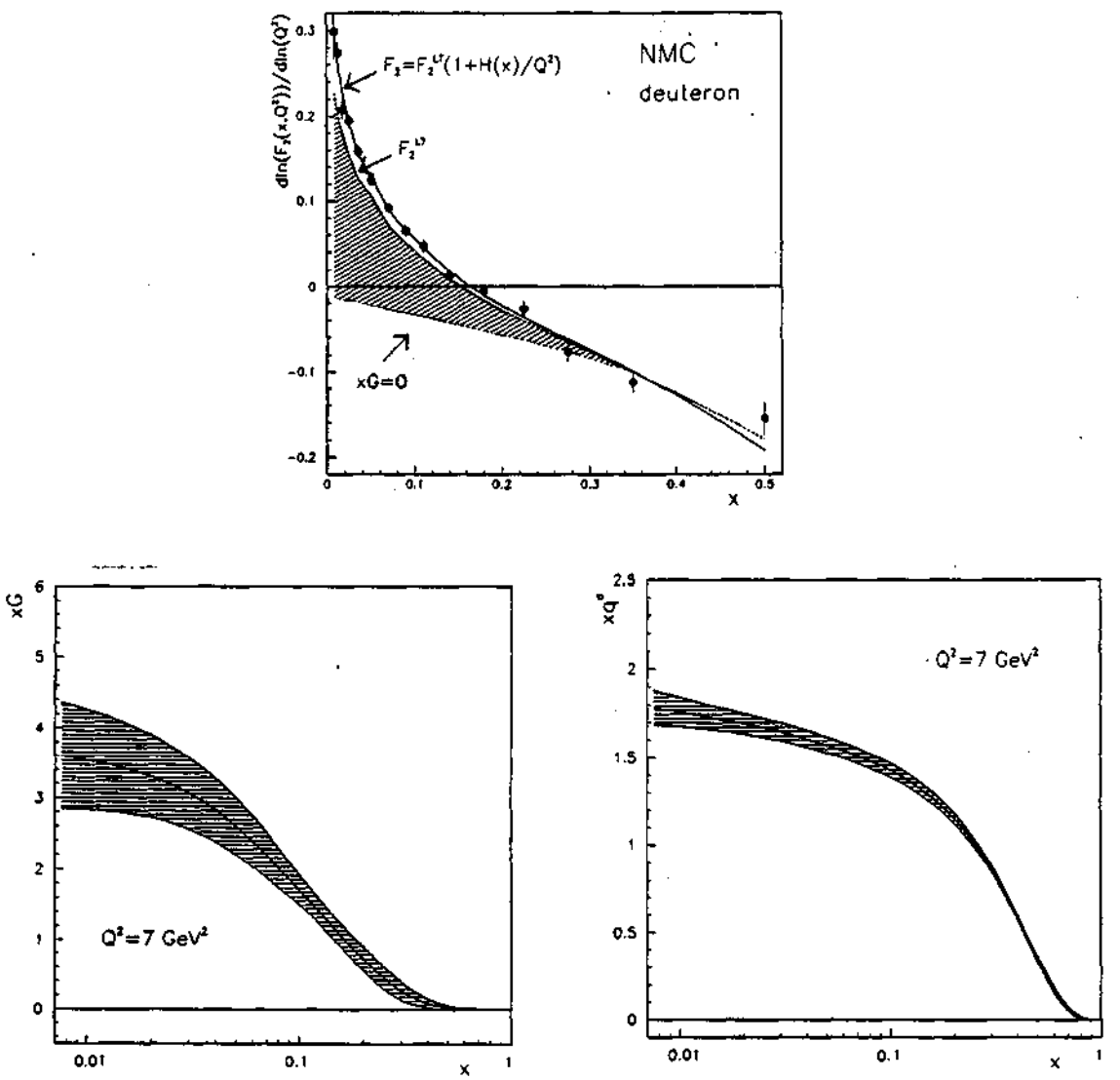

Figure 1.5: Top: Scale breaking of $F_2^D(x,Q^2)$ from NMC (logarithmic slopes $\partial F_2^D/\partial \ln(Q^2)$ vs. x_{Bj}) compared to that predicted by QCD in leading order (dashed line) and next-to-leading order (full line). The lower dotted line represents Q^2 evolution from quarks only (no gluons). Bottom: the deuteron quark (left) and gluon (right) distribution extracted from the fit at $Q^2 = 7$ GeV$^2/c^2$.

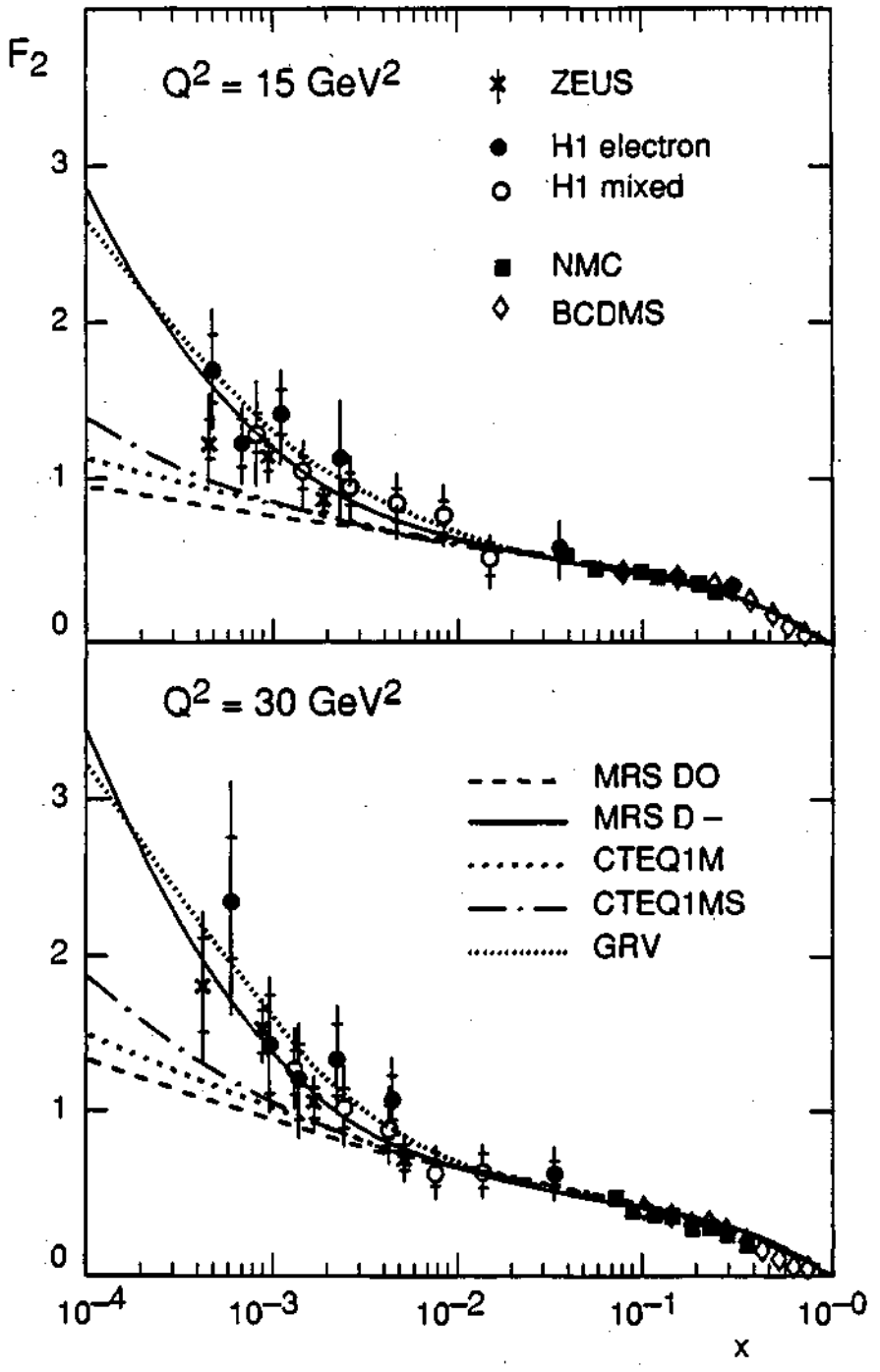

Figure 1.6: $F_2^p(x_{Bj})$ at $Q^2 = 15$ and 30 GeV$^2/c^2$ from NMC, BCDMS and first results from the HERA experiments, ZEUS and H1. Also shown are some recent F_2 parametrizations by Martin, Roberts and Stirling (MRS), Morfin et al. (CTEQ) and Glück, Reya and Vogt (GRV).

In this case, the cross section is slightly different than in the case of tbe electromagnetic interaction of charged muons. Remember we said we assumed parity conservation when deriving 1.2; the weak interaction induced by neutrinos violates parity and thus a third structure function is needed to describe this parity-violating part. Equation 1.5 is thus transformed to:

$$\begin{aligned}
\frac{\mathrm{d}^2\sigma^{\nu N}}{\mathrm{d}x\mathrm{d}Q^2} &= \frac{G^2}{2\pi}\left[y^2 F_1^{\nu N}(x,Q^2) + \left(1-y-\frac{Mxy}{2E}\right)\frac{F_2^{\nu N}(x,Q^2)}{x} + y\left(1-\frac{y}{2}\right)F_3^{\nu N}(x,Q^2)\right] \\
\frac{\mathrm{d}^2\sigma^{\bar{\nu}N}}{\mathrm{d}x\mathrm{d}Q^2} &= \frac{G^2}{2\pi}\left[y^2 F_1^{\bar{\nu}N}(x,Q^2) + \left(1-y-\frac{Mxy}{2E}\right)\frac{F_2^{\bar{\nu}N}(x,Q^2)}{x} - y\left(1-\frac{y}{2}\right)F_3^{\bar{\nu}N}(x,Q^2)\right],
\end{aligned} \tag{1.10}$$

where G is the Fermi weak interaction coupling constant measured in beta decay. The F_3 structure function can thus be extracted from the difference of cross sections measured with a neutrino and an antineutrino beam.

The F_1 and F_2 structure functions are not necessarily the same in neutrino and charged lepton scattering. In fact, a recent comparison of high statistics neutrino F_2 results from the CCFR collaboration with the NMC result [15] shows an enhancement of up to 20% of the neutrino F_2 compared to the charged lepton one. This may be due to the fact that the mechanism of probing the strange and charm sea quark distribution is different in tbe two cases (Fig. 1.7) – the photon-gluon fusion probes either pure $c\bar{c}$ pairs or pure $s\bar{s}$ pairs, whereas cbarged current probes $c\bar{s}$ and $\bar{c}s$ combinations. According to [16] the heavy flavour contribution to F_2 identically vanishes for x_{Bj} greater than

$$x_{max} \approx \frac{Q^2}{Q^2 + 4m_q^2}$$

where m_q is the mass of the quarks cbaracteristic for the reaction. As $m_c > \frac{1}{2}(m_c+m_s) > m_s$ tbe thresholds will evidently be different, the charm contribution in muon scattering being highly suppressed, while in neutrino scattering it will be equal to the strange contribution.

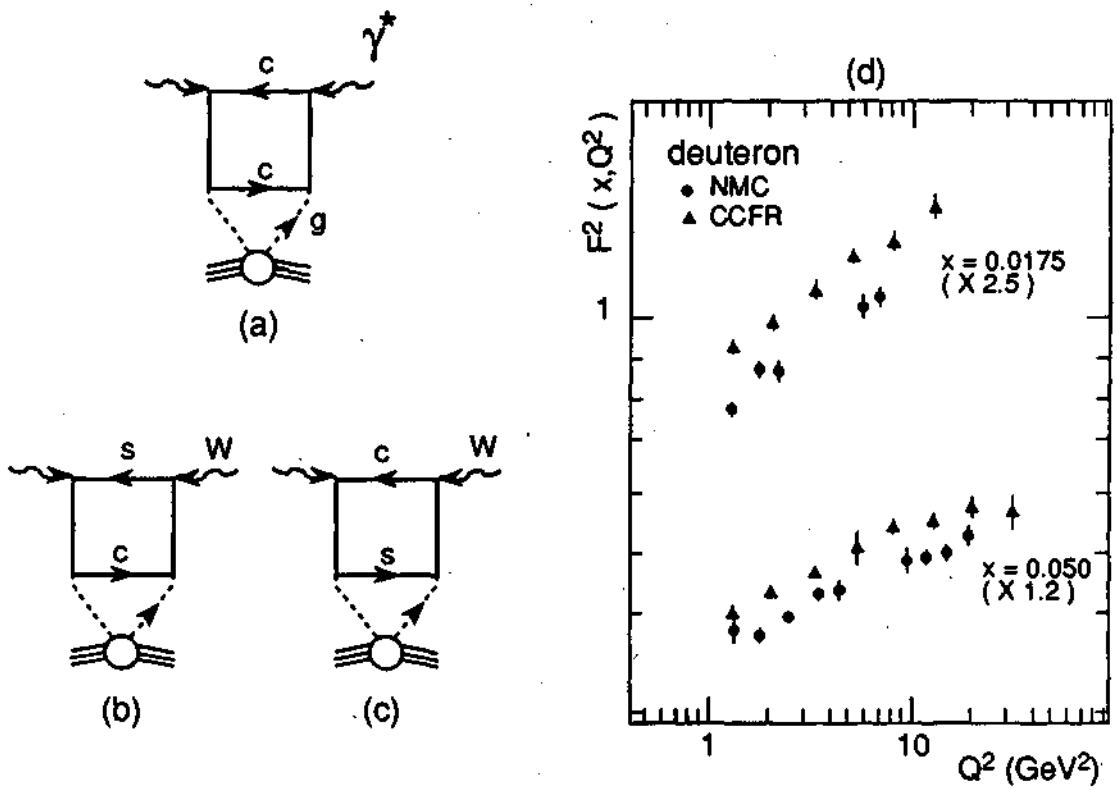

Figure 1.7: **a** Photon-gluon fusion in μN scattering. **b** W^+-gluon fusion in νN scattering. **c** W^--gluon fusion in νN scattering. **d** Comparison of the NMC $F_2^{\mu d}$ (circles) and CCFR $F_2^{\nu d}$ (triangles) in the two lowest x_{Bj} bins

1.2 Nuclear effects in deep inelastic scattering

Let's go back for a moment to our billiards story, and imagine what happens when we apply it to a nucleus. We imagine now a basketball made of the earlier billiards poorly glued together. If we gently nudge the basketball, it will behave as a whole. This is what is called *coherent* scattering on the nucleus. If we hit it a little harder, first the weak glue between billiards will give way, and the struck billiard will break free. This we call *quasielastic*. If we hit harder still, we'll strike one of the marbles and get *deep inelastic* scattering on the basketball – which is actually an elastic scattering on a marble.

So where's the problem? Well, it so happens that the deep inelastic scattering on the basketball doesn't give just the sum of scatterings on the individual billiards, as one would expect. This is what is called the EMC effect (after the European Muon Collaboration which discovered the effect in 1982 [29]).

In order to visualize nuclear effects, we construct the ratio of structure functions:

$$\mathcal{R}^A_{F_2}(x_{Bj},Q^2) = \frac{F_2^A(x_{Bj},Q^2)}{F_2^D(x_{Bj},Q^2)}, \tag{1.11}$$

where $F_2^A(x_{Bj},Q^2)$ is the structure function *per nucleon* in nucleus A, and $F_2^D(x_{Bj},Q^2)$ is the reference structure function, the structure function per nucleon of deuterium. Why do we compare to deuterium, when the choice of a free proton seems so much simpler? Simply because the proton and neutron have different structure functions, a fact which is known since the SLAC experiments [8]. So we need an "average nucleon" reference. Here deuterium is supposed to represent just an incoherent sum of a proton and a nucleon i.e.

$$F_2^D(x_{Bj},Q^2) = \frac{1}{2}\left(F_2^p(x_{Bj},Q^2) + F_2^n(x_{Bj},Q^2)\right). \tag{1.12}$$

This means we are neglecting any possible nuclear effects in deuterium, the deuteron being only loosely bound. Recently this has been disputed [18, 19, 20, 21], but anyway we cannot measure the structure function of a free neutron so the deuteron is the only possible experimental reference.

Now in an experiment of course we measure cross sections, and cross section ratios:

$$\mathcal{R}^A_\sigma(x_{Bj},Q^2) = \frac{\left(\frac{d^2\sigma^A}{dx_{Bj}dQ^2}\right)}{\left(\frac{d^2\sigma^D}{dx_{Bj}dQ^2}\right)} \tag{1.13}$$

If we now plug eq. 1.5 into 1.13, it is easily seen that the term in brackets will cancel in the ratio under the condition:

$$R^A(x_{Bj},Q^2) = R^D(x_{Bj},Q^2) \tag{1.14}$$

Current experimental knowledge supports this assumption [28] (Fig. 1.8), and this enables us to say that we measure a structure function ratio by measuring a cross section ratio. In the remainder of this work, for the sake of simplicity, we will therefore refer only to "the ratio", $\mathcal{R}^A(x_{Bj},Q^2)$.

1.2.1 Experimental evidence and phenomenology

A single predictable (and predicted) difference between a nucleon in a nucleus and a free nucleon was Fermi smearing. That is to say that our billiards aren't statically glued together

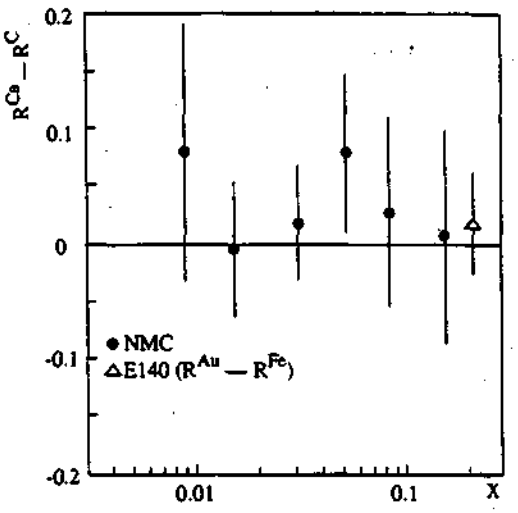

Figure 1.8: Measured values of $R^{Ca} - R^{C}$ as a function of x_{Bj} from NMC and $R^{Au} - R^{Fe}$ from SLAC E140 (from ref. [28]).

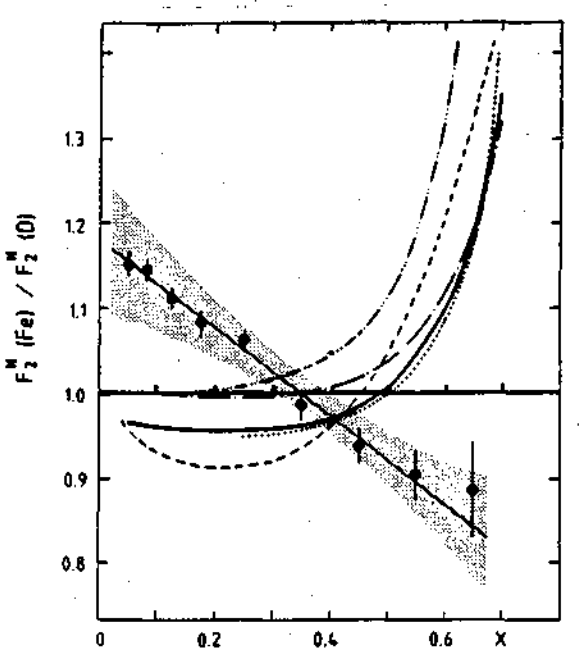

Figure 1.9: The original EMC measurement of F_2^{Fe}/F_2D compared to the expectation taking into account Fermi motion in the nucleus. Figure from [29]

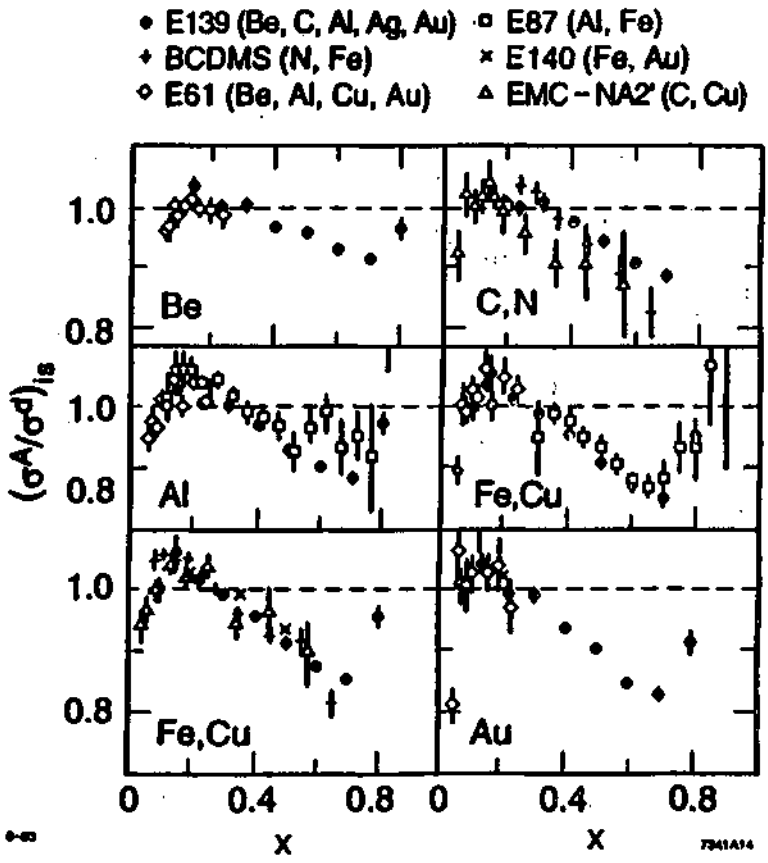

Figure 1.10: Measurements of nuclear effects at intermediate and high x_{Bj} before dedicated low-x_{Bj} experiments came around.

– they are quantum objects and therefore subject to the Heisenberg uncertainty principle. As they are constrained to be inside a nucleus (i.e. in space), they must move around to respect their indetermination in momentum. So the kinematics presented in section 1.1.2 no longer strictly apply since the target nucleon was there assumed to be at rest. The net effect is a shift for the momenta of the marbles (partons) to higher momentum fractions (the momentum fractions are measured with respect to a free billiard, but in a basketball the billiard moves inside the basketball so its momentum it has to share between marbles is bigger, hence an increase in x_{Bj}). This translates into an enhancement of the ratio at high x_{Bj} and a slight depletion at intermediate x_{Bj}.

Much to the surprise of the particle physics community, the EMC discovered a behaviour of the ratio with a slope showing an effect quite opposite to the expected one [29] (Fig. 1.9).

However, a reanalysis of 10-year-old SLAC E87 and E49B data revealed a confirmation of what became known as the *EMC effect*, albeit with somewhat less enhancement in the lower x_{Bj} region.

Very quickly experiments were designed to study in more detail this unexpected effect – SLAC E139, BCDMS and EMC NA2' [30]. Results from these "second generation" experiments are summarized in Fig. 1.10. A clear pattern started to emerge, with the appearance of a rise at high x_{Bj} where Fermi smearing takes over from the EMC effect

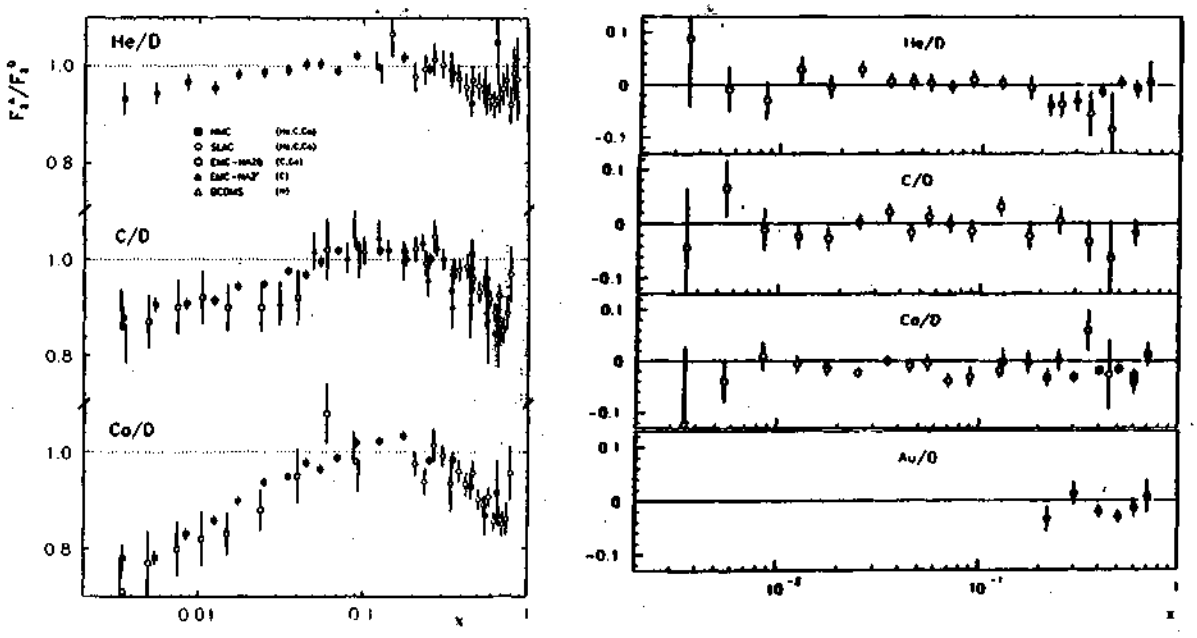

Figure 1.11: Left: measurements of structure function ratios at low and intermediate x_{Bj} by dedicated low-x_{Bj} experiments: EMC-NA28 and NMC, compared to earlier experiments at higher x_{Bj} (notice the logarithmic scale). Right: the logarithmic slopes $b = d(F_2^A/F_2^D)/d(\ln Q^2)$ vs. x_{Bj} – open circles from NMC, black circles from SLAC E139. Black squares are Fe/D points from SLAC E139 compared to Ca/D from NMC. From ref. [23].

dip, and a downwards turn of the ratio at low x_{Bj} where first hints of a depletion become apparent.

A dedicated low-x_{Bj} experiment followed, EMC NA-28 [31], which studied in more detail this depletion, or shadowing, region (see below), and found no Q^2-dependence of shadowing. The New Muon Collaboration (NMC) upgraded the EMC spectrometer (see Chapter 2) especially for the purpose of determining ratios of cross sections with small systematic errors, and accepting events at very low scattering angles. A first set of measurements on He, Ca, C, Li, and D targets gave precise measurements of structure function ratios in the range $0.0035 < x_{Bj} < 0.6$ [32, 33]. Little or no Q^2-dependence of the ratio was confirmed, except in the case of Ca/D where slightly negative logarithmic slopes $b = \mathrm{d}(F_2^A/F_2^D)/\mathrm{d}(\ln Q^2)$ are seen (Fig. 1.11).

A new *calorimeter target setup* was used to measure the A-dependence of the nuclear effects with high statistics [24]. Fig. 1.12 summarizes the A-dependence result. It shows that the depletion, or shadowing, increases with increasing $\log A$, as does the enhancement, or antishadowing. The SLAC data [90] confirm this trend of a global increase of nuclear effects with rising atomic number in the EMC effect and Fermi motion regions. The remarkable feature of this measurement is that the crossing point of the $\log A$ slopes is at $x_{Bj} = 0.05$, a value close to the crossing point for the x_{Bj}-dependence of the ratio itself, which would mean that the crossing point of the ratio (i.e. the value of x_{Bj} where $F_2^A = F_2^D$) is *independent of* A.

In parallel, another experiment (FNAL E665) is currently exploring the very low x_{Bj}

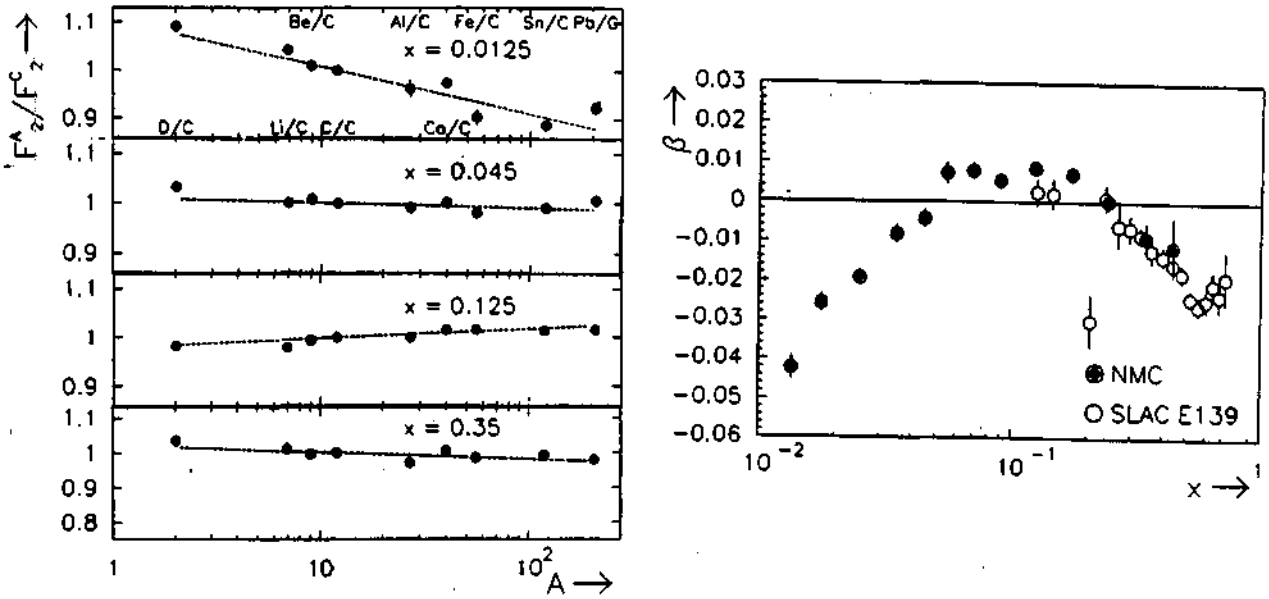

Figure 1.12: A-dependence of nuclear effects. **a** Straight lines were fitted to the ratio F_2^A/F_2^C vs. A in each x_{Bj} bin. Three sample x_{Bj} bins are shown. **b** The log$A$-dependence slopes, $\mathrm{d}(F_2^A/F_2^C)/\mathrm{d}(\log A)$ as a function of x_{Bj} from NMC (preliminary) and SLAC E139.

region (x_{Bj} down to $2 \cdot 10^{-5}$) and has published a first result indicating *saturation of shadowing*, i.e. the ratio is approximately independent of x_{Bj} for $x_{Bj} < 10^{-3}$ [35].

To summarize current knowledge on nuclear effects prior to this work, let us cast a glance on fig. 1.13. Phenomenologically we now know, going from $x_{Bj} = 1$ to 0:

- There is a rise of the ratio due to Fermi motion for $x_{Bj} > 0.6$;
- There is a dip in the region $0.2 < x_{Bj} < 0.6$, called the EMC effect;
- There is an enhancement, or antisbadowing of the ratio between $0.05 < x_{Bj} < 0.2$;
- There is a depletion, or shadowing region at $x_{Bj} < 0.05$ which may exhibit saturation at $x_{Bj} < 0.001$;
- All these effects depend weakly (if at all) on $\log Q^2$;
- All these effects are enhanced with growing atomic number (log$A$.

The motivation to study nuclear effects on lithium and carbon compared to deuterium comes from the fact that they have similar radii (2.6 and 2.5 fm for ^{6}Li and ^{12}C respectively), but different nuclear densities (0.04 fm^{-3} and 0.09 fm^{-3}). As we shall see, some theoretical models rely on overlapping of nucleons to explain the EMC effect, and there a comparison between lithium and carbon could prove a useful check.

Also of course there was an urge to go ever lower in x_{Bj} to see if the sbadowing continues indefinitely, or if it saturates somewhere. If we believe that physics is continuous from $x_{Bj} = 0$ to 1, then we would expect the shadowing to saturate at a value compatible

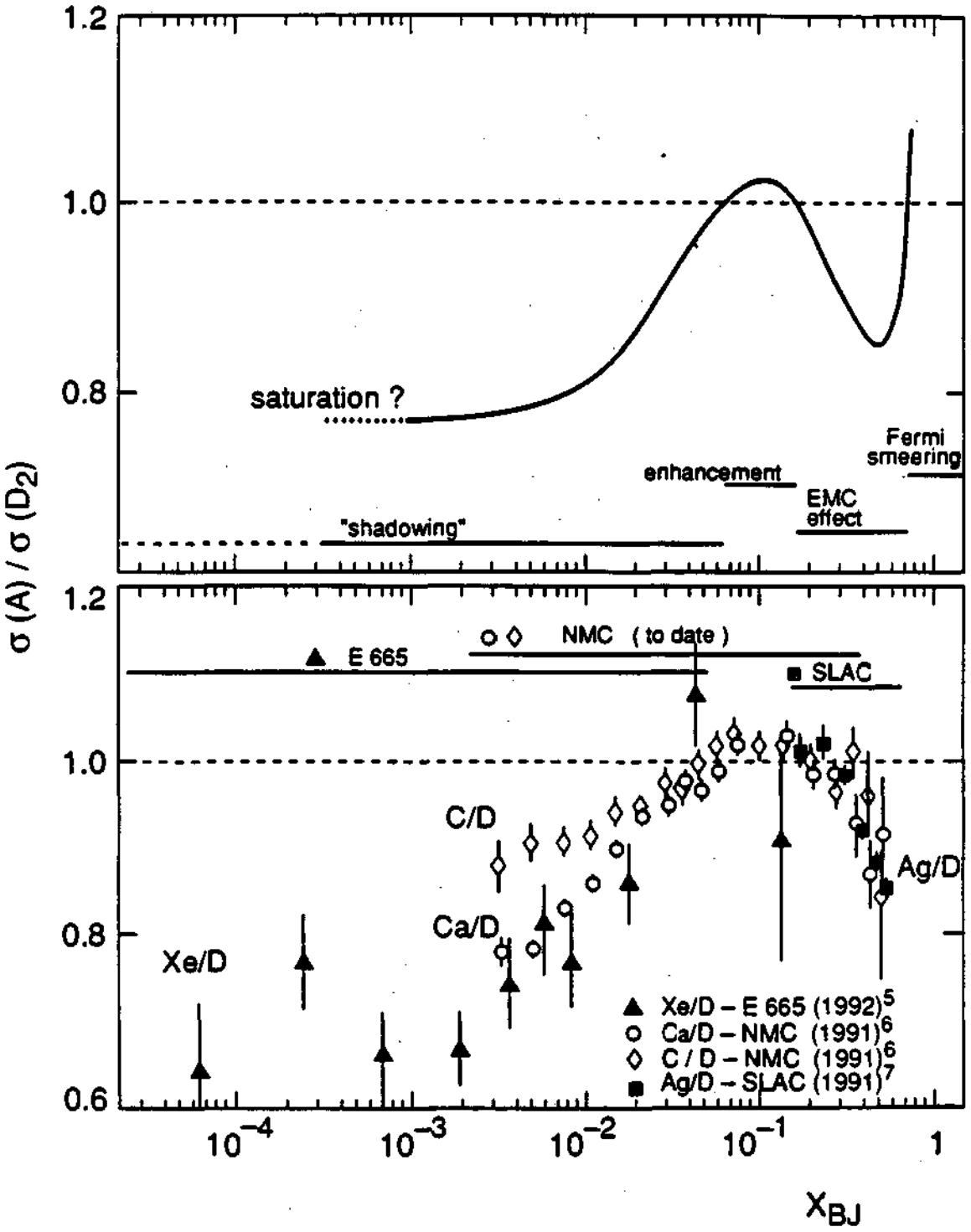

Figure 1.13: Knowledge about nuclear effects prior to this work. **a** A generic shape of σ^A/σ^D and different regions. **b** Some of the latest and most precise data sets from NMC, SLAC, and E665.

with the value obtained by real photon experiments [22] ($\gamma + N \longrightarrow X$), 0.832±0.010 and 0.895±0.006 respectively for $\sigma_{\gamma C}/\sigma_{\gamma D}$ and $\sigma_{\gamma Li}/\sigma_{\gamma D}$.

1.2.2 Some models of nuclear effects

The current understanding of nuclear effects in deep inelastic scattering is incomplete. One theorist said: "All models of the EMC-effect are wrong, including mine." There is a plethora of theoretical models mostly explaining only a part of the effects observed in experiment. Rather than repeat a complete review given in [23] and many past NMC Ph.D. theses [24, 25, 26, 27], we can try to find analogies for some of them in our billiards picture.

Let us start by the intermediate-x_{Bj}, or EMC-effect region. In this region there have been attempts to use "conventional" nuclear physics and invoke an **excess of pions** in nuclei, associated with the nucleon-nucleon interaction. We are thus introducing new "sticky" balls into the basketball (sticky because they represent the glue between nucleons). These billiards are lighter than the usual ones (nucleons) and therefore the x_{Bj} variable is limited to $m_\pi/m_{nucleon}$ (because $Q^2/2m_\pi\nu$ is limited to 1). So one gets excess scattering for $x_{Bj} < m_\pi/m_{nucleon}$. On the other hand, these sticky balls take on some momentum from the billiards and thus reduce their momenta, creating the dip in the region $x_{Bj} > m_\pi/m_{nucleon}$. However, the pionic models are only partially successful in explaining the EMC effect. Furthermore, they are unable to explain shadowing, their prediction being an endless rise of antishadowing at low values of x_{Bj}.

Equivalently in a **nuclear potential** picture rather than the pionic one, one can say that the nucleons themselves are trapped in a negative energy potential well, and since energy is mass this can be seen as an effective reduction of the nucleon mass, and hence a shift to higher x_{Bj} values. This leads to **x_{Bj}-rescaling**. However, the binding energy is a small effect ($\approx 1\%$ of the nucleon mass) and thus unable to explain the totality of the EMC effect.

Another possibility is invoking a hypothetical **swelling of nucleons** in the nucleus compared to their free radius, or better – the enlargement of the confinement region for quarks. This can be motivated by the concept of *overlapping* of nucleons. Let's imagine two of our billiards join into one. This would then form a large billiard twice the volume and each marble would thus be confined to a radius $\sqrt[3]{2}$ times larger. In a real nucleus, the actual overlap between nucleons can be calculated assuming some shape of the internucleon interaction [42]. Now as Q^2 in QCD always appears scaled by some scale Λ^2 or μ^2, which is related to the confinement radius $\lambda = 1/\mu$, this increase in confinement leads to **Q^2-rescaling** (increasing λ decreases μ and thus the effective Q^2/μ^2 is increased). For instance for a Fe nucleus a confinement increase of 15% leads to a reduction of $Q^2 \rightarrow Q^2/2$ and can reproduce the original EMC data. This rescaling in conjunction with nuclear binding can explain the intermediate-x_{Bj} nuclear effects [38]. However, this is contested by other authors, see ref. [23] for details.

Let us now mention a few models explaining the low-x_{Bj}, or shadowing region. In the **Vector Meson Dominance** model we question our probe – the virtual photon. Whereas a purely conventional Coulomb-interacting photon would have virtually resistance-free access to any of the marbles inside any of the billiards of our composite basketball (the white billiard is more like a bullet), we can imagine our virtual, hence massive, photon fluctuating into a quark-antiquark pair with the same quantum numbers as the photon itself ($J^{PC} = 1^{--}$) – a vector meson prone to strong interaction with nucleons. Such a hadronic component of the physical photon (fig. 1.13.) is supported by similarities seen between hard

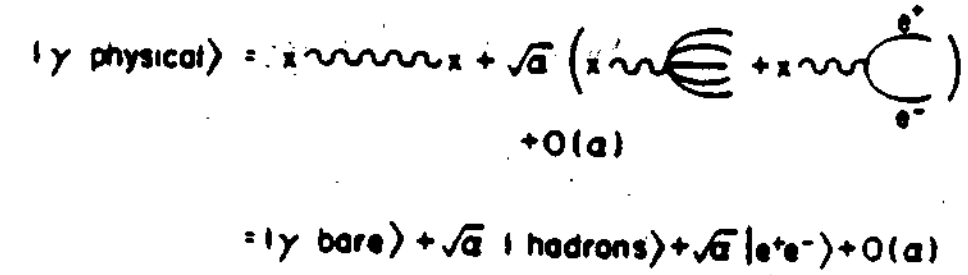

Figure 1.14: The hadron components of the photon, used in the VMD model (see text)

photon-induced reactions and purely hadronic reactions, in energy-, momentum transfer- and quantum number-dependences, the photon cross sections being suppressed by a factor of $\sim \alpha$ (fine structure constant). Now the white billiard is "real" (interacts strongly) and one easily concludes that it will have a preference for bouncing off the surface of the basketball rather than penetrating inside. This then explains shadowing, as an optical analogy – the incoming billiard only "sees" the billiards on the surface of the basketball, which cast a "shadow" on the nucleons inside. For a kinematic dependent explanation one needs to ask oneself how long this fluctuation will last: this follows again from the uncertainty principle. The hadronic fluctuation of our virtual photon with four-momentum $(\nu, \mathbf{q})$ has an energy

$$E_V = \sqrt{M_V^2 + \mathbf{q}^2} = \sqrt{M_V^2 + \nu^2 + Q^2}$$

where M_V is the rest mass of the vector meson; this energy compared to the energy of the virtual photon ν, gives a non-conservation (fluctuation) of:

$$\Delta E = E_V - \nu \approx \frac{Q^2 + M_V^2}{2\nu} \text{ when } Q^2 + M_V^2 \ll \nu^2$$

i.e. in the low-x_{Bj}, high ν limit. The fluctuation may then last ($\hbar = c = 1$) for a distance

$$d(M_v^2, Q^2) = \Delta t \approx \frac{2\nu}{Q^2 + M_V^2} = \frac{1}{Mx} \cdot \frac{1}{1 + M_V^2/Q^2}$$

Qualitatively, it is now evident that this fluctuation is going to be very short at high values of x_{Bj} (at a fixed Q^2). This means that the bullet becomes billiard when it is already inside a target billiard (and therefore has already penetrated the surface of the basketball), so there is no shadowing. Of course, it may have fluctuated into a billiard once *before* arriving to the surface, but as it is short-lived, it will become bullet again before touching it. But at low x_{Bj} the fluctuation may last long, so a fluctuation that starts outside the basketball lasts long enough to traverse a distance comparable to its size, and therefore it is a billiard, not a bullet that hits the surface of the basketball. Such is the x-dependence of shadowing as predicted by the VMD model. One also sees that VMD predicts vanishing of shadowing at $Q^2 \approx 1 - 2\text{GeV}^2/c^2$. Therefore more elaborate Generalized Vector Meson Dominance models exist which include the whole spectrum of known vector mesons ($\rho, \omega, \phi, J/\psi, ...$). These models predict shadowing even at Q^2 values as high as 40 GeV^2/c^2. Also we must note that these models don't attempt to explain effects at larger x_{Bj} – antishadowing and the EMC-effect region.

Another class of models (the **partonic models**) tries to explain shadowing and antishadowing leaving the virtual photon probe in its conventional shape (as a bullet), but

arguing about the modifications in the distributions of the partons (marbles) in the nucleus (basketball). One must say that here a paper by Nikolaev and Zakharov actually *predicted* shadowing and antishadowing in 1975 [36]. The basic idea is that the integrals of structure functions are conserved:

$$A\int_0^1 F_2^A(x)\mathrm{d}x = Z\cdot\int_0^1 F_2^p(x)\mathrm{d}x + (A-Z)\int_0^1 F_2^n(x)\mathrm{d}x$$

but that there may be a redistribution of momenta in nuclear media due to an effective deconfinement of the partons (marbles) inside the nucleus. In the language of quantum field theory authors often speak of *parton fusion*, but one can imagine that at low x_{Bj} the bullet (virtual photon) is somehow forced to scatter off two marbles instead of one. This is understood again with the help of the uncertainty principle which tells us that at low momentum fraction (which is low x_{Bj} in the Breit frame), the marble is "smeared out" over a distance larger than the billiard. Note that only one marble per billiard may have an extremely small x_{Bj} because the three billiards together have to add up to about one-half, the fraction of the nucleon momentum carried by quarks (the rest being carried by gluons, see section 1.1.3). In the neighbouring billiard there will also be a low-x_{Bj} marble which is smeared out, and thus the two will overlap. The incoming bullet will have no choice but to scatter either on both of them or not at all. But if it does scatter on both of them, the apparent momentum fraction will be the sum of the two and hence higher than the original! So we create an excess of higher-x_{Bj} partons and a lack of low-x_{Bj} ones, and we explain (predict!!!) the shadowing-antishadowing mechanism. Quantitatively, in ref. [36] it is argued that the maximal antishadowing should occur at an x_{Bj} value of about

$$x_0 \approx \frac{m_\pi}{m_{nucleon}} \approx 0.1$$

which is the experimentally measured value! In this model a leveling (saturation) of shadowing comes about naturally, at an x_{Bj} value where the quarks are smeared over the whole nucleus.

In a more quantitative calculation by Mueller and Qiu [37] gluon recombination from different nucleons is included to modify the Altarelli-Parisi evolution equations at low x_{Bj}. This reduces the number of gluons and hence sea quarks and brings about shadowing at low x_{Bj}. However, no antishadowing is predicted.

Still in the shadowing region, recently several models based on the exchange of Pomerons were proposed. In the low-x_{Bj} limit, also called the *Regge limit* (see for instance [41]), two-body scattering of hadrons is well described by exchanges of so-called *Regge poles*. They can be thought of as particles (a cross section has a pole at the invariant mass corresponding to the rest mass of a particle) with appropriate quantum numbers. The poles with quantum numbers of the vacuum are called Pomerons, whereas others with different quantum numbers are called Reggeons. Reggeons include known mesons (π, K, ρ,...) but also $q\bar{q}$ pairs with quantum numbers such that we cannot represent them by known mesons. Pomeron exchange on the other hand can be thought of as corresponding to an exchange of a pair of gluons, and will dominate at low x_{Bj}.

The application of this concept to deep inelastic scattering is to say that we are actually probing Pomerons and their structure, rather than that of the nucleons themselves.

One difficulty of the QCD-improved parton models is to describe accurately the extremely low x_{Bj} region presently accessible to experiments, i.e. when also Q^2 is very low (< 0.5 GeV$^2/c^2$) and thus outside the perturbative regime of QCD. Barone et. al. [39]

have recently attacked this region. They start at $Q^2 = 0$ with a nucleon composed of three constituent quarks (a constituent quark contains a valence or "real" quark, gluons, and part of the Dirac sea quarks and antiquarks) and evolve using a "finite difference evolution" technique, radiating gluons from valence quarks at each step and balancing the momentum between the two. After 5 steps they arrive to $Q^2 = 0.5$ GeV$^2/c^2$, and there normal QCD evolution takes over. The EMC effect then emerges as an effect of swelling, or stretching of nucleons. A larger confinement means a narrower momentum distribution of valence quarks (indetermination), hence a depletion at intermediate x_{Bj}; at the same time gluons cannot be radiated with a wavelength greater than the radius of the nucleon (because gluons carry colour, and a nucleon is a colour singlet, i.e. it is "white"). They then use the nucleon radius as an infrared cutoff of an otherwise divergent gluon density at low x_{Bj}. So for a larger (bound) nucleon, the cutoff is lower (in momentum), hence more glue can be generated and less momentum is left to the valence quarks. Shadowing in this model is explained as multiple Glauber scattering of a hadronic $q\bar{q}$ fluctuation of the virtual photon.

Another partonic approach is that of Zhu et al. They assume the nucleon is made up of three "constituent quarks" (each constituent quark contains a valence quark, some glue and some sea quarks and has on the average 1/3 of the nucleon momentum) and thus represent the structure function of the nucleon as a convolution:

$$F_2^N(x,Q^2) = \sum_i \int_x^1 \mathrm{d}y G^c_{N_i}(y) F^c_{N_i}(x/y,Q^2)$$

of the constituent quark distribution, $G^c_N(y)$ and the distribution of quarks and gluons in a constituent quark, $F^c_{N_i}(x/y,Q^2)$. The sum is over the three constituent quarks. Parton recombination (essentially gluon fusion) is responsible for shadowing and antishadowing, and nucleon stretching (in terms of constituent quark confinement) is at the origin of the EMC effect. Good agreement is found with NMC data.

The last two models are the most successful ones in describing presently available data – they use two distinct mechanisms to explain the whole x_{Bj} measured region. More shall be said in chapter 5, when comparing models to our data.

Chapter 2

The experiment

The aims of the NMC experiment in 1985. [43] were defined as follows:

- A high-precision (high-statistics, low-systematics) study of nuclear effects on F_2 in the low, intermediate and high x_{Bj} ranges, their x_{Bj}, Q^2 and A-dependences, a measurement of $R = \sigma_L/\sigma_T$ as a function of A, and of the cross-section for J/ψ production on different nuclei.

- A high luminosity simultaneous measurement of the F_2 structure function on hydrogen and deuterium. This was to provide an accurate measurement of F_2^n and F_2^p and even more accurately, the ratio F_2^n/F_2^p as a function of x_{Bj} and Q^2.

The experiment consisted of a higb energy muon beam, a beam momentum measuring detector, a complementary target setup, and a forward tracking spectrometer. One hundred and fifty-five planes of wire chambers – multiwire proportional chambers, drift chambers, 43 scintillator hodoscope planes, an lead-iron-scintillator calorimeter; two big magnets and a group of three magnets, and an ingenious target setup. All of this is distributed over more than 40 m lengtb (not mentioning the kilometer-long muon beamline that precedes it) in a separate experimental hall, the data read out by hundreds of time-to-digital converter (TDC) channels and virtually countless analog-to-digital converters (ADC's), hundreds of high voltage supply channels, tens of individual gas supplies, not to mention an intricate data acquisition system which manages to write hundreds of events to tape at each spill – this array of apparatus dating from the end of the seventies is the largest fixed target experiment at CERN, only recently surpassed by the giant collider experiments.

Each event used in the analysis has a muon whose momentum is measured before the scattering, and after it. We shall later refer to these as the beam and the scattered muon, but by time coincidences we know that we are measuring the same muon before and after scattering.

The experimental setup (fig. 2.1) being an upgraded version of the EMC spectrometer, built in 1978, has been described in many Ph.D. theses and in [44, 45]. We shall thus give only the essential description, concentrating on the special upgrades relevant to the present work (complementary target setup, small-angle and small-x_{Bj} triggers).

The NMC coordinate system is defined as follows: the x coordinate is along the beam, pointing downstream, with an origin (x=0) in tbe center of tbe Forward Spectrometer Magnet (FSM, see 2.4.2). The z coordinate is pointing vertically upward, and the y coordinate is directed horizontally pointing towards the Jura mountain. Internally in NMC we often

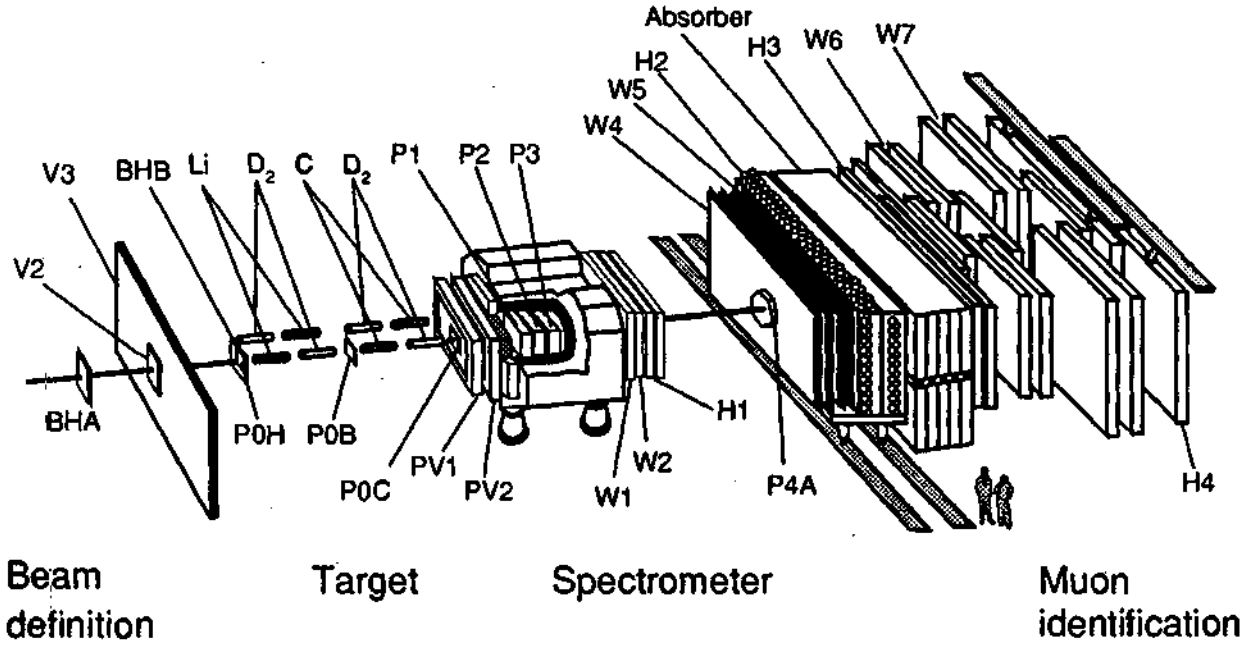

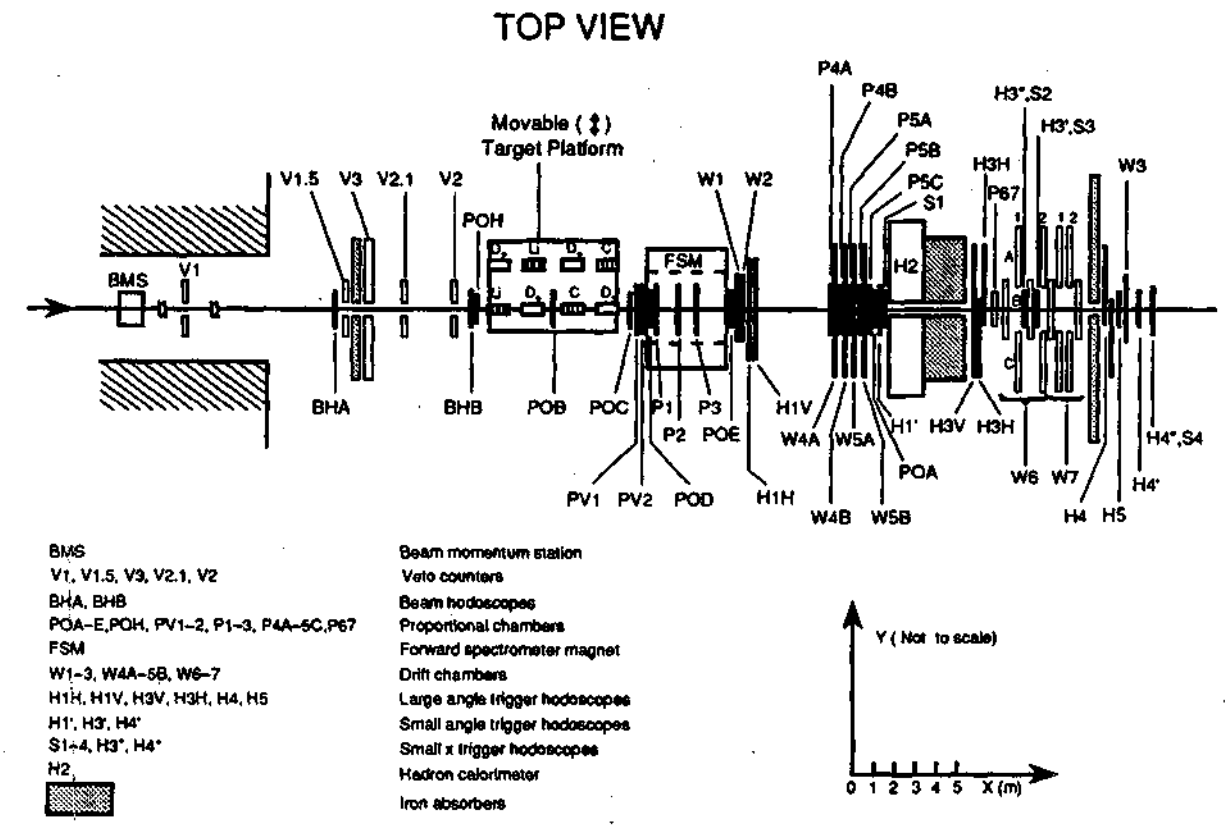

Figure 2.1: The NMC apparatus – an artists view and a more detailed top view. The beam comes in from the left

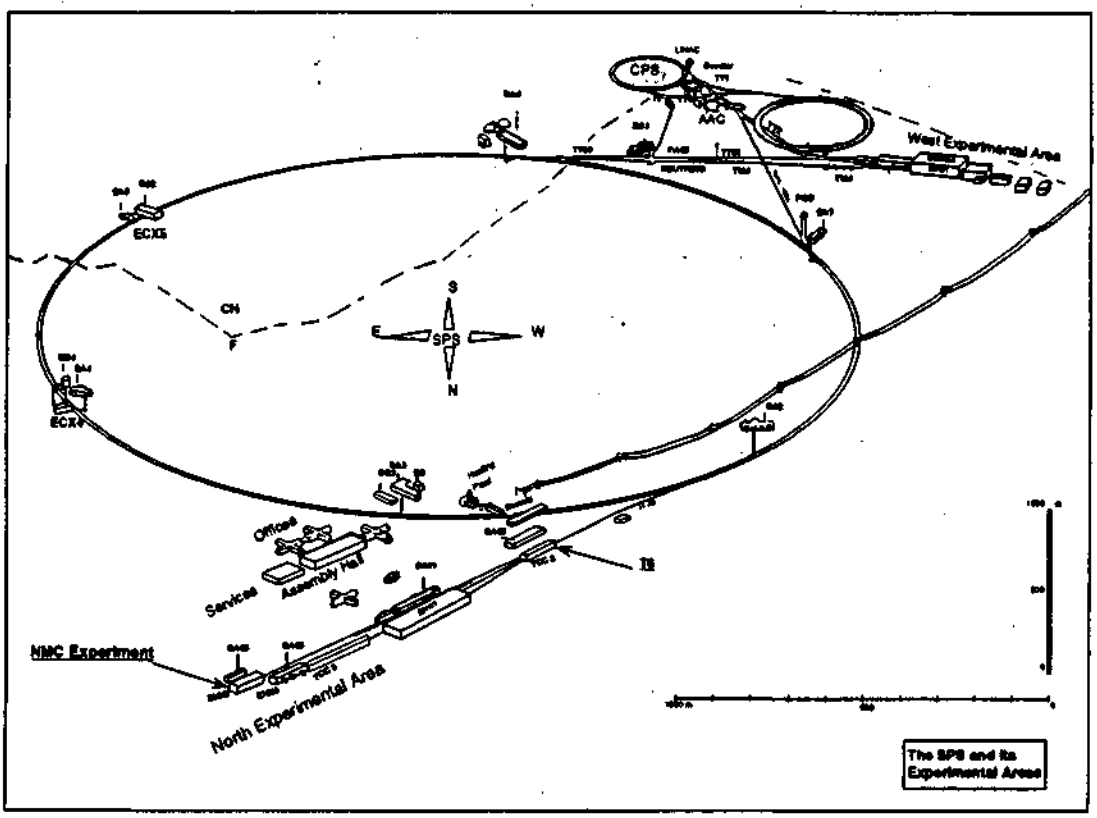

Figure 2.2: The general layout of the Super Proton Synchrotron (SPS), 7 km in circumference, astride on the Franco-Swiss border

speak of Jura and Saleve positions, especially for the alternating target setups, Saleve being a mountain in the negative y-direction.

2.1 The CERN SPS M2 muon beam line

The high energy muon beam of the CERN SPS accelerator makes it possible to perform deep inelastic scattering at energies up to 280 GeV. The SPS accelerator, shown on fig. 2.2. accelerates protons to 400 GeV in a bunch regime – their extraction is performed once every 14 seconds. In our case, it is a *slow* extraction producing a 2-second *spill* rather than a high intensity bunch that would create enough muons to burn all the beam chambers of our experiment, and also too many events for the data acquisition system to handle.

The protons are incident on a tungsten target (T6 on Fig. 2.3) and scatter inelastically, producing a high intensity π and K meson beam. The target is 40 to 500 mm thick depending on the intensity of muon beam desired. The pion/kaon beam is then deflected horizontally in order to dump the unused primary protons and select the charge and a momentum band for the mesons. Positive mesons (π^+, K^+) are used to obtain a μ^+ beam, and negative ones for a μ^- beam. This is achieved by a field lens and momentum slit. The beam is then deflected upwards because of the rising contours of the site, and before entering the decay channel, there is one more horizontal deflection to compensate for dispersion.

Next comes the focussing-defocussing ("FODO") decay channel, where the mesons then

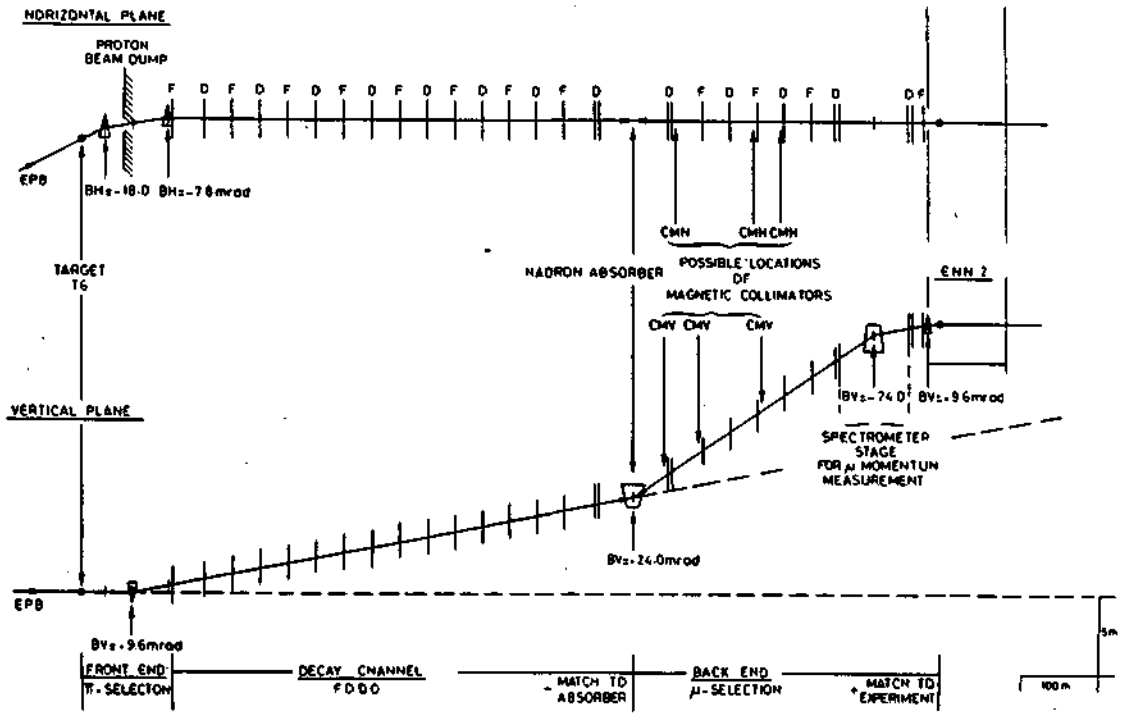

Figure 2.3: The M2 beam line.

weakly decay into muons in flight. About 5% of them decay in the 590 m long channel. The momentum spread of the muons is wide – it lies between 57-100 % of the momentum of parent mesons (the first number representing $(m_\mu/m_\pi)^2$), making it possible to choose the beam energy in a wide range. The beam optics are taken care of by a series of 16 quadrupole magnets set alternately in focussing and defocussing modes. At the end of the channel, an 11m long beryllium target acts as a hadron absorber, providing us with a muon beam contaminated with one hadron per 10^6 muons. A low-Z material is used (Be) to minimize multiple Coulomb scattering of muons. The absorber itself is contained in a set of momentum-analyzing magnets which deflect the muons of selected momentum upwards by 24 mrad. After this, the muons are transported through another 400 m of focussing-defocussing channel and deflected back downwards 24 mrad. This is done in order to spatially separate the muon beam from the continuation of the decay channel. A final bend brings the muon beam back to horizontal. The characteristics of the beam as measured by our experiment during the data taking period of this work are shown in Fig. 2.4.

The reduction of halo muons is a non-trivial task because of the penetrating nature of muons. It is achieved by magnetized iron collimators: rather than stop the halo muons, they deflect them even further away from the beam, outside the acceptance of the next beam optics element. The halo, which would otherwise represent 75 % of the beam intensity, is so reduced to about 7 %. It is interesting to note that the muon beam is *polarized* by the kinematics and the parity non-conservation of the weak decay:

$$\pi^+ \longrightarrow \mu^+ + \nu_\mu.$$

There are no right-handed neutrinos, so the neutrino helicity is negative in the hadron center of mass system. As the pion is spinless, by momentum conservation the μ^+ has to

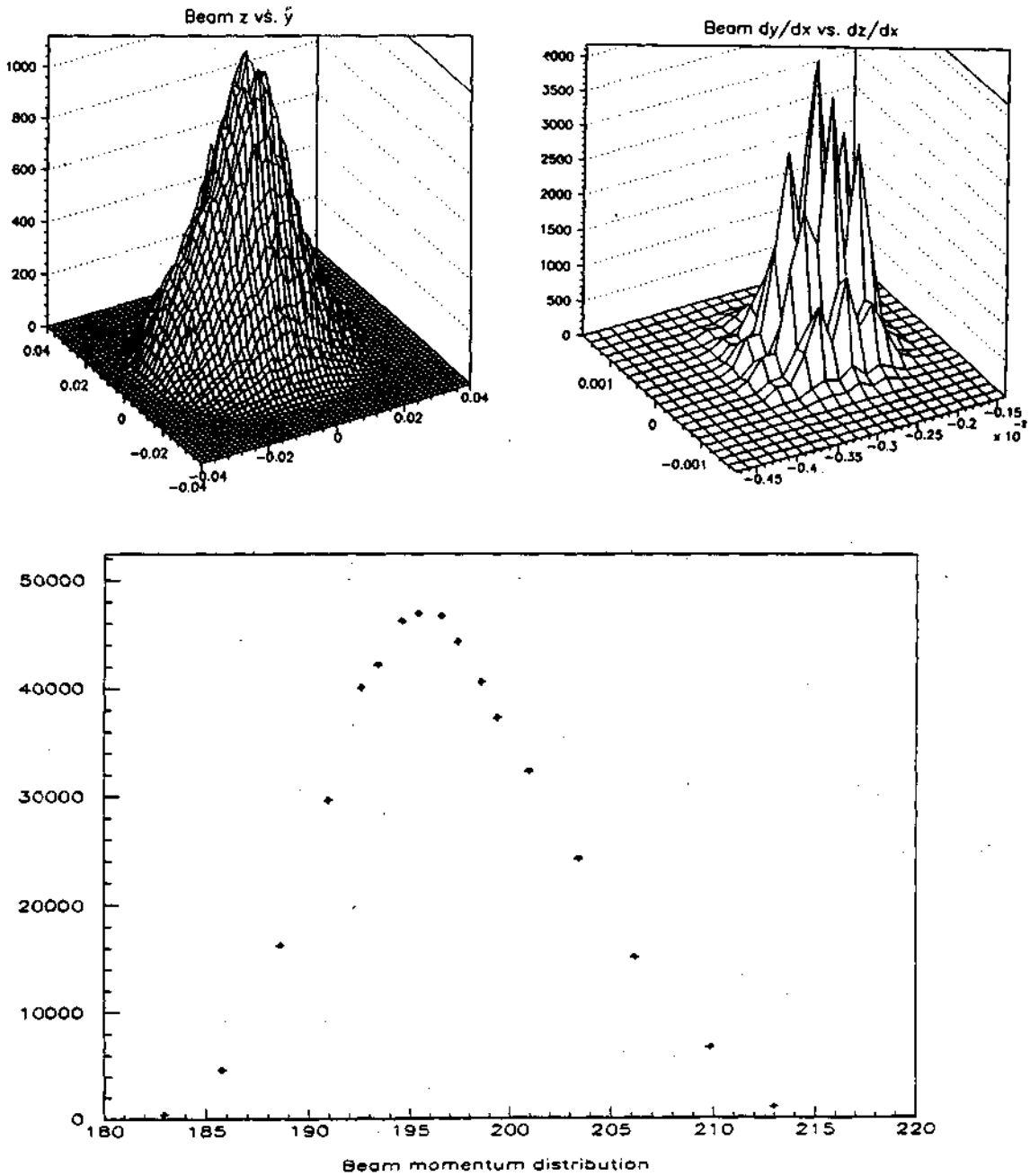

Figure 2.4: The muon beam characteristics in the middle of the target region: beam z vs. y shows a near-Gaussian distribution with 13 mm RMS; beam dz/dx vs. dy/dx – notice the discrete steps due to the 2 cm segmentation of the beam hodoscopes; and the beam momentum: $196.5 \pm .3$ GeV/c (rms)

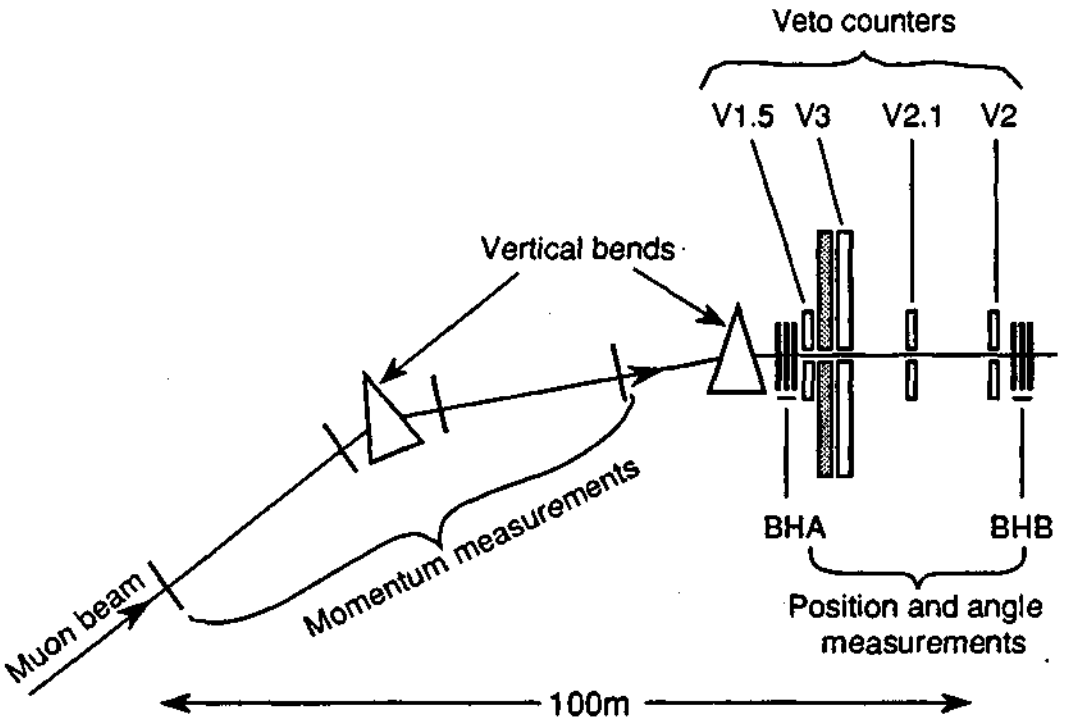

Figure 2.5: The Beam Momentum Station. Figure from [46]

have negative helicity as well. So if the muon is emitted forward in the CMS, it will have a high energy in the lab system, and a negative helicity. If it is emitted backwards, it will have a smaller momentum and positive helicity. Typically in our experiment the muons are 75 % polarized. This was used in the past EMC and present SMC experiments with polarized targets to measure the spin-dependent structure function of the nucleon.

The intensity of the muon beam during the data taking analyzed in this work was typically about $3 \cdot 10^7$/spill originating from about $3 \cdot 10^{12}$ protons/spill on the tungsten target.

2.2 The incoming muon measurement

The incoming muon momentum is measured by the Beam Momentum Station, and its trajectory (needed to find the interaction vertex and scattering angle) is measured by the beam hodoscopes in conjunction with some multiwire proportional chambers.

2.2.1 The Beam Momentum Station

The 24 mrad downward bend mentioned above is used to measure the incoming, or beam muon momentum. The spectrometer consists of the three dipole magnets, two sets of scintillating hodoscopes before them, and two sets after them. For the calibration a Monte Carlo simulation was done. Given the field maps of the magnets, a one to one correspondence between the relative position of the hits in the hodoscopes upstream and downstream of the magnets and the momentum of the muon is established and is stored in a file called "BMS

coefficients". Additional cross-calibrations are made using another magnet – the BCS and the FSM (see below and [47]). An accuracy of $\pm 0.3\%$ is achieved.

An important feature of the BMS is timing. In a beam intensity of $\approx 10^7$ muons/s, a muon arrives in average every 100 ns. The internal timing between hodoscopes of the BMS is important for the reconstruction of the beam track itself (hits are associated to tracks on the basis of their timing); the timing between the BMS and the forward spectrometer is important for establishing the one to one correspondence between incoming and scattered muon. The light in the scintillators is seen by phototubes and the resulting signals are fed into time-to-digital converters (TDC's) measuring the time between the signal and the trigger (see sec.2.6). Online time calibration is achieved by laser illumination of the scintillator blocks – observed timing differences can be corrected by delay lines. Offline, an accuracy of $\pm 150ps$ is attained (see chapter 3).

2.2.2 The Beam Calibration Spectrometer

The **Beam Calibration Spectrometer (BCS)**, located at the far downstream end of the experiment is used for an additional calibration of the BMS to an accuracy of $\pm 0.1\%$. It consists of a dipole magnet with a maximum bending power of 11.5 T·m and an aperture of 48 cm × 10 cm, two multiwire proportional chambers before, two just after it and another two at the end of the hall, 35 m downstream of the magnet. This gives a sufficient lever arm for a precise measurement of the ≈ 18 mrad deflection obtained for a 200 GeV/c muon.

2.2.3 The beam hodoscopes

The beam hodoscopes BHA and BHB consist of 4 planes each: one y-plane, one z-plane and for redundancy in reconstruction two θ-planes set at an angle $\pm 45^\circ$ to the horizontal. Each plane consists of two sub-planes of 20 4mm-wide scintillator strips, the sub-planes being staggered by 2 mm thus covering the interstrip dead region in the other sub-plane and increasing the spatial resolution by a factor of 2. The scintillators are read by phototubes and the resulting signal is then fed to a TDC. The timing is then compared to the BMS time – it should be within 10 ns of the latter. The angular resolution of the reconstructed beam track is ± 0.15 mrad.

Downstream of the target additional hodoscopes, H5 and H6, are used for online flux monitoring and definition of a beam trigger (T5, see section 2.6).

2.2.4 Multiwire proportional chambers P0H, P0B

An improvement to the incoming muon spatial resolution is achieved with a small multiwire proportional chamber, P0H. It is one of a series of small (ø16 cm) MWPC's designed to operate in the high intensity environment (P0H, P0B, P0C, P0D, P0E, P0A). Each circular plane has 144 10μm gold plated tungsten wires with a 1 mm pitch. Again a staggering of consecutive planes is used, this time by 0.5 mm. The spatial resolution of these chambers is 0.29 mm. P0H consists of two y and two z planes.

Another P0 chamber, P0B, is located between the upstream and the downstream target region. Its role is different for events originating in the upstream and downstream targets: for vertices found in the upstream part, a hit in P0B is used to improve the scattered muon fit, while for downstream vertices it can be used to improve the fit of the incoming muon track.

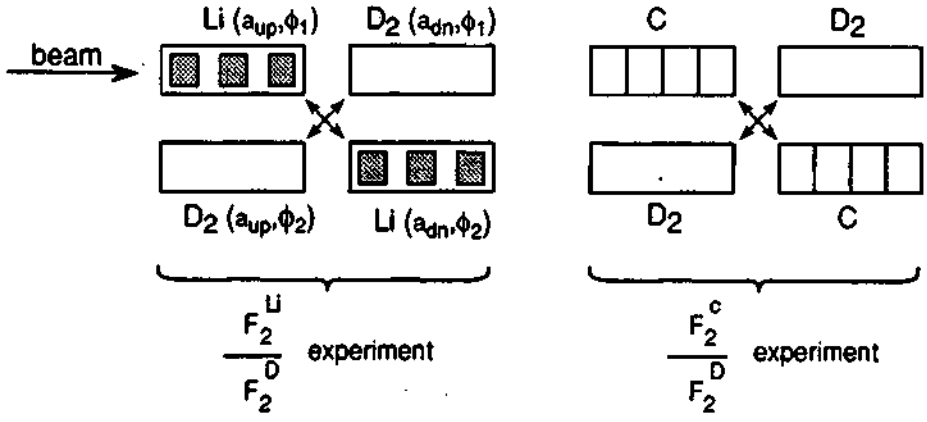

Figure 2.6: Complementary target setups (see text).

2.2.5 The veto counters

About 7% of the muons that reach the experimental area are in the halo. In order not to use these halo tracks for physics analysis (they wouldn't illuminate all targets equally, see section 2.3, and their momentum would not have been measured by the BMS), we need to veto these divergent beam tracks. For this purpose we have five sets of scintillator veto counters. They are constructed in a way to have a ø3 cm hole in the beam region, so that good beam tracks pass undetected.

2.3 The complementary target setup

The target setup shown in Fig. 2.4 enables us to perform two simultaneous experiments in the same beam: an upstream experiment measuring the ratio F_2^{Li}/F_2^D, and a downstream one measuring F_2^C/F_2^D. The two complementary target rows, different in the order of target materials for each pair, were moved alternately into the beam. During the data-taking, they were exchanged every hour (i.e. about 150 times during the whole run).

This method results in the cancellation of acceptances and fluxes in the cross section ratio, thus reducing the systematic uncertainty in the structure function ratio dramatically. This is easily seen if we compute the following "crossed" ratio of event counts:

$$\frac{N_{up}^{Li} \cdot N_{dn}^{Li}}{N_{up}^{D} \cdot N_{dn}^{D}} = \frac{(\sigma^{Li} \cdot \phi_1 \cdot \xi_{up}^{Li} \cdot a_{up}) \cdot (\sigma^{Li} \cdot \phi_2 \cdot \xi_{dn}^{Li} \cdot a_{dn})}{(\sigma^{D} \cdot \phi_1 \cdot \xi_{up}^{D} \cdot a_{up}) \cdot (\sigma^{D} \cdot \phi_2 \cdot \xi_{dn}^{D} \cdot a_{dn})} \tag{2.1}$$

$$= \left(\frac{\sigma_{Li}}{\sigma_D}\right)^2 \cdot \frac{\xi_{up}^{Li} \cdot \xi_{dn}^{Li}}{\xi_{up}^{D} \cdot \xi_{dn}^{D}} \tag{2.2}$$

$$\Longrightarrow \mathcal{R}^A = \frac{\sigma_{Li}}{\sigma_D} = \sqrt{\frac{N_{up}^{Li} \cdot N_{dn}^{Li}}{N_{up}^{D} \cdot N_{dn}^{D}} \cdot \frac{\xi_{up}^{D} \cdot \xi_{dn}^{D}}{\xi_{up}^{Li} \cdot \xi_{dn}^{Li}}} \tag{2.3}$$

In this expression:

- N_{pos}^{mat} is the number of events recorded in target material *mat* at position *pos*;
- ξ_{pos}^{mat} is the corresponding total nucleon surface density;
- ω_i is the integrated flux of muons through the targets in row i – the same for all targets in one row;
- a_{pos} is the spectrometer acceptance in position *pos* – the same for both target rows;
- σ^{mat} is the cross section for deep inelastic scattering in material *mat*.

The flux is the same for all targets in a row because only a tiny fraction of the incident muons actually scatter, so there is practically no attenuation of the beam from one target to the other. Also, the veto counters ensure no halo beam tracks are triggered on, i.e. only beam tracks illuminating equally all 4 targets in a row are accepted.

The frequent exchange of targets ensures that the integrated acceptance is the same for both target rows, even though small time dependences of the acceptance do exist (e.g. 24-hour cycles in the efficiencies of some drift chambers due to temperature fluctuations etc.)

Statistically, it is optimal for the determination of the ratio F_2^A/F_2^D to have an equal number of events in material A as in deuterium (otherwise the statistical error on the ratio is dominated by the lowest count):

$$\sigma_{\mathcal{R}} = \mathcal{R}\frac{1}{2}\sqrt{\frac{1}{N_{up}^{Li}} + \frac{1}{N_{dn}^{Li}} + \frac{1}{N_{up}^{D}} + \frac{1}{N_{dn}^{D}}} \geq \mathcal{R}\sqrt{\frac{4}{N_{up}^{Li} + N_{dn}^{Li} + N_{up}^{D} + N_{dn}^{D}}}$$

the equality being attained when all four targets have the same number of counts.

Therefore the target setup was chosen in such a manner that the total mass per unit area seen by the beam be equal for all target materials. This choice proved to be a fortunate one for one part of the analysis (the hadron method, see sec. 4.2.2). The targets had to be sufficiently separated so as to minimize the attribution of events to the wrong targets (due to smearing of the longitudinal vertex position, see section 4.3.2 on vertex smearing corrections). The maximum overall density was thus limited by the available space and the density of liquid deuterium, the lightest of the targets. The 'nuclear' targets (Li, C) were then segmented in order to best reproduce the longitudinal distribution of scattering centres in the complementary deuterium target. This was done in order to make the acceptances really equal between the different target rows.

The number of nucleons is calculated taking into account the mass defect of nucleons in nuclei, i.e.:

$$\xi^A = N_{Avogadro}\,\rho^A\,\frac{A}{M_A},$$

where ρ^A is the thickness of the target (in g/cm^2), A is the atomic number, and M_A the atomic mass (in units equivalent to 1/12th of the ^{12}C mass).

The targets are designated by material (D, Li, C), their position in the upstream or downstream half (U, D) and finally their position within that half (U1 means most upstream, U2 is the downstream part of the upstream target setup, D1 is the upstream part of the downstream setup, and D2 is most downstream). In short, the positions go from most upstream to most downstream in this order: U1, U2, D1, D2.

row	targ #	radius [mm]	length [mm]	Δ (T1,2) [mm]	Δ (T14) [mm]	density [g/cm^3]	thickness [g/cm^2]
J U R A	9	74.4–74.7	127.3	−0.172	−0.018	0.4663	5.928 (T1,2) 5.935 (T14)
	4	74.6	119.05	−0.904	−0.798	0.4663	5.509 (T1,2) 5.514 (T14)
	8	74.6–74.8	130.15	−5.160	−8.183	0.4663	5.828 (T1,2) 5.687 (T14)
						TOTAL Jura	17.265 (T1,2) 17.137 (T14)
			$\xi^{Li}_{Jura} = 1.0371 \cdot 10^{25}$ nucleons/cm^2 (T1,2) $\xi^{Li}_{Jura} = 1.0294 \cdot 10^{25}$ nucleons/cm^2 (T14)				
S A L E V E	1	74.6	129.0	0.000	0.000	0.4679[1]	6.036 (T1,2) 6.036 (T14)
	7	74.6	120.1	−0.028	−0.056	0.4663	5.599 (T1,2) 5.600 (T14)
	2	74.5	128.7	−0.896	−1.706	0.4663	5.599 (T1,2) 5.922 (T14)
						TOTAL Saleve	17.594 (T1,2) 17.555 (T14)
			$\xi^{Li}_{Saleve} = 1.0569 \cdot 10^{25}$ nucleons/cm^2 (T1,2) $\xi^{Li}_{Saleve} = 1.0545 \cdot 10^{25}$ nucleons/cm^2 (T14)				

Table 2.1: Details of the Li target density, correcting for holes in the target

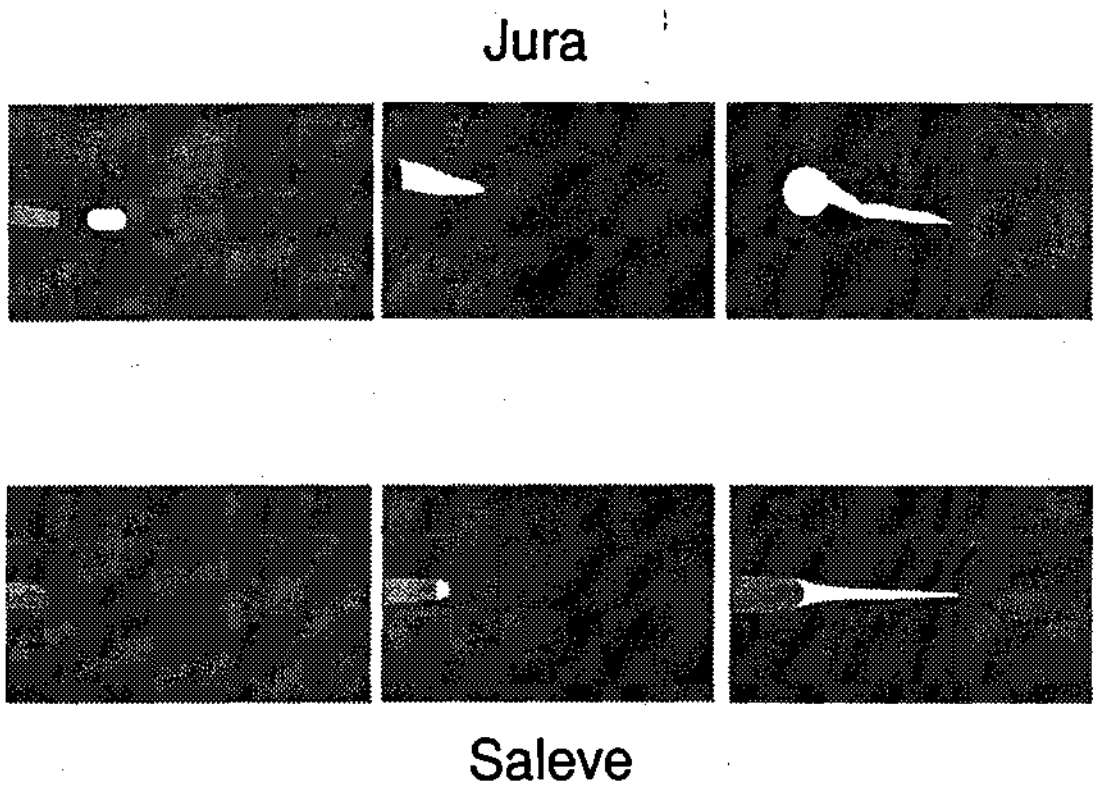

Figure 2.7: The holes in lithium targets. The lighter shaded areas represent the holes that were filled up before data taking. The holes still present during data taking are in white. The slabs were further apart during data taking (see fig. 2.6).

2.3.1 The lithium targets

The Li targets each consisted of three 13 cm long, 7.5 cm diameter cylinders of 95.5% enriched ^{6}Li kept under Ar atmosphere in a plexiglass container. This was done to hinder nitrification of the lithium in contact with nitrogen in the air (Li has more affinity to N than to O!). Nitrification has been a serious problem in the first NMC experiment involving Li targets back in 1986 [48]. Also, when cutting the target cylinders prior to this experiment it was found that the targets had some holes. These holes were then filled up. Other holes however were detected only after the data taking, so they had to be corrected for.

After data taking, the Li cylinders were cut in 2 cm thick slices in order to seek for holes. Some holes were found, and they had to be mapped. This was done in a glove box, copying the contours of the holes onto cards. These cards were afterwards copied to graph paper and in this manner a full reconstruction in three dimensions was possible. The volume of each hole (or part thereof) was measured pouring sand into the holes.

The correction Δ to the effective length had to be computed, convoluting the hole with the beam profile:

$$\Delta = \int\int \mathrm{d}y\mathrm{d}z\delta(y,z)b(y,z),$$

where δ is the longitudinal length of the hole at transverse coordinates (y,z). This integral

[0]The slightly different density in target # 1 is due to a small Al contamination in the molding process

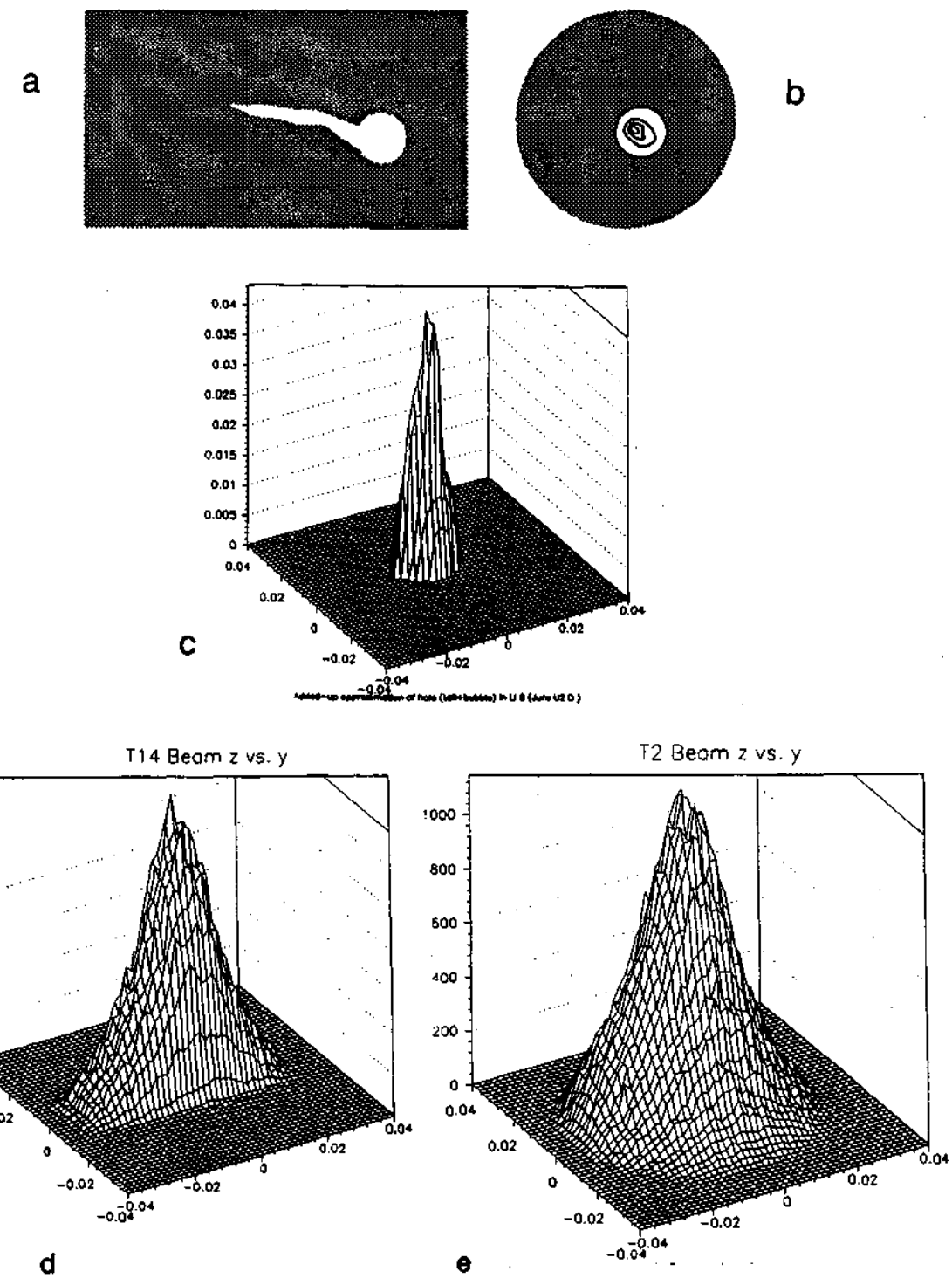

Figure 2.8: Example of parametrization of the largest hole. **a** Side view of the hole **b** Top view with contours at different depths. **c** Parametrized hole (collapsed) **d** Beam profile T1,T2 to be convoluted with c **e** Beam profile T14 to be convoluted with c

Additional material in the beam (Li target)				
Material	length	density	thickness	$\Delta\xi$
	[mm]	[g/cm^3]	[g/cm^2]	[1/cm^2]
Argon Jura	628.5	$2.404 \cdot 10^{-3}$	0.151	$0.0091 \cdot 10^{25}$
Argon Saleve	627.2	$2.404 \cdot 10^{-3}$	0.151	$0.0091 \cdot 10^{25}$
Air	195	$1.22 \cdot 10^{-3}$	0.0238	$0.0014 \cdot 10^{25}$
Mylar/Aclar	0.05	1.741	0.00871	$0.0011 \cdot 10^{25}$
Total Jura:			0.184	$0.0116 \cdot 10^{25}$
Total Saleve:			0.183	$0.0116 \cdot 10^{25}$

Table 2.2: Additional material around Li target, to be added to ξ^{Li}

is in practice converted to a sum, and in the end it actually means multiplying two two-dimensional histograms, the beam profile and the histogram representing the effective hole, and taking the integral of the multiplied histograms. The beam profile is somewhat different for different physics triggers (see section 2.6 on triggers). The results are given in Table 2.1.

In addition to this "hole" correction, we have to apply a correction for the surrounding argon gas (at a pressure of $\approx$ 1450 mbar), and air over a total target length of 1.2 m – corresponding to the total length of the associated deuterium target. Namely, in order for eqs. 2.1 and 2.2 to apply, we must take into account all scatterers within the same length in both materials. Also the 50μm thick mylar windows are taken into account. The details are given in Table 2.2.

2.3.2 The deuterium targets

The liquid deuterium targets were contained in a 1.2 m long, ø120 mm dallite (hard paper) vacuum tight tube with a 250μm mylar window at each end (in order to have the least possible foreign material in the region of 3 cm around the beam axis. The inner liquid deuterium vessel itself was entirely made of 250μm thick mylar as well, of roughly cylindrical shape (ø75 mm, 1 m long), with one rounded edge. The pressure of gaseous deuterium in equilibrium with liquid deuterium was measured in order to deduce its temperature and hence the density. This pressure was maintained at 100 ± 5 mbar overpressure with respect to atmospheric pressure.

In this calculation, an admixture of $3.01 \pm 0.24\%$ of HD molecules [49] had to be taken into account, so that the calculation was iterative:

First, pure deuterium is assumed, and a first approximation of the temperature read from tables [50, 51]. Next, from this temperature and using an empirical formula [50], we can calculate the pressure of the HD component.

Then comes a very important step – we are here dealing with vapours near the boiling point, by no means with ideal gases. So Dalton's familiar law (for ideal gases) of addition

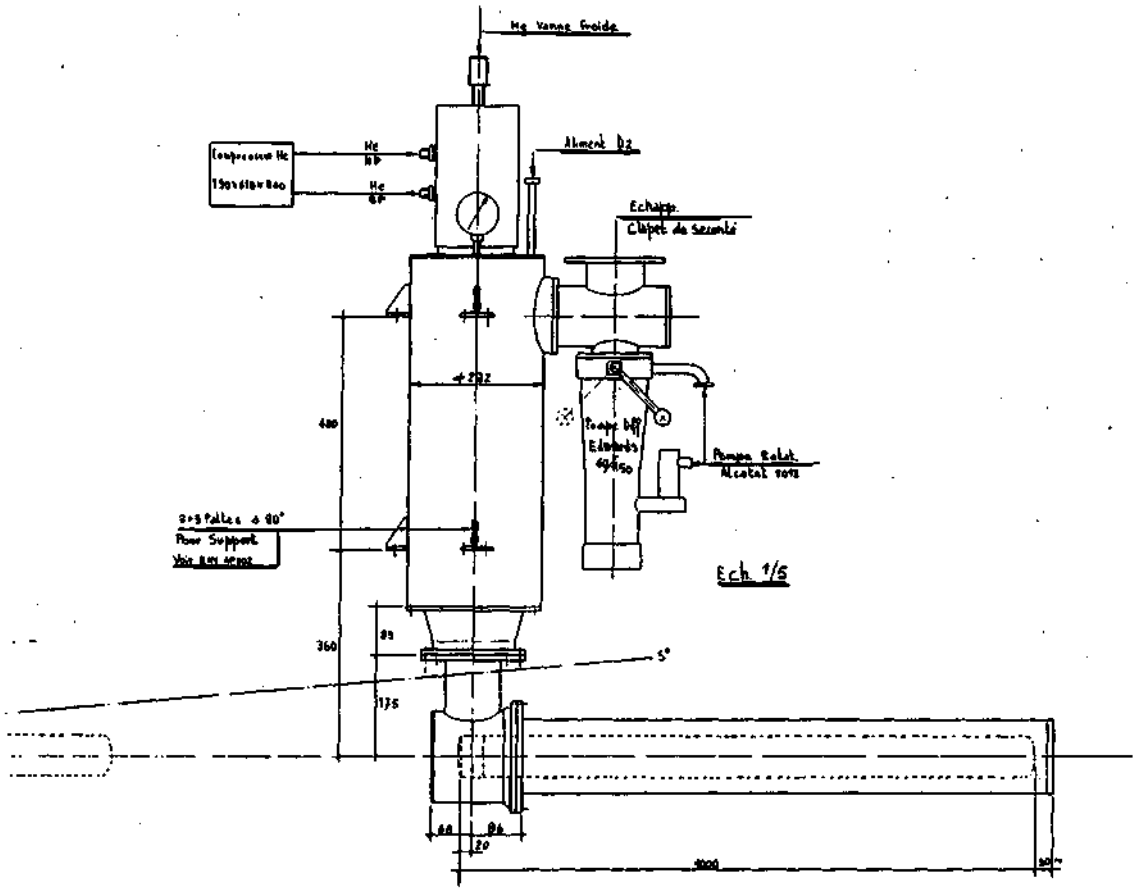

Figure 2.9: The deuterium target

of partial pressures:

$$P = p_1 + p_2 + ... + p_n$$

where P is the total pressure, and $p_i = n_i RT/V$ with n_i the molar fraction of component i in principle *does not* hold. Rather, we should add up *fugacities* [1]. Also, we only know the molar fraction of HD in the liquid phase, but not in the gas. However, the law of ideal solutions says:

If P_{0i} is the vapour pressure of component i in pure form, and x_i is the molar fraction of component i in the liquid phase, then for a vapour in equilibrium with an ideal liquid solution the partial pressure of component i is:

$$p_i = x_i P_{0i}.$$

Now if we use Dalton's law after all (ref. [52] deals with similar experimental conditions and their conclusion is that the difference between using fugacities and partial pressures is of tbe order of 0.3 mbar, much less than our experimental error on the pressure determination), we get the following expression for the total pressure:

$$P = p_{D_2} + p_{HD} = x_{D_2} P_0^{D_2} + x_{HD} P_0^{HD}.$$

Thus as we now have first approximations for P_0^{HD}, and since we have measured P, we can deduce $P_0^{D_2}$, the partial vapour pressure of pure deuterium:

$$P_0^{D_2} = \frac{P - x_{HD} P_0^{HD}}{x_{D_2}}$$

Using this, we go back to the tables and determine a second approximation for the temperature. Tben we again calculate the vapour pressure of HD from the empirical formula, and so on until tbe iteration converges. Two iterations are in our case enough. Tbe total effect is lowering the calculated temperature from 23.77 K to 23.72 K, translating into an 0.07% effect on the density.

The above calculation was done assuming we have in our target so-called E-deuterium, a mixture of 2.2 % para-D_2 and 97.8 % ortho-D_2. This is the low temperature equilibrium state of deuterium. However, immediately after liquefaction, deuterium is in another equilibrium state, 33.33 % para-D_2 and 66.67 % ortho-D_2 known as N-deuterium. We do not know which of tbese we had in our target. If we repeat the above calculation for N-deuterium, we find a temperature of 23.745 K.

From the temperature we next determine the molar volume of our deuterium. Tables exist only for N-deuterium, the prescription for E-deuterium being to increase the molar volume by 0.024 cm^3 (about 0.1 %). For HD, again an empirical formula is used and the total molar volume is:

$$v = x_{D_2} v_{D_2} + x_{HD} v_{HD}$$

resulting in: $v = 24.807$ cm^3 witb an accuracy of $\pm 0.15\%$, taking into account effects such as pressure measurement error, difference between the two reference tables, and dominated by tbe indetermination between E- and N- states. An average molecule of our mixture

[1] Fugacity f is defined as $d(\ln f) = d\mu/RT$ where μ is the chemical potential

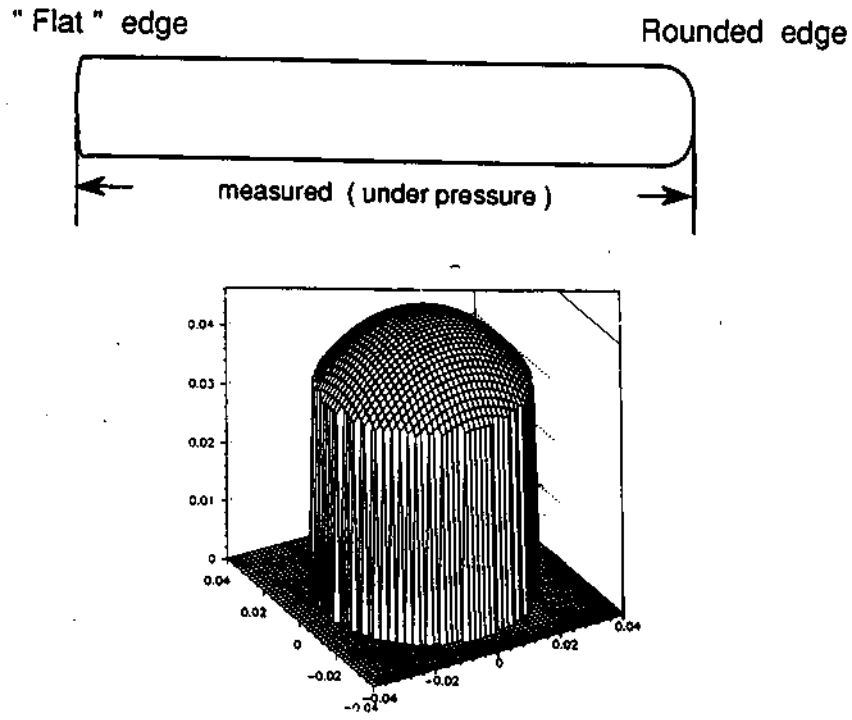

Figure 2.10: Effective shortening due to the rounded edge of the deuterium target. a The target length measurement from tangent to tangent b Parametrization of the rounded edge.

contains 3.97 nucleons (3 for HD molecules, 4 for D_2 ones). So we can calculate ζ_D, the volume density of nucleons in the deuterium targets:

$$\zeta_d = \frac{3.97 N_{Avogadro}}{v} = 9.63753 \cdot 10^{22}/\mathrm{cm}^3.$$

In order to calculate ξ_D, the *surface* density of nucleons seen by the beam, we need to know the effective length.

The length has been measured for the four empty target vessels, at room temperature and with an overpressure of 1 *bar* to simulate the pressure of deuterium vs. the surrounding vacuum. However, several effects are at work determining the effective length in the beam:

- The targets contract due to cooling to liquid deuterium temperature. This contraction has been measured by an optical method [53], where an optical marker was placed on the outer target vessel surface, a precise optical instrument was focussed on it and then the target was cooled. The focus had to be readjusted, and the difference was read on a micrometer scale. The contraction from room temperature to liquid hydrogen temperature was found to be -3.905 ± 0.035mm.

- Both edges of the target are rounded under pressure (even the "flat" edge). The overall length was measured from tangent to tangent, so there has to be an effective shortening of the target. This is calculated by parametrizing the rounded edge and folding it in with the beam profile, exactly in the same way as was done for the lithium holes (fig. 2.7). Again, the effect is different for T1,T2 and T14. The effective lengths are given in table 2.3.

Target	Measured length [mm]	Contraction (cooling) [mm]	$<\Delta>$ round [mm]	$<\Delta>$ "flat" [mm]	Effective length [mm]	Nucleon density [mm]
D_2 U1	1105.8±.2	−3.905±.035	−2.92	−0.76	1097.7±.3	$1.0579 \cdot 10^{25}$
" (T14)	"	"	−1.70	−0.45	1099.2±.3	$1.0594 \cdot 10^{25}$
D_2 D1	1112.0±.2	−3.905±.035	−2.87	−0.75	1104.0±.3	$1.0640 \cdot 10^{25}$
" (T14)	"	"	−1.70	−0.45	1105.5±.3	$1.0655 \cdot 10^{25}$
D_2 U2	1106.2±.2	−3.905±.035	−2.88	−0.76	1098.2±.3	$1.0584 \cdot 10^{25}$
" (T14)	"	"	−1.70	−0.45	1099.7±.3	$1.0599 \cdot 10^{25}$
D_2 D2	1108.65±.2	−3.905±.035	−2.86	−0.75	1100.6±.3	$1.0607 \cdot 10^{25}$
" (T14)	"	"	−1.70	−0.45	1102.1±.3	$1.0622 \cdot 10^{25}$

Table 2.3: Effective length and effective nucleon density of the deuterium targets

Once more some additional material has to be taken into account: the four 250 μm mylar windows, plus an additional superinsulation of 30 layers of aluminized 6 μm foil at each end (i.e. 60 layers seen by the beam) gives a total of 1.36 mm mylar (Table 2.4).

Additional material in the beam (D targets)				
Material	length	density	thickness	$\Delta\xi$
	[mm]	[g/cm^3]	[g/cm^2]	[1/cm^2]
Mylar	1.36	1.39	0.190	$0.0114 \cdot 10^{25}$

Table 2.4: Additional material around D target, to he added to ξ^D

2.3.3 The carbon targets

Like the lithium targets, the carbon targets were segmented in order to cover the same length as the complementary deuterium target. They consisted of five equally spaced 2 cm thick carbon disks set in a 900 mm long dallite (hard paper) tube.

The carbon slices were weighed and corrected for buoyancy in air [54]. The target nucleon density is given in Table 2.5.

Additional material to be taken into account is air around the slices along a total length of 1.2 m (corresponding to the outer length of the deuterium target); after subtracting the lengths of the C disks themselves we take into account 1.1 m of air (table 2.6).

The final results for all targets are presented in Table 2.7. The nucleon densities are given for the full target, taking into account all effects discussed above and additional material.

Table 2.7 gives the total densities and number of target nucleons/cm^2 for each target.

Target row	thickness	ξ
	[g/cm^2]	[1/cm^2]
Jura	18.683±0.006	$1.1251 \cdot 10^{25}$
Saleve	18.653±0.007	$1.1233 \cdot 10^{25}$

Table 2.5: Density of C targets

Additional material in the beam (C targets)				
Material	length	density	thickness	$\Delta\xi$
	[mm]	[g/cm^3]	[g/cm^2]	[1/cm^2]
Air	1100	$1.25 \cdot 10^{-3}$	0.138	$0.0083 \cdot 10^{25}$

Table 2.6: Additional material around D target, to be added to ξ^D

2.4 Measurement of the scattered muon and other final state particles

Two objectives have to be fulfilled: a precise vertex determination and a good momentum measurement.

2.4.1 The first straight line: from vertex to magnet

The first chambers hit by outgoing particles will be P0B (for scattering in the upstream targets) or P0C (for downstream targets) at low angles, and PV1 or PV2 [2] at larger angles. The P0's cover a 16 cm diameter region around the beam axis, wbereas PV1 and PV2 cover 1.50×0.94 m^2 and 1.54×1.00 m^2 respectively. PV1 and PV2 are also proportional chambers, albeit with a 2 mm pitch, and the central region around the beam is deadened by kapton sleeves around the anode wires, since the high beam rate would destroy the chamber. They have two y-planes (vertical wires), and four θ-planes at two different angles each.

2.4.2 The curve: inside the magnet

After this first detection, the particles enter the Forward Spectrometer Magnet. The magnet has an aperture of 2×1 m^2 and is 4.3 m long. For a 200 GeV/c muon beam, a current of 4000 A is used, producing a bending integral:

$$\int B \cdot dl = 4.414\text{T} \cdot \text{m}$$

[2] Groups of identical chambers are often split into hardware modules, e.g. PV1 and PV2. But from a software viewpoint, they are treated as one detector so they are referred to collectively as PV12

Row	Target	Nucleon density [1/cm^2] T1,T2	Nucleon density [1/cm^2] T14
Jura	D_2 U1	$1.0693 \cdot 10^{25}$	$1.0707 \cdot 10^{25}$
Saleve	D_2 U2	$1.0698 \cdot 10^{25}$	$1.0712 \cdot 10^{25}$
Saleve	Li U1	$1.0685 \cdot 10^{25}$	$1.0661 \cdot 10^{25}$
Jura	Li U2	$1.0487 \cdot 10^{25}$	$1.0410 \cdot 10^{25}$
Jura	D_2 D1	$1.0754 \cdot 10^{25}$	$1.0768 \cdot 10^{25}$
Saleve	D_2 D2	$1.0721 \cdot 10^{25}$	$1.0735 \cdot 10^{25}$
Saleve	C D1	$1.1333 \cdot 10^{25}$	
Jura	C D2	$1.1315 \cdot 10^{25}$	

Table 2.7: Summary of target densities

over a length of 4.3 m. The field is constantly monitored for time stability by two independent measurements: an NMR and a Hall probe. The field map is known to a precision of $\sim 0.2\%$, and this is directly reflected in the error of the momentum determination. Namely, a muon is deflected in a magnetic field by an angle:

$$\Delta\theta = \frac{0.3}{k} \int B \cdot dl,$$

where the angle $\Delta\theta$, the muon momentum k and the bending integral are expressed in units of radians, GeV/c and T·m respectively. The error on the field map dominates the systematic error on the momentum measurement. Therefore a special calibration was done using silicon microstrip detectors placed upstream and downstream of the FSM. Additional cross checks were done by comparing at the measured positions of the K^0 and J/ψ peaks with the Particle Data Booklet [47].

Low energy particles (less than ~4 GeV) are bent so much that they hit the wall of the magnet and are either lost by absorption (hadrons) or bent out of the acceptance of the detector (muons) and therefore also lost. This significantly reduces the multiplicity of tracks.

Inside the magnet, three big MWPC's – P1,P2,P3 [3] (active region $1.82 \times 0.80\text{m}^2$) and a small one (P0D – active region ø16 cm) allow the tracking inside the magnetic field. Again, the big chambers are deadened in the high intensity region near the beam.

2.4.3 The second straight line: from magnet to absorber

At the exit from the magnet the particle is seen by P0E at low angles and by the W1 and W2 drift [4] chambers at high angles (active region: $2.24 \times 1.24\text{m}^2$). Proportional chambers are used inside the magnet because drift chambers do not work in high magnetic fields.

[3] P1, P2 and P3 are often collectively referred to as P123

[4] W1 and W2 are often referred to as W12

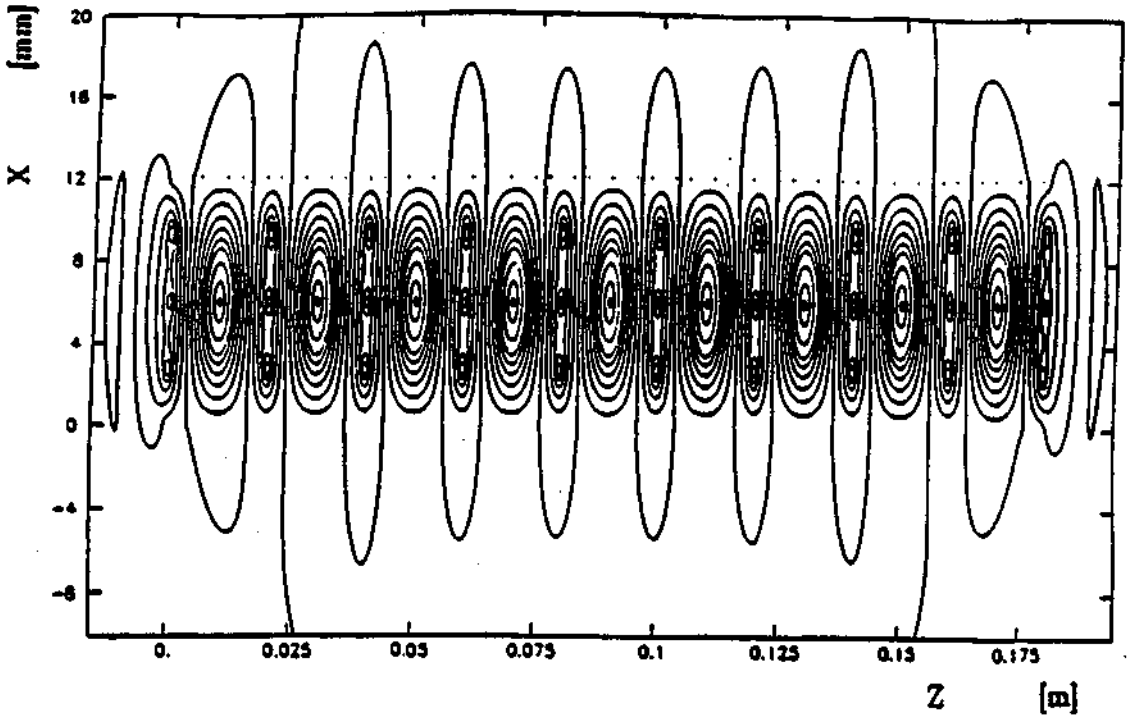

Figure 2.11: Electrical potential distribution in a W12 Z-plane drift chamber. Each drift cell is delimited by three potential wires maintained at a voltage of -400 V. In the center of each drift cell there is a sense wire.

Otherwise, drift chambers are cheaper to instrument, since the same or better resolution can be achieved with 10 or 20 times less channels. Also, drift chambers cannot stand high rates. Therefore we only find them downstream of the magnet, where most of the low-energy tracks are gone.

The principle of a drift chamber is the following:

- a charged particle ionizes the gas in the drift cell,
- the charge thus created drifts in a quasi-uniform electric field to the nearest sense wire,
- the sense wire signal is read by a TDC and the time is compared to that of the trigger,
- the drift time is thus deduced,
- given a known drift velocity we can determine at what distance from the sense wire the particle passed.

Note that there is an ambiguity whether the particle passed left or right of the sense wire, so in the reconstruction both possibilities have to be taken into account. A resolution of $0.3 - 0.4$ mm is achieved with a drift cell size of 2 cm in W12. Plane staggering by 1 cm is again used to increase efficiency, redundancy and precision.

Continuing its flight, the particle encounters another group of chambers: the W4, W5 [5] drift chambers (active: 5.14×2.60 m^2, drift cell size 4 cm), the P4, P5 [6] proportional chambers (active: 0.90×0.90 m^2, pitch: 2 mm) and the P0A proportional chamber for very low angles (active: ø16 cm).

At this stage the outgoing tracks are well measured: before the magnet by (P0B), P0C, PV12, and after the magnet by P0E, W12 and W45/P45. Between the two groups a lever arm of ~ 5 m ensures a good angular resolution.

Now the particles arrive to the H2 calorimeter. It consists of an electromagnetic part and a hadronic part. The electron modules consist of alternating lead and scintillator planes. Lead is chosen for its high ratio of nuclear interaction length (mean free path between inelastic interactions of hadrons) to radiation length (characterizing energy loss by bremsstrahlung for electrons). The scintillator planes consist of 28 cm wide scintillator blades, alternatively horizontal and vertical. The blades are read out by fork-shaped light guides that pipe the light to a single photomultiplier. A total of 4+7 planes of 0.6 resp. 1 cm thick lead and 12 planes of scintillators, with a 2 cm steel plate at face and back amount to about 22 radiation lengths [7], enough to contain virtually all the energy of electrons and photons impinging on it. The energy resolution is about $40\%/\sqrt{E}$, a far cry from today's state-of-the-art.

The two successive hadronic modules (horizontal and vertical) are composed of 4 cm thick iron plates interspersed with scintillator planes as for the electromagnetic module. The only difference is that here one entire module is made of vertically oriented blades, and in the next one the blades are horizontal. The total thickness of the two hadron modules can be expressed as $\approx$4.5 nuclear interaction lengths which together with $\approx$1 interaction length of the electromagnetic module gives a total of $\approx$5.5 interaction lengths. This is quite modest – we can expect 95% containment of the hadronic shower for hadrons at energies up to 10 GeV, at higher energies a larger "punch through" effect is possible. The energy resolution for hadrons is therefore rather poor: $160\%/\sqrt{E}$.

From the above it is evident that the calorimeter is of limited use. However, it proves quite efficient in discriminating between electrons and hadrons. Namely, the electromagnetic energy fraction:

$$EMAGF = \frac{E_{electromagnetic}}{E_{electromagnetic} + E_{hadronic}}$$

gives a good discrimination between hadrons and electrons, as will be discussed in more detail in section 4.2.1.

Let us mention also that the calorimeter has a ø20 cm hole to allow for the beam.

2.5 Muon identification

After the calorimeter, what remains of our particles? Little or no electrons, some hard hadrons, and of course the outgoing muon! We want to identify the muon track unambiguously (let us recall that most of the physics we do has to do exclusively with the scattered muon, all the rest is "noise" most of the time). So we put a 2 m (or about 12 interaction lengths) thick iron wall to absorb all hadrons and what passes through is a muon! The

[5] often referred to as W45

[6] often referred to as P45

[7] meaning (in theory) that all but $1/e^{22}$ of the initial electron energy will be deposited in the calorimeter

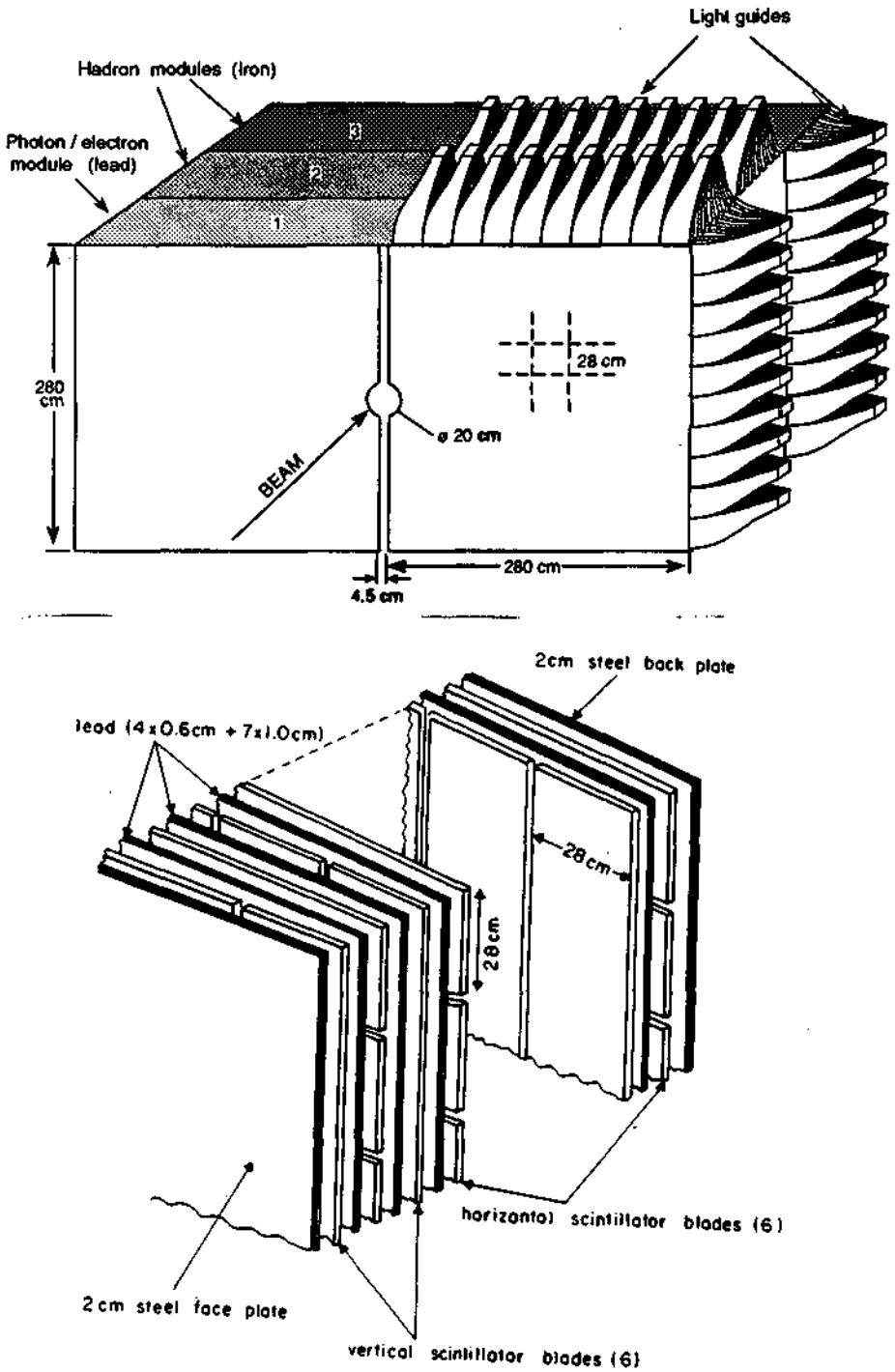

Figure 2.12: The H2 calorimeter and a blowup of the electromagnetic module

muons do suffer a bit, however: they experience multiple Coulomb scattering amounting to a ~ 5 mrad (r.m.s.) deflection from their previous trajectory. This is why the information from detectors downstream of the calorimeter and absorber will not be used in the fitting of the track, it serves only to identify the muon track.

The large lever-arm we have now (we are 13 m away from the magnet, and about 20 m away from the targets) means the transversal dimension we have to cover becomes impressive. Therefore we track the muon in the W6 and W7 chambers, consisting of three modules (A, B and C). Each of these modules covers an area of $3.51 \times 4.37\text{m}^2$, with 4-6 y- and z-planes and 3-4 θ-planes. The A module being shifted to the Salève side, B being centered on the beamline, and C being shifted to the Jura side, they cover an total area of $9.77 \times 4.37\text{m}^2$. The drift cells are 12 cm wide, so that these huge planes consist of typically 25-40 cells. The central region is deadened as usual, and muon tracks at low angles are recorded by proportional chambers P67 ($0.9 \times 0.9\text{m}^2$ active region, 2 mm pitch).

Besides multiple Coulomb scattering, the muon traversing the absorber experiences some energy loss (about 3 GeV for a 100 GeV muon). Now this isn't disturbing for the measurement of the scattered muon by itself, since we already accomplished the momentum and energy measurements further upstream. However, what is of concern are the secondary particles created in this process. Namely, the energy loss proceeds via ionization, e^+e^- pair production, bremsstrahlung and photonuclear reactions. While ionization (amounting to elastic $\mu - -e$ scattering, producing sometimes hard "knock-on" electrons also known as δ-rays) dominates at low energies and up to several hundred GeV, the pair production and bremsstrahlung represent an appreciable fraction of the energy loss of muons from $\sim$40 GeV on. In any case an appreciable amount of electrons and positrons is created in the depth of the absorber. These in turn produce electromagnetic showers creating more electrons and photons through pair production and bremsstrahlung. The result is a quite high multiplicity of tracks behind the absorber, not the truly idyllic situation of only one muon track described above. However these tracks are quite easily discarded in the analysis because they are not pointing to the target. The only inconvenience is that the high multiplicity may cause accidental triggers (see below). Therefore a second absorber is used to stop these electrons – thinner than the first one, for it only has to stop electrons, and it gives less chance to the muon to create new showers. After this second 40 cm or 23 X_0 thick iron absorber wall, an additional drift chamber W3 is the most downstream detector used for identifying scattered muons very close to the beam (especially for the low-x_{Bj} trigger, T14 – section 2.6).

2.6 The triggers

During the two seconds of the spill, about thirty million muons zoom through our apparatus. Only very few of them will actually give an interesting deep inelastic event we want to record on magnetic tape for subsequent analysis. We have to have a fast decision made as to when to read out our chambers. This decision is made by fast electronic triggers.

How does a trigger work? We first have to decide what defines our "good" event. For instance, we want to see a scattered muon at the end of our experiment, i.e. a track after the absorber which points to the target with some allowance for multiple Coulomb scattering in the absorber. We can then also ask for some kinematic requirements, in our case a minimum scattering angle and a minimum momentum of the scattered muon. We also don't want events caused by halo muons, so we can inhibit the trigger with a signal from the veto planes.

2.6.1 Standard physics trigger – T1

How do we go about it? For the standard physics trigger, T1, we use five scintillator hodoscope planes: H4 (horizontal) behind the second absorber for reasons explained in the previous section, H3H (horizontal) and H3V (vertical) just downstream of the first absorber, and H1H (horizontal) and H1V (vertical) next to the FSM exit (fig. 2.8). The planes consist of 7, 13, and 15 cm wide blades respectively for H1, H3 and H4. They are read out by fast phototubes and their signals are then converted to logical pulses by ADC's. These are now ready to be fed to the *trigger matrices* [55], programmable arrays of logical "AND" gates.

- Matrix M2 checks coincidences between appropriate strips in H3H and H1H. If these are found to give a positive answer, we have satisfied the **vertical target pointing** (VTP) condition.
- Next, matrix M3 cross-checks the VTP signal with H4. Historically, this was used to provide a minimum momentum cut for the scattered muon, the hadron absorber having been magnetized and thus deviating low energy scattered muons from their trajectory, outside the H4 acceptance. Low-energy muons have a large background coming from pion decay, the pions being the result of low momentum transfer μ-nucleon scattering.

  In the NMC experiment the absorber wasn't magnetized, but a residual magnetic field was present. The momentum cut was thus not explicitly included in the trigger, but the horizontal target-pointing has in itself an intrinsic cut on lower momenta because of the FSM (lower energy muons will be so much bent by the FSM that they won't satisfy the horizontal target pointing condition). In any case, checking the coincidence with H4 is useful because H4 is behind the second absorber wall where the muon signal is cleanest.
- Matrices M0 and M1 act as a single one checking **horizontal target pointing** (HTP). They compare signals from H3V and H1V.
- Horizontally *and* vertically target pointing events are then combined by the **scaling** matrix M7, which reduces the confusion that comes from the high multiplicity in H1 (from electrons and hadrons) which can generate accidental, fake HTP&VTP signals in coincidence with a low-momentum, low scattering angle muon originating from pion decay. Therefore M7 eliminates combinations of y and z coordinates in H3H and H3V where such events occur.
- HTP and VTP events are also fed into M6, which applies an **angle cut** with the H1V and H3H signals.
- All veto counters are NOR-ed so that a signal is there only if "all's clear", i.e. none of the veto's has a hit.

To summarize, T1 is the following combination:

$$\mathrm{T1} = \mathrm{VTP} \cdot \mathrm{HTP} \cdot \mathrm{SCAL} \cdot \mathrm{ANG} \cdot \overline{\sum \mathrm{Vetoes}}$$

where:

- VTP = H1H $\times_{M2}$ H3H $\times_{M3}$ H4H ($\times$ denotes the matrix correlation)

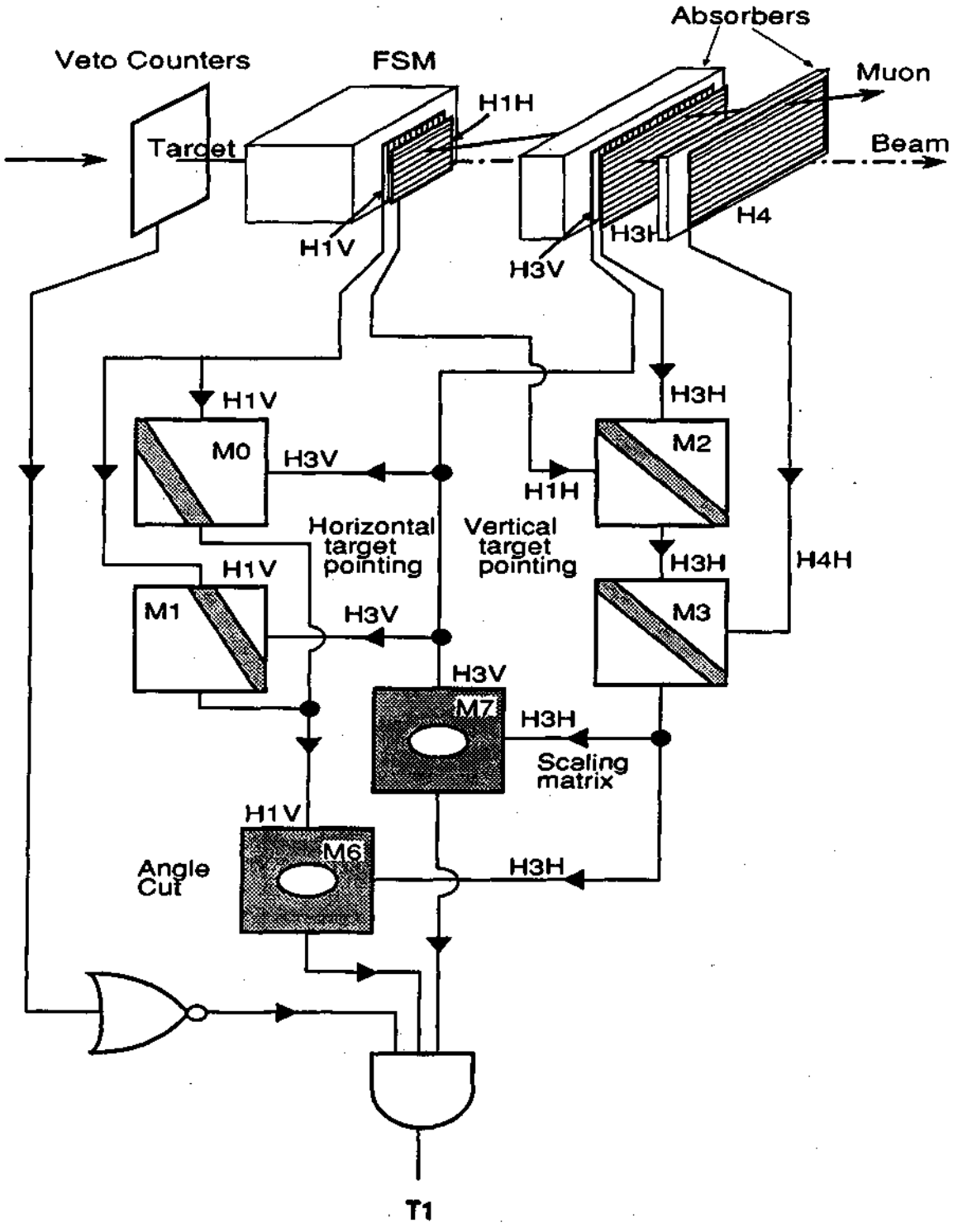

Figure 2.13: T1 logic (see text)

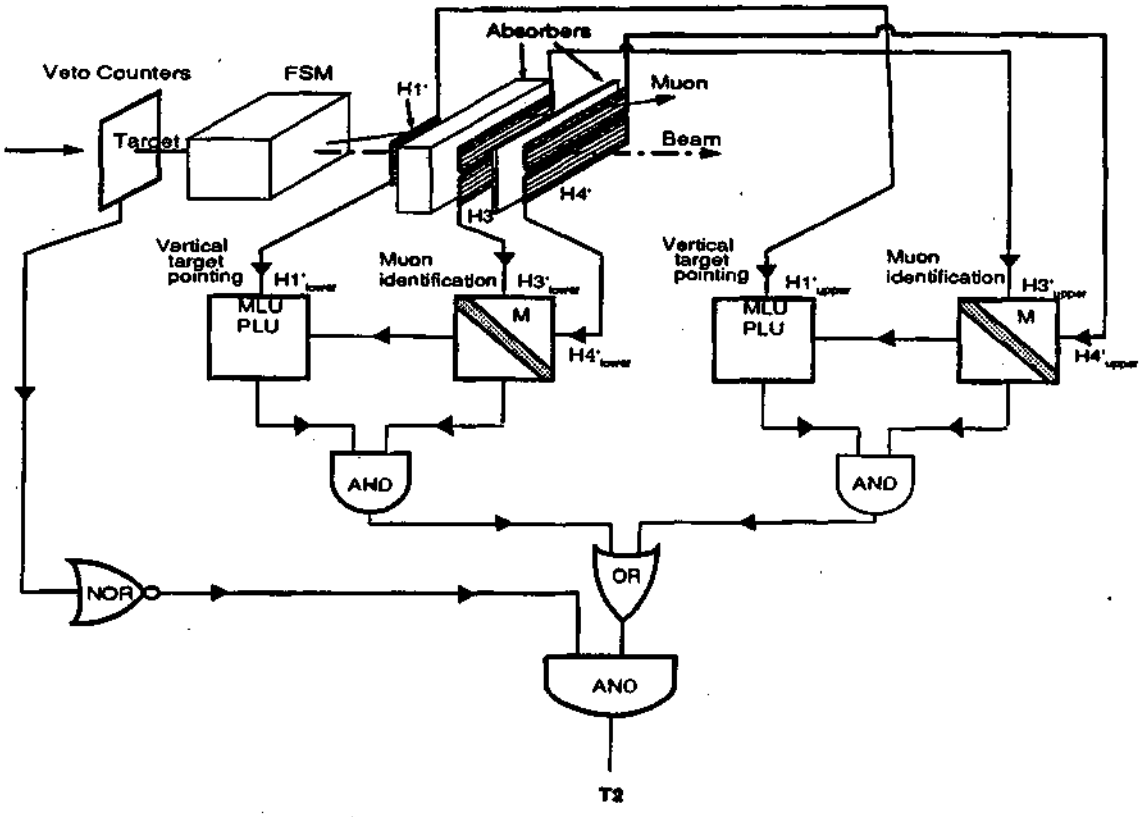

Figure 2.14: T2 logic (see text)

- HTP = H1V $\times_{M0\&M1}$ H3V
- SCAL = H3V $\times_{M7}$ H3H
- ANG = H1V $\times_{M6}$ H3H

Tbe typical rate during the data taking period analysed in this work was about 70 T1/spill.

2.6.2 Small angle interaction trigger (SAIT) – T2

A large fraction of events at small x_{Bj} from the standard trigger bas to be rejected because they have high values of y_{Bj} and therefore large radiative corrections (see sec. 4.3.1). Achieving lower y_{Bj} at a fixed x_{Bj} means lower ν and thus also lower Q^2 (to maintain the same x_{Bj}). And lower Q^2 is to be found at lower scattering angles. T2 is designed to extend the kinematic range down to lower angles.

T2 relies on three planes of hodoscopes with horizontal blades only: H1', H3' and H4'. The difficulty in low-angle scattering are very high rates (the cross section increases as $1/Q^4$ or roughly as $1/\sin^4\theta/2$). Therefore the hodoscope strips have to be narrower than for T1 hodoscopes – 1.4 cm (a large number of events per strip would confuse the phototube).

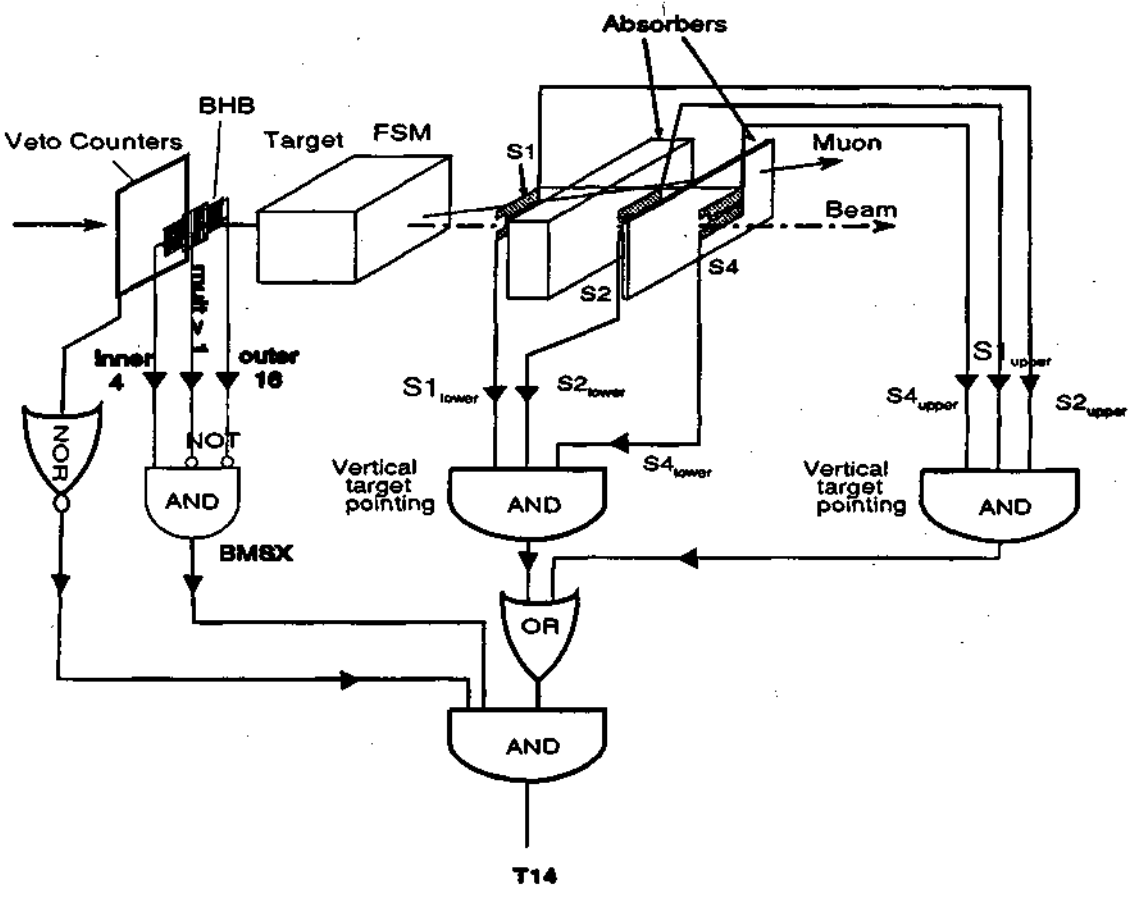

Figure 2.15: T14 logic (see text)

They are also shorter in order to accept only events where the muon scatters at an angle $\theta < 15$ mrad.

As to the logic, again vertical target pointing is required hy a matrix coincidence between H3' and H4'. It is additionally rechecked using a Memory Look Up (MLU) and Programmable Logical Unit (PLU) [8] with hits from H1'. The geometry of the strips is chosen such that the minimum scattering angle be ~ 5 mrad. No horizontal target pointing check is possible, since no hodoscopes with vertical strips are available. However, in analogy to T1, an anticoincidence with the veto counters is demanded.

To summarize, T2 is the following combination:

$$\mathrm{T2} = \mathrm{VTP} \times \overline{\sum \mathrm{Vetoes}},$$

where $\mathrm{VTP} = \mathrm{H3}'_l \times \mathrm{H4}'_l + \mathrm{H3}'_u \times \mathrm{H4}'_u$ (l,u design the lower and upper halves respectively).

The typical rate was about 180 T2/spill.

2.6.3 Small x_{Bj} trigger (SX) – T14

Going to even smaller angles, this trigger enlarges the kinematical region down to lower values of x_{Bj}. We are now so close to the beam that a confusion is possible – a slightly

[8] The MLU/PLU combination is equivalent to a matrix

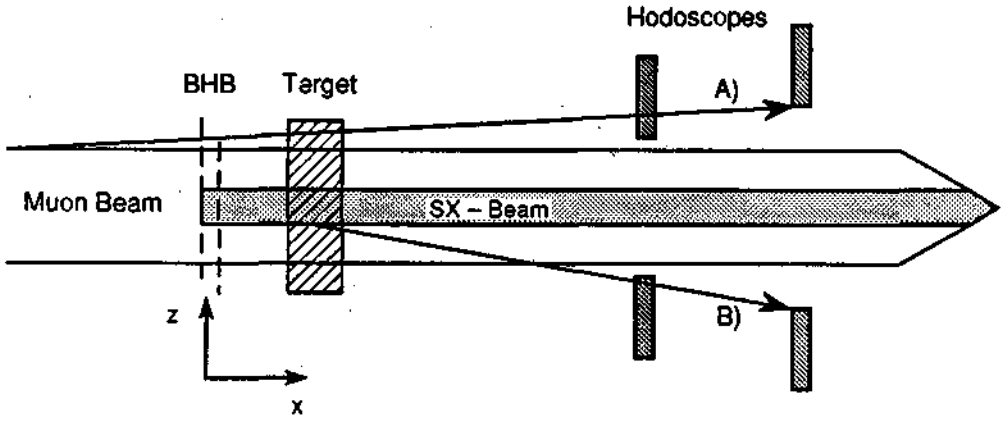

Figure 2.16: The beam restriction. We want to prevent situation A), a slightly divergent beam track causing a trigger. By redefining the beam to a smaller spread in z, only good events like B) are triggered on.

divergent beam track could cause a trigger. Therefore we need to restrict the beam to a smaller vertical spread – by introducing an additional veto of some sort.

Scintillator counters S1, S2 and S4 consist of two elements each – an upper and a lower half in horizontal direction. As usual, one of them is located in front of the absorbers, another one behind the first absorber, and a third one behind the second absorber. The coincidence of the three lower or three upper counters ensures a minimal vertical target pointing check, but accidental triggers are possible.

The beam condition is fulfilled if one of the inner 4 strips of beam hodoscope BHB plane Z4 is hit *and* none of the 16 outer strips sees anything. In addition there is a requirement on the multiplicity – only events with one beam track within a given time window are accepted. For other triggers multiple beam tracks are allowed, the reconstruction can decide which beam track gives the most reliable vertex. But for such extremely low scattering angles (down to 1 mrad or less) a clean situation is needed.

To summarize, T14 is the following combination:

$$\mathrm{T14} = \mathrm{VTP} \times \mathrm{BMSX} \times \overline{\sum \mathrm{Vetoes}}$$

where:

- $\mathrm{VTP} = \mathrm{S1_l} \cdot \mathrm{S2_l} \cdot \mathrm{S4_l} + \mathrm{S1_u} \cdot \mathrm{S2_u} \cdot \mathrm{S4_u}$ (l,u design the lower and upper halves respectively)
- BMSX = (BHB Z4 inner 4 strips) $\cdot \overline{\text{(BHB Z4 outer 16 strips)}} \cdot$ (BHB Y2 multiplicity $\leq$ 1)

The typical rate was about 150 T14/spill.

2.6.4 Exotic physics triggers

T15 triggers on *two* outgoing muons – it is set up for the study of J/ψ muoproduction, the J/ψ being identified by its $\mu^+\mu^-$ decay mode. T6 is the *lepton flavour changing* trigger, it

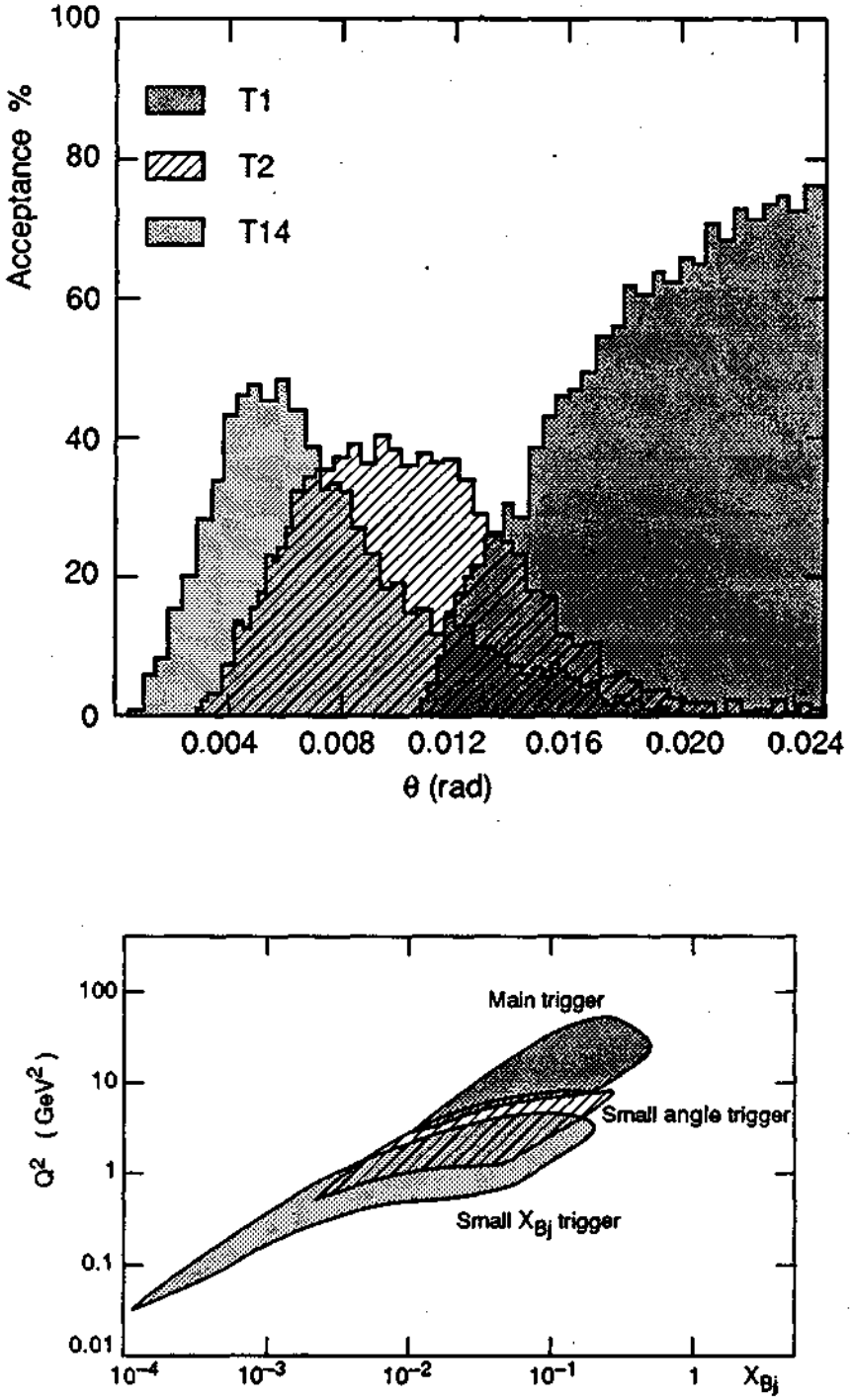

Figure 2.17: **a.** The acceptance of the three physics triggers vs. θ according to a Monte-Carlo study **b.** The kinematic region covered by the three triggers in x_{Bj}, Q^2 (data)

triggers on a large energy deposition in the electromagnetic calorimeter, but the presence of a scattered muon *vetoes* it. It searches for a hypothetical lepton number non-conserving process:

$$\mu^+ + N \rightarrow e^+ + X$$

2.6.5 Other triggers

Other than "real", physics events, we need to record information also for normalization, alignment and calibration of the apparatus, and so on. Here is a brief review:

- T3,T4 [9] and T10 – **normalization** triggers. They are needed for a precise measurement of the beam flux, and provide two independent methods. The T3 and T4 trigger conditions are fulfilled by every 2.56-millionth hit in BHA Z3 and BHB Y1 planes respectively (we don't care if there is a scattered muon or not, in contrast to the above described physics triggers, but we do check that there is no hit in the vetoes – we don't want to count halo). The information from all detectors is then written to tape and the beam track will be reconstructed by the reconstruction chain. From this one can find out how many useful beam tracks one gets from this random sample; multiplying this by $2.56 \cdot 10^6$ gives the flux.

  T3 and T4 are already redundant (allowing for some inefficiency in each BH plane to be taken into account), but a second method is used to further increase the redundancy. T10 is randomly triggered by a radioactive source several hundred meters away from the experiment, nothing to do whatsoever with the muons). During a 60 ns time window, all beam tracks going through the BMS and beam hodoscopes are recorded. The beam tracks are then also put through the reconstruction chain and the integrated flux is then calculated as:

$$\phi = \frac{Number\ of\ reconstructed\ \text{T10}\ beam\ tracks}{time\ window \cdot source\ decay\ rate}$$

- T5, the *beam* trigger, T7, the *near halo* trigger, and T8, the *far halo* trigger are used for alignment and efficiency calculation. Dedicated alignment runs are made with these triggers, without a target and with the FSM turned off. This ensures that the beam goes undeflected through the whole apparatus and enables a precise alignment of chambers, very important for a subsequent precise measurement of muon kinematics. The three triggers illuminate different parts of the apparatus: T5 illuminates the central part close to the beam, and is thus used for the alignment of the small P0 chambers and beam hodoscopes, T7 illuminates a little further out and is used for the alignment of all big chambers (P123, W12, P45, W45,...), whereas the far halo trigger T8 is used essentially for the giant W67 chambers, especially modules A and C which are far from the beam.

- T9 is just a 10 Hz clock, it is useful for background studies, and offline TDC calibration. Also it is used to trigger the online apparatus check tasks during data taking. T11 and T12 are used for alignment and efficiency of T1 and T2 hodoscopes, respectively.

[9] often referred to as T34

Chapter 3

Alignment, calibration and data reduction

A two-week period of data taking in December 1989 is analysed in this work. During that period, 338 magnetic tapes of "raw" data were written. In order for these data to he used in physics analysis, we have to reconstruct tracks, vertices, compute momenta and in the end the kinematic variables for each physics event.

The alignment and calibration, the tuning of the reconstruction and event-geometry programs are the most time-consuming parts of the offline work. They are however mandatory for each data taking period with its characteristic target material, beam energy and distinct hardware problems.

Then comes the actual "production" of data – the CPU-intensive part of running the reconstruction, geometry and reduction programs on more than 300 magnetic tapes of data, with the result of producing 4 micro Data Summary Tapes (micro DST's) that contain all pertinent information about "good" physics events. Only then can the weary physicist start with the actual physics analysis.

Fig. 3.1 shows the NMC data analysis chain:

- The raw data is decoded by the decoding package, a first rough reconstruction is performed hy PHOENIX – tracks are identified, in particular the incoming muon(s) and the scattered muon behind the absorher.

  This program is first used for alignment and calibration, using the data taken with the dedicated alignment triggers – T5, T7, T8 (sec 2.6). It then needs to be tuned, i.e. parameters such as *roadwidths*, χ^2-cuts, minimum plane requirements etc. have to he set so that the program assigns hits to the right tracks without throwing away good events and using up too much CPU time.

- The next step is GEOMETRY, which fits the scattered muon and hadron tracks with a spline fit in the magnetic field of the FSM, checks the match of the scattered muon track before and after the absorber, verifies whether it then satisfies the trigger requirements (or is an artefact of the reconstruction) and reconstructs the vertex. The output from GEOMETRY is stored on magnetic tape. This is then called a Maxi DST (Data Summary Tape) and has roughly the same volume as the initial raw data. Only events where no reconstructihle beam track and/or no target pointing track behind the absorber (no scattered muon) is found in PHOENIX are not recorded. Both raw

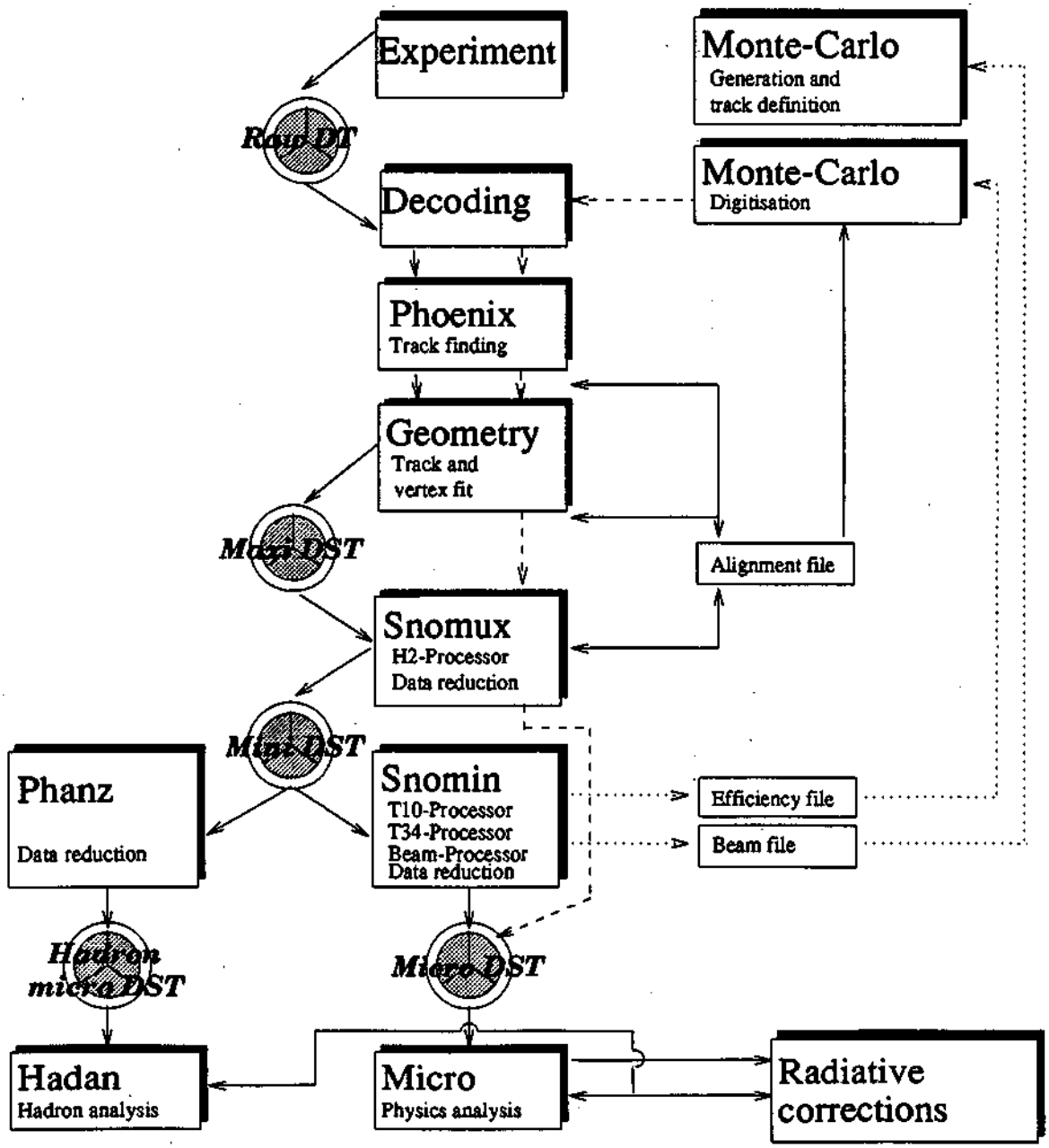

Figure 3.1: The NMC data reduction and analysis chain

data and the results from GEOMETRY fitting are stored on the MAXI DST. This enables us to rerun GEOMETRY on this output if something goes wrong, for even events with no vertex found are still kept and no information is lost.

- SNOMUX is a general purpose program which can in principle be used for physics analysis, but as we still have over 300 magnetic tapes (from a typical two-week data taking period), analysis on the full data sample is virtually impossible. Therefore it operates the first data reduction, discarding the raw data information. At the same time it processes the calorimeter information. The output is written to the *Mini DST*. We are now left with 27 tapes containing all relevant physics information about all of the events. SNOMUX is also used for the veto-tuning – to insure all beam tracks are within an acceptable phase space so that they illuminate all four targets equally.

- SNOMIN reads the output of SNOMUX and writes separate *micro DST's* for different triggers. In doing so, it applies the veto cuts defined by the veto tuning, and writes out a T10 file, with parameters of all accepted beam tracks. These may subsequently be used as input to the MonteCarlo so as to faithfully describe the incoming beam for simulation purposes. It also calculates event weights for the normalization triggers, T34 and T10. It writes out only the information about the incoming and scattered muon to the micro DST. Hence the micro DST's represent only about 4 magnetic tapes of data. These micro DST's can then fit on hard disks and be used for the analysis.

- If we are interested in particles other than muons produced by the deep inelastic scattering – hadrons and electrons in particular, we need a so-called *Hadron micro DST*, produced by the program PHANZ.

For absolute cross section measurement, a full MonteCarlo simulation of the experiment is necessary, and it passes through the whole chain much in the same way as data does. This is not the subject of the present work.

3.1 The reconstruction program – PHOENIX

A typical event is shown on fig. 3.2. (well, not so typical because its hadron multiplicity is quite high – most of our events have 0, 1 or 2 hadrons).

Since the alignment is done by the reconstruction program PHOENIX, let us briefly review its logic (fig 3.3).

For the scattered muon we start from the back – the chambers behind the absorber – W67, P67 and W3 is where we search for a target pointing track. Working its way from there, going upstream all the way to the target region, the reconstruction always independently looks for lines in each detector, using hits compatible with what was found further downstream (this procedure is called tagging, see below).

- Every physics event, if it's recorded on tape, has had a rudimentary check on target pointing by the online trigger matrices (or PLU units or simple AND gates in the case of T2 and T14). PHOENIX takes these hodoscope bits as a starting point to *tag* hits. This simply means – given the coincidence of hits in at least one element of two distinct hodoscopes, we know that the muon should be in a certain solid angle defined by the length and width of both elements and their longitudinal separation. For T1

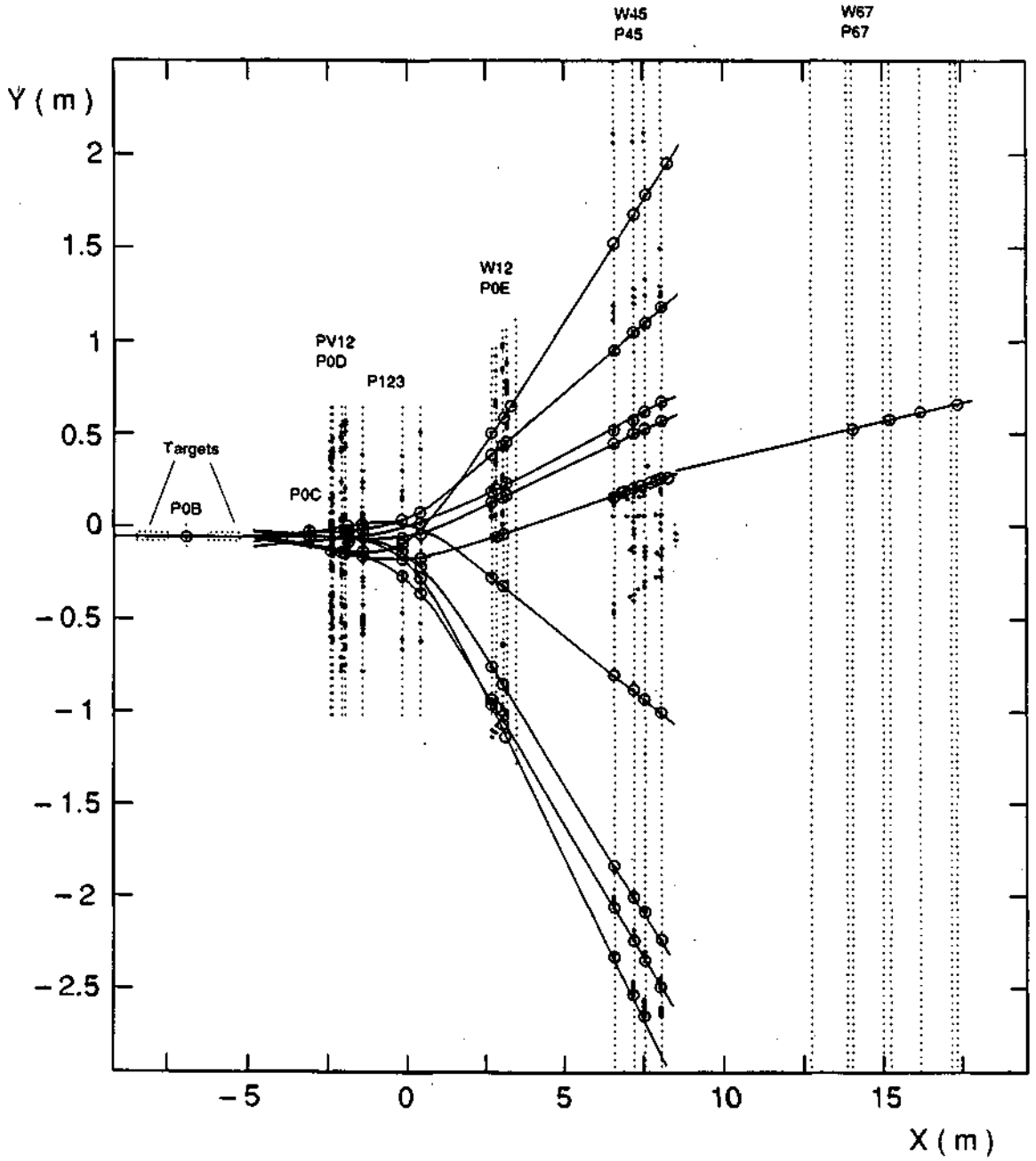

Figure 3.2: A typical event at beam energy of 200 GeV. The muon track is the only one seen behind the absorber. Black dots indicate hits, circled ones are used for the track fits. Note the deflection of the muon track due to multiple Coulomb scattering in the absorber.

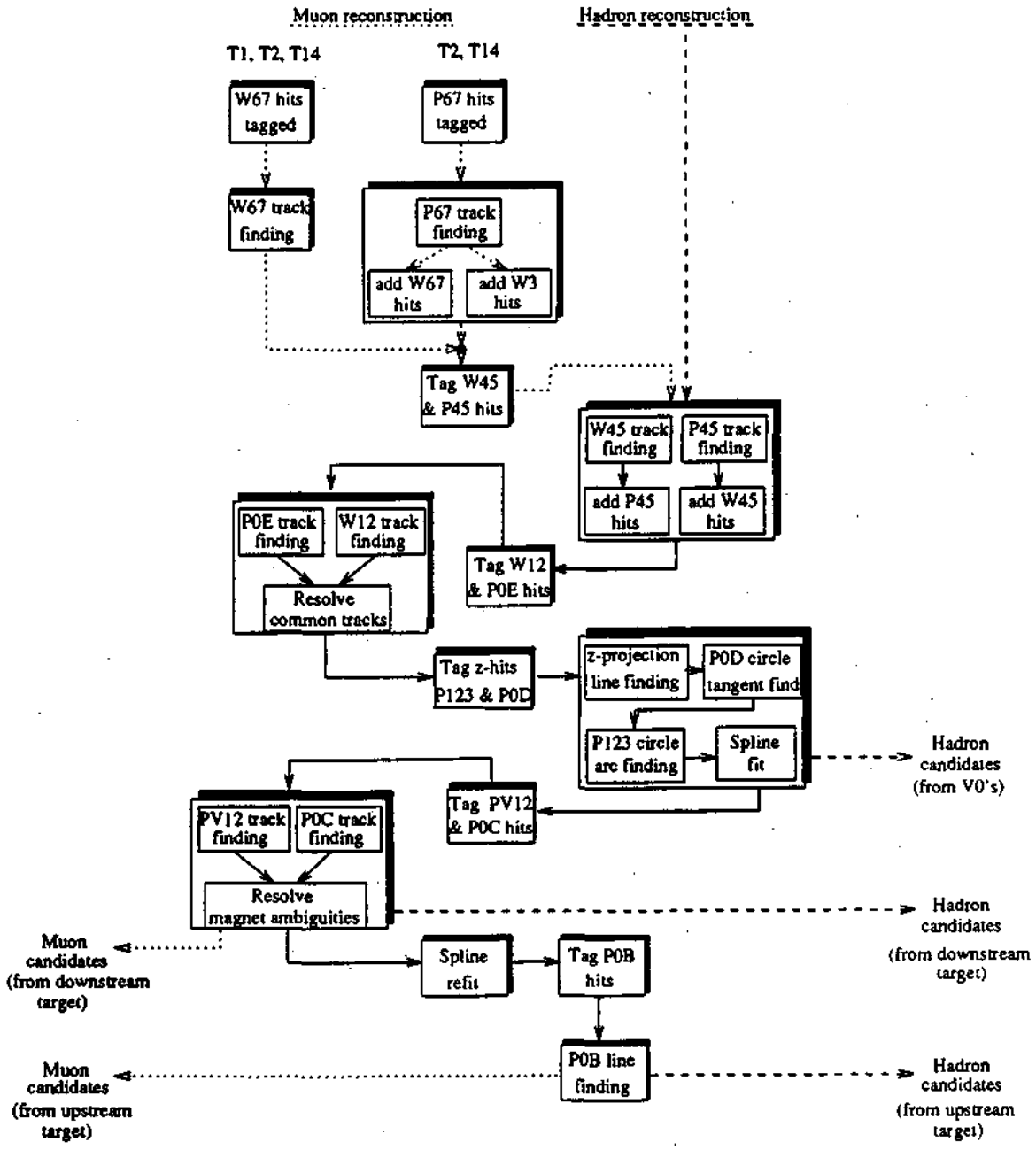

Figure 3.3: The reconstruction logic for the final state tracks in PHOENIX. The dotted lines show the muon reconstruction, the dashed ones the hadron one, and the full lines indicate steps taken for both reconstructions.

and T2 the trigger hodoscopes are used (H3H, H4H and H3V for T1, and H3' and H4' for T2), whereas for T14 the trigger hodoscopes have too poor a segmentation and thus additional hodoscopes H3" and H4" are used. A roadwidth defines by how much a hit can be *outside* this solid angle and still be tagged.

- Using the tagged hits (or candidate hits we might call them), PHOENIX now builds all possible combinations and tries to fit a line through any combination of hits in different planes. These combinations have to satisfy three requirements:
  - A minimum number of planes has to have a hit compatible with the line (this is called *the minimum plane requirement*), e.g. for the W67 B module we require that at least four out of six y-planes, at least four out of six z-planes, and at least three out of four θ-planes have a hit.
  - They should roughly point in the vicinity of the FSM aperture in y and z (roughly means within a factor of two or so – the muon seen in W67, P67 or W3 has undergone some multiple Coulomb scattering in the absorber so its trajectory has been slightly bent).
  - The slope should be within 10 degrees of the beam direction.

  Special routines check the overlap region between the A,B and B,C modules to join candidate lines from each module into a single one if compatible. For T1 events PHOENIX only searches for lines in W67, whereas for the lower-angle T2 and T14 events also P67 lines are sought, improving the line with hits found in W67 and W3. These lines are then called P67-W67 and P67-W3 lines respectively.

- These W67 lines (as well as P67-W67 and P67-W3 lines) are then used for tagging muon hits in W45 and P45 (tagged will be hits lying on the extrapolation of W67, P67-W67, or P67-W3 lines within a certain roadwidth, allowing for e.g. multiple Coulomb scattering in the absorber). The tagged hits in W45 are used to find lines (ideally only one muon line), and then if we are in the overlap region between W45 and P45, these lines are extrapolated to P45 and hits are added to the line if compatible. These are W45-P45 lines. For lower angle tracks, P45 lines are sought and W45 hits are added if existing; these are then P45-W45 lines.

  A similar procedure is followed for the hits that aren't tagged, because we now search for hadron lines. Again plane requirements have to be met, and the track has to point this time exactly to the FSM aperture.

- The W45 (and P45-W45 and W45-P45) lines are now in turn used to tag hits further upstream – in P0E and W12. The reconstruction proceeds as in the P45/W45 group.

- Now we arrive to the magnetic field. Tagging of P123 and P0D hits is straightforward only in the x, z plane, where there is no bending. In the x, y plane an arc-of-circle trajectory is assumed (this would be true in an absolutely homogeneous magnetic field with no edge effects). Extrapolating the W12/P0E lines (actually the tangent to the circle) to the center of the magnet, and assuming the muon comes from the target region, one gets the tagging road for the y direction in P0D. When we find a point in P0D, the arc-of circle is unambiguously defined (by a tangent and a point) and we proceed to tag hits in P123 and reconstruct the circle trajectory (fig 3.14). A simplified spline fit is then made (a more sophisticated fit is coming in GEOMETRY) to proceed further.

- Arriving to the PV12/P0C group, the above spline fit is used to tag hits and find lines in the usual manner. Now some ambiguities resulting from the high multiplicity in the magnet can be resolved.

- A new spline fit is done using the PV12/P0C information and hits in P0B are tagged, allowing for multiple Coulomb scattering in the downstream target.

Beam reconstruction proceeds as follows:

- First, a track is sought in the BMS. Hits outside a 10 ns time window (around the trigger time minus the time-of-flight between the BMS and the trigger hodoscopes) are rejected. There are 4 planes of z-measuring hodoscopes in the BMS ($x - z$ is the bending plane here): two before and two after the bending magnets. Therefore tracks with hits in at least 3 out of 4 planes are sought. Hits are associated to a track on the basis of time cuts (1.3 ns around the expected time for each plane). Using the BMS coefficients on the z-coordinates of the hits, one calculates the momentum of the incoming muon. These coefficients were originally determined from Monte-Carlo simulation, but then corrected with the Beam Calibration Station readings during special calibration runs, see sec. 3.3.3 and [56].

- The beam hodoscopes are used to define the beam track in space. Four sets of each $y-$, $z-$, θ^+ and θ^- planes are available (θ^+- and θ^- strips are mutually perpendicular and at an angle of 45° with respect to both $y-$ and $z-$strips but still in the y, z plane). Tracks are reconstructed with a minimum requirement of three out of four in-time hits in y and z, and the association of y and z hits (in addition to the time cut) is done by hits in the θ planes. This track finding procedure is repeated once more the other way around: requiring three out of four θ^+ and θ^- hits to be in time and associated by y and z hits. In this way the beam hodoscopes have a double redundancy which brings the fraction of events with a reconstructible beam track from about 80% (only y, z reconstruction) to typically 94-97% during NMC running.

- To associate the track with measured position and slope (in the beam hodoscopes) to the one with a measured momentum (in the BMS) again a time cut is used. Such an associated track is then called a beam track. It is then extrapolated to P0B and hits are found which may later be used by GEOMETRY to refit the beam track if the vertex is found in the downstream target.

3.2 Track and vertex fitting: GEOMETRY

PHOENIX sorts out the hits in various detectors and assigns them to tracks. Now the events which survive all the PHOENIX cuts and criteria can be fitted by GEOMETRY. The intersection of the beam and scattered muon gives the **vertex**, the position of which is of prime importance since it is our only way to know in which of the four targets of a row the interaction occurred.

The beam track is refitted using the beam hodoscope hits, and some cuts are applied to avoid confusion when multiple beam tracks are present. Firstly, events are rejected which have two beam tracks too close in time (< 2 ns apart) – they are mostly due to a muon accompanied by an energetic knock-on δ-electron it created on its passage through the different pieces of equipment. In that case we would not know which of the two is a muon

and which an electron, nor would we know the exact momentum of the incoming particle. Second, events having two beam tracks relatively close in space *and* time (4 mm and 10 ns respectively) are rejected for they would have trouble in distinguishing which of the two actually interacted in the target so a wrong attribution could occur. In this way about 10% of the beam tracks are removed, but still about 96% of events have at least one surviving beam track.

The main task of GEOMETRY is a precise fitting of the scattered muon track, especially in the magnetic field of the FSM. The equation of motion of a particle with momentum p in a magnetic field $B = (B_x, B_y, B_z)$ may be written as:

$$\begin{aligned} py'' &= \sqrt{1+y'^2+z'^2}\left[B_x z' + B_y y' z' - B_z(1+y'^2)\right] \\ pz'' &= \sqrt{1+y'^2+z'^2}\left[-B_x z' - B_z y' z' + B_y(1+z'^2)\right], \end{aligned} \tag{3.1}$$

where $y' = \frac{dy}{dx}$, $y'' = \frac{d^2y}{dx^2}$, etc.

GEOMETRY uses for a first approximation of the track a *cubic spline*, i.e. fits a parabola to every interval between two consecutive data points, with the requirement that the fit passes through all points, and that the first derivative is continuous everywhere, whereas the second derivative is a constant that changes in steps between the intervals [1]. This gives a first approximation of the (continuons!) y' and z', and therefore of the right hand side of eqs. 3.1. (the components of B are measured quantities). This gives us a possibility to fit in turn the left hand side of eqs. (3.1) by third-order splines (essentially a Taylor expansion around x_i):

$$\begin{aligned} py''(x) &= A(x) = py''(x_i) + (x-x_i)A'(x_i) + \frac{1}{2}(x-x_i)^2 A''(x_i) + \frac{1}{6}(x-x_i)^3 A'''(x_i) \\ pz''(x) &= B(x) = pz''(x_i) + (x-x_i)B'(x_i) + \frac{1}{2}(x-x_i)^2 B''(x_i) + \frac{1}{6}(x-x_i)^3 B'''(x_i), \end{aligned}$$

where $py''(x_i)$ and $pz''(x_i)$ are calculated from the right hand side of eqs. 3.1 using the first approximations of $y'(x_i)$ and $z'(x_i)$ stemming from the first cubic spline fit. Using then the continuity condition one can find [58] recursive relations for the second derivatives $A''(x_i)$ and then we work up our way to $A(x_i)$.

Integrating the above equations we get a fifth order polynomial for $y(x)$ and $z(x)$:

$$\begin{aligned} y(x-x_i) &= a_1 + a_2(x-x_i) + \\ &\frac{1}{p}\left[\frac{1}{2}py''(x_i)(x-x_i)^2 + \frac{1}{6}(x-x_i)^3 A'(x_i) + \frac{1}{24}(x-x_i)^4 A''(x_i) + \frac{1}{120}(x-x_i)^5 A'''(x_i)\right] \\ z(x-x_i) &= b_1 + b_2(x-x_i) + \\ &\frac{1}{p}\left[\frac{1}{2}py''(x_i)(x-x_i)^2 + \frac{1}{6}(x-x_i)^3 B'(x_i) + \frac{1}{24}(x-x_i)^4 B''(x_i) + \frac{1}{120}(x-x_i)^5 B'''(x_i)\right], \end{aligned}$$

where the term in brackets is now already known – we found the $A^{(n)}(x_i)$ coefficients earlier, so now we make a least-squares fit to the coupled equations to find the three unknown parameters: a_1, a_2, b_1, b_2, and most importantly: p.

[1] In general, a nth order spline fit is an nth order polynomial whose $(n-1)$ first derivatives are continuous and the nth one is changing in steps at the data points (knots). Spline fits are essentially smooth functions passing through data points

Once this is done, we can start all over again, taking now a better estimate for y' and z', derived from eqs. 3.3. Iteration is reached quicker than using a step-to-step Runge-Kutta integration technique (see sec. 3.3.3), and the method is more accurate than the tabulated-trajectory method used e.g. for the BMS momentum.

Some more checks are subsequently done on the scattered muon track – the **match** of the W67 (or P67-W67 or P67-W3) line to the track upstream of the absorber. A maximum acceptable chisquare cut is imposed for this match, taking into account exactly the amount of multiple Coulomb scattering expected in the absorber. The W67 line is however *not* used in the spline fit – multiple Coulomb scattering affects it too much.

The **trigger processor** checks whether the muon could have hit enough hodoscope hits to cause a trigger – fake triggers are rejected this way.

GEOMETRY is now ready to fit the main interaction vertex – as the point where the distance of closest approach of beam and scattered muon is minimal. The vertex itself is found weighing each of the scattered muon and beam tracks with its error matrix. If "hadrons" (may be electrons) are found, their fitting is attempted to the main vertex – if applicable this improves the vertex resolution since the vertex is now an intersection of three rather than two lines. If they do not fit to the main vertex, secondary vertices are sought after – so-called V^0's (neutral particle decaying into charged pair) or other. Here is the exhaustive list of all possible vertex types that can be found by GEOMETRY:

- Type 1 – beam and same sign muon
- Type 2 – beam and more than one same sign muon
- Type 3 – beam and same sign muon and 1 or more other charged tracks
- Type 4 – V^0: no incoming track, opposite charge pair outgoing
- Type 5 – beam and opposite sign muon
- Type 6 – charged V decay: incoming track, 2 decay tracks
- Type 7 – secondary vertex (not charged V) with incident track
- Type 8 – secondary vertex (not V^0) without incident track

3.3 Alignment and calibration

Time calibration is essential for the proper assignment of the measurement of the beam muons ($3 \cdot 10^7$ per spill) to the scattered muon ($\sim$ 400/spill). It is also essential for the correct determination of the drift time in the drift cells and hence the correct translation of drift chamber TDC information into spatial coordinates.

Alignment is understandably of paramount importance – a global misalignment can give a wrong momentum determination and a wrong scattering angle. A relative plane to plane misalignment increases the chances of assigning a wrong hit to a given track, and in general decreases the efficiency of the track finding in PHOENIX and its fitting in GEOMETRY.

A warning is in order: this section is boring. Whereas the reader has the leisure to skip over it to the interesting physics part in the next chapter, the author has spent almost a year working on it!

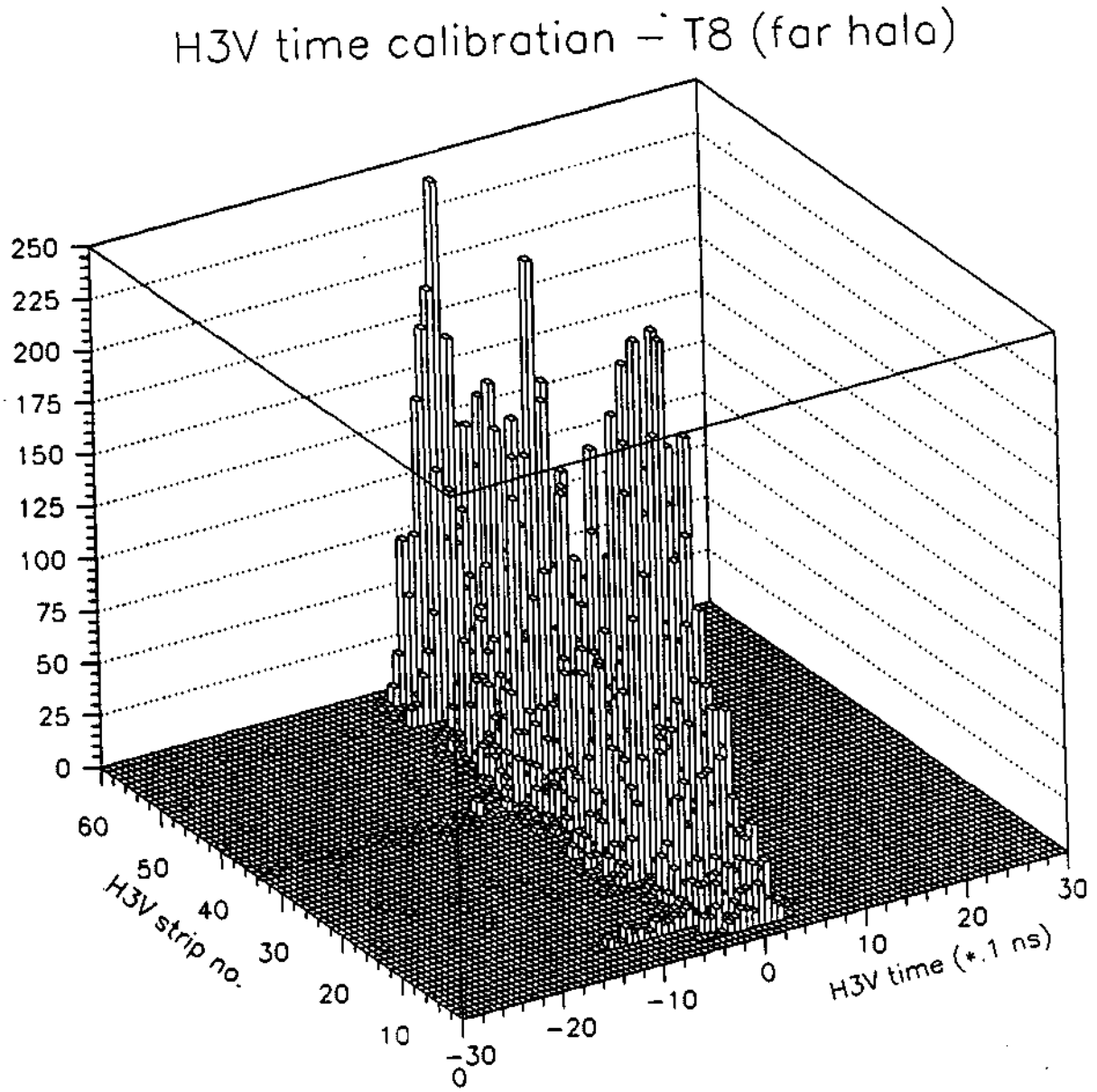

Figure 3.4: H3V time calibration for each hodoscope element done with T8 data. The time is measured in TDC units of 0.1 ns

3.3.1 Time calibration

The origin of all times for a T1 event (so-called trigger time) is H3V time. An internal consistency between the 49 strips (of which the three central ones are split to allow for the beam hole) is thus required - we don't want the time reference to depend on the y-coordinate of the scattered muon. The strips are read out on top and bottom by independent TDC's, the mean of top and bottom times is thus independent of the z-coordinate of the hit. Alignment triggers T8 (far halo for outer strips) and T7 (near halo for inner ones) are used, and events with one hit in each of H3V, H3H and H4H. The method is as follows:

- from the hits in H3H and H4H the z coordinate in H3V is predicted,
- calibration constants (T_0's) are determined such that for a hit at $z = 0$ the time in both top and bottom TDC's is zero, thus ensuring that for any z the mean time will be zero (fig. 3.4).
- a consistency between T8 and T7 can be achieved to the level of ± 1 ns at the strip-to strip level. A check with T1 gives a ± 2 ns scatter. This scatter may be explained by slightly different paths followed by the signals in the trigger logic electronics (2 ns = 60 cm additional path).
- global time shifts for different triggers (all strips by same amount) are adjusted by additional constants.

The calibration is rechecked for all triggers and global time shifts are set, for all triggers except T2 and T14 have their origin of times in H3V time.

For the small angle triggers however, different hodoscopes have to be used since we are recording events closer to the beam and thus not hitting the H3V strips (they pass in the hole between the split elements). These hodoscopes have strips read out only on one side by a TDC, so their calibration consists in adjusting T_0's such to have the time distribution centered around zero. The calibration is run directly on the T2 and T14 data respectively, the halo triggers being too far off the beam axis.

The other important time calibration concerns the Beam Momentum Station and beam hodoscopes. The TDC T_0's for all elements in each BMS plane are adjusted such that the average time (measured with respect to the trigger time) is zero. This is done with T5 data (beam trigger) and checked on T1 (fig. 3.5). However, this proved insufficient as a decrease of T10 events with BMS time was seen [2]. This could be explained by a wrong slope calibration of the TDC's (i.e. one TDC unit doesn't represent exactly .1 ns as it should, but a little more or less). Therefore these slopes were recalibrated using T9 - the 10 Hz clock trigger. A "start" signal was given to all TDC's by the trigger, the same signal was then delayed through a delay line of known length (thus a known delay) and this signal gave a "stop" to the TDC's. The deviations observed were inside a $\pm 5\%$ range.

The beam hodoscope TDC's are synchronized internally in a similar fashion (fig. 3.6). Next, the beam hodoscope TDC's are adjusted to zero with respect to the BMS time - in this way we ensure a good time coincidence (within 2-3 ns) between all three important times: trigger time, BMS time and beam hodoscope time (Fig. 3.6).

[2] Remember T10 is a random trigger and thus its BMS time distribution should be rectangular - a beam can arrive anytime during the time window opened randomly by the trigger

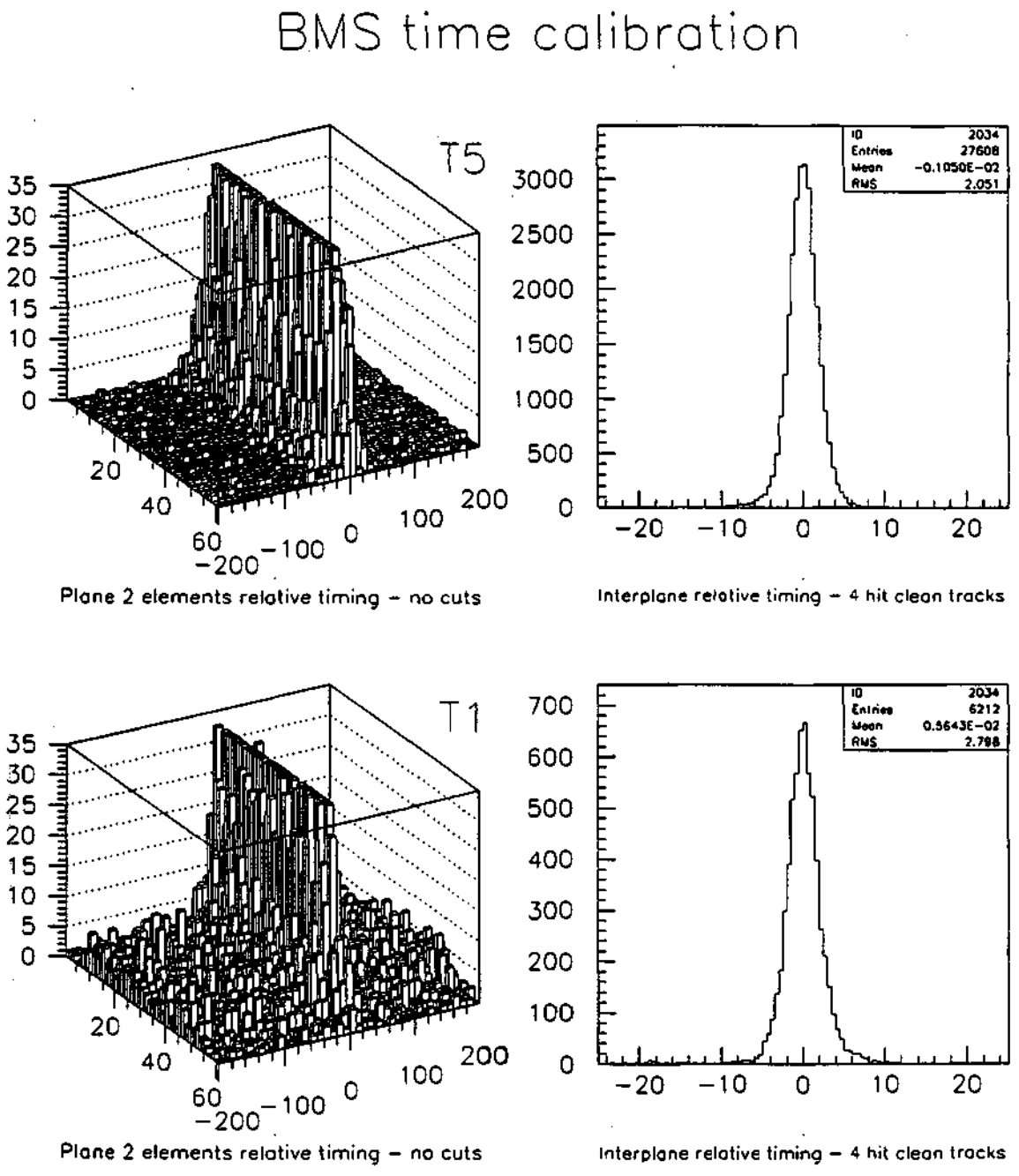

Figure 3.5: The BMS elements time calibration in sample plane 2 before any cuts (Manhattan plot) and interplane timing of clean 4 hit events. The above row is for T5 (alignment beam trigger, with only one beam track), and the lower row is for T1 (physics trigger, multiple beams allowed). Time in units of .1 ns.

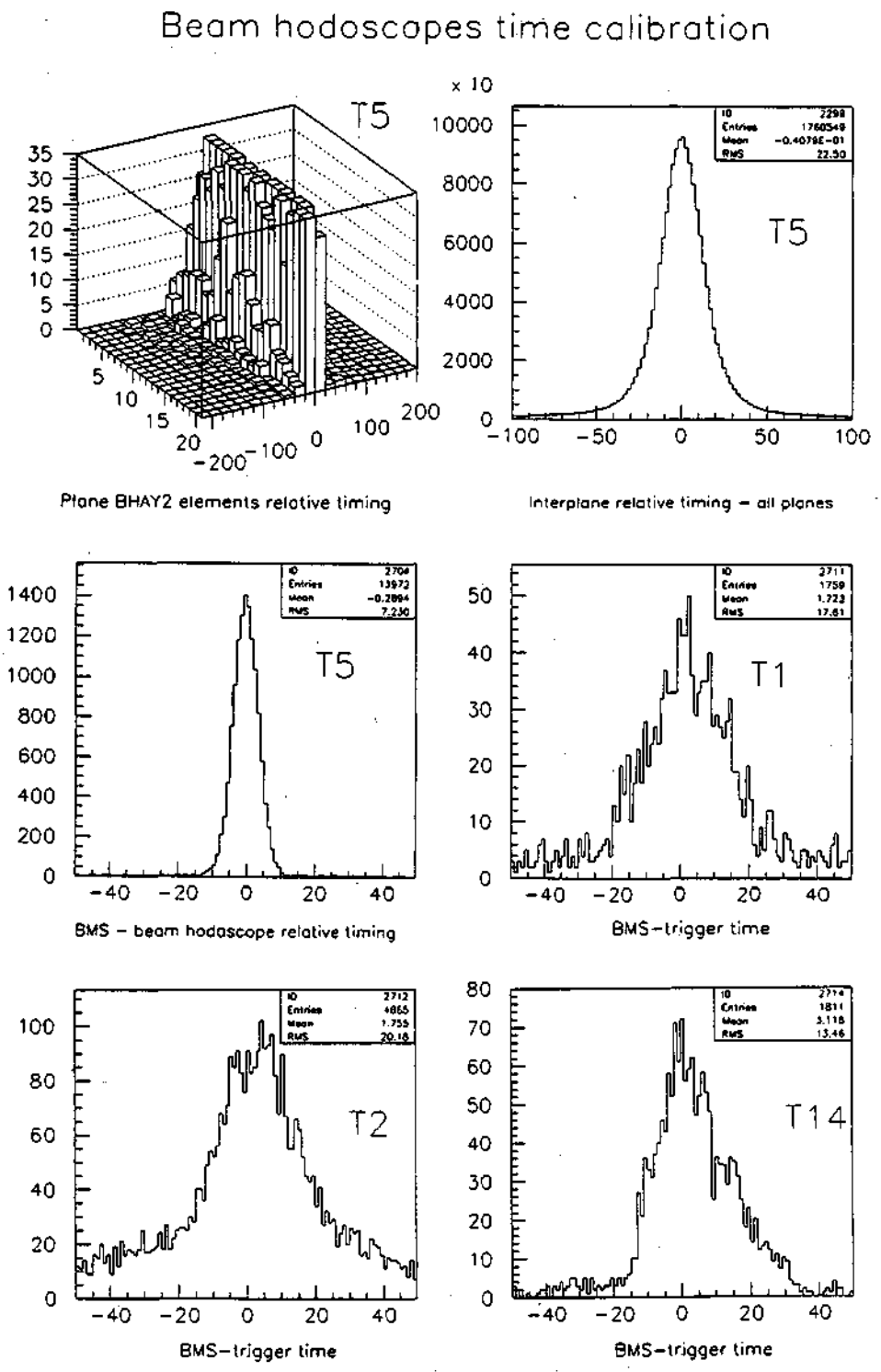

Figure 3.6: Top row: The beam hodoscopes elements time calibration in sample plane BHAY1 (Manhattan plot) and interplane timing. Middle and lower rows: relative time calibration of BMS and beam hodoscopes, and of BMS relative to the trigger time for T1, T2, T14. Time scale always in units of .1 ns

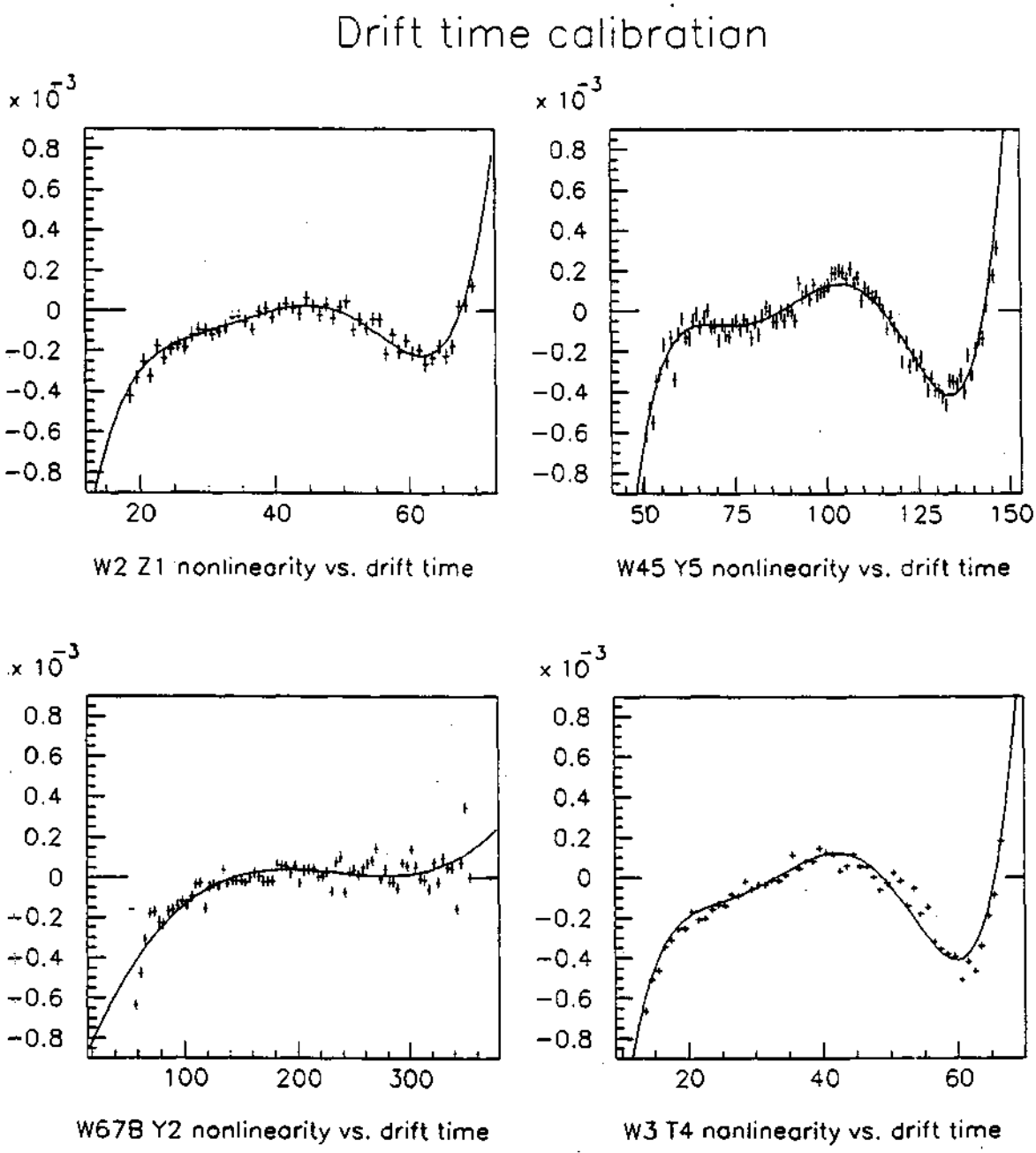

Figure 3.7: The drift time nonlinearity calibrations of sample planes. Plotted is $\epsilon(t)$ vs. drift time in units of 0.1 ns

The remaining time calibrations are the drift times – they are done iteratively, together with the alignment of the drift chambers. The actual coordinate of the hit in the chamber is:

$$\xi(t) = \xi_{0i} \pm (v_{drift}(t - t_0) + \epsilon(t)),$$

where ξ_{0i} is the position of the ith sense wire, v_{drift} is the drift velocity, t is the time recorded by the corresponding TDC, t_0 is the time the TDC would give for a track hitting exactly the sense wire (so $t - t_0$ is the actual drift time), and $\epsilon(t)$ is a correction due to nonlinearity of the electric field. This is parametrized by a polynomial (up to the 5th degree for the most nonlinear fields such as in W45). The calibration consists in finding the t_0, v_{drift} and nonlinearity polynomial coefficients. First the nonlinearity is neglected in order to find the t_0's and v_{drift}'s, and once they are fixed, one iterates on the nonlinearity. The procedure of calibration converges very slowly, mainly because non-orthogonal polynomials are used – however, a reasonable fit can be obtained (fig. 3.7). This calibration has to be done after a first alignment of the respective chambers, and then the alignment has to be rechecked again [3].

3.3.2 Alignment

The starting point for the alignment is an optical survey done in the experimental hall. It is accurate to about a cm, and is done each time a chamber or other piece of equipment is moved (e.g. for repairs). For the x-position, this is going to be the only reference, but in y and z we have a possibility to cross-align the different chambers using the straight line muon tracks recorded with the alignment triggers when the magnet is turned off [4].

The principle of alignment is shown on fig. 3.8. The *residual* is the distance between the actual hit and the fitted line. If the residual is bigger than the *roadwidth* (a parameter which is set later, during PHOENIX tuning), the hit won't be associated with the track at all. Otherwise, the residuals for drift chambers follow a Gaussian distribution with an r.m.s. representing the chamber resolution. The mean of the Gaussian should be centered on zero residual i.e. there should be as many hits above and below (or left and right) of the fitted line. If this is not the case, it means the chamber is *misaligned*, i.e. its y respectively z positions are wrong. We then have to adjust these positions in the *alignment file* which is a file containing all the relevant chamber coordinates and time calibrations. Usually residuals for a whole plane are looked at, but if they present funny shapes, one looks at residuals vs. wire number to check for any anomalous wires. Several such wires were detected in W67, and fig. 3.9 shows an illustration of four consecutive wires being off by about half a mm in W45 Z3 plane. This can only be due to a hardware error in wiring the chambers, i.e. the spacing of the wires was shifted by half a mm compared to other wires (this can easily happen on a 5 × 3 m big chamber with 4 cm wire spacing).

As in the reconstruction philosophy itself, we start from the back towards the front. The first chambers to align are W67, P67 and W3 (fig. 3.10). We start with the central (B) module of W67 on T7 (near halo), using W67B lines to align the planes of module B between themselves (line a). These lines are also extrapolated to P67 and W3 and the three

[3] The alignment changes ξ_{0i} which then implies a direct correlation with $t_0 \cdot v_{drift}$ and also with other parameters.

[4] An effect of residual magnetic field was investigated by comparing alignments from two data sets where the magnet was turned off from opposite sign currents – any residual effect should have opposite sign in both cases.

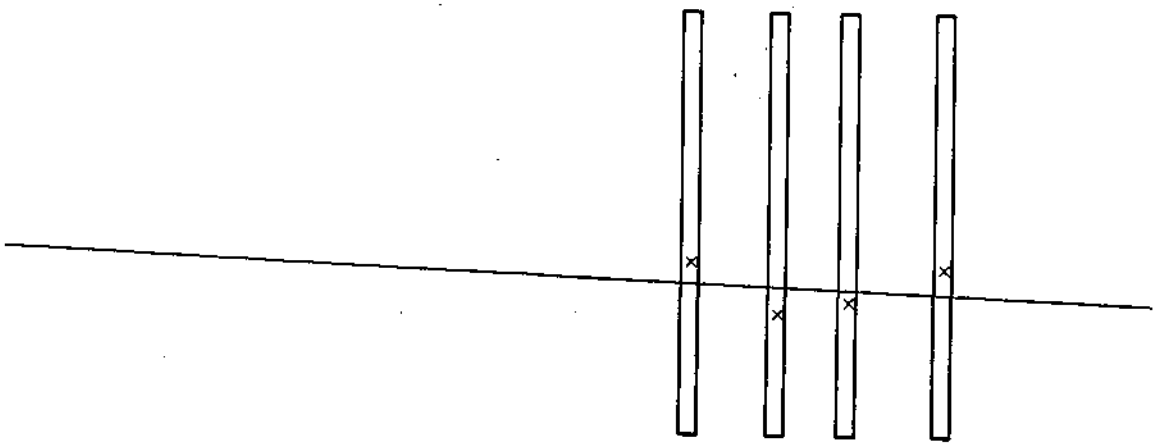

Figure 3.8: A schematic representation of alignment. Crosses are hits, the line is a fit to the hits.

detectors are thus aligned. The alignment in itself is an iterative procedure, for changing the alignment of a few planes changes the line fit in the next iteration. More often than not 3-5 iterations are necessary before the procedure converges for all planes. Once this is done, we have to perform the drift time calibration for W67B and W3, and redo the alignment if the calibration changes. Then we can start on the far halo (T8) to align W67A and W67C internally using W67A and W67C lines respectively; common W67A/W67B and W67B/W67C lines in the overlap region are used to align the off-center modules A and C with respect to the central B module. Now we have to calibrate the drift times of W67A and W67C...

Next comes the alignment/calibration of the W45/P45 group with T7. First we use W45 lines to internally align W45 planes. These lines are also extrapolated to P45, to align P45 with respect to W45. Once this is done, the drift time calibration of W45 has to be done. Then as usual we have to recheck the alignment of the group... Also, it was found that P45 was tilted in the azimuthal direction (in the y, z plane). So W45 lines are used to plot residuals vs. the wire number, lines are fitted through the scatter plots and tilt angles are extracted. Typical tilts found are in the range of 0.2-1.0 mrad.

When the procedure has converged, we may proceed to extrapolate the W45 lines to the W12 group to get a rough first estimate for the W12 alignment. Having done this, we proceed to align W12 more accurately using now W12/W45 lines (a bigger lever arm means better accuracy of lines so we use it whenever possible). Again we now have to calibrate W12 drift times and recheck the alignment...

Trusting now the alignment of these two big groups, W45/P45 and W12 we proceed to align all the other big chambers in the experiment using W12/W45 lines (still working with T7). This means aligning the chambers in the FSM (P123) and upstream of it (PV12), plane by plane.

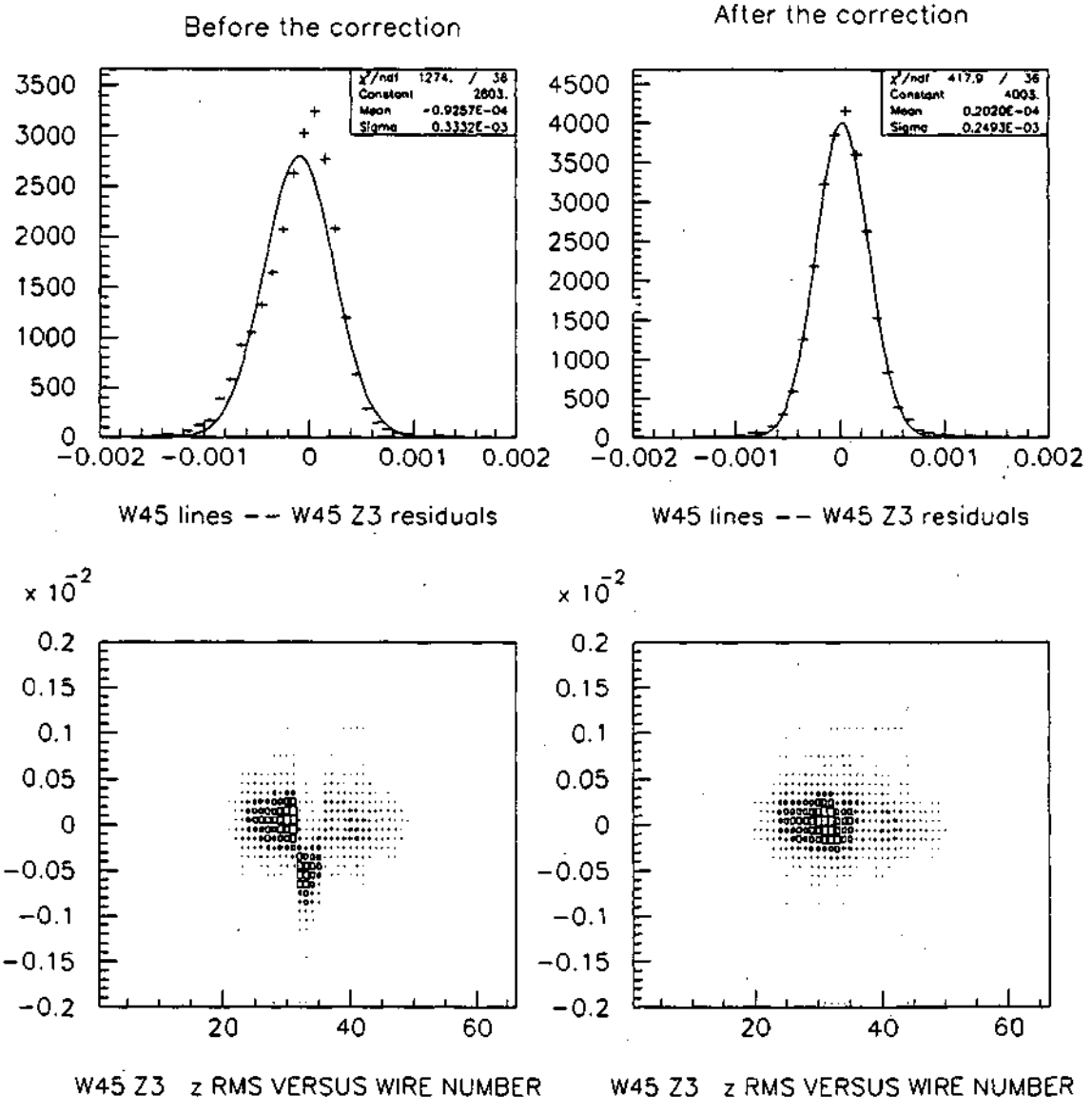

Figure 3.9: The residuals in W45 Y1 before (left) and after the correction (right) for four misspaced wires. The funny non-Gaussian shape in the upper plot goes away when we apply the correction

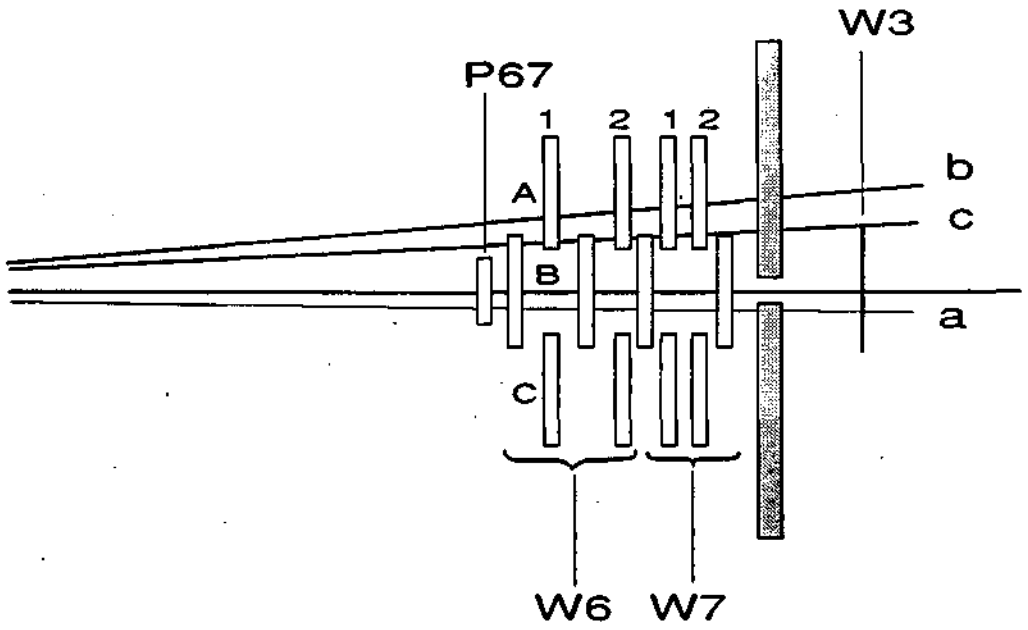

Figure 3.10: The alignment of the group of chambers behind the absorber. A T7 (near halo) muon line (a) can be used to mutually align W67B, P67 and W3 planes. T8 (far halo) muons can align W67A or C planes internally (b). The overlap is used to align the A and C modules respective to B (c).

Looking at the residuals in PV1 plane Y1 a subtle effect meets the eye: starting from wire number 475, the residuals are shifted upward by 1 mm, i.e. half a wire spacing (fig. 3.11). The only explanation [59] for this is that somehow every hit generated a "ghost" hit on the following wire, and PHOENIX then gives a coordinate midway between the two wires. The assumption proves correct in a histogram of cluster size (number of neighboring wires hit) vs. wire number (fig. 3.12). Up to wire number 475, cluster sizes of 1 dominate, some events with 2 and 3-hit clusters are seen. Thereafter, only cluster sizes of 2, 4 and 6 are present! This can be understood by assuming [60] that a bit in the chip readout was always set. The problem can be cured by simply telling the decoding to split the clustersize in half.

Looking at P123 residuals, tilts were also seen as in the case of P45, up to 1.5 mrad. However, the origin of these tilts remains unclear, for significant tilts appear also when one uses MonteCarlo events which are generated with the assumption that the P123 chambers aren't tilted. Moreover, it was estimated [61] that since the equation of motion is used for the spline fit inside GEOMETRY, these tilts would not affect the fit.

Still with the same W12/W45 lines a link is made to the mutually aligned W67/P67/W3 group and trigger hodoscopes behind the absorber(s). As the W12/W45 lines have to pass through the absorber to reach these chambers, their r.m.s.'s are quite big – about a cm typically. This is why it would be imprecise to use these lines to align W67/P67/W3 plane by plane. Rather, the whole group is treated as one and if it shows a global shift this is corrected for (Fig. 3.12).

The big chambers are now aligned. Or are they? Remember we always align chambers relative to each other – we started by aligning W67 planes with each other, then used that

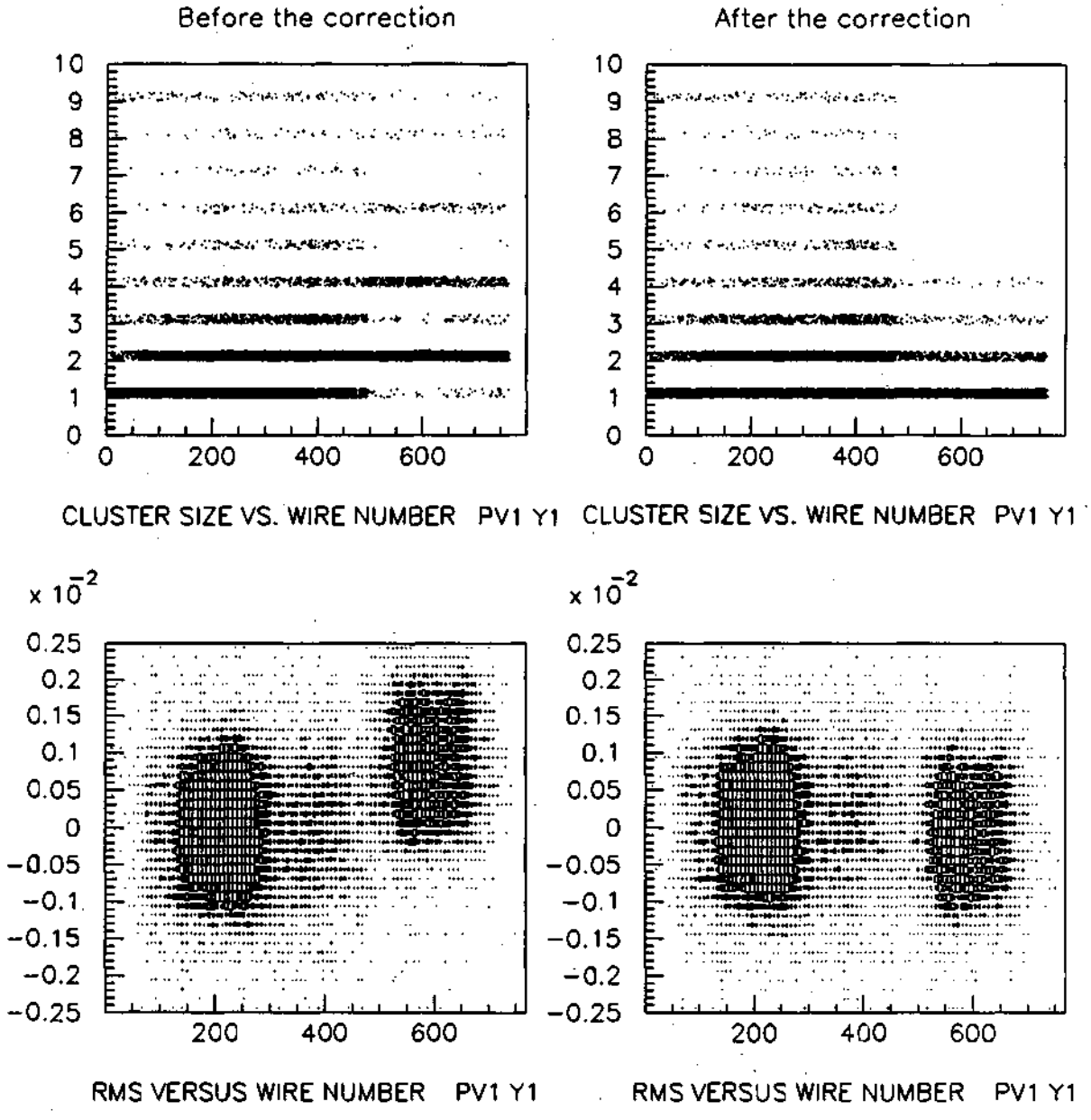

Figure 3.11: The readout error in PV1 Y1. Left plots before the correction, right the corrected ones. R.m.s. are in meters (full scale ±2.5 mm)

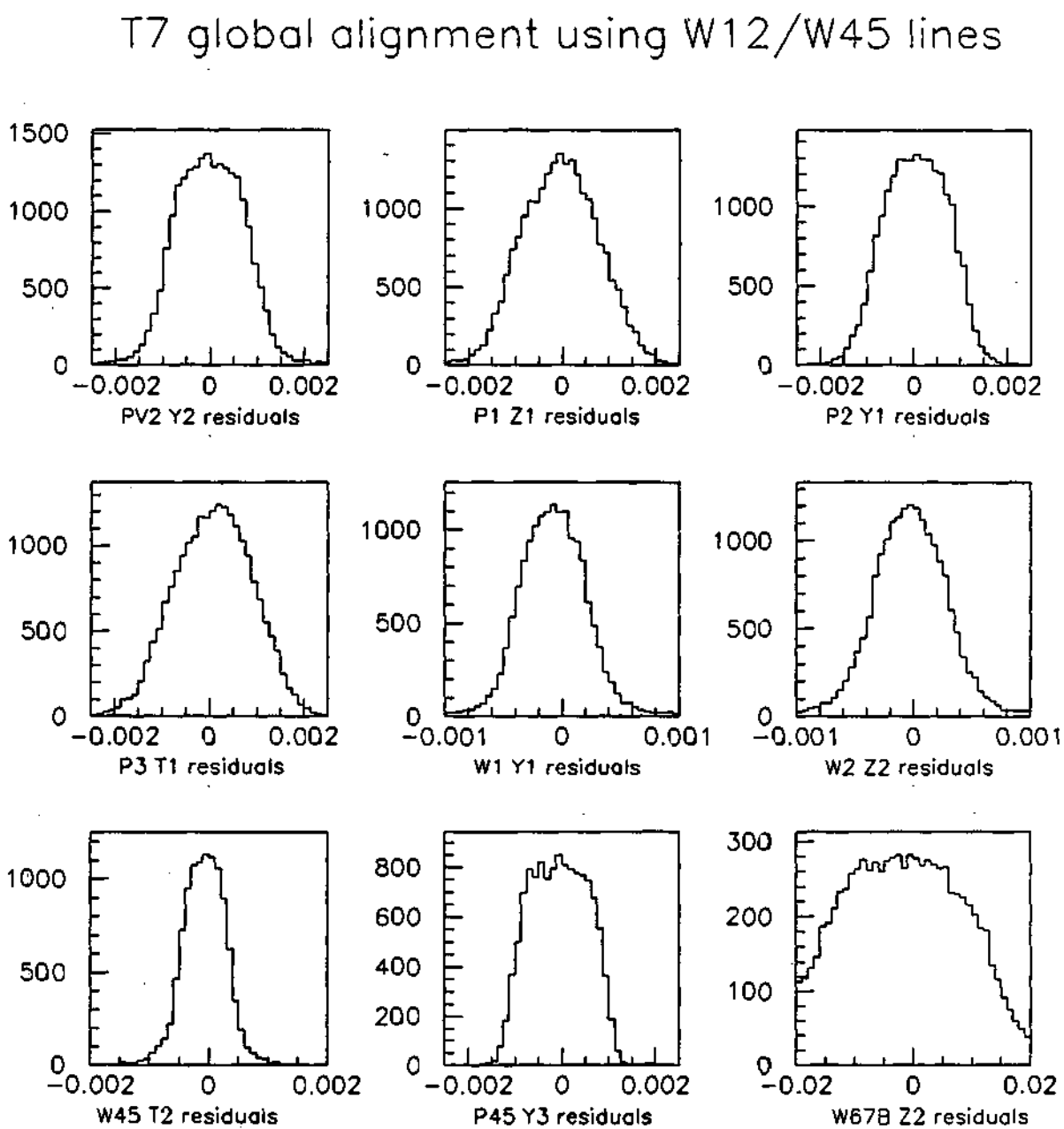

Figure 3.12: The T7 global alignment. Some sample planes are shown for each detector. Notice the square-like residual shape for proportional chambers and the more Gaussian-like ones in drift chambers. W67 residuals with an r.m.s over a cm reflect the multiple Coulomb scattering in the absorber. Where the mean of residuals is off-center, the plane position is readjusted.

Detector	Alignment change (T1-T7 or T5) [mm]	Scatter around mean (T1 throughout period) [mm]
W67	$< \pm 0.20$	$< \pm 0.08$
P67	$< \pm 0.08$	$< \pm 0.05$
W3	$< \pm 0.40$	$< \pm 0.15$
W45	$< \pm 0.04$	$< \pm 0.02$
P45	$< \pm 0.05$	$< \pm 0.08$
W12	$< \pm 0.03$	$< \pm 0.02$
BHA	$< \pm 0.13$	$< \pm 0.06$
BHB	$< \pm 0.16$	$< \pm 0.10$
P0H	$< \pm 0.04$	$< \pm 0.02$
P0B	$< \pm 0.07$	$< \pm 0.02$
P0C	$< \pm 0.03$	$< \pm 0.02$
P0D	$< \pm 0.04$	$< \pm 0.03$

Table 3.1: Maximal shifts of alignment observed during the check throughout the period

reference to align P67 and W3. What if the first plane of W67 we took as a reference was wrong? This is taken into account by the last step described above. But then again, we started W45 alignment relative to one reference plane and what happens if this was wrong? The answer is – everything will be mutually aligned, but not absolutely, with respect to the targets or the beam line! How do we cure this? We take for granted that the FS magnet weighing in excess of a hundred tons, does not move, and therefore the position of the P2 chamber in the center of the FSM is taken as reference. So the whole alignment is "untwisted" to make the P2 position correspond to the survey measurement.

Now we can proceed to use T5 (beam trigger) to align the small P0 chambers and the beam hodoscopes. Of the aligned chambers, only P45 and PV12 go sufficiently close to the beam line to present an overlap with the small chambers we now want to align. So we now use T5 data (the beam trigger) and construct PV12/P45 lines. The residuals in P0H, P0B, P0C, P0D, and P0E permit us to align these detectors. Once the P0's are aligned, we fit the PV12/P45 lines with the P0 hits and use this to align the beam hodoscopes.

This concludes the alignment. Another check is done however, to avoid bad surprises after the production. The alignment of the big chambers is checked on T1 with the same program as the T7 alignment, on 5 random data tapes spanning the data taking period. The same is done for the small chambers with the T5 program, and for time calibrations. Good constancy of the alignment is found as is seen in table 3.1.

3.3.3 BMS calibration using BCS

As mentioned before, the Beam Momentum Station was recalibrated using the Beam Calibration Spectrometer whose strong and homogeneous magnet (11.5 T·m bending power) and long lever arms for both the incoming and deflected muon permit a momentum determination with a precision of ±0.1%.

The tracks are reconstructed before entering the BCS magnet using the P0E, P0A and P45 chambers, and after it using 3 y- and a z-chamber positioned 35 m downstream of the BCS magnet to give a good lever arm (displacement of 200 GeV/c muons: 0.6 m). The momentum is then calculated on an event-by-event basis. We "guess" the first approximation of the momentum (taking the momentum given by BMS for the same track), and then using a Runge-Kutta integration method we calculate the expected deflection in the BCS. Then we compare to the measured deflection, and correct the momentum "guess" by 0.1% up or down, depending on the sign of the difference in deflections (true-calculated). We proceed in such manner and in 0.1% steps until the difference in deflections changes sign and assign the true momentum to be the mean between the last two iterations. The expected accuracy is thus about 0.05%. These momenta are now considered to be more accurate than the ones computed by the "old" BMS coefficients, so new BMS coefficients are computed to make the BMS and BCS momenta agree.

This agreement was checked on the mean and the slope of the whole data sample in a p_{BMS}[5] vs. p_{BCS} scatter plot. The result gives [57]:

$$\begin{aligned} < p_{BMS} > &= 198.8\ \mathrm{GeV}/c \\ < p_{BCS} > &= 198.6\ \mathrm{GeV}/c \\ < \frac{\partial p_{BMS}}{\partial p_{BCS}} > &= 1.029 \pm 0.036, \end{aligned}$$

which shows a 0.1% agreement between BMS and BCS momenta (the original discrepancy with the old BMS coefficients being 0.5%).

3.4 Tuning of the data reduction chain

For PHOENIX and GEOMETRY to be efficient and accurate, tracking parameters have to be *tuned*. In PHOENIX the main parameters are *roadwidths* and *plane requirements*, in GEOMETRY we need accurate *r.m.s. resolutions* for each detector plane.

3.4.1 PHOENIX tuning

The tuning, like everything else, starts behind the absorber. First we need to set hodoscope tagging roads. Their function is illustrated on fig. 3.13. The gray bands represent tagging roads around all possible tracks producing two hits in H3H and two hits in H4H. The dashed bands are excluded by a (very wide) cut on slopes and by the request that tracks point roughly towards the FSM exit. They are obviously impossible tracks, so the dashed bands aren't taken into account for tagging. Only hits within the full grey bands are tagged, i.e. kept in memory. Other hits are simply scratched out from memory – they serve no purpose any more. The next step is the so-called PTRACK algorithm. It takes hits in *keyplanes*

[5] now calculating p_{BMS} with the new BMS coefficients!

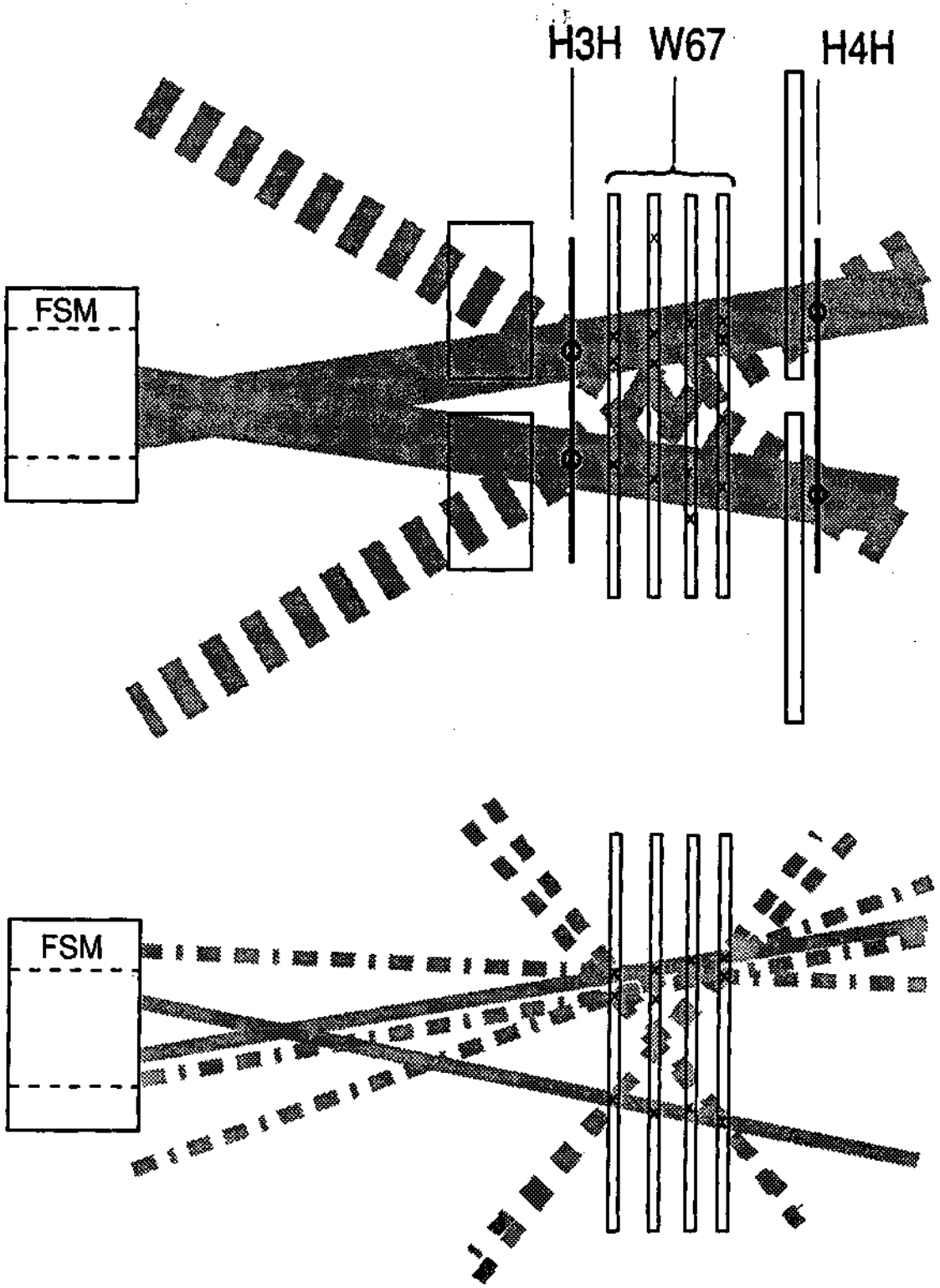

Figure 3.13: Simplified representation of PHOENIX tuning in W67. Hodoscope tagging is shown above, and PTRACK roadwidths helow, acting only on tagged hits. Only four planes are shown for simplicity.

(planes which are required to have a hit for the program to search for a track) – in W67 keyplanes are the most upstream and most downstream of each set (y, z, θ). So for each coordinate all tracks possible with the tagged hits are considered. Some of the combinations (dashed bands) will again be rejected because of crazy slopes or not pointing towards the FSM. Others (dot-dashed bands) need to be rejected by sufficiently tight roadwidths and by requiring a certain number of planes to have hits inside this roadwidth, the so-called plane requirements. One first starts by looking for lines with hits in all four planes (in reality there are 6 planes for y and z in W67, but we consider 4 to simplify the example). One so finds the two full gray bands if the roadwidth is sufficiently small. If the roadwidth were too wide, there would be more combinations possible. When these four-hit lines are found, the algorithm searches for three-hit lines from the remaining hits and so on down to the plane requirement for each detector. Once all lines in one projection are found, the procedure is repeated in the other. Tagging in y for T1 is done by roads set around lines passing through the hit in H3V and the target, no other vertical hodoscope being available. When lines in both coordinates are found, they are *associated* into a three-dimensional line by θ hits. This means that e.g. two z-lines (lines in the x, z-plane) and two y-lines (lines in the x, y-plane) can be associated in four different ways, but there are really only two lines, so we have to associate the projections correctly! This is done by predicting θ hits for each combination, and searching again within a roadwidth for hits in θ planes. And here is another parameter to tune!

The tuning philosophy goes on analogously as we go upstream to W45/P45 and W12/P0E. As described above in section 3.1, the lines found in a given detector always serve for tagging hits further upstream.

Inside the magnet, the method stays the same in the non-bending $x - z$ plane. In $x - y$, the roadwidth must be set for finding the corresponding point in P0D, and then the so-called MOVEUP roadwidths which are used for finding points in P123 lying on the circle approximation of the particle trajectory. Fig. 3.14 illustrates the magnet reconstruction.

Originally these roadwidths and plane requirements were set by MonteCarlo studies, and this is not encompassed by this work. The main task here is to check whether these parameters look reasonable on data. Histograms of residuals were studied and compared to roadwidths to check that good events are not rejected. Chisquared probabilities [6] of line fits are looked at and it is checked that they are reasonably flat, except for a spike at low vertex probabilities. This spike is due to the non Gaussian nature of errors on the discrete proportional chamber coordinates which then enhances the "tails" of the χ^2 distribution itself, resulting in a peak at low χ^2 probabilities. The mean χ^2 probability should also rise as the line is fitted to more detectors. This is observed throughout the detector. For example a typical run has an average χ^2 probability of 0.37 for W45 lines; for those associated to W12 this probability goes up to 0.39 and for lines that get through the magnet it is 0.40.

3.4.2 GEOMETRY tuning

GEOMETRY tuning consists again in looking at residuals and subsequent parameter tuning. But this time the predictions are given by more refined and more accurate spline fits. This means that the alignment can be checked and corrected at the 0.01 mm level for the main chambers. R.m.s.'s are extracted for each chamber in order to assign a valid error to the

[6] The χ^2 probability is defined as the probability that an event has a χ^2 greater than the one observed. For a random distribution with Gaussian errors the χ^2 probability is uniformly distributed from 0 to 1, and its mean value is 0.5.

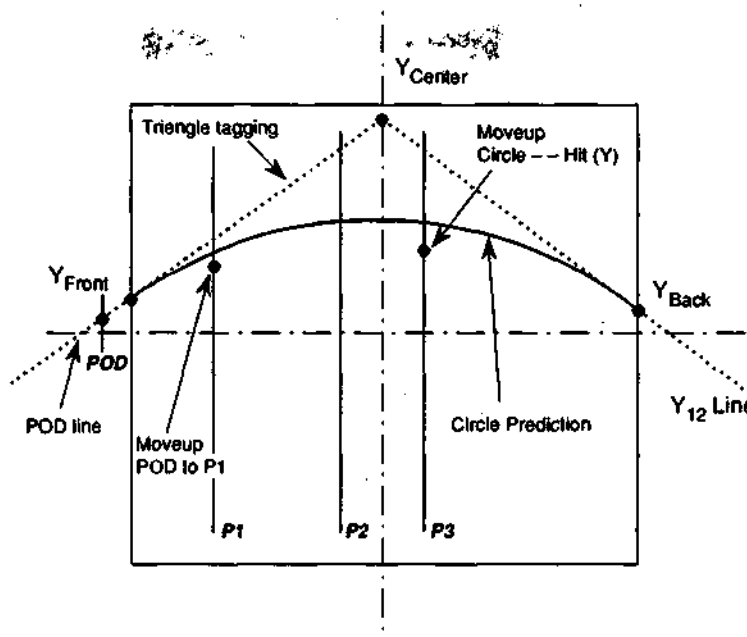

Figure 3.14: The reconstruction inside the magnet (bending plane). A circle is a first approximation to the trajectory, and we know its tangent (the W12 line). It is extrapolated to the center of the magnet, mirrored and this gives a prediction for the P0*D* point. When a P0*D* line is found, the circle can be improved to find the actual hits in P123, using MOVEUP roads.

track fit – they play the role roadwidths did in PHOENIX – if a track has ridiculously low χ^2-probability (10^{-6} or so), it will be rejected even if it has been nicely inside PHOENIX roadwidths before. The alignment and r.m.s. changes are fed in to the alignment file.

Especially the link between the W67 lines and W45/P45 and the rest of the detector is tuned, taking into account the residual magnetic field in the hadron absorber wall. Trigger matrices are checked (the trigger processor in GEOMETRY has to check the same matrices as were actually applied during data taking).

3.4.3 Beam tuning, veto tuning

These steps are only done when MINI DST's are available, and Micro DST's are about to he written. The veto tuning is done for T10. These events, used for normalization, are random triggers and are not vetoed online. Essentially time cuts are set in order to veto the same tracks which would be vetoed online for a T1, 2 or 14.

Beam tuning is done to ensure a uniform illumination of all four targets: cuts on the beam position, slope, and momentum are tuned.

3.4.4 Production

When all the alignment, calibration and tuning is done, we are ready to start production. This is a very CPU time-intensive part of the work, which was performed in about three months' time on three 370/E IBM emulators (each equivalent in computing power to one half an IBM 168 mainframe). In this time the 338 raw data tapes were processed first by PHOENIX, the output of which was temporarily stored on hard disks of our MicroVax cluster and immediately processed by GEOMETRY, the output of which gives again 338 MAXI data

	T1 (standard)	T2 (small angle)	T14 (small x_{Bj})
Raw triggers	2 271 000	6 595 000	3 578 000
PHOENIX Line found in W67/P67/W3	1 814 000 (79.9%)	3 558 000 (54.0%)	1 911 000 (53.4%)
Full muon found (output from PHOENIX)	1 193 000 (52.5%)	2 087 000 (31.6%)	855 000 (23.9%)
GEOMETRY Satisfy trigger	791 000 (34.8%)	1 789 000 (27.1%)	670 000 (18.7%)
GEOMETRY found a vertex	657 000 (28.9%)	1 420 000 (21.5%)	601 000 (16.8%)
SNOMIN Output to Micro DST	525 045 (23.1%)	1 207 102 (18.3%)	542 338 (15.15%)

Table 3.2: Reduction of data sample throughout the chain: out of 12.4 million raw triggers, about 2.3 million are available for physics analysis

storage tapes. These data were also immediately processed further by SNOMUX and 27 MINI DST's were produced.

During the production, the performance of the programs is monitored with *run summaries*. Interesting quantities such as the number of events on input, the fraction of events being output as well as other percentages are stored in special files, and then these numbers can be plotted as a function of the run number. Figure 3.15 illustrates some of these checks, and Table 3.2 gives an overview of the data reduction. An interesting feature is seen for run numbers 60 to 85. The beam intensity was lower during that period. This causes a relatively larger number of T14's per tape (remember T14 has a requirement of a single beam track within the time window, so it is understandable that such a trigger is more likely if the beam intensity is low). Also it seems that the whole detector performs better in lower beam intensity environment: the percentage of events output by PHOENIX is higher for these runs. Figure 3.16 shows some of the GEOMETRY run summaries.

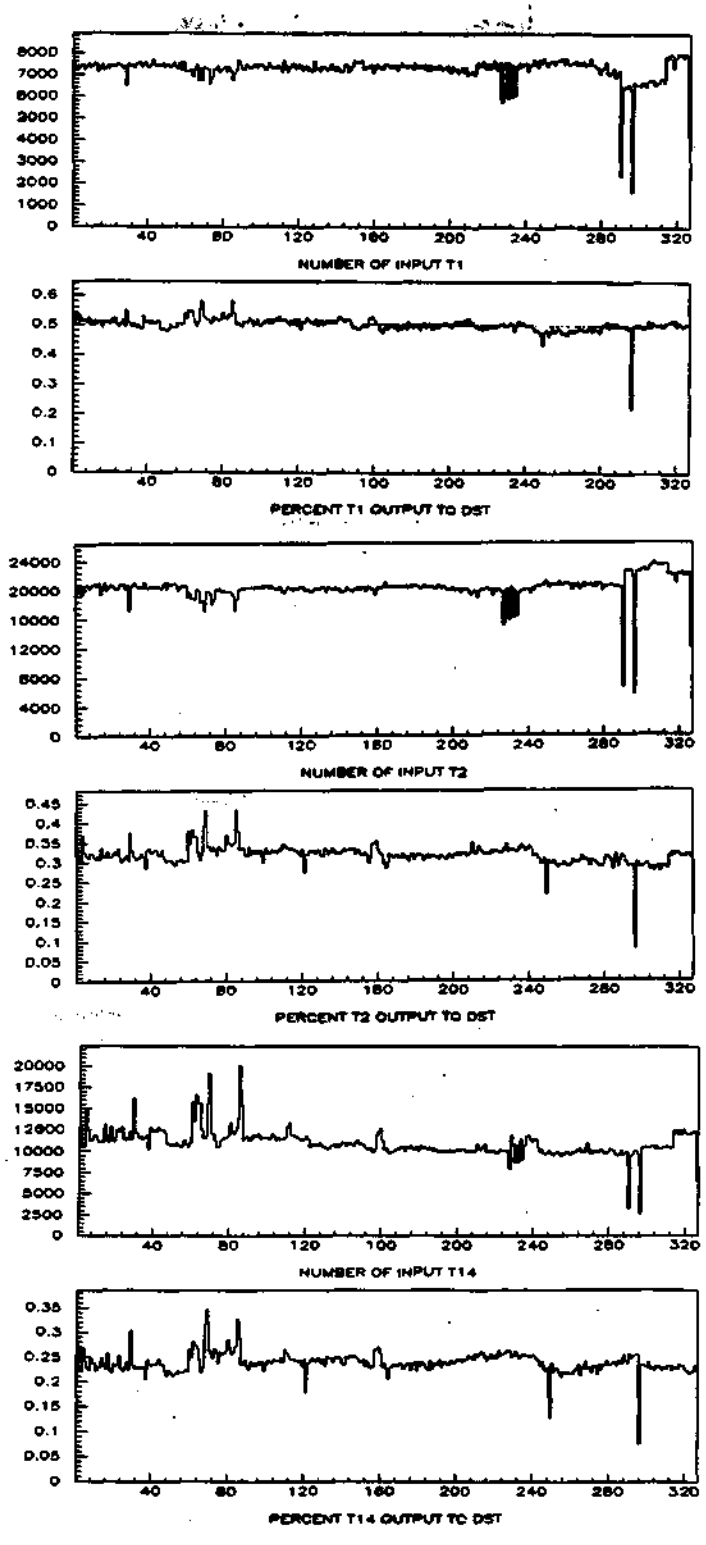

Figure 3.15: Some PHOENIX run summaries for the three physics triggers: number of events on input, and percentage written to output.

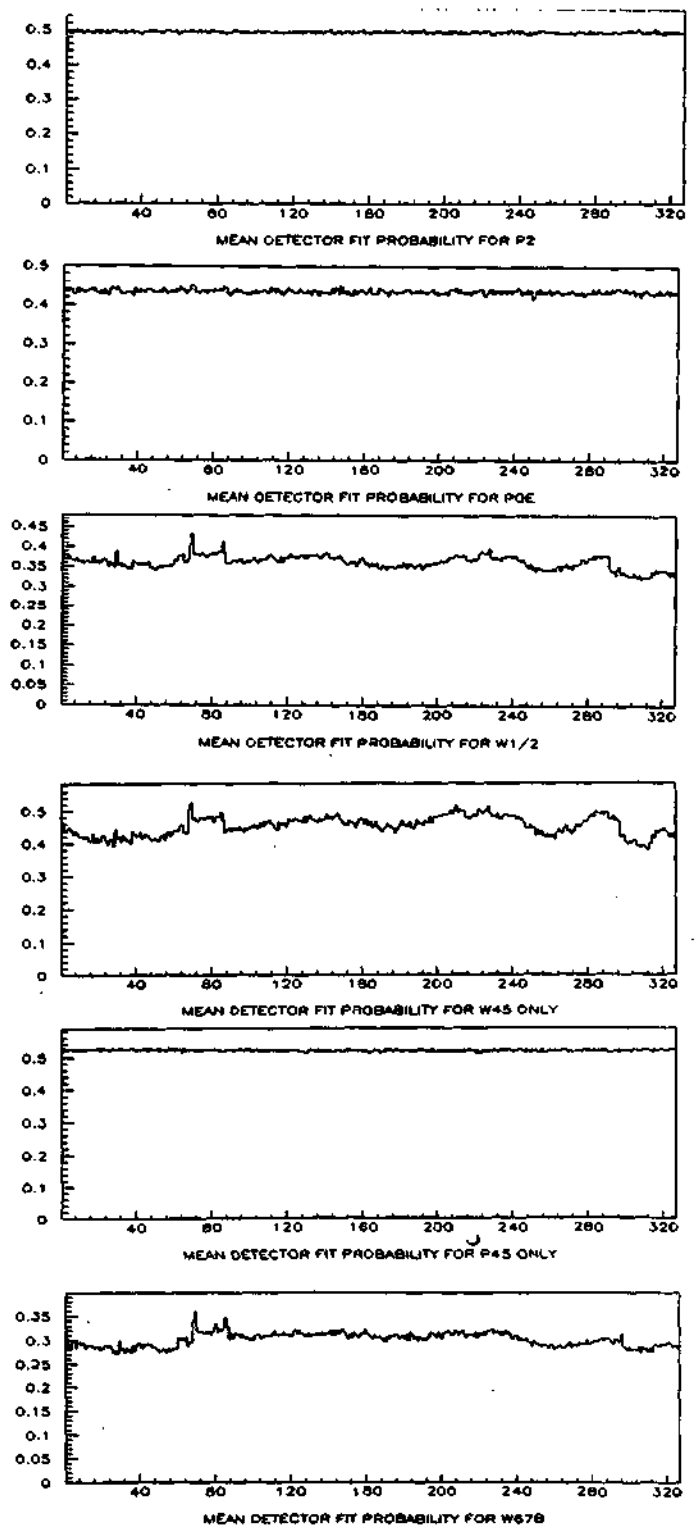

Figure 3.16: Some GEOMETRY run summaries for detector χ^2 probabilities of line fits. Whereas proportional detectors are remarkably time-independent, the time-dependencies of the drift chambers are understood by temperature fluctuations causing changes in the drift properties of the gas mixtures.

Chapter 4

The structure function ratio analysis: F_2^{Li}/F_2^D and F_2^C/F_2^D

Once the data are safely stored on Micro DST, the physics analysis can begin. First we have to look at the **vertex distribution** in order to set *vertex cuts*, the criteria as to which target one should attribute a given event. Then one looks at **rundependencies** of kinematic variables and other quantities, to spot any "bad runs", i.e. suspicious subsets of data which could introduce a bias to the physics results and should thus be excluded from further analysis. A second tool one can use to verify the quality of the data are **flux ratios**. We then set **kinematic cuts**, based on knowledge of our apparatus, essentially aiming to eliminate kinematic regions with poor resolution, high background ($\rightarrow$ radiative processes, see sec. 4.3.1), and rapidly changing acceptance. All this knowledge stems from previous work on MonteCarlo simulations of the NMC detector. However, it is possible to some extent to check the validity of these cuts by studying flux ratios as we shall see in a moment. Finally, when we are sure of our data sample, we can compute the ratio of cross sections (and thus the ratio of structure functions, cf. sec. 1.2) using the so-called ratio method (also sometimes called the geometrical method [1]) by simply counting events in each target and applying the algorithm explained in sec. 2.3. This is a very nice feature of the algorithm – we can obtain physics results without having to rely on lengthy MonteCarlo simulations as is usually the case for experiments of comparable complexity. In this calculation we must not forget to apply **radiative corrections** in order to correct for events that are recorded but do not represent the one photon exchange of Fig. 1.1 that we are interested in, but stem either from higher-order processes, or from elastic and quasielastic scattering. Many other small corrections enter the analysis, such as kinematic and vertex smearing, and other minor corrections.

4.1 Data checks and selection

4.1.1 Validity of the ratio method

Let us first explore into some more detail eq. 2.1. giving the essence of the ratio method. We had written that the fluxes and acceptances cancel, let us now specify under which circumstances this will occur. First of all, we had written down the equation tacitly assuming

[1]- because it is taking a geometrical mean of two ratios, *and* it uses the geometry of the target setup in an intelligent way

that the acceptance for both target rows is the same. This is a reasonable assumption, and assuming the whole setup is consistent, the acceptance should only depend on the x position of the interaction point, not on which target row is currently used. However, let us for the moment assume this is not *a priori* fulfilled. One of the reasons for it not being fulfilled would be e.g. the time dependent efficiencies of some chambers [2] (as seen for example in the GEOMETRY run summaries, fig. 3.16). However, the target changes being frequent (every two runs), only very rapid changes of acceptance (e.g. one "bad run") could influence the ratio.

Second, we must remember that the cross sections and acceptances are functions of kinematic variables, and strictly speaking, eq. 2.1 is only valid in *one point* of the x_{Bj}, Q^2 plane. However, although the statistics we accumulated is quite impressive, it is still *finite* and we can only compute our ratio in finite-size bins.

If we now write the expression for the number of counts in each target bearing the above in mind, for example the number of events occurring in the upstream lithium target, in the Salève target row, in a finite x_{Bj}, Q^2 bin spanning $x_0 \pm x, Q_0^2 \pm Q^2$, we have:

$$N_{up}^{Li} = \xi_{up}^{Li}\phi_S \int_{x_0-x}^{x_0+x}\int_{Q_0^2-Q^2}^{Q_0^2+Q^2} \mathrm{d}x\mathrm{d}Q^2 \frac{\mathrm{d}^2\sigma_{Li}(x,Q^2)}{\mathrm{d}x\mathrm{d}Q^2} a_u^S(x,Q^2) \tag{4.1}$$

where, as before, ξ is the nucleon density of the Li target, ϕ_S is the integrated flux in the Salève position [3], $d^2\sigma/dxdQ^2$ is the double differential cross section and a the acceptance.

In order to evaluate any deviation of this expression from the simple picture of eq. 2.1, let us develop the subintegral functions in Taylor series in x_{Bj} and Q^2. Now, since the full range of x_{Bj} is from 0 to 1, a bin in x_{Bj} will always he much smaller than 1, so it is legitimate to expand in powers of x_{Bj} around x_0. Not so for Q^2, which can span a range of several GeV^2/c^2, so a more appropriate variable for expansion is $u = \log Q^2$. We can also explicitly take into account the steep $1/Q^4$ slope of the Mott cross section (cf. eq. 1.5) by writing:

$$\frac{\mathrm{d}^2\sigma_D}{\mathrm{d}x\mathrm{d}Q^2} = \frac{1}{Q^4} s_D(x,Q^2), \tag{4.2}$$

s_D is thus defined as containing all the structure function terms (the terms in brackets from (1.5)).

We then have:

$$N_{up}^{Li} = \xi_{up}^{Li}\phi_S \int_{x_0-x}^{x_0+x}\int_{u_0-u}^{u_0+u} \mathrm{d}x\mathrm{d}u\, \mathcal{R}^{Li}(x,Q^2) e^{-u} s_D(x,Q^2) a_u^S(x,Q^2) \tag{4.3}$$

where we have written the Li cross section as a product of the deuterium cross section (4.2) and the ratio we wish to extract.

We may now proceed to develop in Taylor series up to the second order:

$$\begin{aligned}\mathcal{R}^{Li}(x,Q^2) \;=\; & \mathcal{R}^{Li}(x_0,Q_0^2) + \partial_x\mathcal{R}^{Li}(x_0,Q_0^2)x + \frac{1}{2}\partial_x^2\mathcal{R}^{Li}(x_0,Q_0^2)x^2 + \\ & \partial_x\partial_u\mathcal{R}^{Li}(x_0,Q_0^2)ux + \partial_u\mathcal{R}^{Li}(x_0,Q_0^2)u + \frac{1}{2}\partial_u^2\mathcal{R}^{Li}(x_0,Q_0^2)u^2\end{aligned} \tag{4.4}$$

[2] what we call "acceptance" means the geometrical acceptance times the detector and reconstruction efficiency

[3] remember the vetoes ensure that the same beam flux illuminates upstream and downstream targets, so we needn't introduce an additional index for the fluxes!

$$s_D(x,Q^2) = s_D(x_0,Q_0^2) + \partial_x s_D(x_0,Q_0^2)x + \frac{1}{2}\partial_x^2 s_D(x_0,Q_0^2)x^2 + \partial_x\partial_u s_D(x_0,Q_0^2)ux + \partial_u s_D(x_0,Q_0^2)u + \frac{1}{2}\partial_u^2 s_D(x_0,Q_0^2)u^2 \quad (4.5)$$

$$a_u^S(x,Q^2) = a_u^S(x_0,Q_0^2) + \partial_x a_u^S(x_0,Q_0^2)x + \frac{1}{2}\partial_x^2 a_u^S(x_0,Q_0^2)x^2 + \partial_x\partial_u a_u^S(x_0,Q_0^2)ux + \partial_u a_u^S(x_0,Q_0^2)u + \frac{1}{2}\partial_u^2 a_u^S(x_0,Q_0^2)u^2 \quad (4.6)$$

where $\partial_x = \partial/\partial x$; $\partial_x^2 = \partial^2/\partial x^2$; etc.

We see that when we multiply the three, we will have 216 terms. For the calculation we will therefore use the *Mathematica* [62] package. But even so, we can leave out the terms of order higher than 2 in hoth x and u (the third and higher orders are anyway incomplete as we stop the Taylor expansion at order 2). This leaves us with a suhintegral function with 28 terms. After integration by *Mathematica*, the output (half a page) can in turn he expanded in series around x_0, u_0. The leading term is of order 2 (ux), and the next leading term is of order 4 (u^3x, ux^3). These leading and next-to-leading terms for each of the four integrals are then taken into account when evaluating the crossed ratio of events as in (2.1). The result is yet again expanded in series and gives:

$$\frac{N_{up}^{Li}N_{dn}^{Li}}{N_{up}^{D}N_{dn}^{D}} = \frac{\xi_{up}^{Li}\xi_{dn}^{Li}\phi_S\phi_J}{\xi_{up}^{D}\xi_{dn}^{D}\phi_S\phi_J}\left[\frac{a_u^S(x_0,u_0)a_d^J(x_0,u_0)}{a_u^J(x_0,u_0)a_d^S(x_0,u_0)}\mathcal{R}^{\mathrm{Li}}(x_0,u_0)^2 + \alpha\mathbf{u}^2 + \beta\mathbf{x}^2 + O(\mathbf{u}^2\mathbf{x}^2)\right] \quad (4.7)$$

where the coefficients α and β depend on all the suhintegral functions and derivatives:

$$\alpha = \alpha\ (\mathcal{R}^{Li}, \partial_x\mathcal{R}^{Li}, \partial_x^2\mathcal{R}^{Li}, \partial_u\mathcal{R}^{Li}, \partial_u^2\mathcal{R}^{Li}, s_D, \partial_x s_D, \partial_x^2 s_D, \partial_u s_D, \partial_u^2 s_D, a_{pos_i}^{row_j}, \partial_x a_{pos_i}^{row_j}, \partial_x^2 a_{pos_i}^{row_j}, \partial_u a_{pos_i}^{row_j}, \partial_u^2 a_{pos_i}^{row_j})$$

$$\beta = \beta\ (\mathcal{R}^{Li}, \partial_x\mathcal{R}^{Li}, \partial_x^2\mathcal{R}^{Li}, \partial_u\mathcal{R}^{Li}, \partial_u^2\mathcal{R}^{Li}, s_D, \partial_x s_D, \partial_x^2 s_D, \partial_u s_D, \partial_u^2 s_D, a_{pos_i}^{row_j}, \partial_x a_{pos_i}^{row_j}, \partial_x^2 a_{pos_i}^{row_j}, \partial_u a_{pos_i}^{row_j}, \partial_u^2 a_{pos_i}^{row_j})$$

We see that if the acceptances are not identical, we have a prohlem to the zeroth order. However, if they do cancel, the first correction will only he of second order, and the crossed ratio reduces to:

$$\frac{N_{up}^{Li}N_{dn}^{Li}}{N_{up}^{D}N_{dn}^{D}}\cdot\frac{\xi_{up}^{D}\xi_{dn}^{D}\phi_S\phi_J}{\xi_{up}^{Li}\xi_{dn}^{Li}\phi_S\phi_J} = \mathcal{R}^{\mathrm{Li}}(x_0,u_0)^2 + \left[-\frac{2}{3}\partial_u\mathcal{R}^{Li}|_{x_0,u_0}\mathcal{R}^{Li}(x_0,u_0) + \frac{1}{3}\frac{\partial_u a_1|_{x_0,u_0}\partial_u\mathcal{R}^{Li}|_{x_0,u_0}\mathcal{R}^{Li}(x_0,u_0)}{a_1(x_0,u_0)} + \frac{1}{3}\frac{\partial_u a_2|_{x_0,u_0}\partial_u\mathcal{R}^{Li}|_{x_0,u_0}\mathcal{R}^{Li}(x_0,u_0)}{a_2(x_0,u_0)} + \frac{1}{3}\mathcal{R}^{Li}(x_0,u_0)\partial_u^2\mathcal{R}^{Li}|_{x_0,u_0} + \frac{2}{3}\frac{\partial_u\mathcal{R}^{Li}|_{x_0,u_0}\mathcal{R}^{Li}(x_0,u_0)\partial_u s_D|_{x_0,u_0}}{s_D(x_0,u_0)}\right]\mathbf{u}^2 + \left[\frac{1}{3}\frac{\partial_x a_1|_{x_0,u_0}\partial_x\mathcal{R}^{Li}|_{x_0,u_0}\mathcal{R}^{Li}(x_0,u_0)}{a_1(x_0,u_0)} + \frac{1}{3}\frac{\partial_x a_2|_{x_0,u_0}\partial_x\mathcal{R}^{Li}|_{x_0,u_0}\mathcal{R}^{Li}(x_0,u_0)}{a_2(x_0,u_0)} + \frac{1}{3}\partial_x^2\mathcal{R}^{Li}|_{x_0,u_0}\mathcal{R}^{Li}(x_0,u_0) + \frac{2}{3}\frac{\partial_x\mathcal{R}^{Li}|_{x_0,u_0}\mathcal{R}^{Li}(x_0,u_0)\partial_x s_D|_{x_0,u_0}}{s_D(x_0,u_0)}\right]\mathbf{x}^2 + O(\mathbf{u}^2\mathbf{x}^2) \quad (4.8)$$

We notice at once that the coefficient of the u^2 term *directly* depends on the size of the first and second partial derivatives of the ratio and the acceptance with respect to u. Likewise, the x^2 correction depends solely on the x-derivatives. This is a very intuitive result!

We now see that since the Q^2-dependence of the ratio is weak (see Fig. 1.11h), the bins in $u = \log Q^2$ may be relatively large without disturbing the ratio algorithm. However, in x one needs fine bins as the x-dependence is strong. Also the necessity of staying away from kinematic regions with sharply falling acceptance, and of very small absolute acceptance is now evident, since the derivatives of acceptances appear in the numerator and the absolute acceptances in the denominator.

Let us now come back to (4.7). In leading order, we must be sure that the acceptances in Jura and Salève positions are the same. One way to check this is of course looking at time dependencies of different quantities, and see whether some of these show a periodicity with target changing (every two runs). Another way is to construct so-called **flux ratios**. We now multiply the counts in one target row and divide by the other row. Unlike eqs. (2.1) and (4.7), now the cross sections (and the ratio) cancel, and the acceptances should, as well, if they are equal. We get:

$$\frac{N_{up}^{Li}N_{dn}^{D}}{N_{up}^{D}N_{dn}^{Li}} = \frac{\xi_{up}^{Li}\xi_{dn}^{D}\phi_S\phi_S}{\xi_{up}^{D}\xi_{dn}^{Li}\phi_J\phi_J}\left[\frac{a_u^S(x_0,u_0)a_d^S(x_0,u_0)}{a_u^J(x_0,u_0)a_d^J(x_0,u_0)} + O(\mathbf{u}^2) + O(\mathbf{x}^2) + O(\mathbf{u}^2\mathbf{x}^2)\right] \tag{4.9}$$

We aren't here interested in the higher order corrections. This means that the flux ratio defined as:

$$\Phi_R \equiv \sqrt{\frac{N_{up}^{Li}N_{dn}^{D}}{N_{up}^{D}N_{dn}^{Li}}\frac{\xi_{up}^{D}\xi_{dn}^{Li}}{\xi_{up}^{Li}\xi_{dn}^{D}}} = \frac{\phi_S}{\phi_J}\sqrt{\frac{a_u^S(x_0,u_0)a_d^S(x_0,u_0)}{a_u^J(x_0,u_0)a_d^J(x_0,u_0)}} \stackrel{?}{=} \frac{\phi_S}{\phi_J} \tag{4.10}$$

really *is* the ratio of fluxes only if the acceptances *do* cancel. In particular, the flux ratio has to be flat in any kinematic or detector variable, not only x_{Bj} and u. This is a capital tool in ratio analysis.

In the same spirit we may construct *acceptance ratios* defined as:

$$A_R \equiv \sqrt{\frac{N_{up}^{Li}N_{up}^{D}}{N_{dn}^{D}N_{dn}^{Li}}\frac{\xi_{dn}^{D}\xi_{dn}^{Li}}{\xi_{up}^{Li}\xi_{up}^{D}}} = \sqrt{\frac{a_u^S(x_0,u_0)a_u^J(x_0,u_0)}{a_d^S(x_0,u_0)a_d^J(x_0,u_0)}} \tag{4.11}$$

However these ratios are of limited use since they are allowed to be kinematic dependent, the acceptance changes going from upstream to downstream (the detector is seen at a different solid angle as we approach it!).

4.1.2 Vertex cuts

Before we proceed with the above tools, we would like to know in which material the interaction happened in the first place. Fig. 4.1 shows the distribution of vertices for the

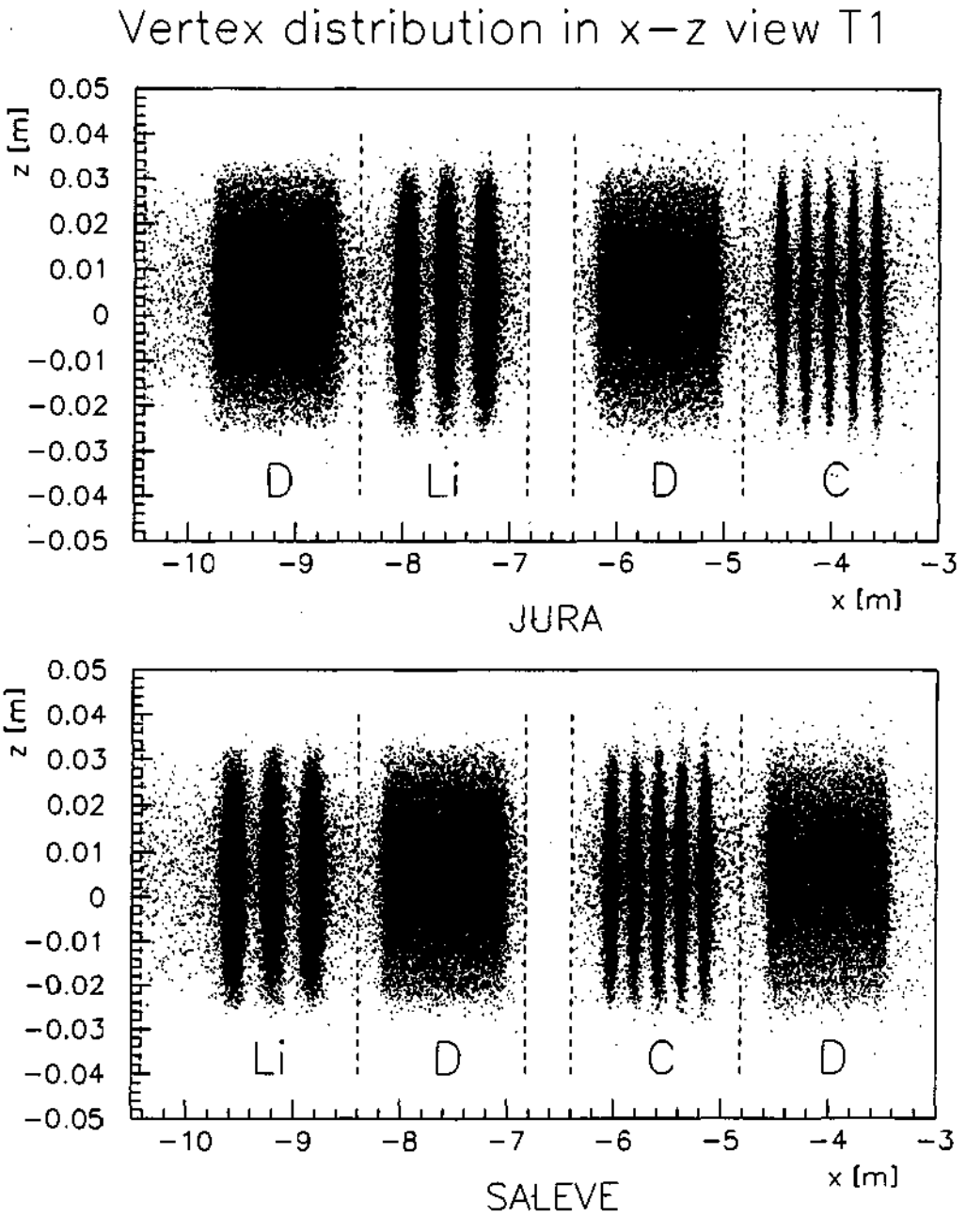

Figure 4.1: The vertex distribution in the $x - z$ plane for the Saleve row (above): from left to right: the three lithium slabs, the deuterium target, the five carbon disks and the other deuterium target. The Jura row (below) is complementary. The beam comes in from the left.

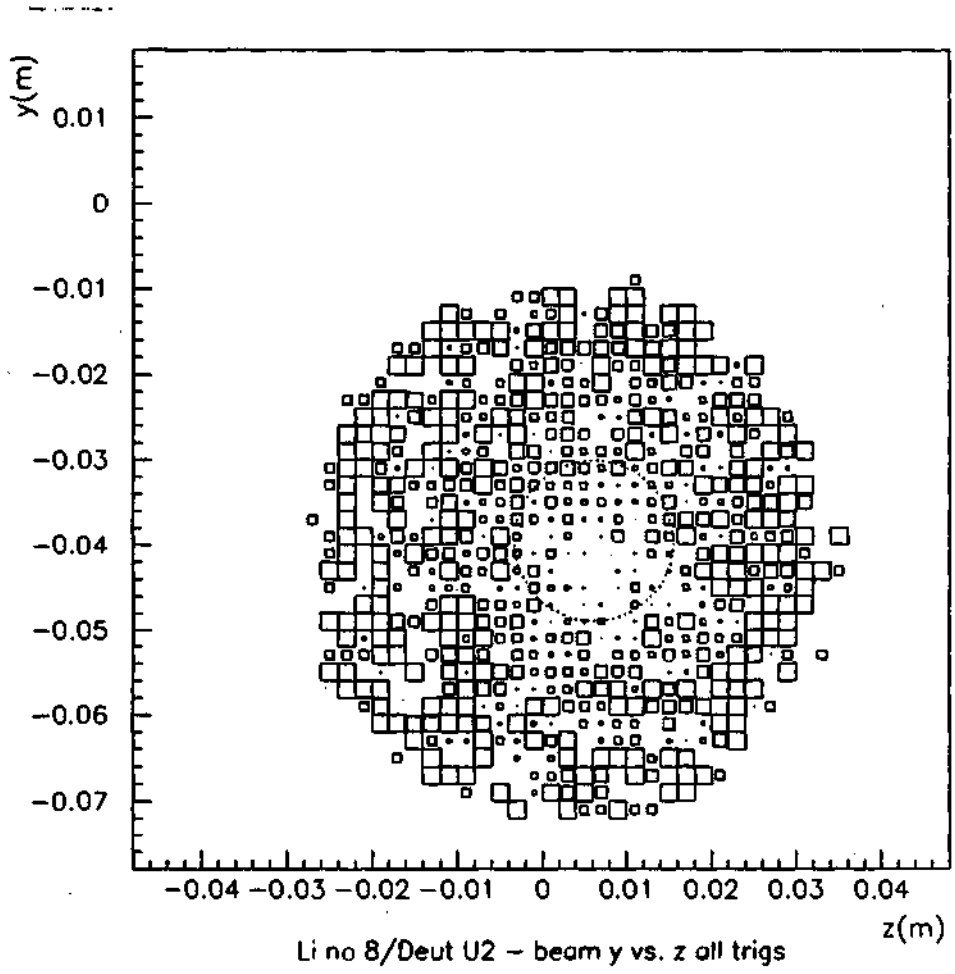

Figure 4.2: Evidence for the hole in lithium target slab number 8. Shown is the ratio of vertex distributions in the lithium slab in question and in the deuterium target at an identical x position. A blank represents a ratio of less than 0.8 (threshold) and a full box corresponds to more than 1.2 (saturation). The circle indicates the position of the hole as mapped (cf. sec. 2.3.1).

Jura target row in the $x - z$ plane. The cuts applied are indicated in the plots. The small spillover due to smearing will be taken into account later (sec. 4.3.2).

Fig. 4.2 illustrates how we can visualize the presence of holes in the lithium targets, at least in the case of the biggest hole in target number 8 (fig. 2.8). It shows the ratio of vertex distributions in the $y - z$ plane in an x interval corresponding to the lithium slab in question, divided by the same interval in the other target row, corresponding to a part of the deuterium target.

4.1.3 Run dependencies

Fig. 4.3 shows some rundependencies. All mean kinematic variables were inspected, Q^2 and ν are shown. They show nice stability throughout the data taking, except for two runs, numbers 168 and 289. That something went wrong with these two runs is also visible from the T3/T1 and T3/T2 ratios which deviate by several standard deviations in these two runs (the T3/T1 ratio of run 168 is below the mean T3/T2 level, and its T3/T2 is close to the tickmark). A look in the data taking log book reveals absolutely nothing special about run 168 and for run 289 the beam was off for about 5 hours, but nothing else to indicate this is a bad run. The T3/T1 and T3/T2 ratios should be constant since it represents the number of beam tracks per physics trigger. If the acceptance (and cross section) is constant, this should be constant. However T14 was left out of this plot. Remember that its trigger logic depends on the beam (only one beam track inside a defined inner region required) and if the beam shifts a little, a different fraction of the beam will be used for the trigger. This is why T14 cannot be normalized by the usual normalization triggers. However, as we are here extracting a ratio, the absolute flux does not matter. The two runs which are seen to stick out are discarded from further analysis.

The run dependence of the acceptance ratio also gives an idea on the smoothness of data taking, as does the F_2 ratio per run (fig. 4.4). They are evaluated per target cycle: we need counts from both target rows to calculate these ratios, so typically four runs are taken to compute acceptance and F_2 ratios in a target cycle: 2 runs in Saleve position, and 2 in Jura. The flux ratio however is allowed to fluctuate. The deviations from unity just tell us that the two runs in the Jura row had more or less integrated flux pass through them than the two Saleve runs. There are also many values around 2 and 0.5 – this just means that the target cycle is composed of three runs – one Jura and two Saleve or vice-versa.

4.1.4 Flux ratios

Now that we have rejected bad runs, we may have a look at flux ratios. Fig. 4.5 is a nice illustration of the power of this tool. In a first try, the flux ratios vs. all variables looked reasonably flat, but the flux ratio of upstream events vs. the vertex χ^2 probability of the vertex was manifestly completely wrong. The vertex probability is assigned on the basis of errors assigned to the beam and scattered muon track – this enables us to compute a χ^2, and from this, a probability that we could have found a vertex with an even higher χ^2. As mentioned earlier, the errors in our experiment are of a non Gaussian nature, due to the presence of discrete detectors such as hodoscopes to determine the beam (cf. fig. 2.4) and proportional chambers contributing to the scattered muon fit. This means that the tails of the χ^2 distribution are enhanced with respect to the theoretical one computed for Gaussian errors, and the χ^2 probability computed starting from that theoretical distribution has a peak at low probabilities. Thereafter, it should be quite flat, and it is (if the errors were

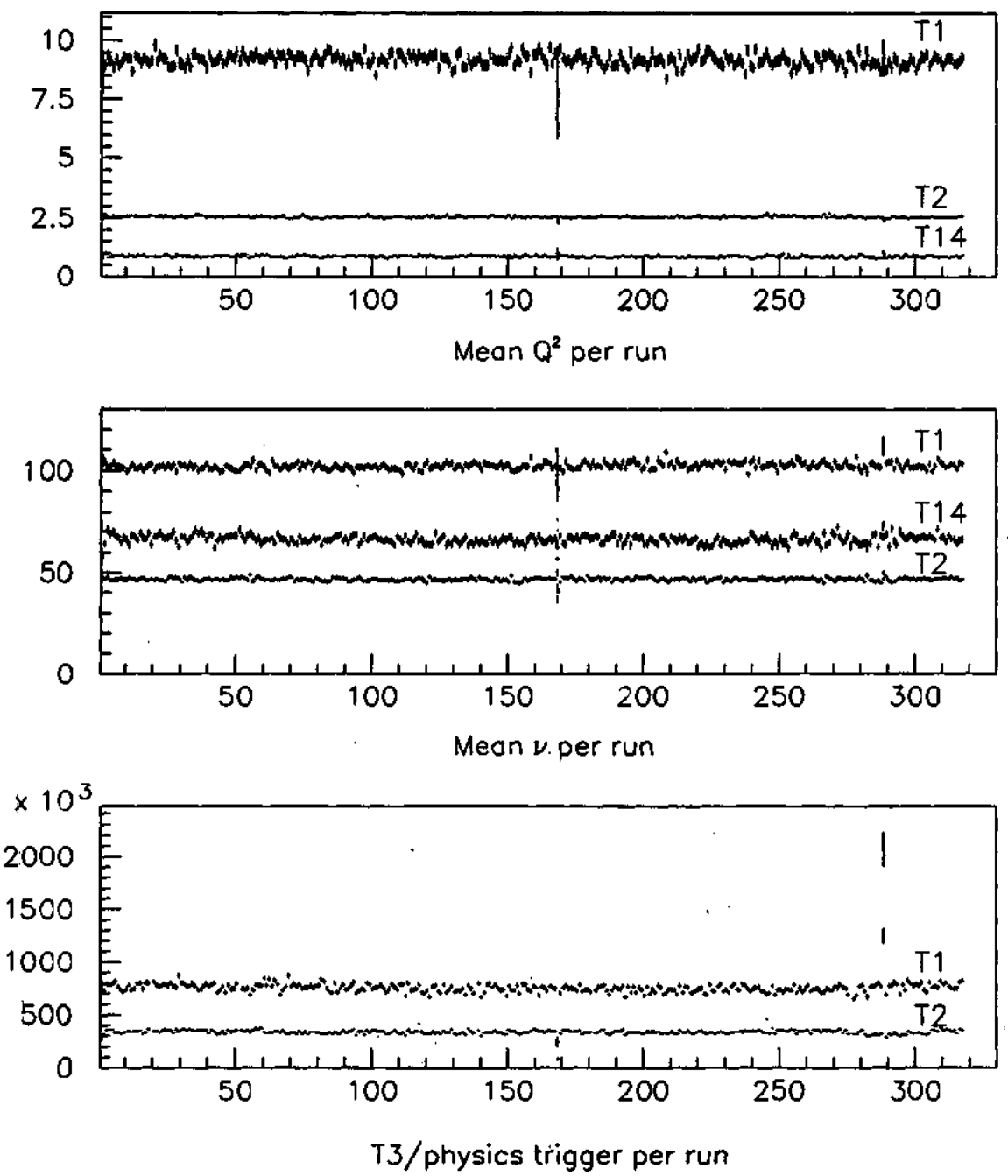

Figure 4.3: Run dependencies of mean Q^2 (top) and ν (middle) and the ratio of normalization trigger T3 rate divided by the two of tbe physics triggers.

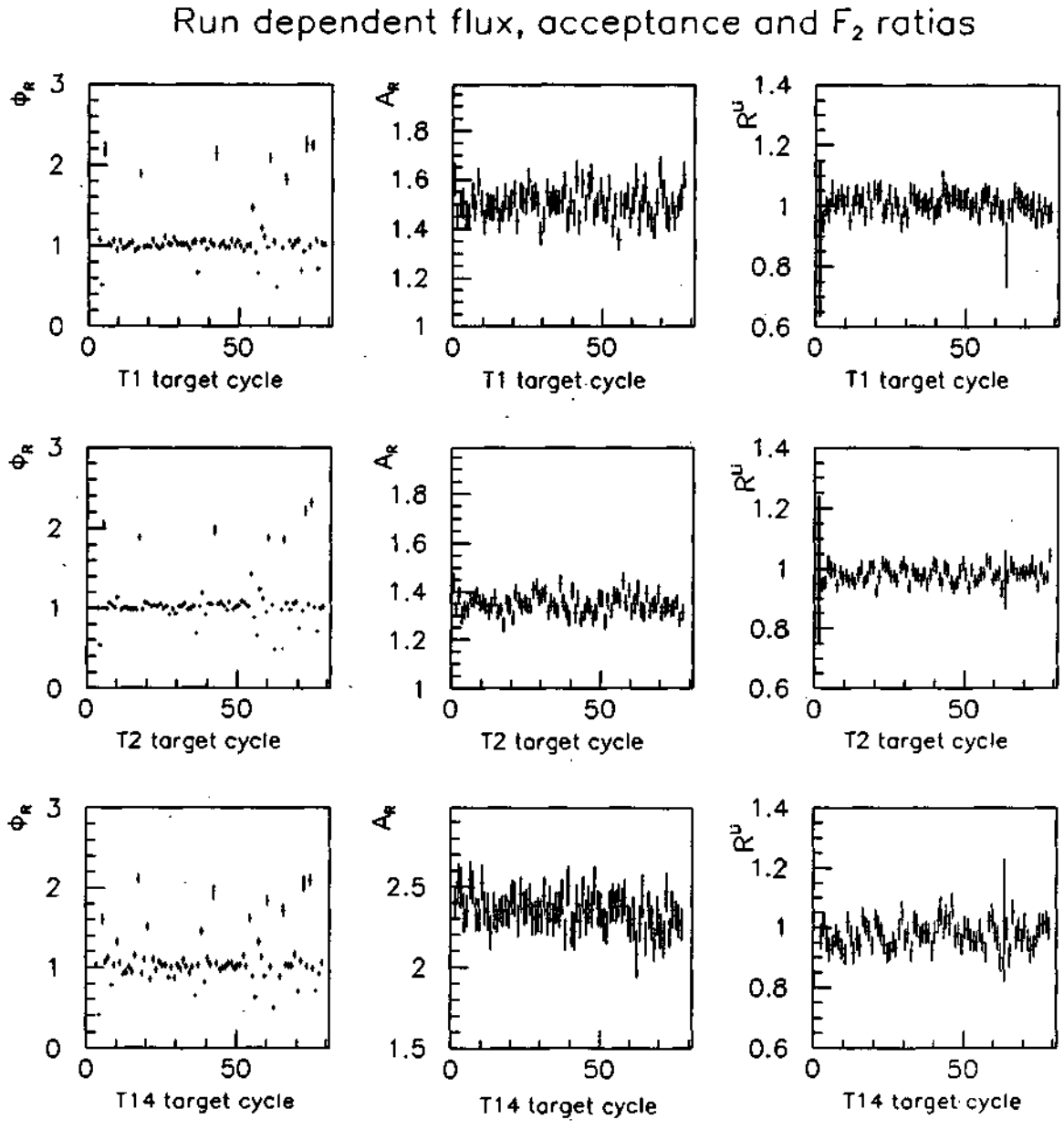

Figure 4.4: Run dependencies of mean flux ratios (left column), acceptance ratios (middle column) and F2 ratios (right column) for the three physics triggers (T1 top, T2 middle, and T14 bottom row).

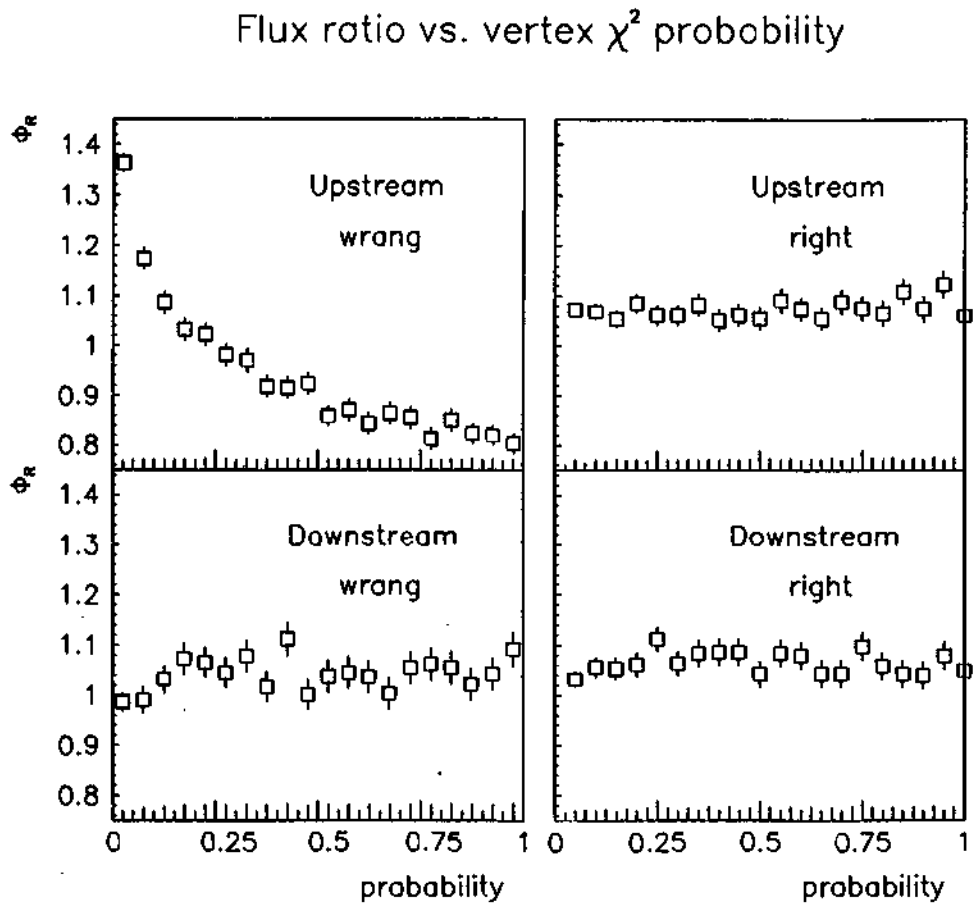

Figure 4.5: Flux ratio vs. vertex probability. The left column corresponds to a first erroneous production of data (see text).

ideally Gaussian, it would be flat in the whole range from 0 to 1). However, this behaviour should be the same for all targets, and should cancel in the flux ratio!!

So where is the error? Well it so happens that the author made a mistake in describing the target setup. Namely, before starting production, one also has to describe all possible scatterers in the target. This information is used by GEOMETRY to evaluate multiple Coulomb scattering each beam and scattered muon has undergone in order to attribute a correct error to it. The geometrical sizes, shapes and radiation lengths are the relevant information. A somewhat hasty look in the Particle Data Booklet was responsible for the inclusion of the radiation length of liquid argon to describe the gas surrounding the Li targets! This is a sizeable effect: liquid argon has a radiation length of 14 cm, to be compared e.g. with the other scatterer nearby – the lithium slabs themselves (155 cm). Gaseous argon has a radiation length of 110 m ! Since the angle of deflection of a muon through multiple Coulomb scattering (neglecting Molière tails, cf. [63]) is computed as:

$$\Delta\theta = \frac{13.6\text{MeV}}{\beta cp}\sqrt{x/X_0}[1 + 0.0038\ln(x/X_0)] \tag{4.12}$$

where p and $\beta c \approx c$ are the momentum and velocity of the muon, x is the length of the muon path through the medium and X_0 is the radiation length, we see that for a 100 GeV muon this mistake means additional 0.3 mrad scattering, and for a 20 GeV muon it gives 1.5 mrad!

This meant that the GEOMETRY production had to be redone from the MAXI DST's, for this affects the vertex finding itself. GEOMETRY propagates the scattered muon to the x coordinate where the beam track is given (usually at P0H), propagating the error accordingly (including multiple Coulomb scattering effects, which were too high), finds the point of closest approach of the two tracks (this is done using the respective errors to weight the tracks – the scattered muon shall have less weight than it should, due to the excessive error attributed to it). Then the two tracks are propagated to this new x coordinate modifying the covariance matrices accordingly, and the point of closest approach is again evaluated. This procedure is then repeated until no improvement is found. We see now that the vertices are wrong if multiple Coulomb scattering is wrong.

After this new production, the flux ratios vs. vertex probability are quite flat as may be seen in fig. 4.5.

We may now cast a glance at the other flux ratios. Figs. 4.6-4.9 show the flux ratios vs. ν and θ, the two variables in which the essential cuts are made. These cuts are indicated by arrows in the figure. The angle cut is applied to match the trigger definition essentially. Trigger 1 is designed to accept events with scattering angles over 0.5° (12 mrad). It doesn't need a high-θ cut, the counts being limited by the $1/\sin^4(\theta/2)$ behaviour of the cross section. Trigger 2 has a lower limit of about 5 mrad for the upstream targets and about 6 mrad for the downstream ones, and a higher one of about 17 and 19 mrad for upstream and downstream respectively. The lower θ-cut for T14 was chosen at 2 and 2.65 mrad for upstream and downstream targets respectively, even though the acceptance of the trigger goes down to 1 mrad, because of vertex smearing which becomes too large and impossible to estimate and correct for (cf. sec 4.3.2). A high-θ cut was imposed by the observation that the χ^2 of a constant fit to the ν flux ratio decreases from 27/15 to 22/15 if such a cut is imposed. This is the general idea: if the flux ratio doesn't look good – look at the edges. If the edges are deviating from a constant, cut on them and see what happens to the other flux ratios. If the edges are fine, but there is some funny behaviour in between (slope, step, or non-statistical fluctuation of any kind) – look at other flux ratios and try to find the one

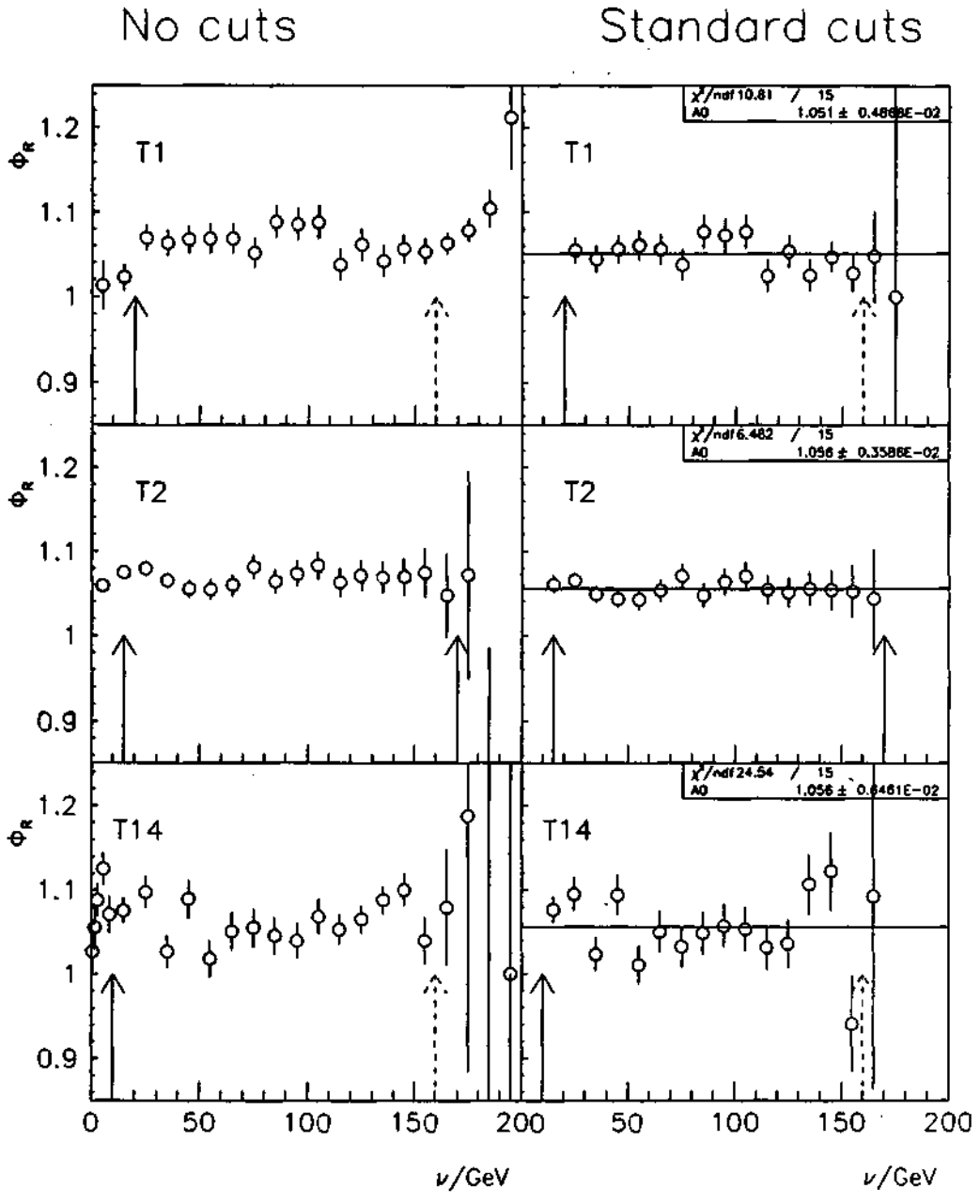

Figure 4.6: Flux ratios vs. ν for the upstream target pair. Left column before cuts, right one after cuts indicated by arrows. Dashed arrows show the approximate cutoff of the y-cut. The lines are constant fits through the flux ratios.

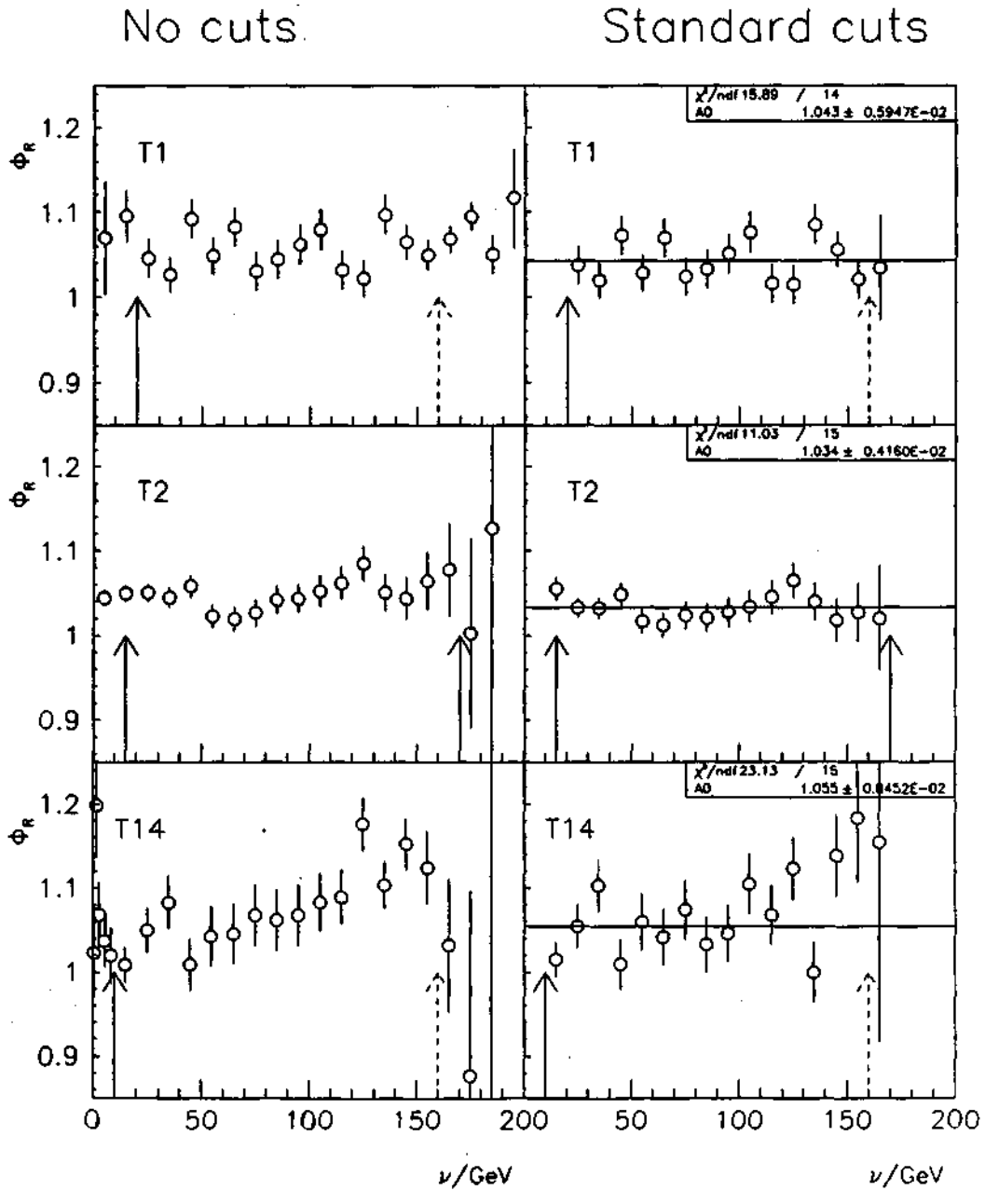

Figure 4.7: Flux ratios vs. ν for the downstream target pair. As fig. 4.6.

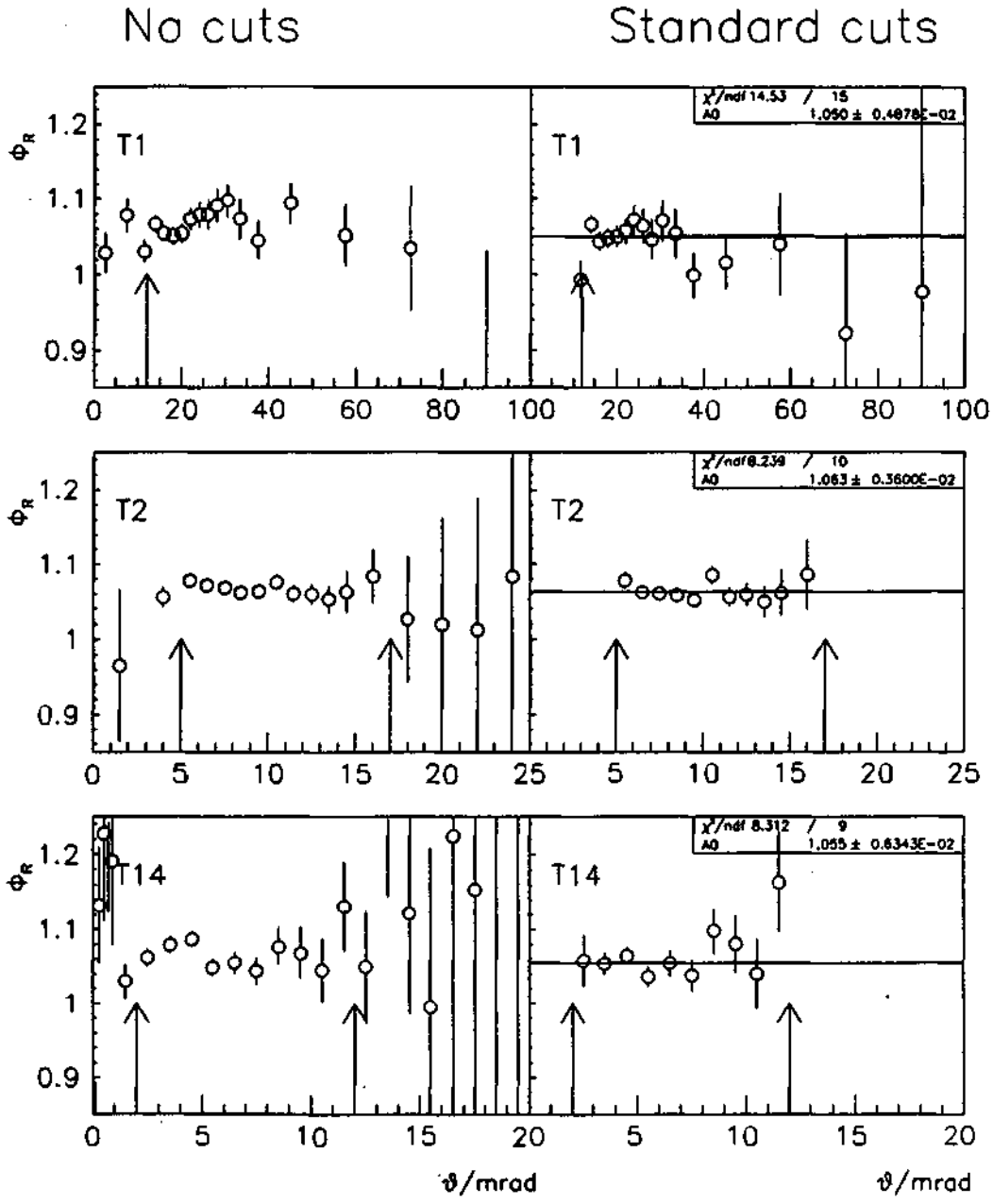

Figure 4.8: Flux ratios vs. scattering angle for the downstream target pair. As fig. 4.6.

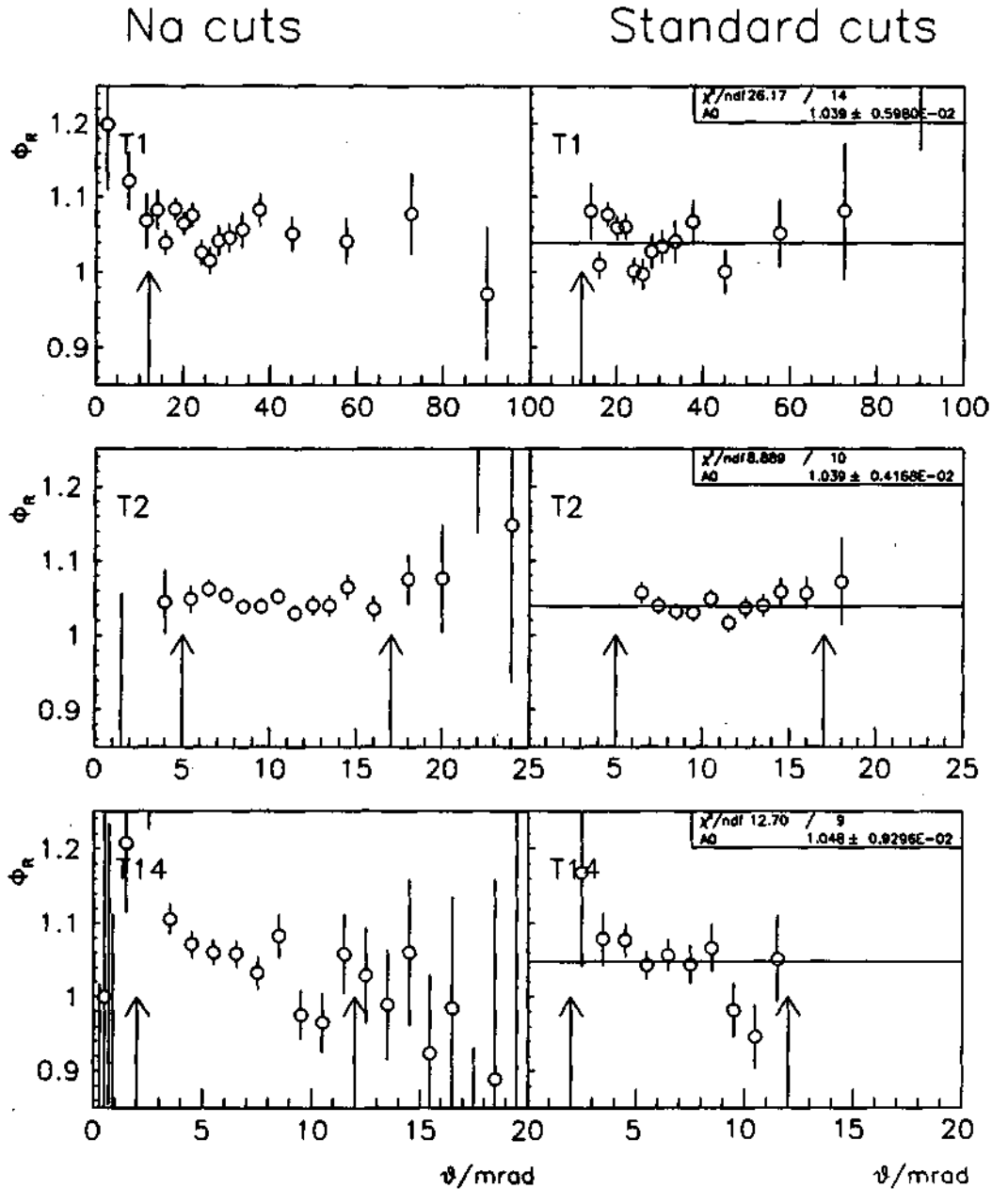

Figure 4.9: Flux ratios vs. scattering angle for the downstream target pair. As fig. 4.6.

to cut on.

As to the cuts on ν, a low-ν cut is imposed because of the large kinematic smearing which affects it at low values. ν is the difference of two measured quantities:

$$\nu = E - E';$$

the energies of the incoming and scattered muon. Small errors on each add up to a large error on their difference. As to the high-ν cut, which is equivalent to high $y_{Bj} = \nu/E$ and low muon momentum p_μ, there are two main reasons to impose it. Firstly, high y_{Bj} is the region where there is a predominance of radiative coherent and quasielastic events. This means the radiative corrections (and thus the uncertainties related to them, cf. 4.3.1) in this region are large. Secondly, the low-p_μ is a region contaminated hy muons from hadron decays. In itself, this would not be bad, for the presence of a hadron indicates that a deep inelastic event did occur. However, the real scattered muon might have gone lost somewhere in the tracking, and we would attrihute false kinematics hy assuming this muon from hadron decay to he the scattered mnon.

In addition to these cuts, an explicit x_{Bj}-cut had to be applied on T14 data, to eliminate the region of the $\mu - e$ elastic scattering peak. Going hack to the reasoning of 1.1.1 we see that the condition for elastic $\mu - e$ scattering is:

$$Q^2 = 2m_e\nu$$

i.e. if we had calculated x_{Bj} with the electron mass rather than with the proton one, this "x^e_{Bj}" would he equal to one. However, as we use the proton mass, $\mu - e$ scattering shall occur at:

$$x_{Bj} = \frac{m_e}{m_p} = 5.45 \cdot 10^{-4}$$

Allowing for some smearing, we cut at 0.0008.

The set of cuts applied in this analysis are shown in Table 4.1, and the effect on the distribution of events in the $Q^2 - \nu$ and $x_{Bj} - Q^2$ kinematic planes is shown in figs. 4.10 and 4.11.

The χ^2's of all constant fits to flux ratios seem to be satisfactory, and the value of the constant is compatible with the flux ratio obtained from the normalization triggers T34 and T10:

$$\begin{aligned} \frac{\Phi_{Saleve}}{\Phi_{Jura}} &= 1.046 \pm 0.003(T3) \\ &= 1.051 \pm 0.003(T4) \\ &= 1.046 \pm 0.006(T10) \end{aligned}$$

Some other cuts were found to be necessary:

- a stronger cut on the timing between the BMS and the trigger time than had been applied in PHOENIX – at micro level we can decide for events which satisfy more than one trigger to which trigger time we wish to refer. It was decided to always privilege the larger angle trigger – for T1&T2 events T1 time is used, for T2&T14 T2 time is used.

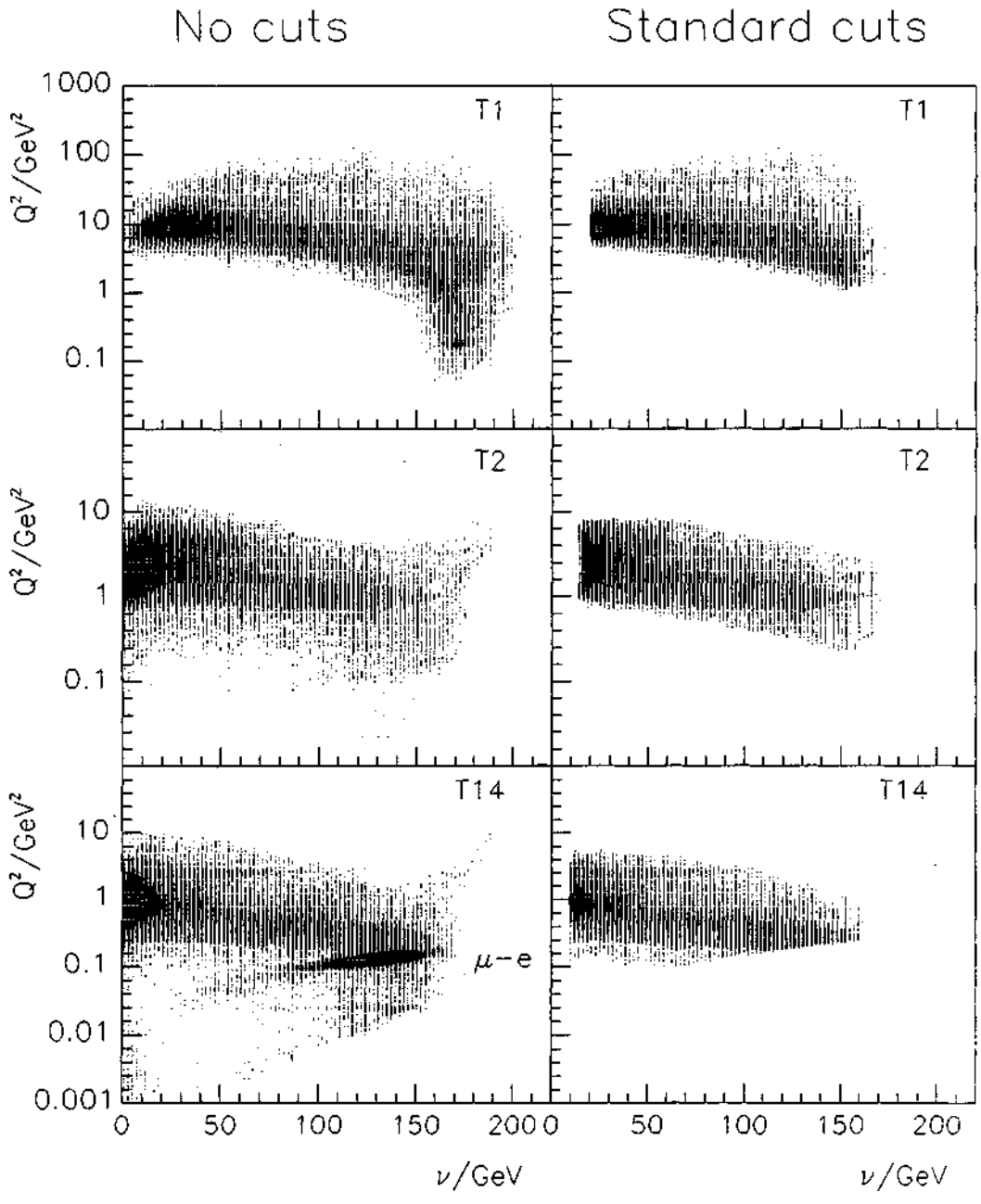

Figure 4.10: Events in the $Q^2 - \nu$ plane before and after cuts for all three triggers

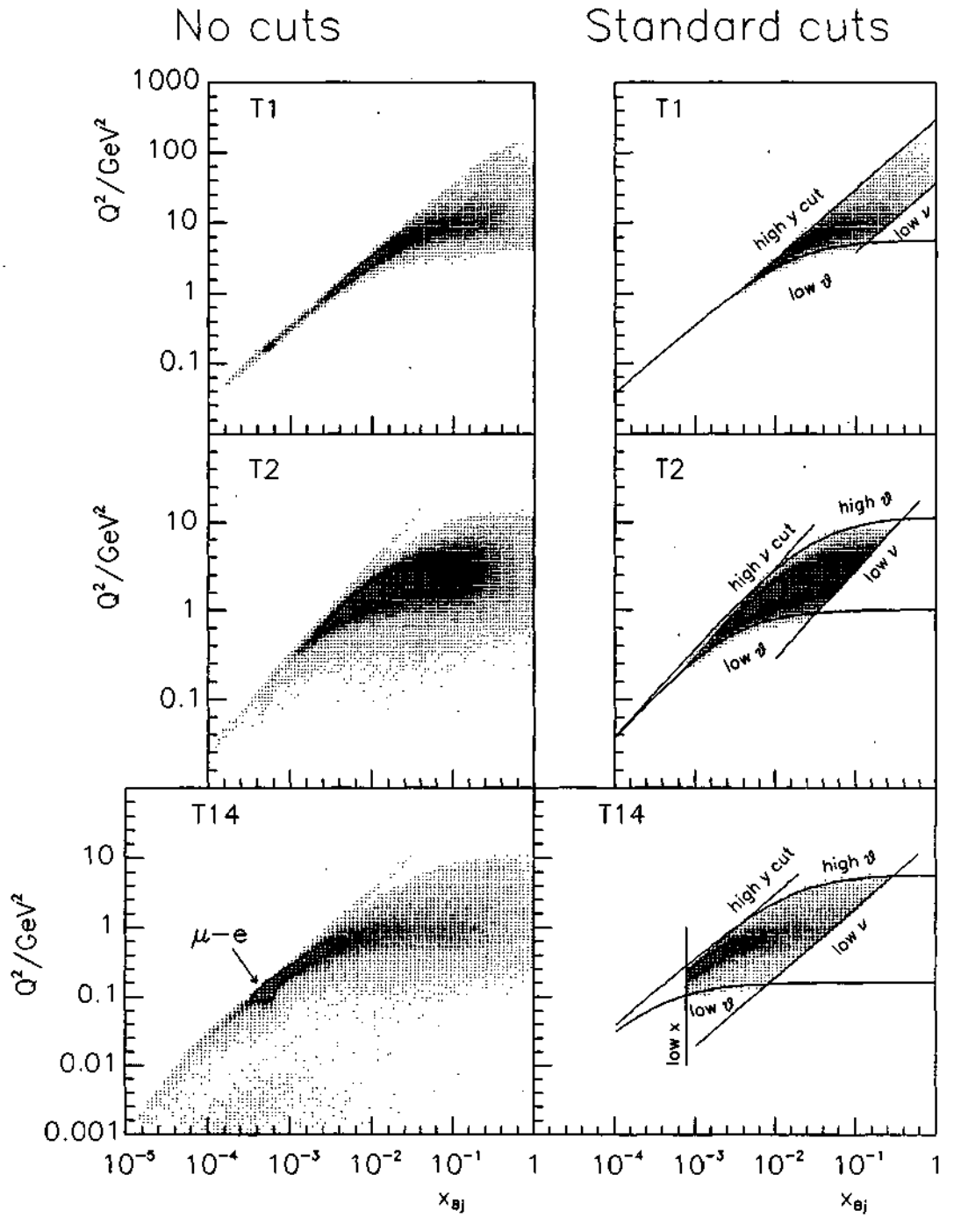

Figure 4.11: Events in the $x_{Bj} - Q^2$ plane before and after cuts for all three triggers

variable		Main trigger	Small angle trigger	Small x_{Bj} trigger
θ^{min}/mrad	Li/D	12	5	2
θ^{max}/mrad	Li/D		17	12
θ^{min}/mrad	C/D	13	6	2.65
θ^{max}/mrad	C/D		19	12
ν^{min}/GeV		20	15	10
ν^{max}/GeV			170	
x_{Bj}^{min}				0.0008
y_{Bj}^{max}		0.8	0.85	0.8

Table 4.1: Kinematic cuts applied in standard analysis. Blank indicates no cut applied.

- an extra cut had to be applied because of a bug in GEOMETRY. It was found that a class of events exists having a vertex situated downstream, but the scattered muon was fitted using the hit in P0B. This is of course wrong, for if the vertex is located downstream, the hit in P0B belongs to the beam, not to the scattered muon. Somehow GEOMETRY didn't check this and attributed the P0B hit to the scattered muon. These events are thus removed from further analysis.

- additional cuts on the beam were applied. It turned out that the veto counters were slightly higher ($\sim$ 5 mm) than the targets, so that the equal illumination of the targets was not ensured. Strict cuts on the beam slopes was also applied because suspicious behaviour in flux ratios vs. beam z slope and y slope was seen. Therefore tracks with slopes of more than 1-1.2 mr from the central value were removed from the analysis. Divergent beam tracks cause different illumination of targets.

4.2 The hadron method or semi-inclusive measurement

Let us come back to T14 data. In the previous section, we just applied a cut in x_{Bj} to eliminate the contamination by $\mu - e$ elastic scattering. This was the only reasonable thing to do in an inclusive measurement, for the contribution of this "parasite" process completely dominates the scattering below $x_{Bj} = 0.008$.

However, even though the NMC spectrometer is fully optimized on muons, the hadron acceptance being limited to the forward hemisphere in the center of mass system (see chapter 5) and to high energy hadrons (low energy hadrons end up hitting the wall of the FSM and they are then lost for tracking), we can exploit the information we have for a **semi-inclusive** measurement.

This means we will require a hadron in the final state, to be sure that we are dealing with a deep inelastic scattering event. This has another benefit: it removes all the coherent and quasielastic events from the data sample, thus eliminating the largest contributions to radiative corrections at low x_{Bj} (see sec. 4.3.1).

4.2.1 The method

What is a hadron? The question seems ludicrous in general, but when looking at hits from detectors, it is no longer trivial. It was quite easy to identify the muon by its presence behind the iron wall, as described in chapter 3 and visualized in fig. 3.2. In the reconstruction programs, all other tracks are labelled as "hadrons". Of course some of them may be electrons or positrons, but for the inclusive measurement this doesn't matter. The "hadrons" are only background as far as we only look at the muon in the final state. Electrons are now our enemies: we have to look for them and kill the events having an electron in the final state (signature of a $\mu-$e event).

The only real means of distinction of hadrons from electrons is the information from the H2 calorimeter (for a description see section 2.4.3 and fig. 2.12; more detailed information in [76, 77]). As argued in sec 2.4.3, the calorimeter resolution is far from impressive, both in energy ($40\%/\sqrt{E}$ and $160\%/\sqrt{E}$ respectively for electromagnetic particles and hadrons), and spatially (a segmentation of 28×28 cm correspondiog to a ~ 32 mrad resolution on the angle of the track after the magnet). However the electromagnetic energy *fraction* EMAGF, defined as:

$$\text{EMAGF} = \frac{E_{em}}{E_{em} + E_{had}}, \tag{4.13}$$

where E_{em} and E_{had} are the energies deposited in the electromagnetic and hadron modules respectively, can be used to eliminate electrons from the sample. That a cut on this variable at a value of 0.8 (all tracks with EMAGF > 0.8 are rejected as electrons) permits a rejection of electrons with an efficiency nearing 100% was established since EMC times [78], by looking at EMAGF distributions of pairs of tracks with low invariant mass (interpreted as e^+e^- pairs created from photons) and high fractional energy (to use hard photons). The efficiency was plotted as a function of the invariant mass cut on the e^+e^- pairs, and extrapolated to zero invariant mass.

The result of applying this cut on the x_{Bj} distribution is shown in fig. 4.12b. The big bad peak is well reduced, the residuum of $\sim 3\%$ turns out to be due less to the inefficiency of our cut, than to the acceptance hole of H2. Namely, as described in 2.4.3, there is a hole of 10 cm radius in H2 to allow for the beam. Together with edge effects (tracks only partly traversing the modules near the hole, this means a region of ~ 15 cm around the beam line is ineffective.

Now we could of course cut away all the events where the "hadron" (i.e. non-muon) track passes through this ineffective region, but we would be losing good deep inelastic events in the process as well. Rather than that, we shall use the event topology now to reject $\mu-$e events.

We must think of $\mu-$e events as a two-body process: two particles in both the initial and final states, as opposed to the many-body final state in the case of deep inelastic scattering where several hadrons are created. Conservation of energy and momentum tells us that in the $\mu-$e scattering the electron has to carry the totality of the virtual photon energy and momentum:

$$\begin{aligned} \vec{p}_e &= \vec{p}_{\gamma^*} \text{ and} \\ E_e &= E_{\gamma^*}, \end{aligned} \tag{4.14}$$

whereas for deep inelastic events the momentum and energy of the virtual photon are split

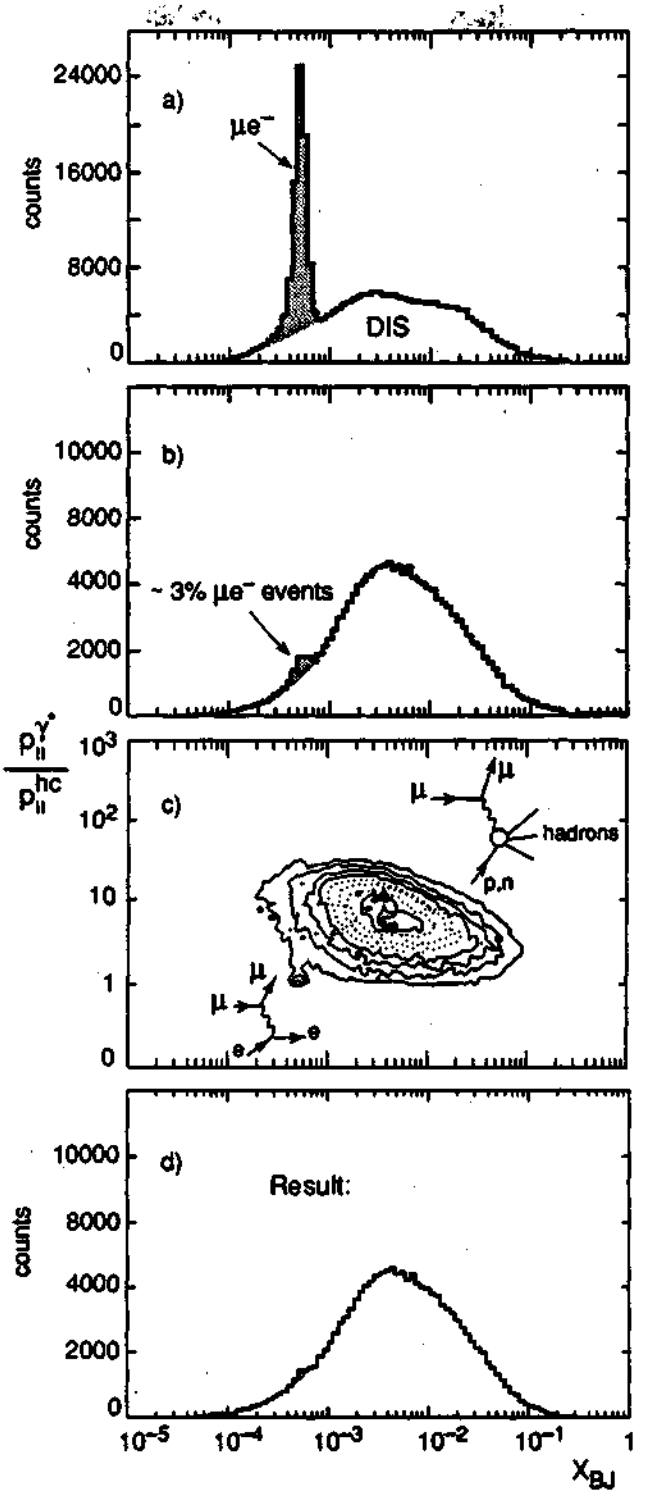

Figure 4.12: The hadron method. **a** The original x_{Bj} distribution dominated by the μ–e elastic peak at low x_{Bj}. **b** After requiring a charged track in the spectrometer not identified as an electron or positron by the calorimeter. **c** Virtual photon momentum divided by the hadron candidate momentum. The isolated island around $p_{\|}^{\gamma^*}/p_{\|}^{h.c.} = 1$ and $x_{Bj} = 1$ represents the two-body μ–e interaction. A cut is set around that island and the result is shown in **d**.

between several final state particles, so the hadron energy and momentum will be smaller than that of the virtual photon:

$$\begin{aligned} \vec{p}_{had} &< \vec{p}_{\gamma^*} \text{ and} \\ E_{had} &< E_{\gamma^*}, \end{aligned} \tag{4.15}$$

If we now build the ratio of the longitudinal component of the hadron candidate [4] momentum and the longitudinal component of the virtual photon momentum (measured as the difference between the incoming and scattered muon momenta), and plot it vs. x_{Bj}, we get fig. 4.12c. A nice isolated island of μ–e events can be seen around the values $p_{\gamma^*}/p_{h.c.} = 1$ and $x_{Bj} = m_e/M_p$. We may now introduce an additional cut for μ–e rejection: events with

$$0.0003 < x_{Bj} < 0.0008 \quad \text{and} \quad \frac{p_{h.c.}}{p_{\gamma^*}} < 1.5 \tag{4.16}$$

and the resulting x_{Bj} distribution is shown in 4.12d. The elastic peak is nearly completely gone! The residuum of μ–e processes is due to higher-order processes, mainly events where the final state electron undergoes bremsstrahlung *and* passes through the H2 hole; it thus escapes both our cuts.

However these events represent now less than 6% of all events in the affected x_{Bj} bin; this is judged satisfactory to proceed with structure function ratio determination. The effect of this residual contamination can only "dilute" the nuclear effects (departure of the F_2 ratio from unity) by at most 6% [5] – for an e.g. 10% shadowing effect this means a maximum possible bias of 0.6%, much less than the statistical error in this bin.

4.2.2 Possible biases of the method

The hadron method is effectively an offline trigger – we are selecting a subset of events originally available. We must be sure that this subset represents the same subsample of events in each material, in order to be sure we are not introducing an bias to the F_2 ratio we want to extract.

The EMAGF cut at 0.8 cuts out nearly all electrons. That this is really so can be checked with our topology cut, selecting only events form the region of eq. 4.16. These events are the cleanest sample of electrons we can find. The EMAGF distribution of the so-tagged "electrons" is shown in fig. 4.13. Here 95.7% of the tracks are contained in the region EMAGF>0.8, and 96.5% have EMAGF>0.75. This is only a lower limit to the efficiency of the EMAGF cut, since the sample still has some hadrons in it. Tightening the cut even more, the efficiency rises to 97.0% and 97.8% respectively for EMAGF>0.8 and 0.75. This is the highest figure ever actually obtained from data, without any extrapolation. The earlier methods of determination were based on e^+e^- pairs as explained above, and the efficiency was estimated at 100%, but the highest efficiency actually measured was either about 80-85% (reaches $\sim$ 100% by extrapolation to zero invariant mass), or was obtained from a very small sample of events (reaches 100% but with little statistic significance, they quote a 5% error in [78]). The EMAGF cut was lowered to 0.75 for the rest of the analysis.

[4] a hadron candidate is a non-muon track surviving the EMAGF cut

[5] we assume the cross section ratio for μ–e scattering to be exactly 1

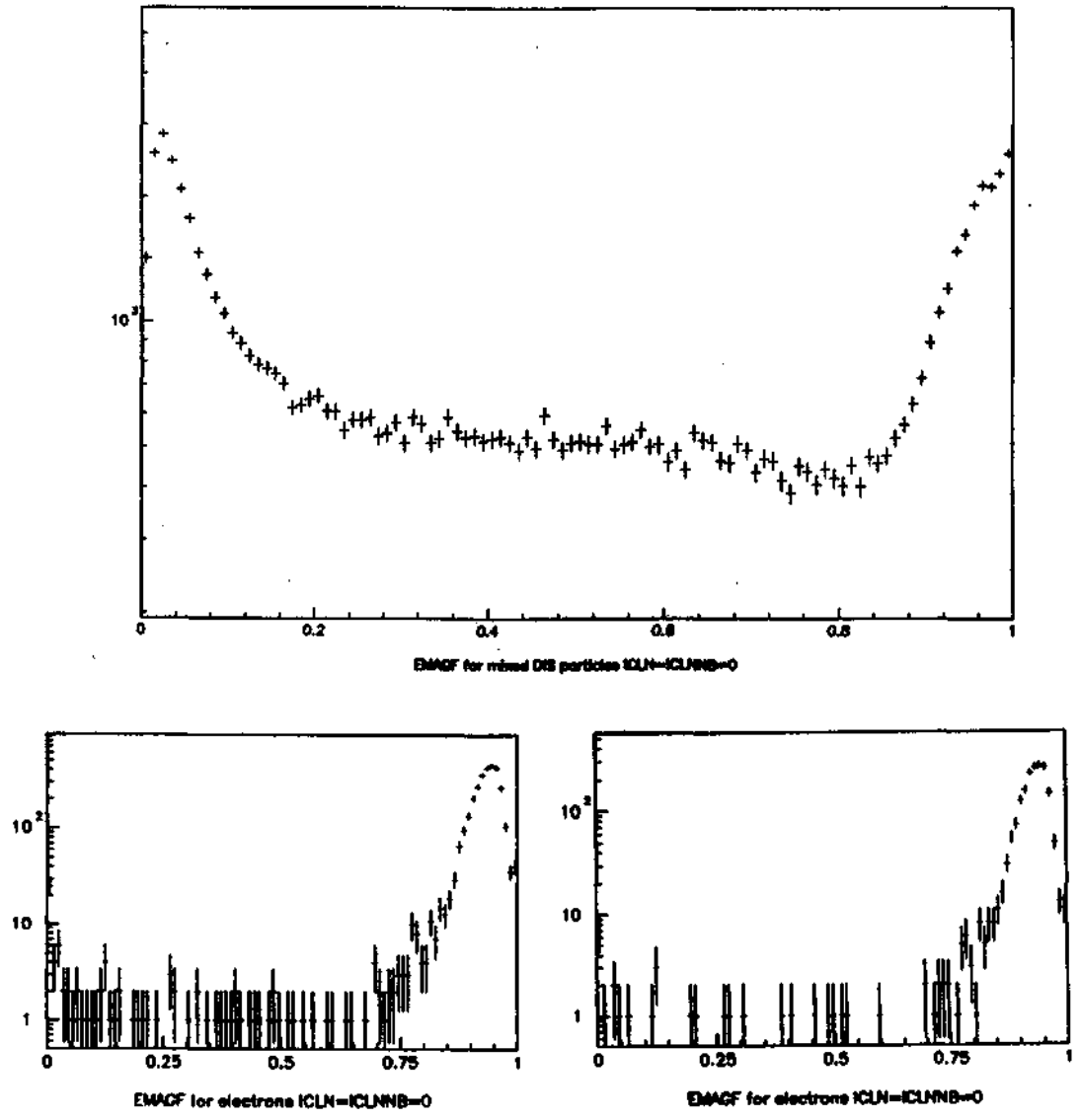

Figure 4.13: EMAGF distribution for mixed particles from deep inelastic events (top), including some electrons from photoconversion of bremsstrahlung photons. EMAGF distributions for a sample of electrons defined by a cut as in fig 4.12. (bottom left). The cut is tightened and the efficiency rises (bottom right).

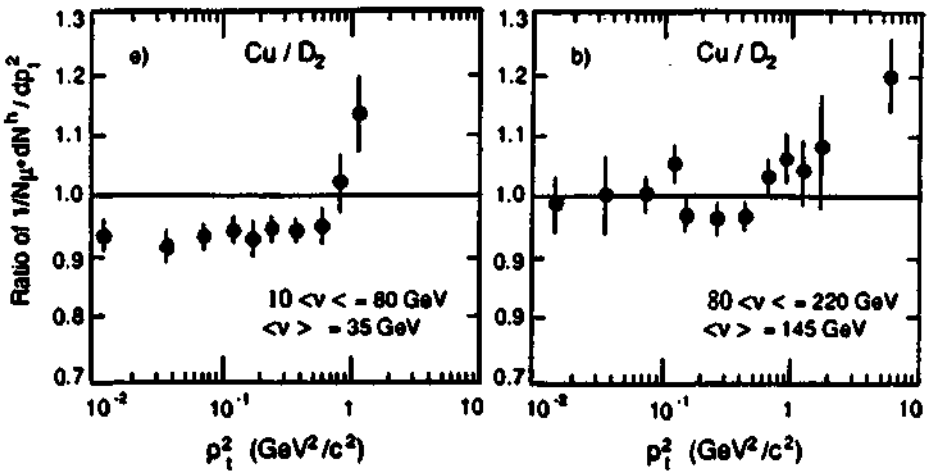

Figure 4.14: Ratio of differential hadron multiplicity in copper and deuterium as measured by the EMC. Left, low ν events show a depletion in the copper target, whereas right, for high ν the multiplicities are equal.

One of the possible biases is known to be negligible from earlier NMC [26] results with the same beam energy and almost identical target setup (with calcium instead of lithium), and was not repeated:

- The fraction of hadrons (defined by looking at pairs of tracks with invariant mass higher than 200 MeV) rejected with the EMAGF cut is 3-5% and is found to be equal between targets [26], the largest difference being found between the most upstream targets to be $1.2\% \pm 0.5\%$ (but the next target pair shows a difference of opposite sign, so the effect on the ratio is again reduced, thanks to the complementary target method).

Other possible sources of bias are secondary interactions of hadrons:

- Inside the target nucleus; the hadron is produced in a deep inelastic scattering event on one of the nucleons, but is stopped in the nuclear medium before breaking free of the nucleus.
- Reinteraction on the path through the remaining target material between the vertex and the detector.

The first effect is understandably material-dependent and could bias the ratio: a hadron is more easily stopped in a big nucleus as carbon, than in a small one, as deuterium. This effect has been studied by the EMC collaboration, comparing hadron multiplicities from copper and deuterium [82]. A $\sim$ 5% suppression of the hadron multiplicity is observed for energy transfers lower than 80 GeV (fig. 4.14), but an equal multiplicity is observed

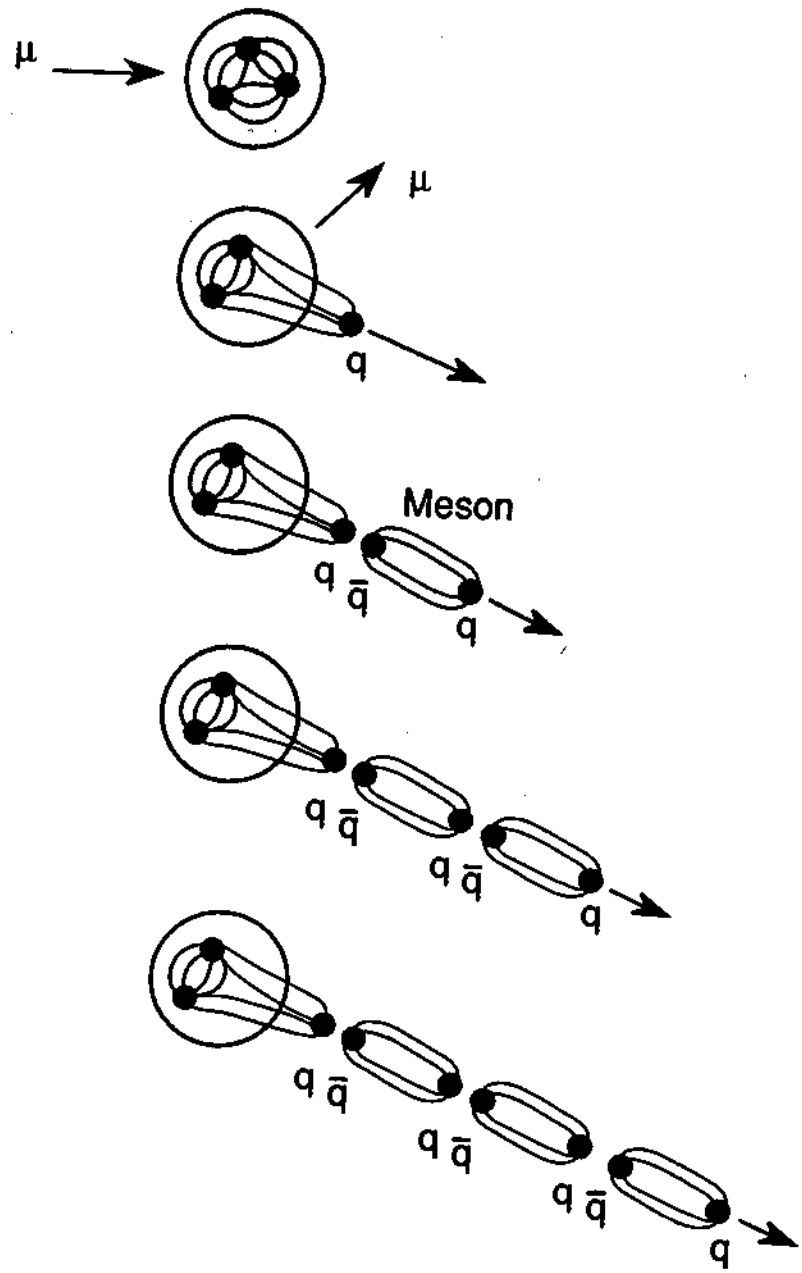

Figure 4.15: Hadronisation in the string model. The struck quark stretches the string until it breaks to form a $q\overline{q}$ pair, and the process continues until all the energy is spent.

at higher energy transfers. This is explained by the fact that at large energy transfers the Lorentz boost is so large that the struck quark actually hadronizes ("dresses") as it is leaving the nucleus. The actual hadronization is a complicated picture as described by the string model, with two different time scales – first for the quark to create an open string, and then for this string to break and create a hadron (a qualitative rendering of this model is shown in fig. 4.15). However, the idea is that the absorption of quarks in nuclear medium is negligible compared to the absorption of full hadrons [82] (the latter having a well known cross section of $\sim$ 20 mb), and so since the dressing occurs outside the nucleus when the Lorentz boost is sufficient, we shall have no systematic bias due to this effect in our ratio. Special care shall be taken to vary this ν cut to estimate the systematic effects due to this.

Actually it is found that the cut at $\nu = 60$ GeV brings into agreement the C/D ratio determined from the standard method, and that form this hadron method, in the region where they overlap. In the region where the standard method cannot be applied, we are lucky since there is no data at low ν, anyway. In the case of lithium, which is lighter and therefore presents fewer reinteraction centers, no discrepancy between the standard method and the hadron method is found in the first place, so the ν cut stayed at the same value as for the standard method. Why are we comparing to the standard method? Because of course it is insensitive to the hadron reinteraction, since only a muon is required in the final state.

The second effect of reinteraction in the target material may be argued away by saying that the reinteraction cross section is approximately the same in all materials – it is about 20 mb per nucleon encountered for pions, the most common of hadrons produced in deep inelastic scattering. Further, the thicknesses of all targets are roughly the same – 1.04-1.13 10^{25} nucleons/cm^2 (see sec.2.3), and thus the probability of absorption of a hadron is roughly independent of the target row, depending solely on the position of the vertex. And in the ratio it should cancel out.

However, a more quantitative estimate of this effect has been made. Take a hadron produced at the vertex and travelling through material. It has a probability $P(l)$ of "surviving" at a distance l from the vertex. In the continuum limit, the probability -d$P(l)$ for this hadron to be absorbed on the infinitesimal path between l and l+dl is just the cross section times the number of absorbing centers (nuclei) encountered times the probability it is there at l:

$$-\mathrm{d}P(l) = \sigma_{absorption} \cdot \frac{N_{Avogadro}}{M_A} \rho \mathrm{d}l \cdot P(l) \tag{4.17}$$

where M_A and ρ are the atomic mass and the density of the material traversed. This gives for $P(l)$:

$$P(l) = \mathrm{e}^{-l/\lambda} \tag{4.18}$$

where λ is the interaction length:

$$\lambda = \frac{M_A}{\rho\, \sigma_{absorption}\, N_{Avogadro}} \tag{4.19}$$

In the simplest case where each deep inelastic event creates exactly one hadron, it would be easy to correct for absorption: one would simply weight all events which are seen by a weight inversely proportional to the probability that the hadron passes through all the material unscathed:

$$g = \frac{1}{P(l_{tot})} = e^{l/\lambda}. \tag{4.20}$$

In this way, events having survived on a long path through material would get a large weight, and vice versa.

This was easy. Now we have to take into account that not one hadron is produced, but several. The bias due to absorption of hadrons is connected to losing an *event*, not a single hadron. Soft hadrons are anyway lost in the FSM, as stated several times before, typically we see hadrons of 3-4 GeV and more in our detector. If we have a single fast hadron, the probability of losing the event due to absorption is just $P(l_{tot})$.

For the case of higher multiplicities let us introduce:

x = number of created hadrons (unknown)
n = number of detected hadrons (known)
w_x = fraction of events having x created hadrons (unknown)
f_n = fraction of events having n detected hadrons (known)

In the data, we measure:

f_1 = 0.573 (57.3% events have multiplicity 1)
f_2 = 0.297
f_3 = 0.096
f_4 = 0.0272
f_5 = 0.00574
f_6 = 0.00112
f_7 = 0.000224
f_8 = 0.0000498

To establish a connection between the measured and detected multiplicity distributions we construct a matrix A_{xn}:

A_{xn} = fraction of events with x created and n detected hadrons

The elements of this matrix can easily be computed. For instance A_{11} is the fraction of events having one created and one measured hadron – it is just the fraction of events with one created hadron w_i times the probability $P(l)$ (or just P for short) that this hadron survives to be detected:

$$A_{11} = w_i P,$$

while A_{10} is the fraction of events with one created, but no detected hadrons and is therefore:

$$A_{10} = w_i(1 - P),$$

(1-P) being the probability that the hadron is absorbed in flight.

Most generally we have:

$$A_{xn} = \left(\begin{array}{c} x \\ n \end{array} \right) w_x P^n (1-P)^{x-n} \tag{4.21}$$

where the binomial coefficient counts all possihle combinations of n detected ont of x created hadrons, w_x measures the fraction of events with x created hadrons, P^n is the probability for n hadrons to survive, and $(1-P)^{x-n}$ the probahility for $x-n$ hadrons to he ahsorhed.

For our purposes the detected multiplicity x goes from 0 to 9, and the created one from 1 to 9 [6]. We so end up with a 9×10 matrix which looks like this:

$$A_{xn} = \left(\begin{array}{cccccc} w_1(1-P) & w_1 P & 0 & \dots & \dots & 0 \\ w_2(1-P)^2 & 2w_2P(1-P) & w_2P^2 & 0 & \dots & 0 \\ w_3(1-P)^3 & 3w_3P(1-P)^2 & 3w_3P^2(1-P) & w_3P^3 & \dots & 0 \\ \vdots & & & & \ddots & \vdots \\ w_9(1-P)^9 & \left(\begin{array}{c} 9 \\ 1 \end{array} \right) w_9P(1-P)^8 & \left(\begin{array}{c} 9 \\ 2 \end{array} \right) w_9P^2(1-P)^7 & \dots & \dots & w_9P^9 \end{array} \right) \tag{4.22}$$

The sums of the columns of A_{xn} give the fraction f_n of events with n observed hadrons:

$$\sum_x A_{xn} = f_n, \quad \text{for } n = 0, \dots, 9 \quad , \tag{4.23}$$

which are measured (except for f_0). The sum of the whole matrix represents *all* deep inelastic events, so we need to correct for the unseen fraction: f_0. The aim is to find weights g_n for each *seen* multiplicity such that:

$$\sum_{i=1}^{9} g_i f_i = \sum_{i=0}^{9} f_i. \tag{4.24}$$

This is the only constraint! In other words, we have 9 weights to determine from one equation. This gives us a liherty of choice.

The simplest choice is to say: OK, let's weigh ouly the multiplicity 1 events. They are anyway the most likely to "disappear", the higher multiplicity events would have to have *all* their hadrons disappear for us not to see them. We choose the weights in the following way to satisfy eq. 4.24:

$$\begin{aligned} g_1 &= \frac{f_0 + f_1}{f_1} = \frac{\sum_{x=1}^{9} w_x(1-P)^x + \sum_{x=1}^{9} x w_x P(1-P)^{x-1}}{\sum_{x=1}^{9} x w_x P(1-P)^{x-1}} \\ g_n &= 1, \quad n = 2, \dots, 9 \end{aligned} \tag{4.25}$$

We call this choice **method 1**. Of course it is impossible to calculate directly g_1 since the w_x's are in principle unknown. Bnt for a first approximation, one can take $w_x = f_x$, the assumption that the created fractions approximately equal the measured fractions, which is approximately true if the absorption effects are small. Then if necessary one can iterate on weighted multiplicities, i.e. in the next iteration one would take $w_x = g_x f_x$. P is readily

[6] events with 0 created hadrons are of no interest to this calculation, and we expect that since we at most measure multiplicity 8, created multiplicities higher than 9 are very unlikely

computed knowing the position of the vertex and intersecting its trajectory with the targets it encounters.

Another, more sophisticated, and perhaps more rigorous choice is to try to correlate all the columns (measured fractions) with all the rows (created fractions) of A_{xn}. This gives:

$$g_n f_n = w_n, \quad n = 1, \ldots, 9 \tag{4.26}$$

where we correlate multiplicities with the same number of created and measured hadrons[7]. From eq. 4.26, we find the expression for g_x:

$$g_n = \frac{w_n}{f_n} = \frac{w_n}{\sum_{x=1}^{9} w_x \begin{pmatrix} x \\ n \end{pmatrix} P^n (1-P)^{x-n}} \tag{4.27}$$

We call this choice **method 2**. Again in the first iteration we take $w_n = f_n$, and then iterate with weighted multiplicities if necessary.

One more remark is in order. In the above we have tacitly supposed all P's to be equal, i.e. there is a simplification in the sense that all hadrons created in the same vertex have the same probability of being absorbed. This is not true, of course, since the hadrons are emitted at different angles and therefore some will pass through all the intervening target material, whereas others will "see" only part of it.

The reason why we made this simplification is simply that otherwise the calculation becomes unmanageable. Not only would the expressions be even more complicated, but it is impossible to guess what trajectories the unseen hadrons have. This would only be possible in a fine-tuned MonteCarlo program with secondary interaction simulation.

Now to get an idea of the maximum systematic effect this bias can create, we use the following procedure:

- In method 1 we use only multiplicity 1 events, so we calculate P using the track of this one seen hadron.
- In method 2 we use two extremes: once we use the track with the minimal path through material for the calculation (we call this then MIN2), and once we use the maximum path through the material (and call this MAX2).

The interaction lengths were calculated from absolute cross sections from Serpukhov and Fermilab measurements refs. [84, 83, 85, 86]. An apparent discrepancy between the cross sections measured by these two groups is due to the fact that the Serpukhov group quotes a cross section which correspond to total–elastic contribution, whereas the Fermilab group quotes total–elastic–quasielastic [104]. Therefore we use the cross section from the Fermilab group, since the hadron is really lost for us if it is absorbed; if it only interacts elastically or quasielastically we will still see it afterwards in our detector[8]. The cross section shows virtually no energy dependence upwards from 20 GeV, and between 5 and 20 GeV the cross section falls by about 20% – this has been neglected here. Only the high energy average of the cross section is thus used:

[7] Of course the most general method would be to have a weight matrix, g_{xn} to correlate all measured multiplicities with all created ones. But we'll refrain from such complication.

[8] One can argue that an elastically scattered hadron will not fit to the main vertex and thus be rejected by the tracking programs. However, the total–elastic–quasielastic cross section shows the largest nuclear dependence, hence it is a worst case scenario anyway

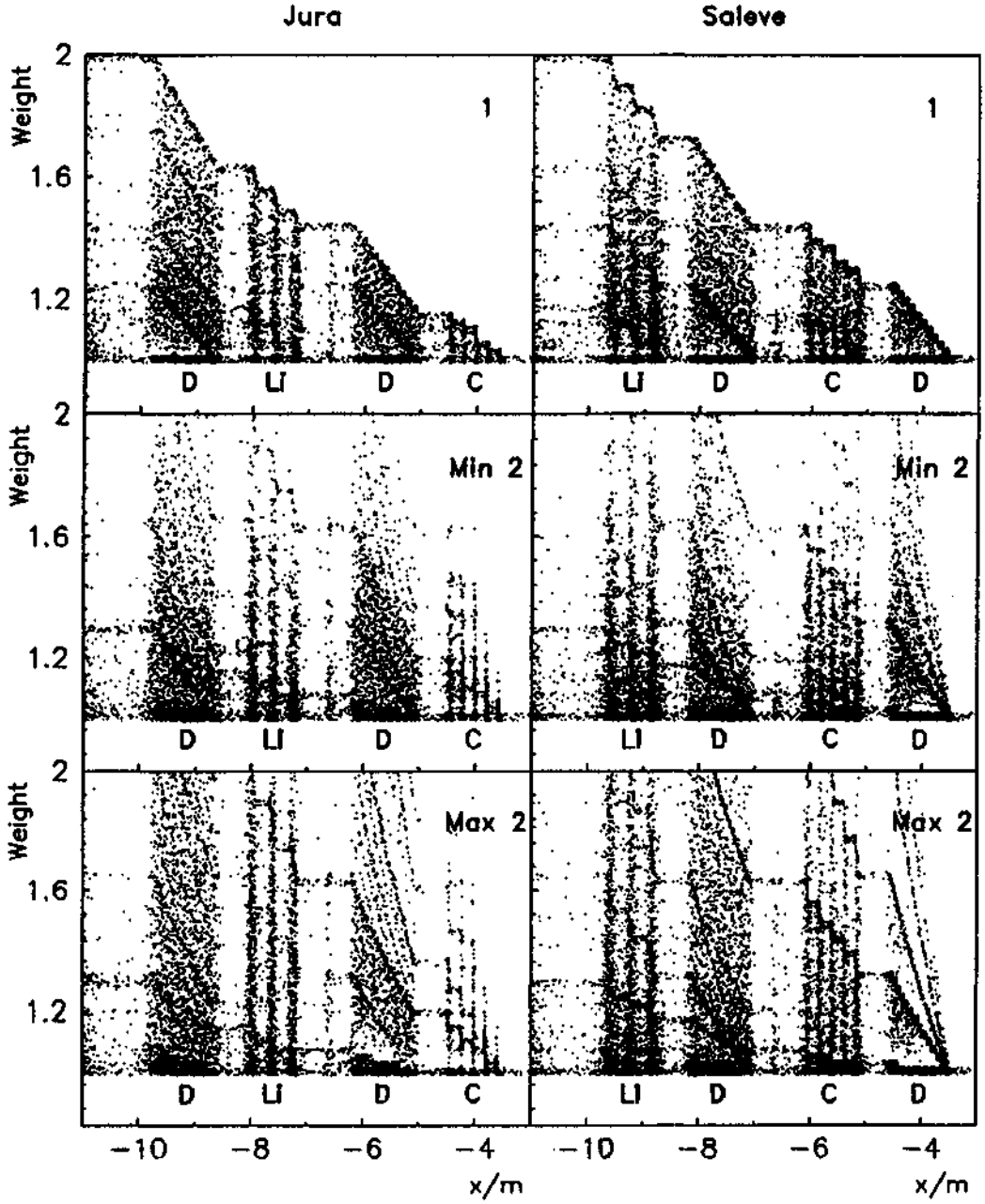

Figure 4.16: Weights calculated for the evaluation of the reinteraction in targets with the three different methods vs. the vertex position for both target rows. See text.

$$\begin{aligned}\sigma(\pi^{\pm\,2}\mathrm{D} \to \mathrm{X}) &= 46 \text{ mbarn} \\ \sigma(\pi^{\pm\,6}\mathrm{Li} \to \mathrm{X}) &= 101.5 \text{ mbarn} \\ \sigma(\pi^{\pm\,12}\mathrm{C} \to \mathrm{X}) &= 168 \text{ mbarn},\end{aligned}$$

the cross section for ^{6}Li having been deduced from the quoted cross section for natural (mostly ^{7}Li) and the A–dependence power law: $\sigma = \sigma_0 A^{.76}$. The calculated values for the interaction lengths in the targets are:

$$\begin{aligned}\lambda_D &= 4.42 \text{ m} \\ \lambda_{Li} &= 2.13 \text{ m} \\ \lambda_C &= 0.632 \text{ m},\end{aligned}$$

the targets themselves thus representing 0.249, 0.177, and 0.158 interaction lengths respectively for deuterium, lithium and carbon.

The weights obtained in this way are shown in fig. 4.16, plotted vs. the vertex position for the three weighting procedures. Let us start from the weights for method 1. They go from 1 to 2, the highest weights corresponding to the tracks having traversed all intervening material between the vertex and the detector. Going to lower weights, one sees concentrations of events on lines parallel to the high edge. On the example of the most upstream deuterium target in the Jura row (top left frame), the first faint diagonal line (starting at weight 1.75 at the upstream end) parallel to the top edge corresponds to events having traversed all material except the most downstream carbon targets. The next, more visible line (starting at weight 1.4) corresponds to events whose hadron traverses only the lithium slabs and doesn't go through the downstream targets at all. The lowest and most pronounced diagonal (starting at weight 1.2) corresponds to events missing also the lithium slabs. Higher multiplicity events are assigned weight 1 in this method.

The interpretation of the pictures concerning method 2 is a little more complicated. Let us say only that the different slopes seen in the lines of concentration are due to the higher multiplicity events. If a high multiplicity event is seen, the created multiplicity must be the same or even higher and thus a higher power of the probability shall contribute (for higher multiplicity, a higher power of P contributes to the weight, see eq. 4.26. Conversely, the multiplicity 1 events now have much smaller weights and constitute the concentration near weight 1. This is so in order to satisfy eq. 4.24 – the sum must remain the same.

It is now evident that these two methods are quite complementary, and should represent the extreme limits of what is actually going on. The deviations obtained by these three methods from the unweighted structure function ratio are *everywhere* less than one-half the statistical error on the ratio itself. The deviations found are tabulated in Table 4.2 for the lowest four x_{Bj} bins, the domain where the hadron method is the only possible one. These deviations are taken into account as a systematic uncertainty in sec-sys. **No weights shall be applied to the central value of the ratio.**

Another possible bias was mentioned by authors in EMC and NMC:

- Coherent ρ^0 and ϕ^0 production is a *quasielastic* process, but will pass our cuts, for the ρ^0 decays immediately into $\pi^+\pi^-$ (100 % branching ratio), and the ϕ^0 decays into $\mathrm{K}^+\mathrm{K}^-$ (49.5 %) or $\mathrm{K}^0_L\mathrm{K}^0_S$ (34.4 %) which in turn decay into $\pi^+\pi^-$ etc. The result is

x_{Bj}	stat. error	Deviation of F_2^{Li}/F_2^D		
		Method 1	Min 2	Max 2
$1.4 \cdot 10^{-4}$	$6.55 \cdot 10^{-2}$	$-0.65 \cdot 10^{-2}$	$-1.59 \cdot 10^{-2}$	$-1.10 \cdot 10^{-2}$
$2.8 \cdot 10^{-4}$	$5.01 \cdot 10^{-2}$	$-0.58 \cdot 10^{-2}$	$-2.62 \cdot 10^{-2}$	$-0.21 \cdot 10^{-2}$
$4.5 \cdot 10^{-4}$	$3.70 \cdot 10^{-2}$	$-0.86 \cdot 10^{-2}$	$-1.83 \cdot 10^{-2}$	$-1.58 \cdot 10^{-2}$
$6.7 \cdot 10^{-4}$	$3.47 \cdot 10^{-2}$	$-0.84 \cdot 10^{-2}$	$-0.08 \cdot 10^{-2}$	$-1.31 \cdot 10^{-2}$

x_{Bj}	stat. error	Deviation of F_2^{Li}/F_2^D		
		Method 1	Min 2	Max 2
$1.5 \cdot 10^{-4}$	$8.70 \cdot 10^{-2}$	$0.00 \cdot 10^{-2}$	$-2.58 \cdot 10^{-2}$	$-3.15 \cdot 10^{-2}$
$3.1 \cdot 10^{-4}$	$5.58 \cdot 10^{-2}$	$-0.49 \cdot 10^{-2}$	$-2.45 \cdot 10^{-2}$	$+0.08 \cdot 10^{-2}$
$4.8 \cdot 10^{-4}$	$5.92 \cdot 10^{-2}$	$-0.77 \cdot 10^{-2}$	$-2.43 \cdot 10^{-2}$	$-1.70 \cdot 10^{-2}$
$6.7 \cdot 10^{-4}$	$4.46 \cdot 10^{-2}$	$+0.04 \cdot 10^{-2}$	$-1.97 \cdot 10^{-2}$	$-0.31 \cdot 10^{-2}$

Table 4.2: Effects of secondary interactions on the structure function ratio to be taken into account for the systematic error

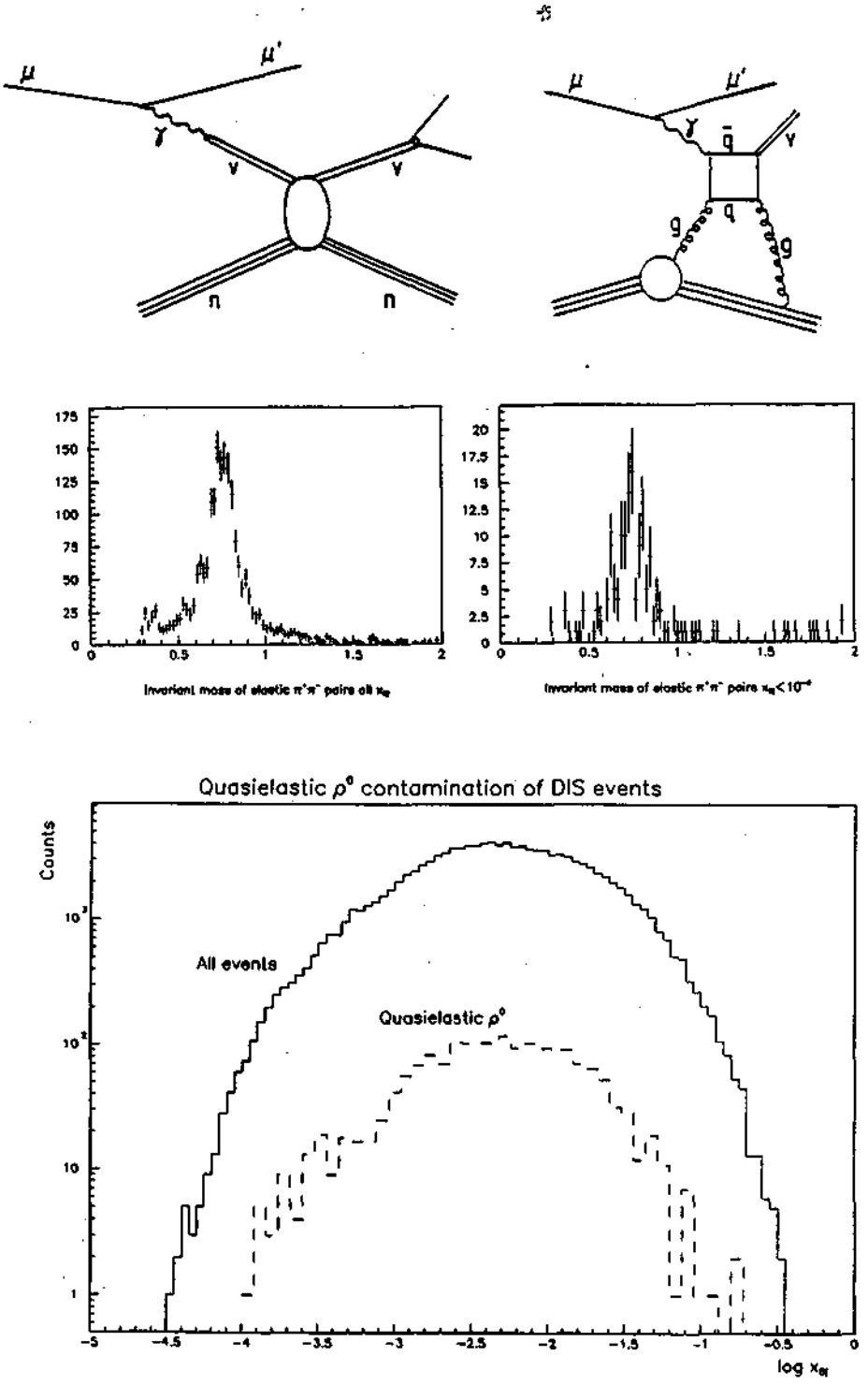

Figure 4.17: The quasielastic ρ^0 contamination in the data sample after hadron cuts. **a** The Vector Meson Dominance picture. **b** The photon-gluon fusion model. **c** The invariant mass plot of tracks after cuts explained in the text, under the pion hypothesis. A clean ρ^0 peak is visible (m_ρ = 768.1 MeV, natural width 151.5 MeV). **d** The same for events with $x_{Bj} < 10^{-3}$. **e** The number of events with invariant mass between 400 and 1200 MeV in the above plots plotted vs. x_{Bj} in the same plot with all events passing the hadron cuts. Both scales are logarithmic.

always two or more charged hadrons which carry only a fraction of the virtual photon momentum each, something we may interpret as a deep inelastic scattering event.

The Feynman diagram of this process is shown in fig. 4.17a, in the Vector Meson Dominance model, where the virtual photon fluctuates into a *virtual* vector meson. This meson can then come on mass shell (i.e. become a real vector meson) by elastic scattering off a nucleon. This is also called diffractive muoproduction. In the QCD-based picture of the colour singlet model (fig. 4.17b) the process proceeds via *photon-gluon fusion.* This may be thought of equivalently as a gluon fluctuating into a virtual $q\bar{q}$ pair (sea quarks), the pair being put on shell by the virtual photon. In order to satisfy colour conservation, a second gluon is exchanged with the nucleon. (A gluon carries colour charge, whereas real particles don't. Therefore the second gluon "brings back" to the nucleon the colour the first one took away).

We have looked for quasielastic ρ^0's in our data sample. Such events are defined as follows:

- Exactly two opposite sign hadrons (i.e. passing the two crucial hadron method cuts) are required (representing presumably the $\pi^+\pi^-$ pair of the ρ decay), fitted to the main vertex.
- Elasticity requirement: the pair is required to carry at least 90% of the virtual photon momentum.

When invariant masses of such pairs are computed, a clear ρ^0 signal emerges. One can then plot the fraction of events in our sample where a quasi- elastic ρ^0 is reconstructed. It is seen that this fraction is almost constant throughout the x_{Bj} range of T14 and its value is about 3 %. Based on MonteCarlo studies done for ρ^0 production [81], one can guesstimate the real fraction of quasielastic ρ^0 events in the sample to about 4-5%.

This contamination is however present in any measurement of F_2, it is just one of the subprocesses of the inclusive cross section. There is no difference here between the standard and the hadron method. Radiative tails of this process are corrected for by the inelastic tail of the radiative corrections (see sec 4.3.1), but the process itself is included in the cross section.

4.3 The structure function ratio determination

Now that the cuts are defined, we are ready to proceed with the ratio determination. Or are we? Different corrections have first to be applied. **Radiative** corrections are the most important ones in the low x_{Bj} region, **vertex smearing** corrections are also applied, and **kinematic smearing** corrections shall be considered in this section. For consistency, in this section all correction factors are defined as the "true" divided by the "measured". This means we have to multiply the measured cross section (or the ratio) with the corresponding factor to get what we believe is the true value.

4.3.1 Radiative corrections

Radiative corrections are a large field and no attempt shall be made here to present their treatment in great detail. Only the essentials shall be discussed, for more the reader is referred to [7, 68, 70] and references therein.

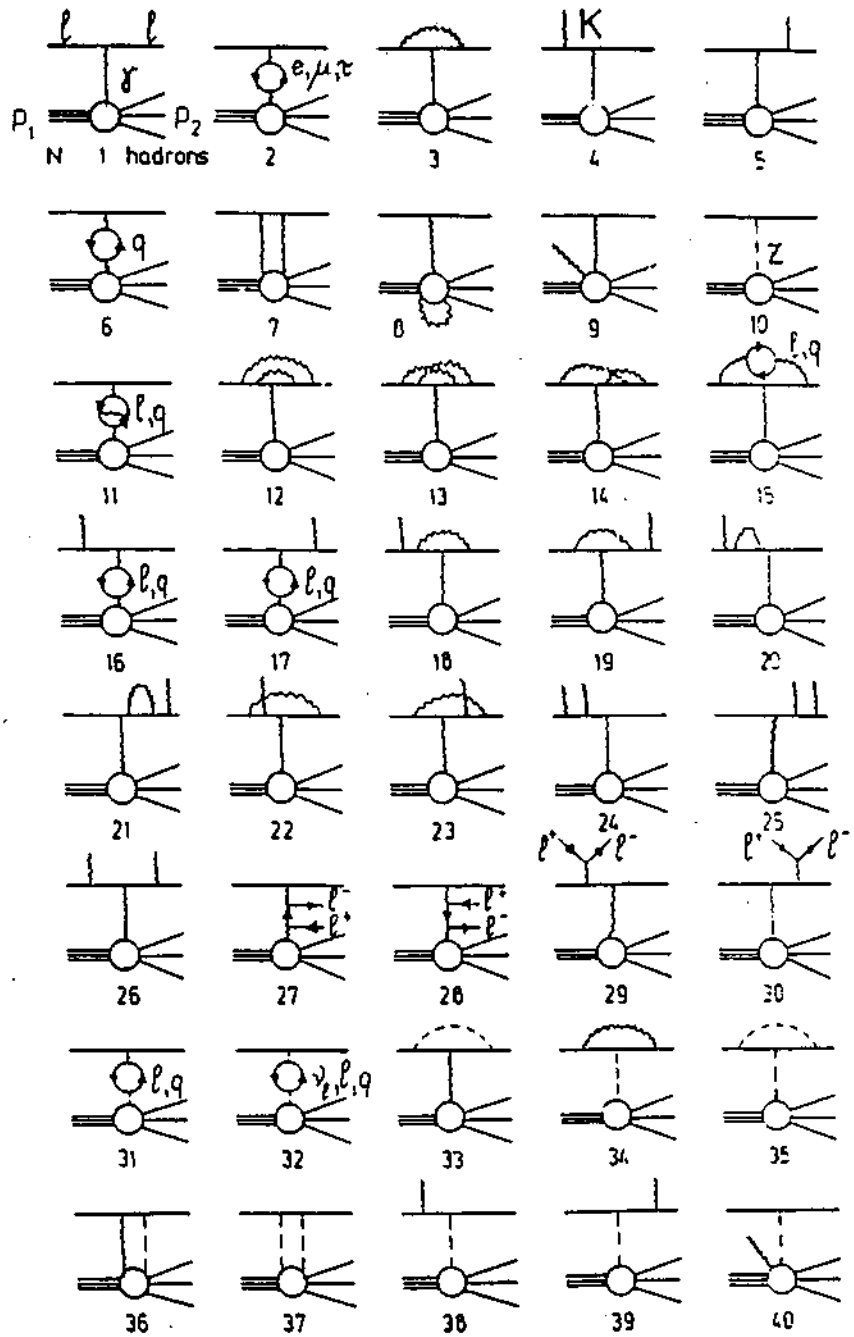

Figure 4.18: One-photon exchange (diagram 1) and higher order processes contributing to the measured cross sections. An identical set of diagrams can be drawn for elastic processes (quark lines not separating after the interaction).

We are interested in measuring ratios of cross sections of the process shown in Fig. 1.1, i.e. the one photon exchange. Real life is more complicated though, since many other processes contribute to the actual cross section. We thus have to apply a correction factor $\eta(x_{Bj}, y_{Bj})$ for each material to get the ratio of one-photon exchange cross sections:

$$\mathcal{R}^A_{1\gamma}(x_{Bj}, Q^2) = \frac{\sigma^A_{1\gamma}(x_{Bj}, Q^2)}{\sigma^D_{1\gamma}(x_{Bj}, Q^2)} \tag{4.28}$$

$$= \frac{\eta^A(x_{Bj}, y_{Bj}) \cdot \sigma^A_{measured}(x_{Bj}, Q^2)}{\eta^D(x_{Bj}, y_{Bj}) \cdot \sigma^D_{measured}(x_{Bj}, Q^2)} \tag{4.29}$$

$$= \frac{\eta^A(x_{Bj}, y_{Bj})}{\eta^D(x_{Bj}, y_{Bj})} \cdot \mathcal{R}^A_{measured} \tag{4.30}$$

The F_2 ratio shall thus be most affected by corrections *differing* in different nuclei.

The radiative processes can be divided in two big groups (in decreasing importance as a correction to the F_2 ratio):

- The coherent elastic and quasi-elastic processes. Scattering on the nucleus as a whole is referred to as *coherent* scattering, for the nucleons act coherently. *Quasi-elastic* scattering refers to scattering from a single nucleon. All the diagrams shown in fig. 4.18 can be drawn with the quark lines not separating after the interaction, they then represent the elastic scattering of which we see a far tail in the inelastic region. These events have to be corrected for since they don't represent the deep inelastic cross section we are interested in (we must subtract them from our observed counts).

- The inelastic higher order processes. A representative set of Feynman diagrams up to the fourth order in the electromagnetic coupling constant α (i.e. corrections of order up to α^2) is given in fig. 4.18. These events have kinematics modified with respect to the one photon exchange we wish to extract. We thus have to correct for these events.

From these two groups, the contributions related to bremsstrahlung diagrams 4 and 5 (as well as their interference with other terms) are treated separately and referred to respectively as elastic and inelastic tails. Elastic tails represent the dominant contribution at low x_{Bj} and high y_{Bj}.

A common feature of these radiative processes is that they change the kinematics of the primary interaction because of an additional interaction on the initial or final state muon, or both. This is easy to see in the simple case of e.g. diagram 5 of fig 4.15, where the outgoing muon radiates a hard real photon. The measured momentum of the muon will be smaller than the "true" momentum that the muon had directly after the virtual photon vertex, and the scattering angle shall be modified. It is thus easy to imagine that we may see the tails of the very big coherent and quasielastic peaks, even though they occur in a kinematic region where we have practically no acceptance (coherent scattering occurs at true $x_{Bj} = A$, $Q^2 \sim 0.01$ GeV$^2/c^2$, and quasielastic at $x_{Bj} = 1$, $Q^2 \sim 0.1$ GeV$^2/c^2$ cf. e.g. [64]).

For the kinematics to be sufficiently changed for us to see such an event in our acceptance, and use it as a deep inelastic one, the photon has to be really hard (90-100 % of the scattered muon energy), for in an elastic event the incident muon hardly transfers any momentum, the nucleus being much heavier than the muon. Therefore nearly all the energy loss occurs by bremsstrahlung. En résumé, elastic scattering occurs at very low Q^2

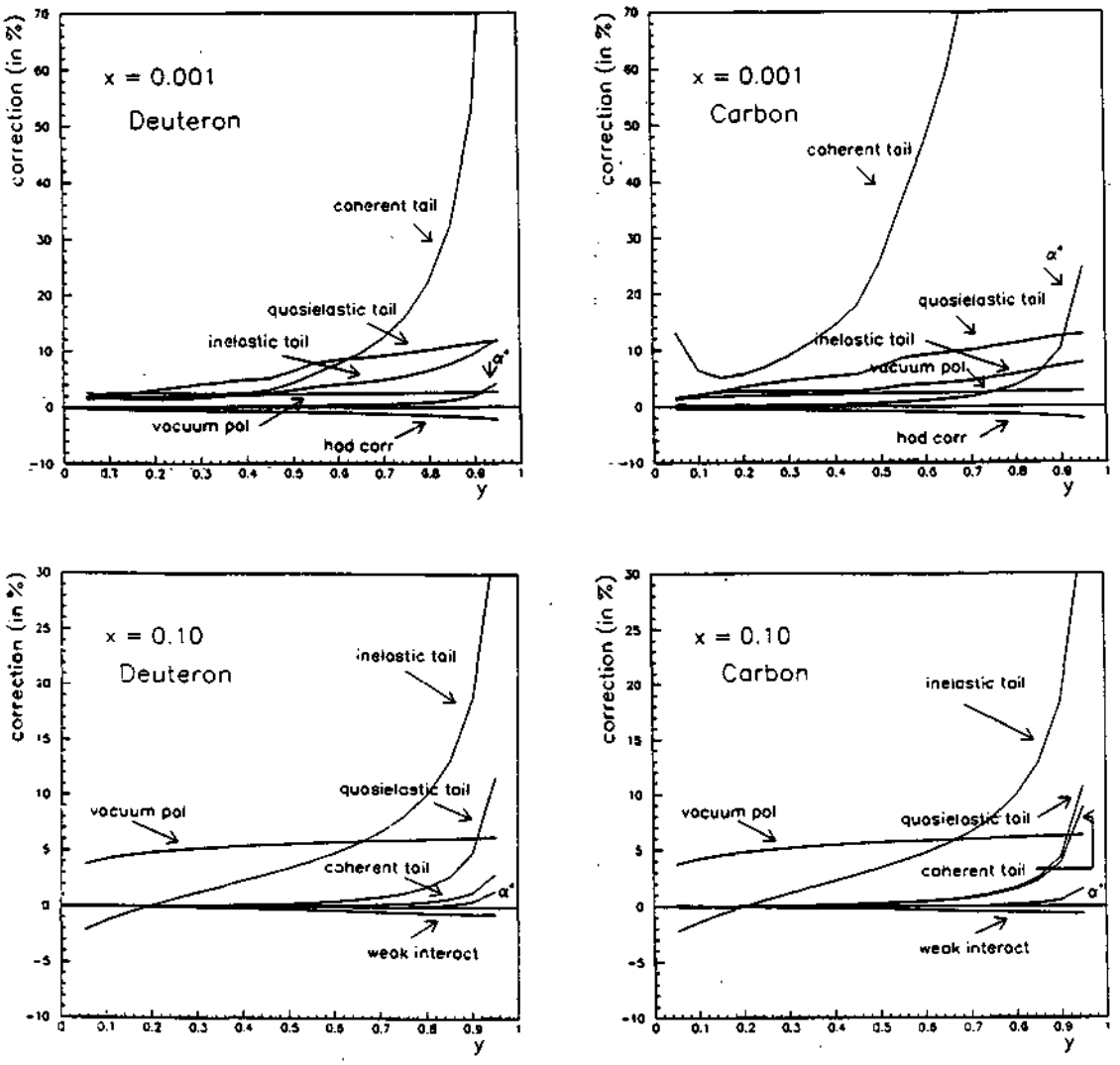

Figure 4.19: Different contributions to the radiative corrections on the example of carbon and deuterium in a low x_{Bj} and a high x_{Bj} bin. The coherent and quasielastic contributions are seen to diverge at low x_{Bj} and high y_{Bj}, whereas the other contributions are almost the same for both materials and nearly cancel in the ratio. Figure courtesy A. Brüll

(of the order of 0.1 GeV^2/c^2 or less) and very low ν ($= Q^2/2M_p x_{Bj}$, where $x_{Bj} = 1$ or A respectively for quasielastic and coherent scattering), and it is followed by a bremsstrahlung process at Q^2=0 (*real* photon) and high ν. We measure the total (small) Q^2 and total (high) ν.

That such hard photons exist is not only described in QED [65, 66] but was confirmed by direct experimental observation [67]. These hard photons are especially abundant in the low-x_{Bj}, high-y_{Bj}. This is an apparent paradox: this region is located in tbe far *deep inelastic* region. Understanding this apparent paradox requires a detailed study of the bremsstrahlung kinematics [71] revealing that with cbanging y_{Bj}, the minimal four-momentum transfer t (equivalent to Q^2 in this case) allowed by energy and momentum conservation varies by several orders of magnitude [72]. Since tbe Mott cross section varies as $1/Q^4$ this means that we can catch tails of an enormous elastic peak at very low Q^2. To resume, this means that we are looking at the result of two processes: one is extremely unlikely (the radiation of a very hard photon), but the otber is extremely abundant (elastic scattering at very small Q^2), much more so than the deep inelastic process we are bent on. The corrections thus obtained can be well in excess of a hundred per cent at low x_{Bj} and higb y_{Bj} (fig.4.19)! This explains our cut at $y_{Bj} = 0.8$.

The tails of tbe coherent scattering are understandably different between nuclei – we are scattering off different targets altogether. The tails of the quasielastic scattering (scattering off an individual nucleon) are different due to different suppression factors (the Pauli principle restricts scattering into certain states – this results in the suppression of tbe quasielastic scattering cross section off a bound nucleon at small Q^2).

As to tbe inelastic contributions, they are integrated over the whole kinematically accessible region – form the single pion tbresbold ($W \approx 1.06$ GeV) to tbe kinematic point where tbe event is measured. "Inelastic" contributions comprise also tails of the quasielastic ρ^0 production discussed above. Yes, even if it is a quasielastic process in the sense tbat the nucleon didn't break up in the process, for radiative corrections this is an inelastic tail, because there is an additional particle in tbe final state ($W > M_p$).

Not shown in Fig. 4.18 is tbe contribution due to the emission of multiple soft photons. This contribution is infrared divergent, but when evaluated togetber with the vertex correction diagram (diagram 3 of fig. 4.18), the divergences cancel to all orders of α, and the residuum may be summed to give an exponential term.

Historically, two approaches bave been used for radiative corrections in NMC. Tbe first approach is the classical one pioneered by Mo and Tsai in the sixties [65] , developed for tbe SLAC electron experiments. It is model-independent in the sense that it doesn't assume anything about the structure of tbe proton, and calculates the contribntions to the lepton vertex only (hadron vertex contributions like diagrams 8 and 9 in fig. 4.18 are not taken into account). However, it is not covariant since it uses an infrared cutoff parameter to treat tbe infrared divergent part of the soft photon emission separately. Tbe result of the radiative corrections does not depend on the cutoff parameter if the procedure is properly tuned.

The second approach was originally developed for the BCDMS experiment at CERN by tbe Dubna group (Akhundov, Bardin and Shumeiko, see e.g. [69] and references therein). It does not contain any cutoff parameter, the divergences of the photon emission and vertex correction cancelling in the integration over the whole photon phase space. It uses the Quark Parton Model in tbe sense tbat it considers scattering off pointlike quarks at the hadron vertex. This allows an explicit calculation of the hadron current corrections.

In this work the second approach was adopted, because it takes into account more

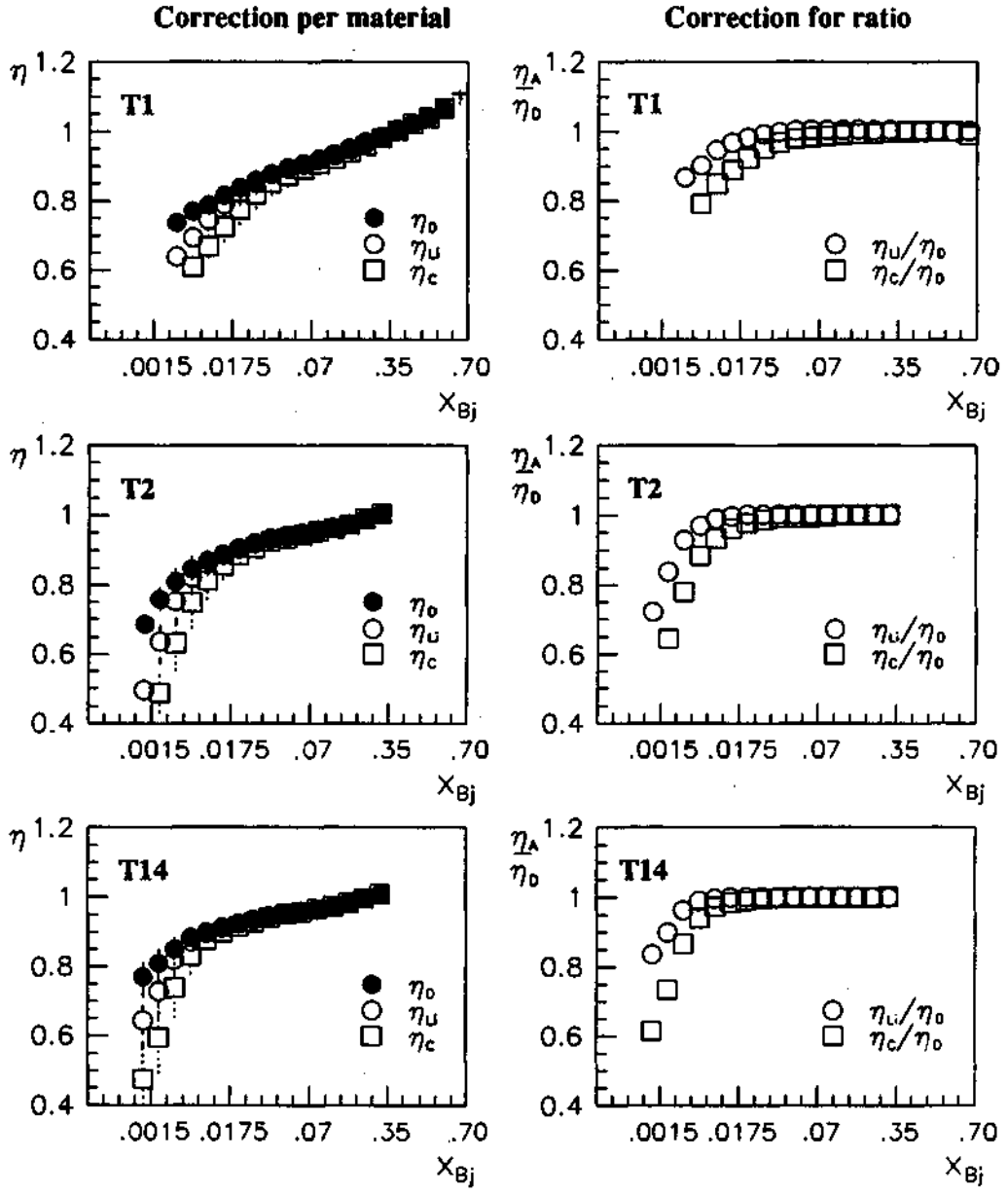

Figure 4.20: Average radiative corrections as applied in the standard method to each material (left) and the resulting effect on the ratio itself (to the right). The correction to the ratio reaches almost 40% in the lowest x_{Bj} bin (0.0009). For the hadron method, the correction stays smaller than 1% even at $x_{Bj} = 0.0001$!

processes and is believed to be more accurate. One should mention however that the two approaches are found to be numerically in agreement to within 2% even where the corrections are largest [68].

We should mention however that the Mo and Tsai approach – based program FERRAD ran into numerical instabilities when used to compute the radiative corrections down to $x_{Bj} = 10^{-4}$, problems which were not encountered by TERAD, a program based on the Dubna approach.

The radiative corrections are tabulated for each material, and applied on an event-to-event basis. Fig. 4.20. shows the correction factors applied to the data in all three materials, as a function of x_{Bj}. The correction factor is mostly smaller than one (we are subtracting unwanted events), but in the high x_{Bj} region it is greater than one. Why? Firstly, the elastic contributions are small. For the inelastic part, we shouldn't forget that not only do we have to subtract events coming from different kinematic regions, but we have to *add* events effectively having occurred in the kinematic region in question, but having "moved" elsewhere because of radiative processes.

For the **hadron method**, we don't need to correct for the quasielastic and coherent part, since these processes don't have a hadron in the final state. Only the inelastic tail contributes, i.e. radiative processes where the invariant mass of the final state is higher than the nucleon mass. In this sense also for example radiative tails of the ρ^0 quasielastic production are considered as inelastic tails, because in the final state we have the nucleon and the ρ^0. Besides these inelastic tails, also the small vertex and hadron current corrections have to be applied.

In summary, the radiative corrections are of crucial importance for the standard method, correcting the *ratio* by 30% or more at very low x_{Bj} whereas for the hadron method the average corrections to the ratio stay well below a percent.

4.3.2 Vertex smearing corrections

Because of multiple Coulomb scattering in the targets (the muons traverse up to one radiation length in the targets, which corresponds roughly to .3 mrad for the lowest energy scattered muons accepted, to be compared to the lowest scattering angles accepted – 2 mrad for T14) and finite resolution for the beam and scattered muon track, the vertices show some smearing in their x position. Remember that our only criterion for the attribution of a given event to a certain material is its vertex position. As the vertex smearing depends on kinematics (especially on the scattering angle, θ), we have to correct for this effect.

This can be corrected for in two ways. The most reliable, albeit quite tedious and time-consuming way would be to do so-called long chain Monte Carlo as shown in fig. 3.1. The other method that has been adopted here is based on fitting the vertex distribution obtained from the data with a fit function and finding how the tails from the distribution extend into the region of the neighbouring target. As long as the tails are symmetric, i.e. the same number of events smears from material A to material B as from material B to material A, we don't have to correct for the effects compensate. We only have to correct for the *asymmetry* of the smearing.

The fit function used is the so-called LOGAUBOX function. It is a convolution of a Lorentzian, a Gaussian and a box (rectangular) function, hence its name. The box is supposed to represent the true vertex distributions, and the Lorentzian and Gaussian reproduce the smearing effects. Such a convolution, essentially reducing to the integral

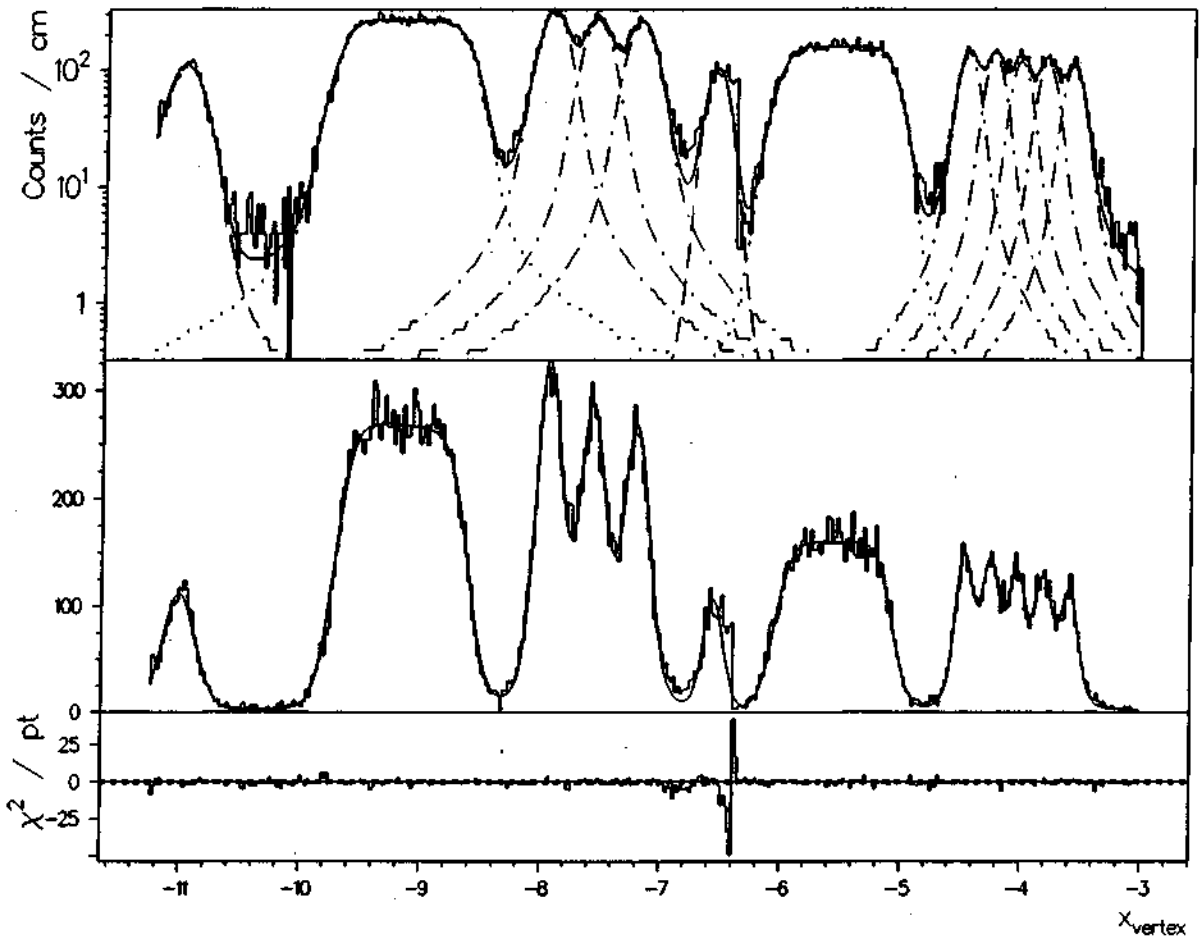

Figure 4.21: Fit of the whole vertex distribution by the LOGAUBOX function. The upper plot is on a log scale, the middle is linear scale, and the lower plot is the χ^2 per point. The peaks from left to right: the P0H proportional chamber, the deuterium target, the three lithium targets, P0B chamber, the downstream deuterium target, the five carbon slices. The function cannot reproduce the artificial step created by the cut on downstream events using P0B in the scattered muon fit.

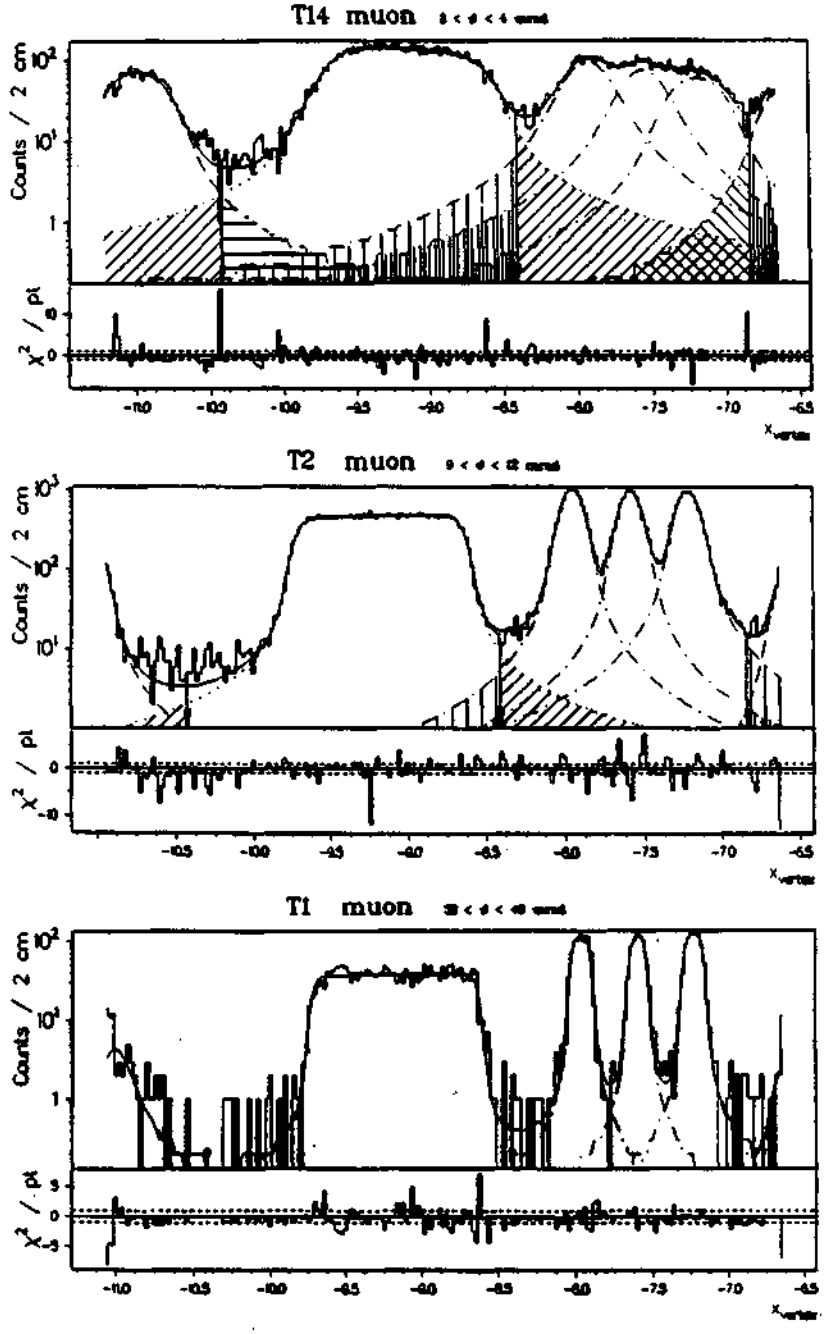

Figure 4.22: Fit of the upstream part of the vertex distribution by the LOGAUBOX function in three bins – a low–θ, low resolution T14 bin (up), an average resolution T2 bin (middle) and a high resolution T1 bin (down). The hatched areas represent the tails of wrongly attributed events (logarithmic scale). Jura target row.

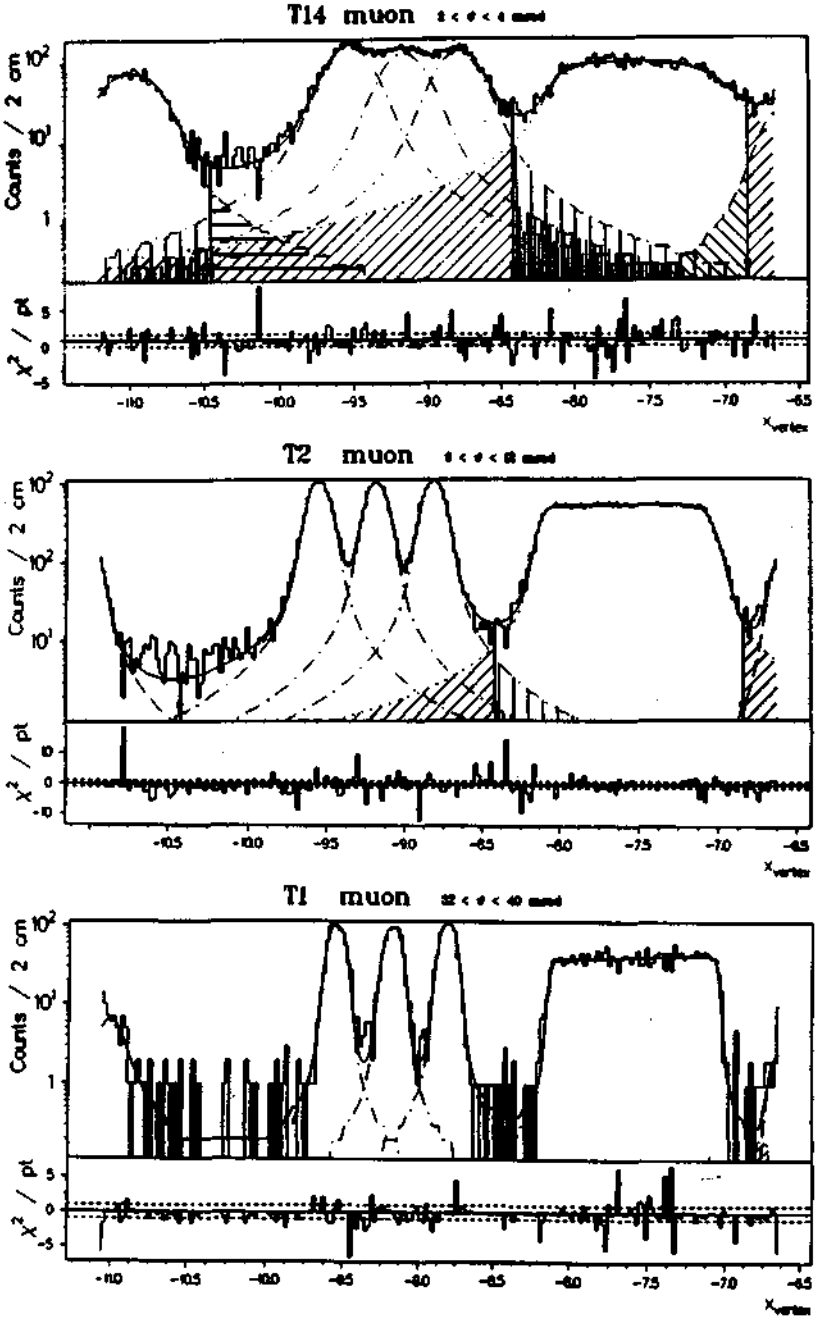

Figure 4.23: Same as 4.22 for the Saleve target row

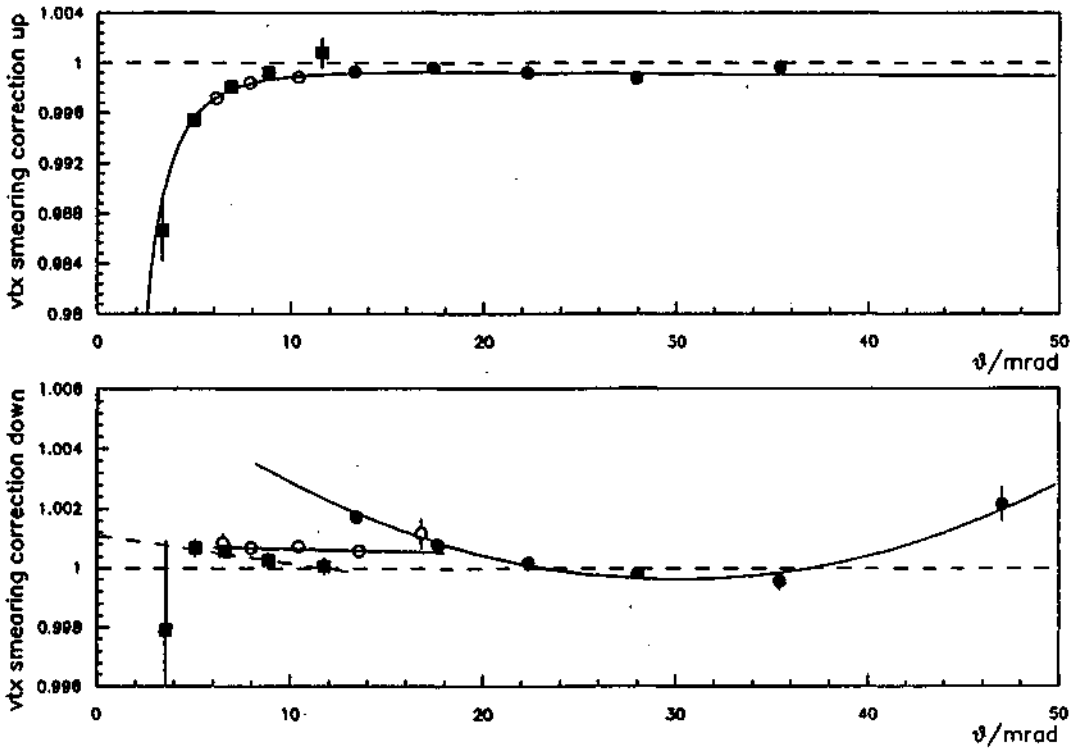

Figure 4.24: The vertex correction factor in θ bins. Full boxes correspond to T14 fits, open circles are T2, and full circles T1. The upstream target pair shows a smooth behaviour with the scattering angle and is fitted independently of trigger by the function shown. The downstream correction is fitted differently for each trigger, but is much smaller in general, never exceeding 0.2%

representation of tbe complex error function [73] was found to give tbe best fit of the vertex distributions observed in our experiment, after simpler functions involving only a Gaussian or only a Lorentzian have failed.

In principle it was shown that with such a function it is possible to fit the whole distribution, including the vertices from P0H all the way to tbe most downstream target. However, due to the cut on events having a vertex downstream and baving used P0B for tbe scattered muon (see above), our vertex distribution has an artificial step at the x coordinate where this cut is applied. This step is impossible to fit witb the LOGAUBOX fit.

But since we bave independent experiments going on upstream and downstream - Li/D upstream and C/D downstream, we can fit separately tbe upstream and tbe downstream part. This procedure is shown for three representative theta bins: tbe one with the worst resolution (2-4 mrad in T14), a "typical" one (9-12 mrad in T2) and tbe best resolution bin (32-40 mrad in T1) in figs 4.22 and 4.23.

In order to get reliable fits and resulting corrections, some constraints are applied. Firstly, vertex distributions on Jura and Saleve rows are fitted in tbe same time, constraining widtbs of the Lorentzian and Gaussian tails to be the same for both target rows, at the same acceptance position. The resolution only depends on tbe acceptance position, not on the target row. So for example the width of the lithium upstream tails (of botb tbe Lorentzian and the Gaussian) in the Salève row is constrained to be the same as tbe width of the upstream deuterium tails in the Jura row. Tbe three lithium slabs are also constrained to have the same tail widths, and also the widtbs boxes are constrained to the same value. Furthermore, the distance between the lithium slabs is fixed, only globally can their position change. In this way we end up fitting simultaneously two vertex distributions containing over 260 points eacb with a function of only 28 parameters! Once tbe fit is found satisfactory, the tails are integrated and compared. The correction factor for each target material is computed as:

$$\kappa_v^{mat} = \frac{\int_{-\infty}^{+\infty} dx f_{mat}(x)}{\int_{x_{low}}^{x_{high}} dx f_{mat}(x) + \int_{-\infty}^{x_{low}} dx f_{other}(x) + \int_{x_{high}}^{+\infty} dx f_{other}(x)} \tag{4.31}$$

where $f_{mat}(x)$ represents the function fitting the material observed; $f_{other}(x)$ is the sum of the functions representing the otber materials (especially tbe first neighbours upstream and downstream); x_{low} and x_{high} represent the vertex cuts applied to mat. Less formally, but maybe more understandably this can be written as:

$$\begin{aligned} \kappa_v^{mat} &= \frac{\text{true}}{\text{accounted for}} \\ &= \frac{\text{bulk}^{mat} + \text{tails}^{mat}}{\text{bulk}^{mat} + \text{tails}^{other}} \\ &\approx 1 + \frac{\text{tails}^{mat} - \text{tails}^{other}}{\text{bulk}^{mat}}, \end{aligned}$$

where the numerator has been split into "bulk", the integral between tbe cuts, and "tails", the integrals from $-\infty$ to x_{low} and from x_{high} to $+\infty$. The approximation is valid for tails small compared to the bulk. It is now evident that only an asymmetry of the tails contributes to the correction factor. In addition, the correction factor to the ratio shall be:

$$\kappa_v(\mathcal{R}^A) = \frac{\kappa_v^{A_{up}} \kappa_v^{A_{dn}}}{\kappa_v^{D_{up}} \kappa_v^{D_{dn}}}. \tag{4.32}$$

In other words, we have to correct for the residuum of residua. This is due to the virtues of the ratio method: all effects (almost) cancel.

The resulting correction factors are generally speaking small (fig. 4.24). A function can be fitted through the points obtained at different angles. For the upstream targets the correction rises steeply with falling angle, so a parametrization in $1/\theta$ was chosen, which fits points from all three triggers nicely. The errors shown contain systematical errors. The statistical errors are given by the fitting program. The systematic errors are evaluated by fitting the same θ bin 3-5 times, slightly varying constraints. For instance, one can couple the width of POB to the widths of the downstream lithium targets, or not etc. For the downstream setup, the corrections are smaller, as expected, because they are closer to the spectrometer and thus the scattered muon undergoes less multiple Coulomb scattering. Also the lever-arm is smaller for the translation of θ-smearing into x-smearing. A separate parametrization was chosen for each trigger.

4.3.3 Kinematic smearing corrections

Another effect of finite resolution is linked to kinematics. From the measured momenta and scattering angle we compute a certain x_{Bj} and Q^2 of the interaction. In the average, they correspond to the average of the true kinematics (that is the reason to have done so much alignment, calibration and tuning!). However, they are *smeared* around the true value. The cross section not being constant, this smearing can contribute to an error on the determination of our cross section ratio. Even if the tails are symmetric, they may contribute differently to the total measured cross section.

Again there are two possible approaches: long chain MonteCarlo, if properly tuned, gives the most reliable answer. However this requires a detailed study of efficiencies of detectors and endless checks. It is a job on a year's time scale (for each trigger!), and this time was not available.

Another possible approach is used here. Knowing approximately the resolutions of the apparatus from earlier MonteCarlo studies [74, 75], we may compute the correction by simple numerical integration as follows:

$$\sigma^{mat}_{meas}(E',\theta) = \frac{\int_{E'_{min}}^{E'_{max}}\int_{\theta_{min}}^{\theta_{max}} \mathrm{d}E'\mathrm{d}\theta\,\sigma^{mat}_{true}(E',\theta)\frac{1}{\sqrt{2\pi}\sigma_{E'}}e^{-\frac{(E'-E'_0)^2}{2\sigma^2_{E'}}}\frac{1}{\sqrt{2\pi}\sigma_\theta}e^{-\frac{(\theta-\theta_0)^2}{2\sigma^2_\theta}}}{\int_{E'_{min}}^{E'_{max}}\int_{\theta_{min}}^{\theta_{max}} \mathrm{d}E'\mathrm{d}\theta\frac{1}{\sqrt{2\pi}\sigma_{E'}}e^{-\frac{(E'-E'_0)^2}{2\sigma^2_{E'}}}\frac{1}{\sqrt{2\pi}\sigma_\theta}e^{-\frac{(\theta-\theta_0)^2}{2\sigma^2_\theta}}}, \quad (4.33)$$

where the numerator represents a convolution of the true cross section σ^{mat}_{true} with Gaussian resolution functions in the scattered muon energy, E' and the scattering angle, θ. The denominator is just for normalization, if the limits were set to $\pm\infty$ it would he exactly 1. In practice, the limits applied to E' and θ are the central value plus or minus four standard deviations, but with absolute limits set by the physical kinematic region: 3 GeV (the minimal energy for the muon to pass through the FSM) and 200 GeV (the beam energy) for E' and for θ a minimum value of one tenth of the kinematic cut value:

$$\begin{aligned} E'_{min} &= \max\left(E'_0 - 4\sigma_{E'}, 3\mathrm{GeV}\right) \\ E'_{max} &= \min\left(E'_0 + 4\sigma_{E'}, 200\mathrm{GeV}\right) \end{aligned}$$

$$\theta_{min} = max(\theta - 4\sigma_\theta, \theta - cut/10)$$
$$\theta_{max} = \theta + 4\sigma_\theta$$

The calculation was done in the kinematic region covered by each trigger, at the center of each x_{Bj} and Q^2 bin. Only in some bins close to the kinematic cuts is the denominator smaller than 0.999, and only in one bin for T1 does it show a value less than 0.995 (it goes down to 0.97 in this one bin). This means that we are integrating over a region sufficient to describe at least 99.5 % of the effects, often more than 99.9%.

Parametrizations were used for the resolutions in E' and θ as follows:

$$\begin{aligned}
\frac{\sigma_{E'}}{E'} &= (0.53 + 0.0052E')\% \quad \text{for trigger 1} \\
&= (0.46 + 0.0070E')\% \quad \text{for trigger 2} \\
&= (0.395 + 0.0038E')\% \quad \text{for trigger 14 upstream} \\
&= (0.43 + 0.00815E')\% \quad \text{for trigger 14 downstream}
\end{aligned} \tag{4.34}$$

$$\begin{aligned}
\sigma_\theta &= \sqrt{\left(\frac{\partial\theta}{\partial Q^2}\sigma_{Q^2}\right)^2 + (\Delta\theta_{MCS})^2} \quad \text{for triggers 1 and 2} \\
\frac{\sigma_{Q^2}}{Q^2} &= (0.349 + \frac{1.7}{\log_{10}Q^2})\% \quad \text{for trigger 1} \\
&= (2.69 + \frac{0.477}{\log_{10}Q^2})\% \quad \text{for trigger 2}
\end{aligned} \tag{4.35}$$

$$\begin{aligned}
\sigma_\theta &= \sqrt{(\sigma_\theta^{res})^2 + (\Delta\theta_{MCS})^2} \quad \text{for trigger 14} \\
\sigma_\theta^{res} &= 0.150\text{mrad} \quad \text{upstream} \\
\sigma_\theta^{res} &= 0.114\text{mrad} \quad \text{downstream}
\end{aligned} \tag{4.36}$$

The correction to the ratio is calculated analogously as for vertex smearing (eq. 4.32), and the results are shown in fig. 4.3.3. The correction is seen to be small – over the greatest part of the x_{Bj} and Q^2 range it is less than 0.01 %. Where is it large? Remember we are again looking at residua of residua – we have to ask ourselves: what is different that won't cancel in the ratio? One thing is the cross section (the effect we are measuring!), another is multiple Coulomb scattering (especially for the downstream target, for the deuterium target corresponds to .145 radiation lengths, whereas the carbon one corresponds to .439; the effect on upstream targets is diluted by the scattering in both downstream targets experienced by all scattered muons). The largest corrections are present where the resolution is poorest – for T14 they are most pronounced in the low Q^2 bins of each x_{Bj} bin – more so for carbon than for lithium, because of the above mentioned effect of multiple Coulomb scattering. The effect is largest at low Q^2 of each x_{Bj} bin because this corresponds to the lowest angles where the multiple Coulomb scattering relatively has the greatest influence. That the correction depends on the F_2 ratio is also nicely visible from fig. 4.3.3 – if one follows the correction from low to high x_{Bj}, one sees at first a dip in the shadowing region, then an enhancement in the antishadowing region, and finally a strong dip at very high $x_{Bj} = 0.7$ where the EMC effect is largest.

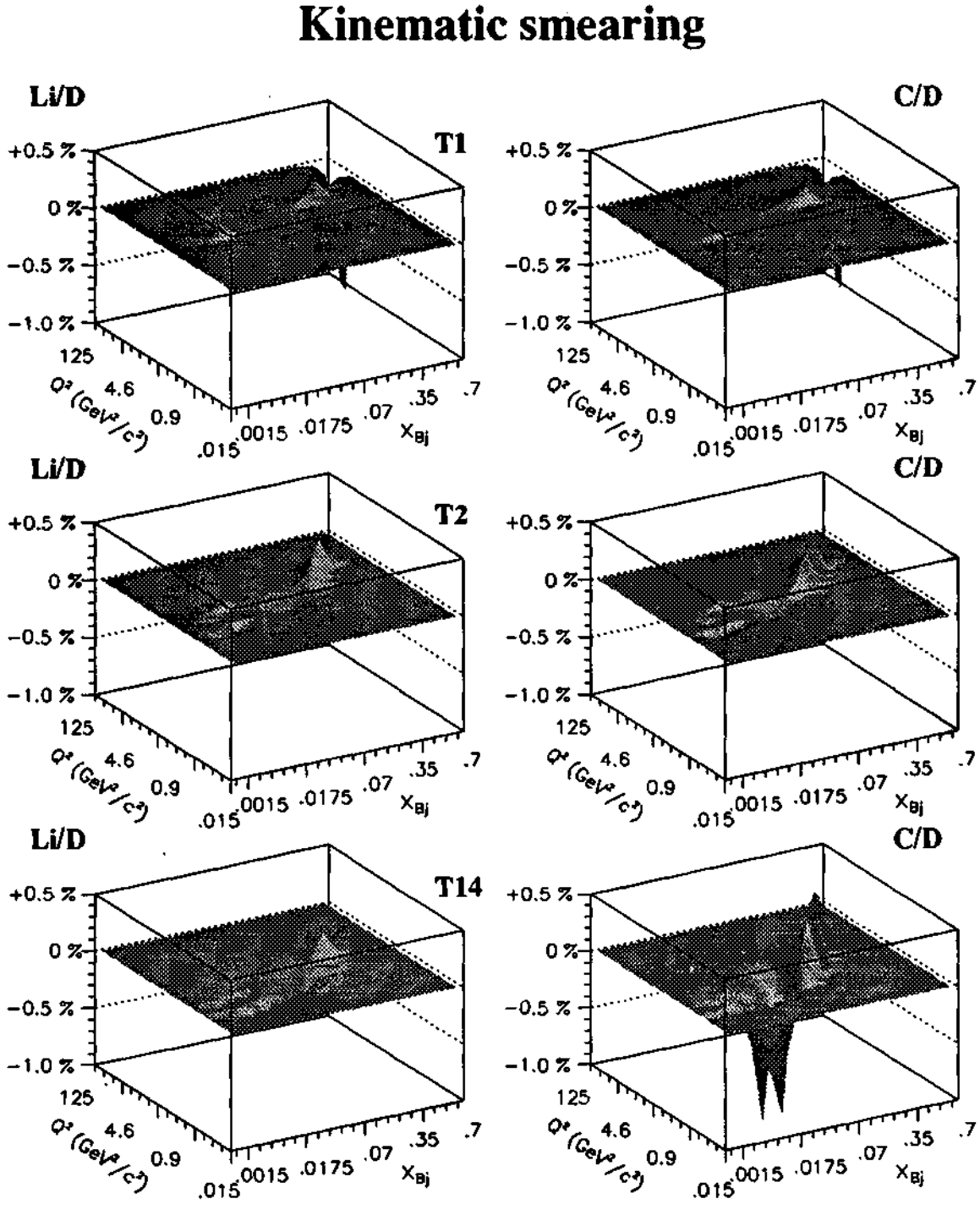

Figure 4.25: The kinematic smearing factor as calculated in the x_{Bj}, Q^2 plane. It is plotted only in the bins not cut away by kinematic cuts, in the other bins it is set to zero.

4.3.4 Non-isoscalarity correction

We wish to measure the structure function ratio for *isoscalar* nuclei, that is, we wish to separate the effect of nuclear medium on F_2 (which is the subject of this work) from the difference between the structure functions of the proton and neutron (which isn't). The nuclei we use are nearly isoscalar: the lithium is 95.5% enriched ^{6}Li, and the natural isotopic mixture of carbon consists of 98.89% ^{12}C, and deuterium is the reference, isoscalar by definition. However, a contamination of HD molecules of $3.01 \pm 0.24\%$ [9] was present in the target, making also deuterium non-isoscalar. The cross section for a mixture (A) of an isoscalar (IS) and non-isoscalar (NI) isotope can be written as:

$$F_2^A(x_{Bj},Q^2) = (1 - f_{NI})F_2^{IS}(x_{Bj},Q^2) + f_{NI}F_2^{NI}(x_{Bj},Q^2), \tag{4.37}$$

where f_{NI} represents the fraction of nucleons in non-isoscalar nuclei in the sample,[10] and the structure functions are per nucleon, as usual. Further we have:

$$F_2^{IS}(x_{Bj},Q^2) = F_2^D(x_{Bj},Q^2)\mathcal{R}^A \tag{4.38}$$

$$F_2^{NI}(x_{Bj},Q^2) = \frac{1}{A}(ZF_2^p(x_{Bj},Q^2) + (A_{NI} - Z)F_2^n(x_{Bj},Q^2))\mathcal{R}^A \tag{4.39}$$

and from the hypothesis of no nuclear effects in deuterium we may write:

$$F_2^D(x_{Bj},Q^2) = \frac{1}{2}\left(F_2^n(x_{Bj},Q^2) + F_2^p(x_{Bj},Q^2)\right) \tag{4.40}$$

$$\Longrightarrow F_2^n(x_{Bj},Q^2) = \frac{2F_2^D(x_{Bj},Q^2)\mathcal{R}^{\frac{n}{p}}(x_{Bj},Q^2)}{1 + \mathcal{R}^{\frac{n}{p}}(x_{Bj},Q^2)} \tag{4.41}$$

$$\text{and} F_2^p(x_{Bj},Q^2) = \frac{2F_2^D(x_{Bj},Q^2)}{1 + \mathcal{R}^{\frac{n}{p}}(x_{Bj},Q^2)} \tag{4.42}$$

which lets us express the mixed structure function we measure with the isoscalar one:

$$F_2^A = \frac{-f_{NI} + 2f_{NI}Z/A_{NI} + (1 + f_{NI} - 2f_{NI}Z/A_{NI})\mathcal{R}^{\frac{n}{p}}(x_{Bj},Q^2)}{1 + \mathcal{R}^{\frac{n}{p}}(x_{Bj},Q^2)F_2^{IS}(x_{Bj},Q^2)} \tag{4.43}$$

giving for the correction factor we must apply to the measured structure function:

$$\kappa_{NI}(x_{Bj},Q^2) = \frac{1 + \mathcal{R}^{\frac{n}{p}}(x_{Bj},Q^2)F_2^{IS}(x_{Bj},Q^2)}{1 - f_{NI} + 2f_{NI}Z/A_{NI} + (1 + f_{NI} - 2f_{NI}Z/A_{NI})\mathcal{R}^{\frac{n}{p}}(x_{Bj},Q^2)} \tag{4.44}$$

$$\approx 1 + f_{NI}(1 - 2Z/A_{NI})\frac{1 - \mathcal{R}^{\frac{n}{p}}(x_{Bj},Q^2)}{1 + \mathcal{R}^{\frac{n}{p}}(x_{Bj},Q^2)} \text{ when } f_{NI}(1 - 2Z/A_{NI}) << 1$$

and the ratio $\mathcal{R}^{\frac{n}{p}} = F_2^n/F_2^p$ is borrowed from our NMC colleagues analyzing the hydrogen/deuterium data.

This correction is typically less than 0.1 % up to $x_{Bj} = 0.15$ where the ratio $\mathcal{R}^{\frac{n}{p}}$ is between 0.8 and 1, and may go up to 0.4negative for the D_2/HD mixture. For carbon it was not applied, since it was estimated to be less than 0.05% over the whole range.

[9] translating into 1.5% atoms or 0.75% nucleons

[10] roughly corresponding to the mass fraction, if one neglects the difference in mass defect between isotopes

Chapter 5

Nuclear effects on F_2 in Li and C: results and discussion.

Our primary goal is the extraction of the x_{Bj} dependence of the ratios F_2^{Li}/F_2^D and F_2^C/F_2^D, and its comparison to existing theoretical predictions. In virtue of eq. 4.8., we shall assume no Q^2 dependence in this stage, and apply the ratio method in x_{Bj} bins. In a second stage, we may compute the ratio in x_{Bj}, Q^2 bins and investigate the $\log Q^2$ dependence in each x_{Bj} bin. Finally, an attempt shall be made to compute the integral:

$$\int (F_2^A - F_2^D) dx_{Bj},$$

which may give us some information on the possible change in the momentum fraction carried by quarks in the bound nucleon vs. that in a deuteron. If the integral is negative, it would mean that the quarks carry less momentum in the nucleus, and if it is positive, this would mean they carry more momentum in the nuclear medium with respect to the deuteron.

5.1 x_{Bj} dependence of the ratios F_2^{Li}/F_2^D and F_2^C/F_2^D

The ratios obtained with the standard method are shown in fig. 5.1. for the three triggers separately. They are seen to be in fair agreement with each other, except perhaps the T1 point of F_2^C/F_2^D at $x_{Bj} = 0.0055$ which seems a bit low compared with the two other triggers. However, the next point in T1 is higher than T2 and T14, so it may just be a statistical fluctuation. The total statistics in this bin is dominated by T2 and T14 anyway, so we decide to leave this bin in.

The results from the three triggers are now merged. An arithmetic weighted mean (the weight being taken as $1/(\text{stat. error})^2$) is used to compute the mean x_{Bj} and Q^2, and a bin centering correction is applied to the ratios from individual triggers. The bin centers of the same bin from different triggers are slightly different, so we apply a correction to the ratio to take this into account. Using a fitted function, we can compute the correction needed to bring the actual ratios calculated in their respective x_{Bj} bin centers to the newly determined x_{Bj} average. These bin-centering corrections are less than 0.5% in all the data points, and rarely exceed 0.2%. An arithmetic weighted mean is then taken of the thus corrected ratios.

The merged ratios are shown in fig. 5.2, together with the ratios extracted by the hadron method. In general the agreement between the two methods is seen to be fair within the

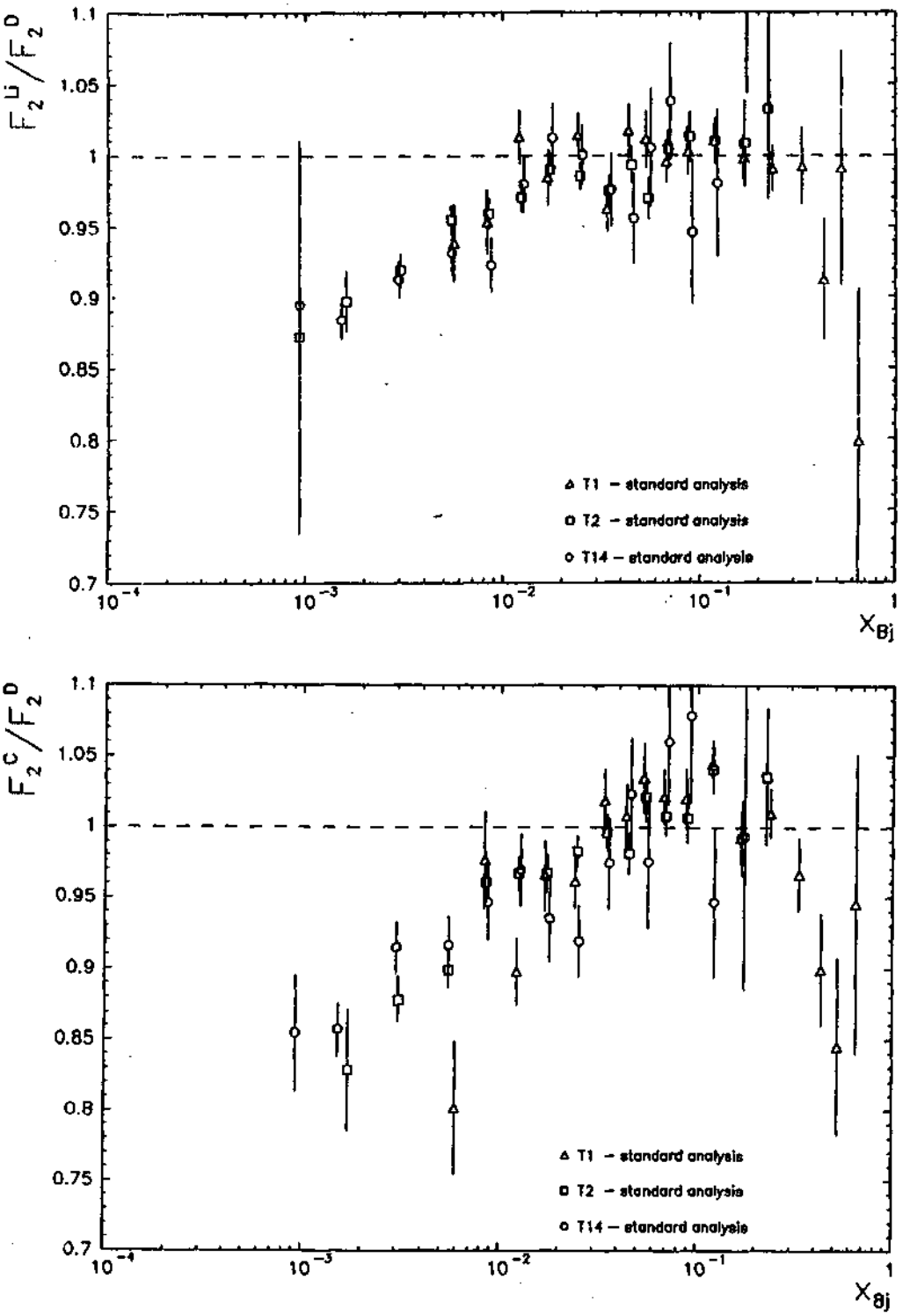

Figure 5.1: x_{Bj}-dependence of the ratios F_2^{Li}/F_2^D and F_2^C/F_2^D obtained by the standard method for all three triggers. The errors shown are statistical only.

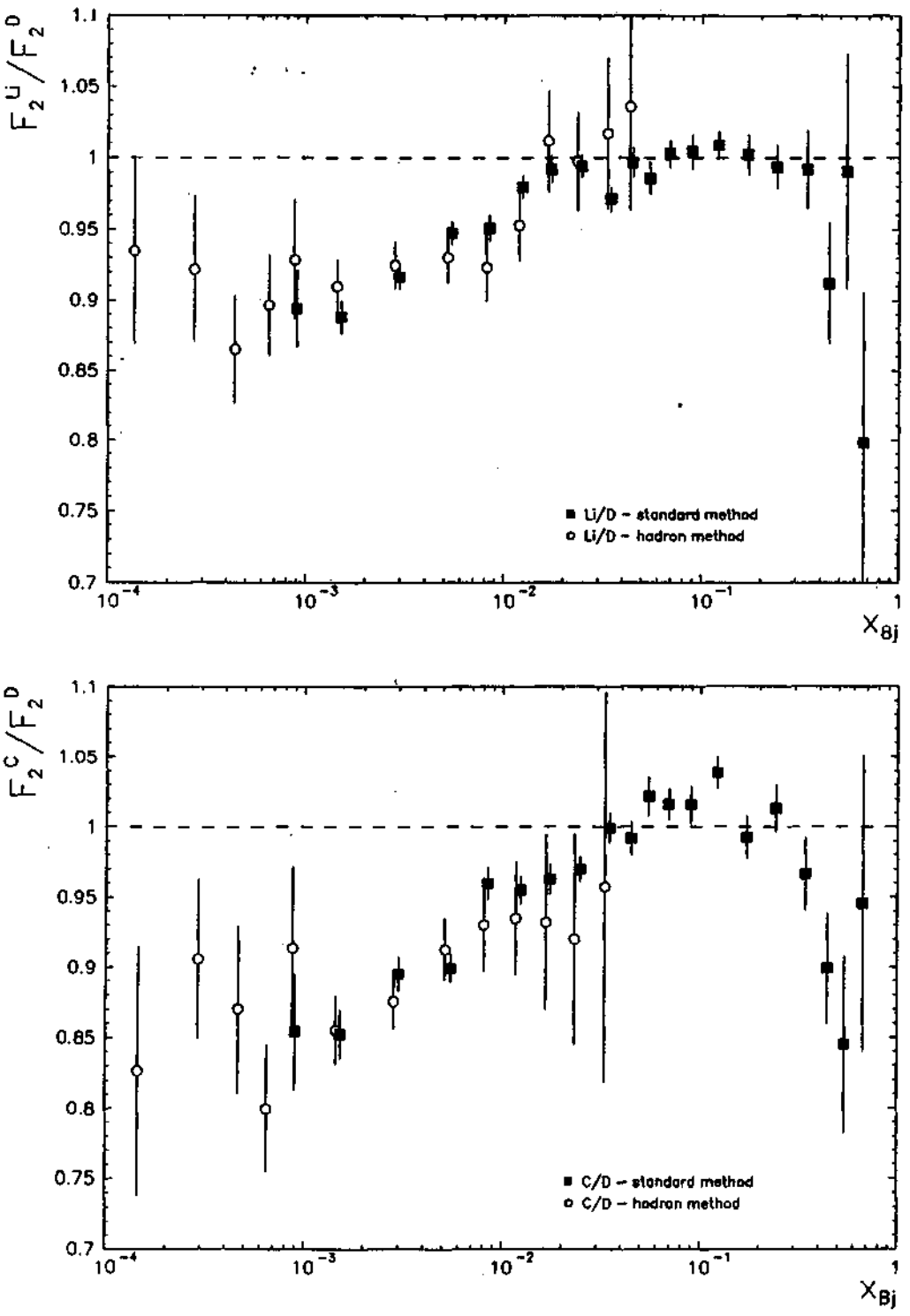

Figure 5.2: The merged data from all three triggers (full hoxes) compared to the ratios obtained with the hadron method on T14 data (open points). F_2^{Li}/F_2^D (up) and F_2^C/F_2^D (down). The errors shown are statistical only.

large statistical errors of the hadron method. It may be argued that the last 5 bins of the hadron method ratio F_2^C/F_2^D are all lower than that obtained by the standard method, but then the T14 standard method points are also lower in these bins in fig 5.1, so it is not the hadron method which is biasing the sample.

The agreement between the two methods confirms – within the error bars – that our calculation of the (very large) radiative corrections for the standard method (cf. sec 4.3.1) is correct. Remember the corrections to the ratio in the standard method may reach 30 % whereas for the hadron method they never exceed 1%, so we may assume they are almost independent of the radiative corrections applied.

Once this agreement is established, we shall in the following use the hadron method only for the lowest four x_{Bj} bins where the standard method is inoperative, preferring the standard method points at $x_{Bj} > 0.0008$ because of their better statistical accuracy.

5.1.1 Systematic errors

The dominant contribution to the systematic error in the standard method is the error on the radiative corrections. As we have mentioned several times, their influence on the final result is large, the uncorrected ratio would not show any shadowing; on the contrary it would be enhanced (greater than 1) at very low x_{Bj}, the coherent scattering on a heavier nucleus being much more important than on the deuteron.

In this respect there is an established procedure in the NM collaboration to calculate the systematic errors. Not all the details shall be exposed here; the interested reader is referred to [56] for more details.

The essence of the estimation of systematic errors is to vary the input parameters for the calculation of radiative corrections, within the limits of current knowledge:

- F_2^D is varied $\pm 5\%$ with respect to the best existing fit to the data, in the measured region. This corresponds to roughly twice the absolute normalization error from the NMC measurement of F_2

- In the unmeasured region, the extrapolation to $x_{Bj} = 0$ and $Q^2 = 0$ is done in three different ways: the standard extrapolation used for the central values stems from a combined generalized vector meson dominance and partonic model by Badelek and Kwieciński [87], another extrapolation is based on the Regge parametrization by Donnachie and Landshoff [88] including terms due to Pomeron and vector meson exchange. A third extrapolation stems from a phenomenological fit to world data on F_2^D [89], including a fit to the resonance region. In this latter fit F_2 is suppressed at low Q^2 by a term depending on the electromagnetic form factor of the nucleon (because elastic scattering on the nucleon dominates there [89]); it is also the only one containing a contribution from the nucleon resonances. The two latter extrapolations are used for the evaluation of systematic errors.

- The ratio of longitudinal to transverse polarized virtual photon cross sections, R used as input to the radiative corrections program is that of the SLAC parametrization [5] down to $Q^2 = 0.35$ GeV$^2/c^2$, with its upper and lower limits from the same reference used for the evaluation of the systematic error. Below this value of Q^2, the value of R at $Q^2 = 0.35$ GeV$^2/c^2$ is used, with a 100% error taken for the evaluation of systematics.

- The proton form factor is needed for the quasielastic tail calculation. It is well known and the variation between the parametrization by Gari and Krümpelmann [91] and the one by Atwood [92] gives a very small contribution to the overall systematic error.

- The suppression factor measuring the suppression of quasielastic scattering in nuclear environment:

  - For the deuteron the central value is calculated using the parametrization by Bernabeu [97], the alternative being the Arenbövel [95] parametrization.
  - For lithium a relativistic Fermi gas model [96] was used. No alternative suppression factors were found in the literature.
  - For carbon the same model was used as an alternative to the Bernabeu model.

- The nuclear form factor is needed for coherent scattering on the nucleus.

  - Two parametrizations are again used to estimate the systematic uncertainty for deuterium: the Locher-Švarc [93] one for the central value and the one by Stein [94] for the variation.
  - For lithium again only one form factor is found in the literature, the one by Li et al. [98]
  - For carbon two approaches are available: one as a sum of Gaussians [99], and a two-parameter Fermi gas model [100]

The contribution of the variation of the functional form of the F_2 low x_{Bj}, low Q^2 extrapolation, is given separately in tables 5.1 and 5.2 in the column labelled "RC2". All other contributions are added up (some of them in a fully correlated way) and listed in the column "RC1".

Other contributions to the systematic error in the standard method:

- The uncertainty on the measured momenta of the incoming and scattered muon. In particular we are sensitive to a relative error between the two measurements. The scattered muon momentum was varied inside their errors quoted in [47], about 0.2%. The effect was computed analytically, starting from the fit to the ratio. Applying the momentum shift to individual bins gives large bin-to-bin fluctuations impossible to interpret (only a few events change bins). The influence on the ratio is shown in the column "momentum" in tables 5.1 and 5.2 where larger than 0.05%.

- The kinematic smearing correction is attributed a 100% error on its size; the influence on the ratio is reported in column "ksm" of tables 5.1 and 5.2.

- The mean vertex smearing correction was varied inside limits permitted by different fits performed (see sec. 4.3.2); the influence on the ratio is reported in column "vtx".

Systematic errors on the hadron method are less sensitive to the radiative corrections (as the corrections themselves are small). The error on the radiative corrections is determined in the same way as for the standard method.

The dominant contribution to the systematic error on the hadron method comes from the uncertainty on the secondary interactions of the hadrons in the target as discussed in 4.2.2. The largest changes of the ratio observed by applying the different weighting methods

$< x_{Bj} >$	$< Q^2 >$	Li/D	stat	syst	RC 1	RC 2	had. reint	ksm	μ–e
$1.4 \cdot 10^{-4}$	0.034	0.935	0.066	0.020		0.003	0.016	0.011	
$2.8 \cdot 10^{-4}$	0.066	0.922	0.051	0.030		0.003	0.026	0.013	
$4.5 \cdot 10^{-4}$	0.11	0.865	0.038	0.021		0.003	0.018	0.006	0.008
$6.7 \cdot 10^{-4}$	0.15	0.897	0.036	0.015		0.003	0.013	0.004	0.006
							momentum		vtx
$9.0 \cdot 10^{-4}$	0.21	0.894	0.027	0.020	0.011	0.016		0.002	0.002
$1.5 \cdot 10^{-3}$	0.34	0.888	0.012	0.021	0.013	0.016		0.001	0.001
$3.0 \cdot 10^{-3}$	0.61	0.917	0.009	0.009	0.008	0.005			0.001
$5.5 \cdot 10^{-3}$	1.0	0.947	0.008	0.006	0.006	0.002			
$8.5 \cdot 10^{-3}$	1.4	0.951	0.009	0.004	0.003	0.002			
$1.2 \cdot 10^{-2}$	1.8	0.980	0.008	0.003	0.002	0.002			
$1.7 \cdot 10^{-2}$	2.3	0.992	0.009	0.002	0.002	0.001			
$2.5 \cdot 10^{-2}$	2.8	0.994	0.007	0.001	0.001	0.001			
$3.5 \cdot 10^{-2}$	3.6	0.971	0.008	0.000					
$4.5 \cdot 10^{-2}$	4.2	0.997	0.010	0.000					
$5.5 \cdot 10^{-2}$	4.8	0.986	0.011	0.000					
$6.9 \cdot 10^{-2}$	6.0	1.003	0.010	0.000					
$8.9 \cdot 10^{-2}$	7.2	1.004	0.012	0.000					
0.12	9.2	1.009	0.010	0.000					
0.17	12.	1.002	0.014	0.001				0.001	
0.24	17.	0.994	0.015	0.001				0.001	
0.34	23.	0.992	0.027	0.001			0.001	0.001	
0.44	29.	0.912	0.043	0.001			0.001	0.001	
0.54	33.	0.990	0.082	0.003			0.001	0.003	
0.66	39.	0.798	0.108	0.013			0.001	0.013	
Additional overall normalization error: 0.004 (not included above)									

Table 5.1: The ratio F_2^{Li}/F_2^D in x_{Bj}-bins. The mean x_{Bj} and Q^2 for each bin are followed by the ratio with its statistical and systematic error. A breakup of individual systematic error contributions is given in the right hand part of the table, for contributions exceeding 0.0005. The normalization error is quoted separately at the bottom. The intrinsic error of the ratio method following eq. 4.8 is not evaluated.

$< x_{Bj} >$	$< Q^2 >$	C/D	stat	syst	RC 1	RC 2	bad.reint	ksm	μ–e
$1.5 \cdot 10^{-4}$	0.035	0.826	0.088	0.033		0.005	0.031	0.010	
$3.0 \cdot 10^{-4}$	0.072	0.906	0.057	0.027		0.005	0.025	0.009	
$4.8 \cdot 10^{-4}$	0.11	0.870	0.060	0.026		0.005	0.024	0.005	0.008
$6.7 \cdot 10^{-4}$	0.16	0.799	0.045	0.024		0.005	0.020	0.003	0.012
							momentum		
$9.0 \cdot 10^{-4}$	0.22	0.854	0.041	0.034	0.017	0.029		0.002	
$1.5 \cdot 10^{-3}$	0.36	0.852	0.018	0.033	0.020	0.026		0.001	
$3.0 \cdot 10^{-3}$	0.68	0.895	0.012	0.016	0.013	0.010			
$5.5 \cdot 10^{-3}$	1.1	0.899	0.010	0.009	0.008	0.004			
$8.5 \cdot 10^{-3}$	1.6	0.959	0.011	0.006	0.005	0.004			
$1.2 \cdot 10^{-3}$	2.1	0.955	0.010	0.004	0.004	0.002			
$1.7 \cdot 10^{-2}$	2.6	0.962	0.011	0.004	0.003	0.002			
$2.4 \cdot 10^{-2}$	3.3	0.970	0.009	0.003	0.002	0.002			
$3.5 \cdot 10^{-2}$	4.0	0.999	0.011	0.001	0.001	0.001			
$4.5 \cdot 10^{-2}$	4.7	0.992	0.012	0.000					
$5.5 \cdot 10^{-2}$	5.5	1.021	0.013	0.000					
$6.9 \cdot 10^{-2}$	6.5	1.016	0.011	0.000					
$8.9 \cdot 10^{-2}$	8.0	1.015	0.013	0.001				0.001	
0.12	10.	1.038	0.011	0.001				0.001	
0.17	14.	0.993	0.015	0.001				0.001	
0.24	20.	1.013	0.016	0.001				0.001	
0.34	27.	0.966	0.026	0.001			0.001	0.001	
0.44	32.	0.899	0.039	0.001			0.001	0.001	
0.54	36.	0.845	0.062	0.003			0.001	0.003	
0.67	40.	0.945	0.105	0.010			0.001	0.010	
Additional overall normalization error: 0.003 (not included above)									

Table 5.2: The ratio F_2^C/F_2^D in x_{Bj}-bins. The mean x_{Bj} and Q^2 for each bin are followed by tbe ratio with its statistical and systematic error. A breakup of individual systematic error contributions is given in the right hand part of the table, for contributions exceeding 0.0005. The normalization error is quoted separately at the bottom. The intrinsic error of the ratio method following eq. 4.8 is not evaluated.

were taken as systematic errors, and are reported in column "had. reint" of tables 5.1 and 5.2.

An additional error was attributed due to an estimated 6% residual contamination by $\mu-$e events of bins 3 and 4, and is reported in column $\mu-$e of tables 5.1 and 5.2.

Kinematic smearing is again assigned a 100% error. Vertex smearing is assumed to be negligible, because we are using type 3 vertices in the hadron method (the vertex is found as a crossing point of three, not two lines). The vertex distributions are thus much more sharply defined for the same scattering angle[1]. The greatly reduced statistics of the low-x_{Bj} hadron method data anyway doesn't permit meaningful fitting. The momentum contribution is negligible and therefore not listed.

The overall normalization error is computed from different contributions on the uncertainty on the number of nucleons in the targets. The F_2^{Li}/F_2^D normalization is dominated by the uncertainty on the position of the holes in the lithium targets, and hence the correction applied in sec. 2.3.1., whereas the F_2^C/F_2^D is dominated by the deuterium density uncertainty, including our ignorance of which one of E- or N- deuterium phases we had, the uncertainties on the measured pressure, the discrepancies between different temperature-density tables, etc. The normalization errors amount to 0.004 and 0.003 respectively for F_2^{Li}/F_2^D and F_2^C/F_2^D.

Unfortunately time has lacked for a numerical application of formula 4.8 to estimate the systematic effects inherent to the usage of the ratio method in finite x_{Bj} bins - for this a functional form of the acceptance would have to be obtained from existing Monte Carlo studies, for all three triggers.

5.1.2 Comparison to other data sets

We are now able to compare our results to other measurements of same or similar structure function ratios.

The comparison with earlier NMC measurements of the same ratios is shown in fig. 5.3. The F_2^{Li}/F_2^D of the present data set is compared to a recent reanalysis [101] of earlier published data [102]. The result previously obtained for F_2^{Li}/F_2^D is a combined indirect result:

$$\frac{F_2^{Li}}{F_2^D} = \left(\frac{F_2^{Li}}{F_2^C}\right)_{90GeV} \cdot \left(\frac{F_2^C}{F_2^D}\right)_{200GeV}, \text{ and}$$

$$\frac{F_2^{Li}}{F_2^D} = \left(\frac{F_2^{Li}}{F_2^{Ca}}\right)_{90GeV} \cdot \left(\frac{F_2^{Ca}}{F_2^D}\right)_{200GeV},$$

and reaches only down to $x_{Bj} = 0.0085$. The present data show good agreement with the previous data set in the overlap region and extend the kinematic region by nearly two orders of magnitude towards lower x_{Bj}. There is a very slight indication of antishadowing (enhancement) for $0.06 < x_{Bj} < 0.17$, the data still being compatible with no antisbadowing at all. Below $x_{Bj} = 0.06$, the shadowing region begins and shows an indication of saturation below $x_{Bj} = 0.002$ at a value of:

$$0.890 \pm 0.010(stat.) \pm 0.021(syst.).$$

[1] with respect to the standard method

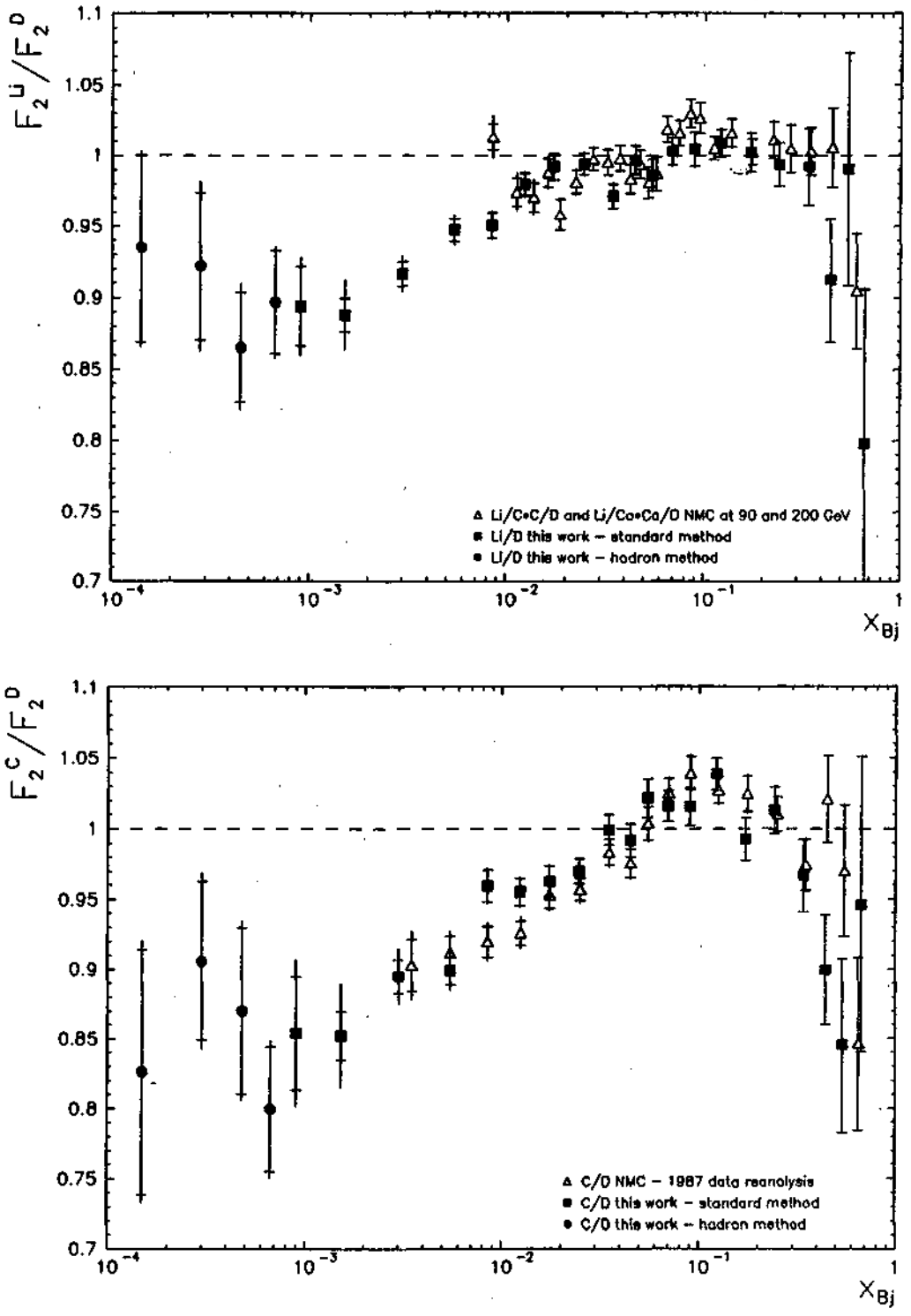

Figure 5.3: The present data sets compared to earlier NMC measurements. Above: the present result for F_2^{Li}/F_2^D compared to the recent reanalysis of an earlier *indirect* result obtained by multiplying ratios F_2^{Li}/F_2^C and F_2^{Li}/F_2^{Ca} at a beam energy of 90 GeV with F_2^C/F_2^D resp. F_2^{Ca}/F_2^D at a beam energy of 200 GeV. Below: the present F_2^C/F_2^D compared to a reanalysis of the previous measurement of the same ratio at the same beam energy. The inner error bars represent the statistical errors, the outer ones are statistical and systematic errors added in quadrature.

This value is obtained as a weighted average of the first six x_{Bj} bins (weights being taken as $1/(\text{stat. error})^2$), and taking the average systematic error of the bins for the systematic error.

Whereas the significance of both data sets in the high $0.2 < x_{Bj} < 0.6$ region is quite poor, one would be tempted to note the absence of a significant dip of the ratio in this region, also known as the the EMC effect region. This observation, in conjunction with the very small size of the antishadowing would favour the explanation of the EMC effect based on overlapping nucleons as discussed in 1.2.2. Lithium is is a large and light nucleus – the overlap between nuclei is smaller than in carbon, for instance. However the data are still compatible with the existence of the EMC effect in ^{6}Li as shall be seen later.

The present F_2^C/F_2^D ratio is compared to the earlier NMC measurement of the same ratio. Fair agreement is found in the overlap region, with the exception perhaps of the two bins at $x_{Bj} = 0.0085$ and 0.012 which show a 2.1 and 1.8 standard deviation discrepancy between the two data sets. However, the bin at $x_{Bj} = 0.0055$ shows a fluctuation in the opposite direction. No amount of careful double-checking reveals a problem with these two bins in the present data set.

Antishadowing is significant in F_2^C/F_2^D between $0.05 < x_{Bj} < 0.3$, reaching a maximum of 3-4% at $x_{Bj} \approx 0.1$. Below $x_{Bj} = 0.05$ shadowing sets in, and shows a tendency of saturation below $x_{Bj} = 0.002$ at a value of:

$$0.851 \pm 0.014(stat.) \pm 0.029(syst.).$$

Above $x_{Bj} = 0.3$, the fall of the ratio below unity known as the EMC effect, is visible and significantly larger than in F_2^{Li}/F_2^D.

Now we may proceed to compare the present data to further data sets. No other measurements of F_2^{Li}/F_2^D are available, but we may compare the present data to measurements of F_2^{He}/F_2^D. There are two motivations for such a comparison: firstly these nuclei are close in atomic number, and secondly nuclear models can describe the ^{6}Li well as an α–d cluster. Especially in the shadowing region the two nuclei are expected to have a similar behaviour [104]. This is because if we imagine the α–d aligned *perpendicular* to the beam, the incoming muon has an equal chance of hitting either the α or the deuteron, and hence the shadowing effect is *diluted* with respect to the helium nucleus. Conversely, if the cluster is aligned *along* the beam direction, the α will shadow the d or vice versa (depending on the orientation), the shadowing is so *enhanced* with respect to helium. These two effects cancel out, giving the same result for ^{6}Li and ^{4}He. This almost perfect equality is confirmed in fig. 5.4.

We also see that the present lithium data at high x_{Bj} agree with the helium data from SLAC [90], the latter being much more statistically significant in this region. Of course this agreement tells us nothing, because the nuclei are different and the error bars of the present data set are large. The only conclusion that meets the eye is that one cannot exclude the existence of the EMC effect in lithium.

The present F_2^C/F_2^D ratio is compared with preliminary data from the Fermilab E665 experiment [105] at low x_{Bj} and with SLAC reanalysed data [90]. The preliminary E665 data seem to have a normalization shift with respect to the present data, within their quoted systematic error of $\sim 6 - 7\%$. The agreement with SLAC data is good within our large errors in the region of overlap.

5.1.3 Comparison with theoretical predictions

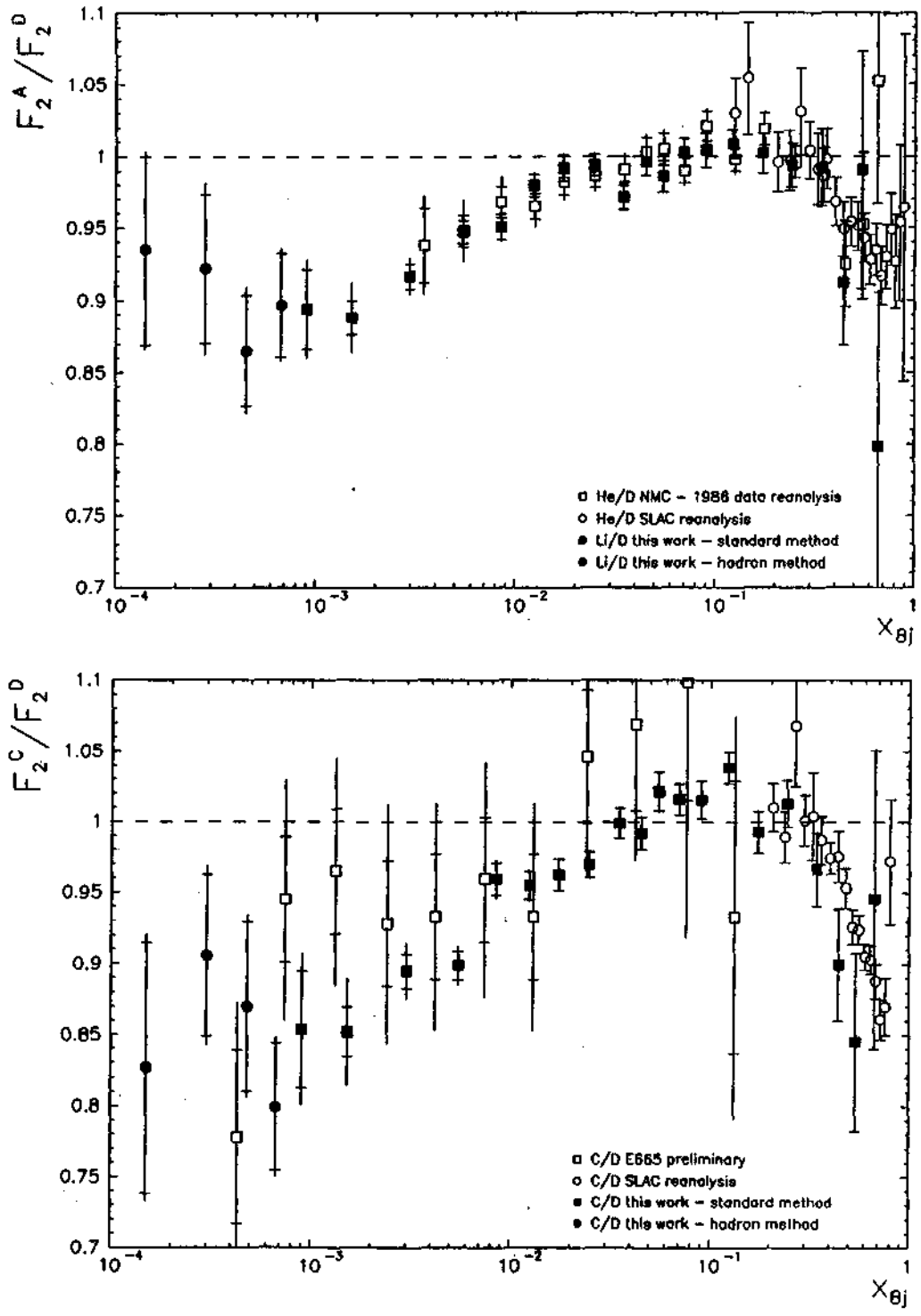

Figure 5.4: The present F_2^{Li}/F_2^D data set compared to an NMC and a SLAC measurement of F_2^{He}/F_2^D (above). The present F_2^C/F_2^D data set compared to an E665 preliminary measurement at low x_{Bj} and a SLAC one at high x_{Bj} (below). The inner error bars represent the statistical errors, the outer ones are statistical and systematic errors added in quadrature.

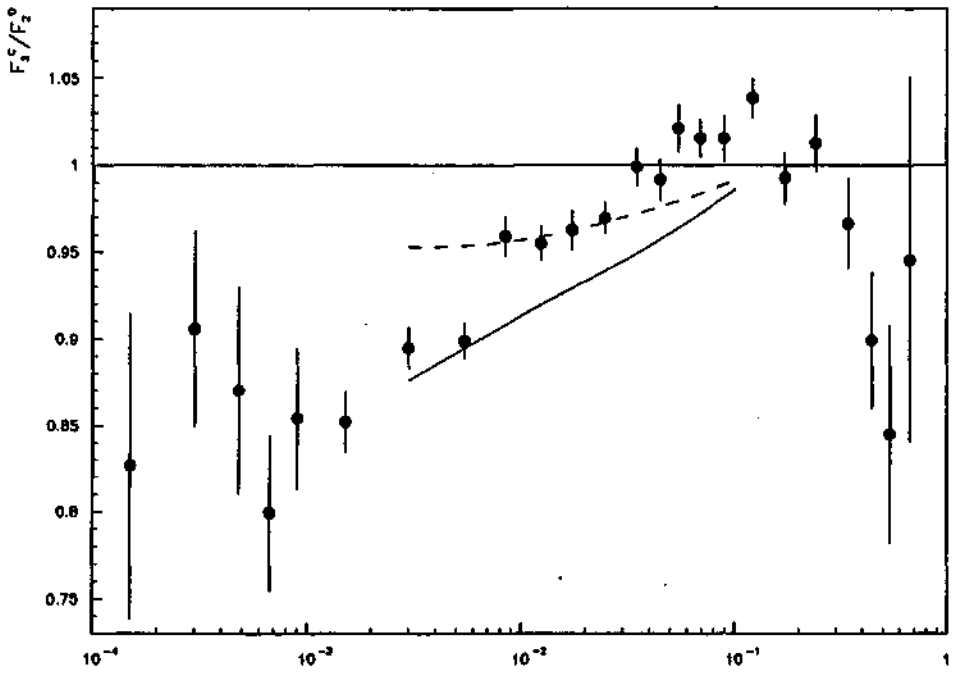

Figure 5.5: The Vector Meson Dominance model prediction by Kulagin et al. compared to the present data set for F_2^C/F_2^D. The dashed curve represents the scaling part of F_2, whereas the full curve is the full calculation with the vector meson contributions.

A comparison to all existing theoretical models of nuclear effects is beyond the scope of this work. Many predictions exist for the F_2^C/F_2^D ratio, since it is a ratio which has been measured to some precision earlier. However, the predictions usually stop at about $x_{Bj} = 0.003$, corresponding to the kinematic region previously covered by experiments. As to the F_2^{Li}/F_2^D ratio, no predictions were found in the literature. The only possibility to get a theoretical curve for this ratio was found in the work by Zhu et al. [17] where a theoretical prediction for F_2^C/F_2^{Li} and F_2^C/F_2^D are given.

We may start by a recent vector meson dominance prediction by Kulagin et al. [106] (fig. 5.5). The dashed curve shows the leading twist, or Q^2-independent term. This is calculated on the basis of Glauber multiple scattering theory of the $q\bar{q}$ fluctuation of the virtual photon using the scaling part of F_2 to describe scatterers. The full curve uses also a part of F_2 described purely as sum of vector meson cross sections, dominating at low Q^2. This full prediction is however quite low with respect to the data.

The prediction of Brodsky and Lu [107] (Fig. 5.6) is also based on a $q\bar{q}$ fluctuation of the virtual photon before the target over a distance proportional to $1/x_{Bj}$. In their gauge, only the antiquark undergoes Glauber multiple scattering. At small x_{Bj} it is dominated by Pomeron exchange and the $\bar{q}N$ amplitude is mainly imaginary, whereas in the antishadowing region the real part dominates and creates constructive interference.

Now we may compare the partonic model of Castorina and Donnachie [108, 109] based on Pomeron exchange at low x_{Bj} and x_{Bj}-rescaling at high x_{Bj}, the antishadowing region being an interplay of the two effects. The full curve in fig. 5.7 shows the original prediction, whereas the dashed one was obtained in a later paper after readjusting parton densities [109] to fit the EMC-NA28 measurement of F_2^C/F_2^D. It is seen that this improved curve describes better the antishadowing region but is too low in the shadowing region.

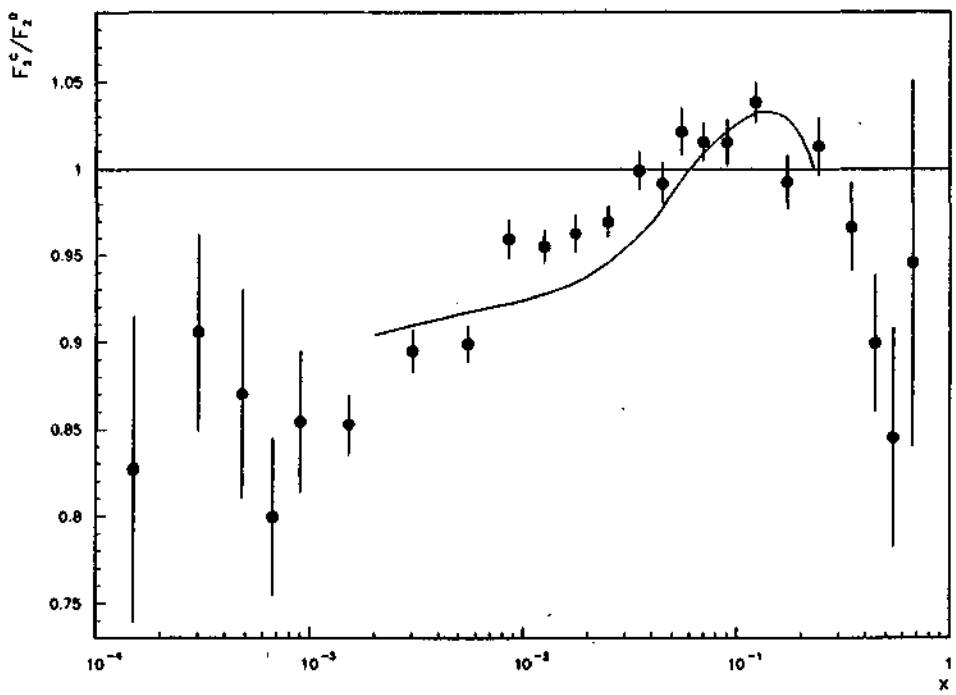

Figure 5.6: The model prediction by Brodsky and Lu compared to the present data set for F_2^C/F_2^D

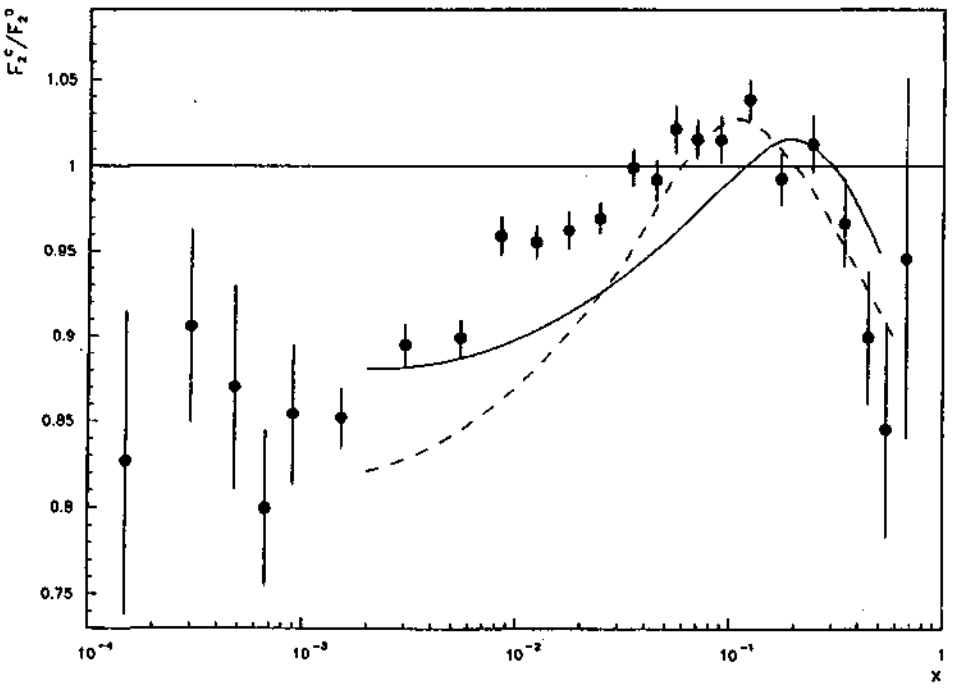

Figure 5.7: The partonic model prediction by Castorina and Donnachie compared to the present data set for F_2^C/F_2^D. For the explanation of curves see text

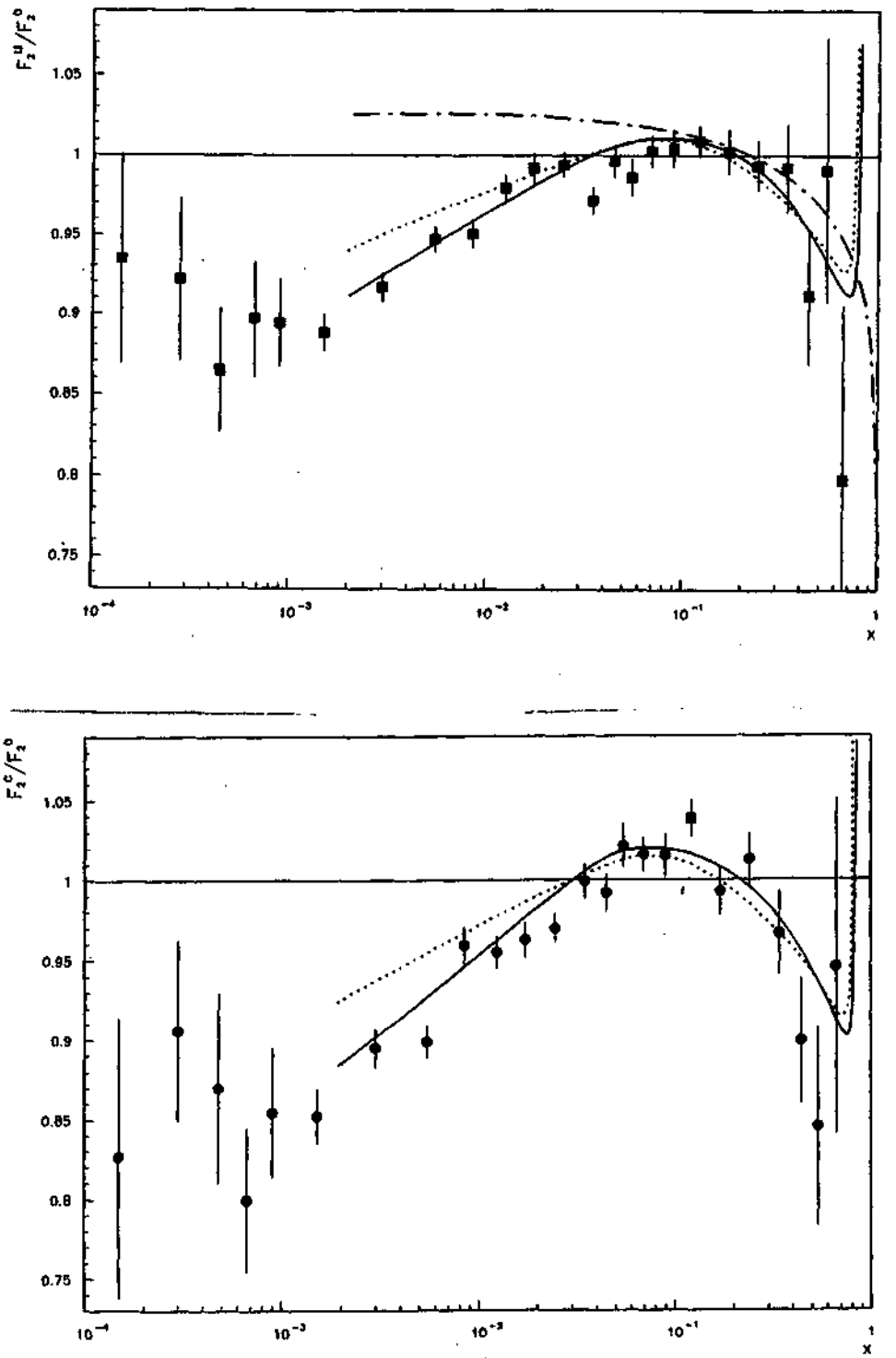

Figure 5.8: The partonic model prediction by Barone et al. for F_2^{He}/F_2^D compared to the present F_2^{Li}/F_2^D (above). The dot-dashed curve represents the contribution from nucleon swelling, the full and dashed curves are the full calculation at $Q^2 = 1$ and 10 GeV$^2/c^2$ respectively. Below, their prediction for F_2^C/F_2^D is compared to the present data

The model of Barone et al. [39], discussed in 1.2.2, seems to reproduce the data well. Their model predicts two opposite contributions at low x_{Bj}, a small enhancement due to stretching of nucleons, and a depletion (shadowing) coming again from Glauber multiscattering of the $q\overline{q}$ hadronic fluctuation of the virtual photon. In the experiment we measure the sum of the two contributions. A comparison is given in fig. 5.8. of the present F_2^{Li}/F_2^D with their prediction for F_2^{He}/F_2^D, because it has been learned in a private communication with N. N. Nikolaev that in their model ^{6}Li = ^{4}He (see discussion above). The dot-dashed line shows the contribution of stretching only, whereas the full and dashed curves correspond to the full effect at a Q^2 of 1 and 10 GeV$^2/c^2$ respectively. Our data at low x_{Bj} are closer to $Q^2 = 1$ GeV$^2/c^2$ (see tables 5.1 and 5.2). Also shown in fig. 5.8, a comparison of the present F_2^C/F_2^D with the corresponding prediction. Good agreement is found, only the saturation is not predicted.

In the framework of the constituent quark model by Zhu and collaborators [17], mentioned in 1.2.2, the effect of shadowing and antishadowing is due to parton recombination between sea partons belonging to different nucleons bringing about a hardening (shift to higher x_{Bj}) of the sea quark distribution in the nucleus, with respect to a free nucleon. The parton fusion is made possible because of nucleon swelling and a resulting overlapping. This effect is competing with another effect – the modification of the distribution of constituent quarks in the nucleus. A harmonic oscillator model is assumed for this distribution with the spring constant reduced in the nucleus with respect to a free nucleon [110]. This model reproduces well our data down to $x_{Bj} \simeq 10^{-3}$, but again the saturation of shadowing is not predicted (fig. 5.9).

In the saturation region only one prediction is found in the literature, that by Kumano [111] concerning the F_2^{Xe}/F_2^D ratio. The saturation is obtained by plugging in a "soft" gluon distribution as computed by Martin, Roberts and Stirling in [112], the "hard" and "$1/\sqrt{x}$" not being suited to fit the data. Unfortunately, no prediction of saturation is available for lithium or carbon nuclei.

As a conclusion after this small sample of theoretical models, we might say that different models may describe the experimental observations with varying degrees of success, the agreement often being achieved by tuning one or more parameters such as parton distributions, radii of swelling nucleons, binding strengths and so forth. Furthermore, models with apparently different approaches describe the data equally well as is illustrated on the Zhu et al. and the Barone et al. models. Take the shadowing region for example: the first model explains it in terms of parton fusion in the target nucleus, whereas the second one uses a combination of nucleon stretching and multiple Glauber scattering of the $q\overline{q}$ fluctuations of the virtual photon!

A clear and unified picture of nuclear effects on the x_{Bj}–dependence of the F_2 structure function has yet to emerge.

5.2 Q^2 dependence of the ratios F_2^{Li}/F_2^D and F_2^C/F_2^D at fixed x_{Bj}

We have mentioned in 1.1.2 that the F_2 structure function of the nucleon shows a certain scale breaking (i.e. Q^2–dependence) described by the DGLAP evolution equations (1.6, 1.7) in the framework of PQCD. This gives us an incentive to look for Q^2–dependence in the F_2^A/F_2^D ratios as well.

We apply the ratio method in two-dimensional logx_{Bj} and logQ^2 bins. The result is

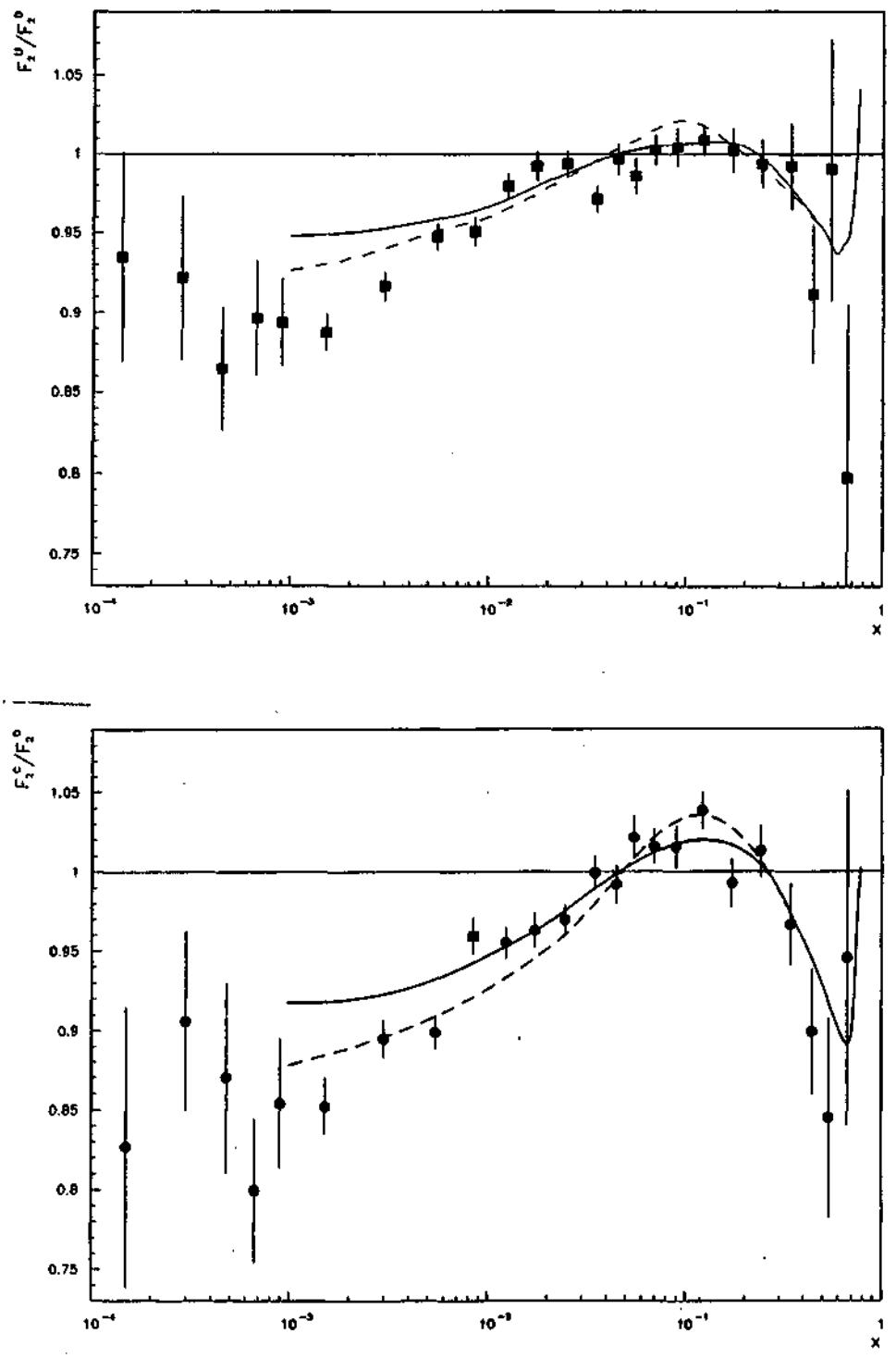

Figure 5.9: The constituent quark model predictions by Zhu et al. compared with the present data sets. The prediction for F_2^{Li}/F_2^D (above) is obtained by dividing the published predictions for F_2^C/F_2^D and F_2^C/F_2^{Li}. The dashed curve corresponds to $Q^2 = 1$ GeV$^2/c^2$, the full one is for $Q^2 = 40$ GeV$^2/c^2$. Below: the prediction for F_2^C/F_2^D compared to the present data set.

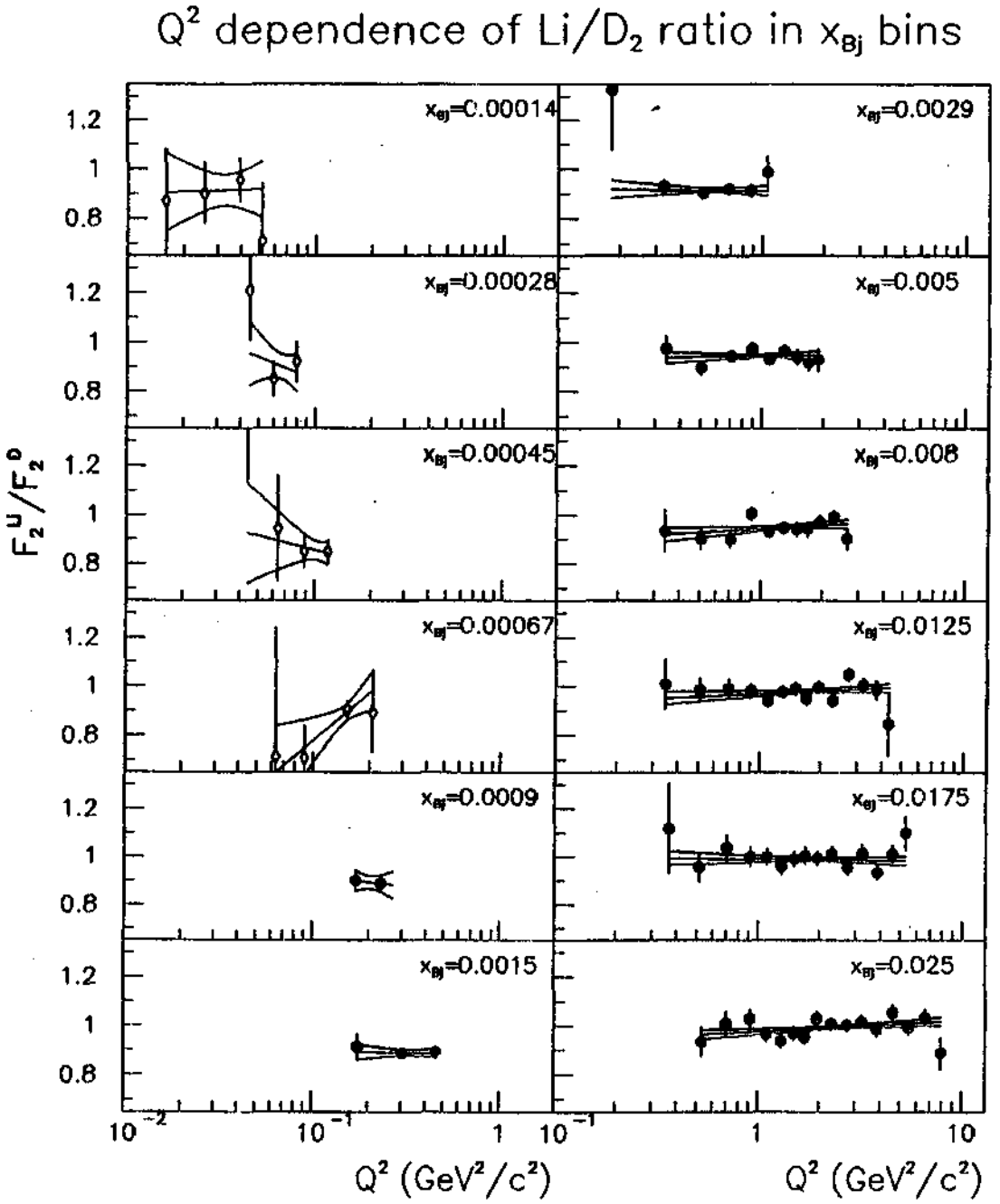

Figure 5.10: The ratio F_2^{Li}/F_2^D vs. $\log Q^2$ in x_{Bj} bins. The mean x_{Bj} of each bin is indicated in the figure. The diamonds correspond to T14 data analysed by the hadron method, and the black points are the merged data from all triggers analysed by the standard method. The lines represent least-squares fits to the data, drawn with their error bands

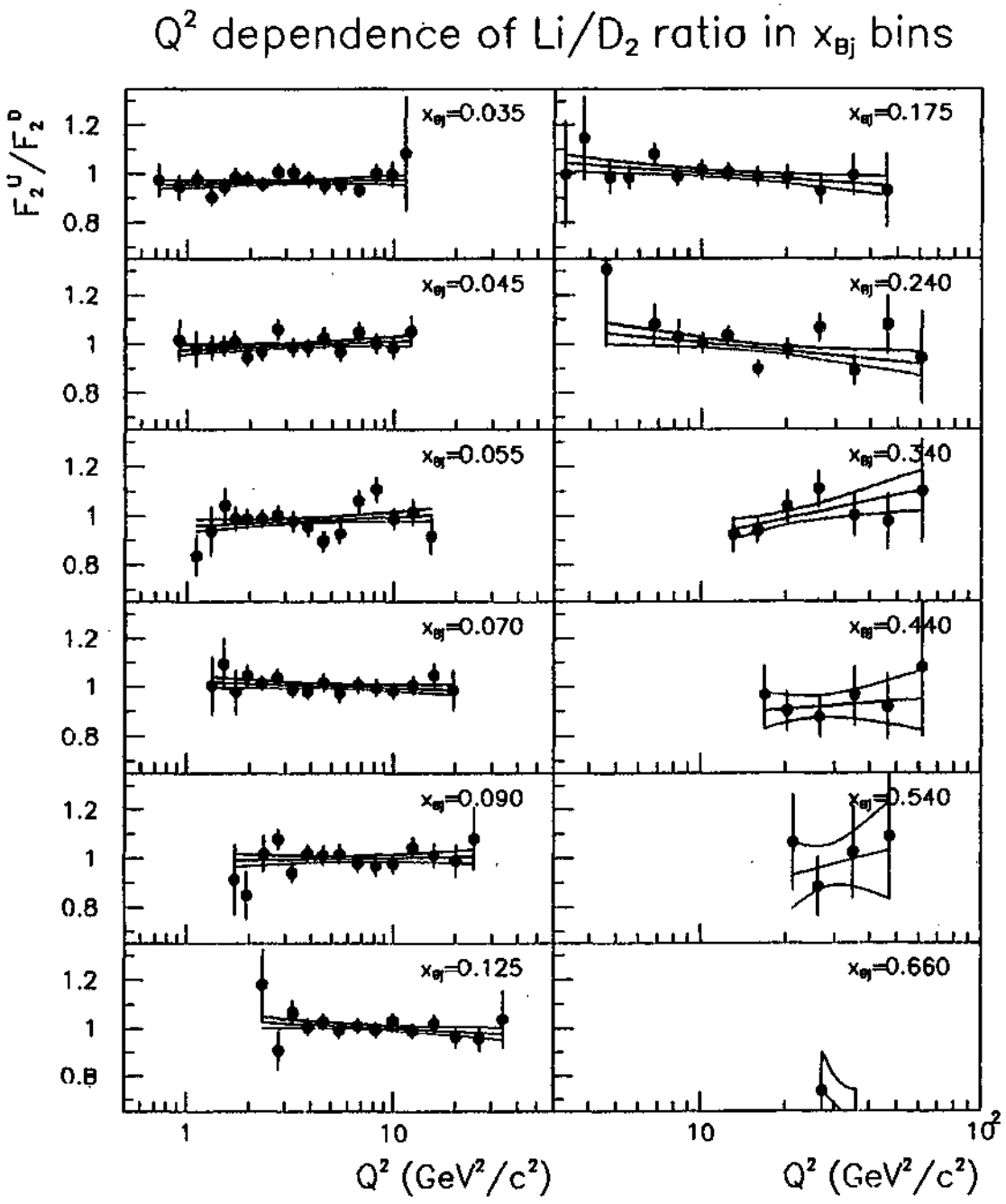

Figure 5.10: (continued) The ratio F_2^{Li}/F_2^D vs. $\log Q^2$ in x_{Bj} bins. The mean x_{Bj} of each bin is indicated in the figure. The diamonds correspond to T14 data analysed by the hadron method, and the black points are the merged data from all triggers analysed by the standard method. The lines represent least-squares fits to the data, drawn witb their error bands

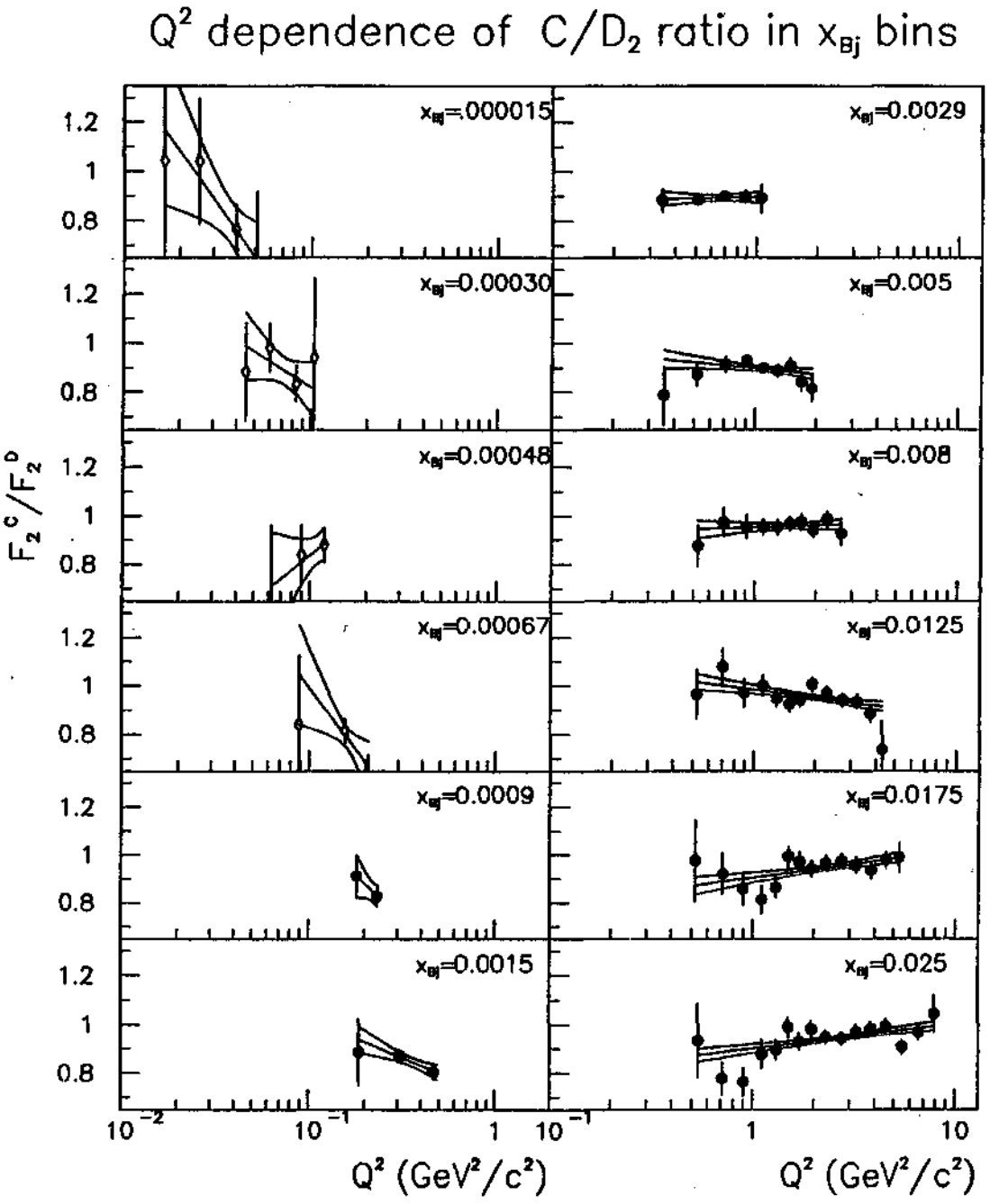

Figure 5.11: The ratio F_2^C/F_2^D vs. logQ^2 in x_{Bj} bins. The mean x_{Bj} of each bin is indicated in the figure. The diamonds correspond to T14 data analysed by the hadron method, and the black points are the merged data from all triggers analysed by the standard method. The lines represent least-squares fits to the data, drawn with their error bands

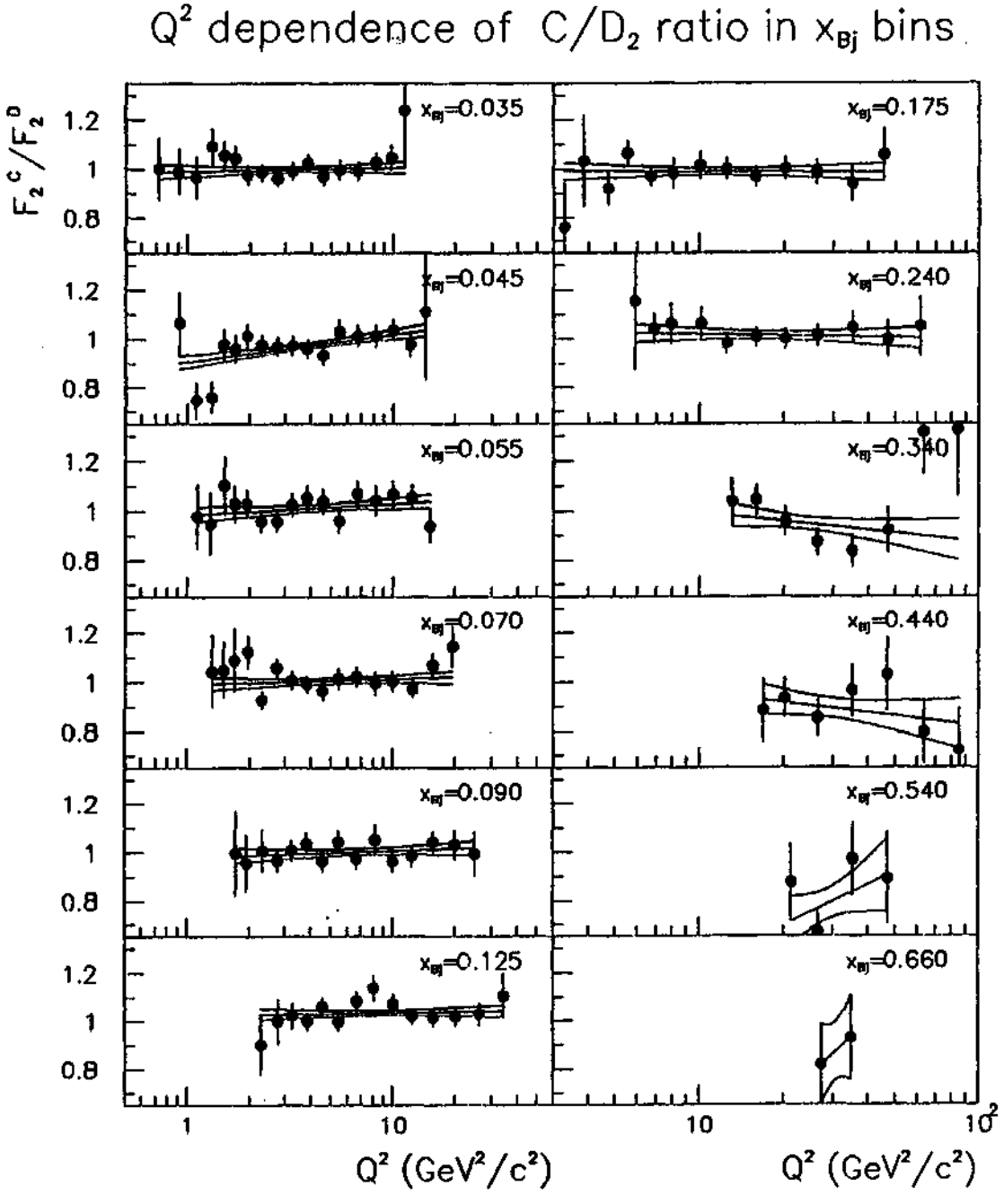

Figure 5.11: (continued) The ratio F_2^C/F_2^D vs. $\log Q^2$ in x_{Bj} bins. The mean x_{Bj} of eacb bin is indicated in the figure. Tbe diamonds correspond to T14 data analysed by tbe badron method, and the black points are the merged data from all triggers analysed by tbe standard method. The lines represent least-squares fits to tbe data, drawn with their error bands

$< x_{Bj} >$	$\frac{\partial(F_2^{Li}/F_2^D)}{\partial(\ln Q^2)}$	stat.
$4.8 \cdot 10^{-4}$	0.018	0.097
$1.5 \cdot 10^{-3}$	-0.006	0.048
$2.9 \cdot 10^{-3}$	-0.003	0.030
$5.3 \cdot 10^{-3}$	0.005	0.021
$8.4 \cdot 10^{-3}$	0.021	0.020
$1.2 \cdot 10^{-2}$	0.016	0.016
$1.7 \cdot 10^{-2}$	-0.004	0.017
$2.4 \cdot 10^{-2}$	0.020	0.012
$3.4 \cdot 10^{-2}$	0.007	0.013
$4.5 \cdot 10^{-2}$	0.014	0.015
$5.5 \cdot 10^{-2}$	0.016	0.017
$6.9 \cdot 10^{-2}$	-0.011	0.015
$8.9 \cdot 10^{-2}$	0.006	0.019
0.12	-0.017	0.017
0.17	-0.036	0.026
0.24	-0.048	0.034
0.34	0.101	0.070
0.44	0.034	0.130
0.54	0.131	0.362
0.66	-0.514	0.793

Table 5.3: The logarithmic slopes $\partial(F_2^{Li}/F_2^D)/\partial(\ln Q^2)$ as obtained from least squares fits fig. 5.11

presented in figs. 5.10 and 5.11. Straight lines are fitted through the data points by a least squares fitting program. As before, the hadron method is used in the lowest four bins, and the standard method thereafter.

The logarithmic slopes $\partial(F_2^A/F_2^D)/\partial(\ln Q^2)$ obtained by these fits are summarized in tables 5.3 and 5.4. In fig. 5.12, these slopes are compared to the logaritbmic slopes from earlier NMC measurements. Slopes from the five lowest x_{Bj} bins are averaged to increase the significance of the result.

Unfortunately no previous measurement of $\partial(F_2^{Li}/F_2^D)/\partial(\ln Q^2)$ exists, so the present data are compared with $\partial(F_2^{He}/F_2^D)/\partial(\ln Q^2)$ because of tbe analogy mentioned above. The agreement is quite striking! The agreement of the two measurements of $\partial(F_2^C/F_2^D)/\partial(\ln Q^2)$ is good within the errors.

The slopes in each x_{Bj} bin are statistically compatible with no Q^2-dependence. However, a trend towards slightly positive $\partial(F_2^{Li}/F_2^D)/\partial(\ln Q^2)$ slopes between $0.005 < x_{Bj} < 0.06$ seems to be suggested. In the $\partial(F_2^C/F_2^D)/\partial(\ln Q^2)$ slopes, a similar trend to positive slopes seems to he suggested between $0.015 < x_{Bj} < 0.1$.

5.3 The integrals $\int(F_2^{Li} - F_2^D)dx_{Bj}$ and $\int(F_2^C - F_2^D)dx_{Bj}$

We mentioned in 1.1.2 that the integral of F_2 is proportional to the total momentum carried by quarks. The integral of the difference $\int(F_2^A - F_2^D)dx_{Bj}$ thus measures the difference of

$< x_{Bj} >$	$\frac{\partial(F_2^C/F_2^D)}{\partial(\ln Q^2)}$	stat.
$4.7 \cdot 10^{-4}$	-0.239	0.152
$1.5 \cdot 10^{-3}$	-0.139	0.081
$2.9 \cdot 10^{-3}$	0.053	0.044
$5.3 \cdot 10^{-3}$	-0.035	0.032
$8.4 \cdot 10^{-3}$	0.012	0.033
$1.2 \cdot 10^{-2}$	-0.049	0.023
$1.7 \cdot 10^{-2}$	0.050	0.023
$2.4 \cdot 10^{-2}$	0.045	0.016
$3.4 \cdot 10^{-2}$	0.006	0.018
$4.5 \cdot 10^{-2}$	0.048	0.018
$5.5 \cdot 10^{-2}$	0.020	0.020
$6.9 \cdot 10^{-2}$	0.010	0.017
$8.9 \cdot 10^{-2}$	0.012	0.020
0.12	0.005	0.017
0.17	-0.002	0.024
0.24	-0.009	0.031
0.34	-0.053	0.063
0.44	-0.062	0.088
0.54	0.242	0.276
0.66	0.452	0.976

Table 5.4: The logarithmic slopes $\partial(F_2^C/F_2^D)/\partial(\ln Q^2)$ as obtained from least squares fits fig. 5.12

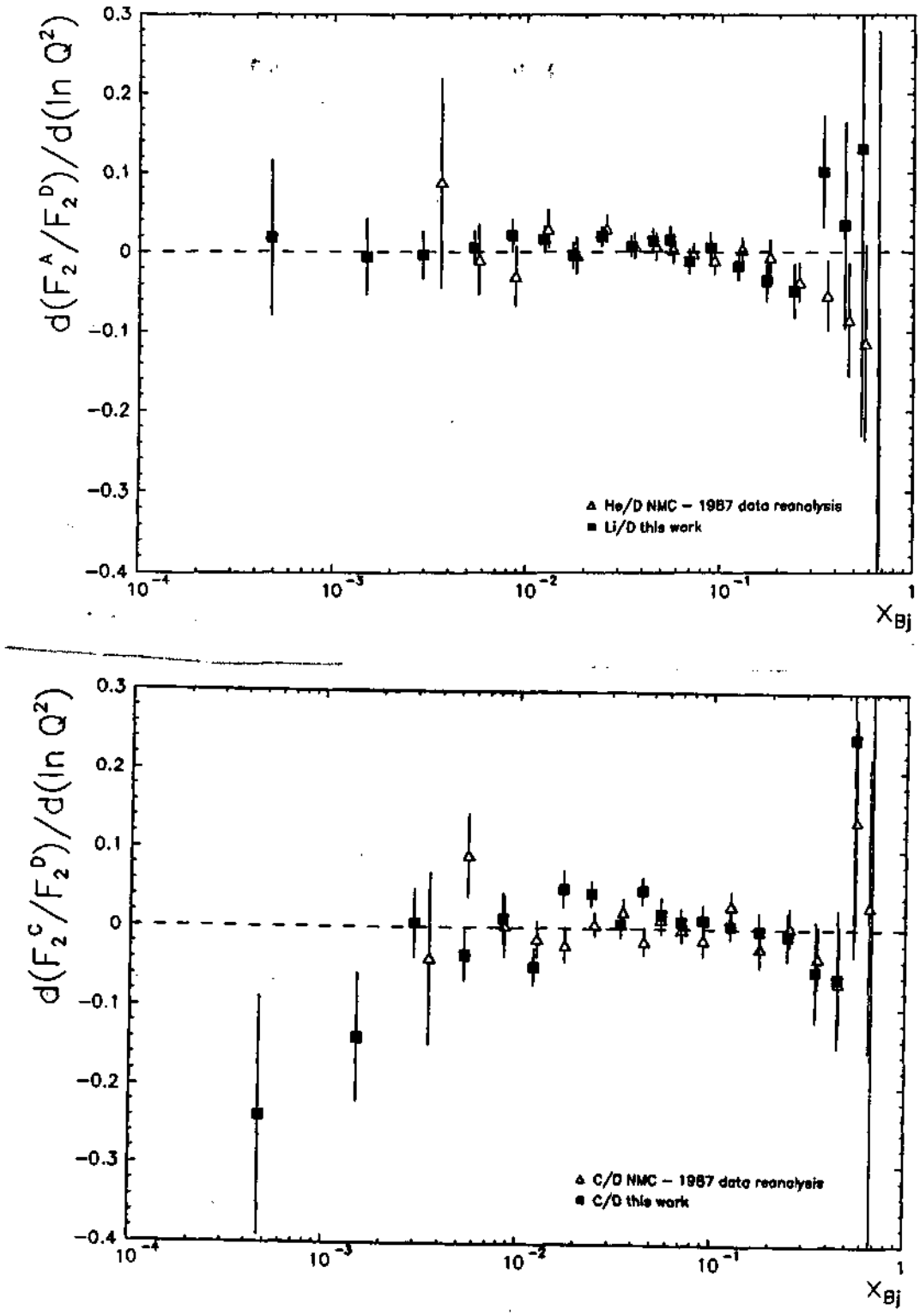

Figure 5.12: Above: the logarithmic slopes $\partial(F_2^{Li}/F_2^D)/\partial(\ln Q^2)$ as obtained by the linear fits vs. x_{Bj}, compared to the earlier NMC measurement of $\partial(F_2^{He}/F_2^D)/\partial(\ln Q^2)$. Below: the logarithmic slopes $\partial(F_2^C/F_2^D)/\partial(\ln Q^2)$ as obtained by the linear fits vs. x_{Bj}, compared to the earlier NMC measurement of the same slopes

the total momenta carried by quarks in a bound nucleon vs. a nucleon in deuterium (the closest we have to a free nucleon).

Tbe integral of the difference is to a first approximation:

$$\int (\frac{F_2^A}{F_2^D} - 1) F_2^D dx_{Bj},$$

where we must put in our measurement of the ratio, and a fit to world data on F_2.

However, tbis integral would not measnre exactly wbat we want, because:

- x_{Bj} is computed using the free proton mass; in order to find any new effect we must correct for well known ones and thus recompute x_{Bj} using the bound nucleon mass instead.

- x_{Bj} only measnres the momentum fraction of tbe struck quark in the infinite momentum ($Q^2 \to \infty$) frame. When Q^2 is finite, x_{Bj} has to be replaced by the Nachtmann scaling variable [113, 114]:

$$\xi^A = x_{Bj} \cdot \frac{M_p}{M_A} \cdot \frac{2}{1 + \sqrt{1 + \frac{4M_p^2 x_{Bj}^2}{Q^2}}}$$

Since we have measured all quantities as functions of x_{Bj}, we use a correction function $K_2(x_{Bj}, Q^2)$ (actnally the Jacobian for the transformation $\xi^A \to x_{Bj}$) and integrate over x_{Bj} after all. As a result, we compute tbe integral:

$$I^{A-D}(Q^2)|_{x1}^{x2} = \int_{x1}^{x2} (\frac{F_2^A(x_{Bj}, Q^2)}{F_2^D(x_{Bj}, Q^2)} - 1 + f_M) F_2^D(x_{Bj}, Q^2) K_2(x_{Bj}, Q^2) dx_{Bj},$$

where K_2 deviates from unity at low Q^2 and high x_{Bj}, and

$$f_M = \left(\frac{AM_p}{M_A} - \frac{DM_p}{M_A}\right)$$

is the difference in binding energies between the deuteron and nucleus A.

Now this integral may in general depend on Q^2, and is meaningful only if the input is given at a fixed Q^2. For F_2^D this is not a problem – the Q^2 evolution is well described by PQCD and fits the measurements.

However the Q^2–dependence of the F_2 ratios is less well known, as shown in the previous section. Tberefore there are two possible cboices:

- Assnme no Q^2–dependence of the ratio (the data are compatible with this hypotbesis) and evalnate the integral nsing tbe ratio as measured, at a different Q^2 in each x_{Bj}–bin, and a structnre function at the mean value of our data, ahout $Q^2 = 5$ GeV$^2/c^2$.

- Use the logarithmic slopes as measured to propagate the measured Q^2–averaged ratio from its mean Q^2 value to tbe value chosen to evalnate the integral.

The first method gives a good statistical significance of the integral, since the ratio is used in high-statistics x_{Bj} bins with no Q^2-propagation. However, it presents a slight disadvantage of the hypothesis of rigorously no Q^2-dependence of the ratio being slightly arbitrary: whereas no significant Q^2-dependence is visible inside our statistical errors, there is little grounds to believe that it is identically zero. All of the theoretical models describing nuclear effects well (e.g. the models by Barone et al. [39] and the one by Zhu et al. [17]) all predict a small, logarithmic Q^2-dependence (cf. different curves for different Q^2-values).

The second method has the disadvantage of using the measured Q^2-slopes for the propagation of the ratio to the desired Q^2-value, but is introducing no arbitrary assumptions for the Q^2-dependence.

We shall choose the second method, using the first method only as a consistency cross check: our data being consistent with no Q^2-dependence, the integral should be so, too!

For the lithium nucleus, integrating from $1.4 \cdot 10^{-4}$ to 0.66 we find:

$$\begin{aligned} I^{Li-D}(Q^2 = 5\ \mathrm{GeV}^2/\mathrm{c}^2)|^{0.66}_{0.00014} &= -0.0035 \pm 0.0081(stat.) \pm 0.0007(syst.) \\ I^{Li-D}(Q^2 = 30\ \mathrm{GeV}^2/\mathrm{c}^2)|^{0.66}_{0.00014} &= -0.0016 \pm 0.0011(stat.) \pm 0.0007(syst.), \end{aligned}$$

both results being compatible with the result obtained using no Q^2-dependence: $-0.0021 \pm 0.0010(stat.)$, and with zero. The systematic error reflects the systematic error on the ratio itself (especially the overall normalization error plays a dominant role) and on the knowledge of F_2^D.

The better statistical significance of the result at 30 $\mathrm{GeV}^2/\mathrm{c}^2$ is due to the fact that the largest contribution to the integral comes from the high x_{Bj} bins (simply because the bin width is largest – we integrate over x_{Bj}, whereas our bins are spaced equally in $\log x_{Bj}$!); these bins have very large statistical errors on the logarithmic Q^2-slopes and thus if we extrapolate them very far in Q^2 (which is the case for $Q^2 = 5\ \mathrm{GeV}^2/c^2$) the statistical error on the integral gets very large. On the contrary, if we place ourselves close to the mean Q^2 value of these high-x_{Bj} bins, the propagation is minimal and the resulting significance increased.

For the carbon nucleus, the result is:

$$\begin{aligned} I^{C-D}(Q^2 = 5\ \mathrm{GeV}^2/c^2)|^{0.66}_{0.00014} &= -0.0079 \pm 0.0084(stat.) \pm 0.0006(syst.) \\ I^{C-D}(Q^2 = 30\ \mathrm{GeV}^2/\mathrm{c}^2)|^{0.66}_{0.00014} &= -0.0022 \pm 0.0011(stat.) \pm 0.0006(syst.), \end{aligned}$$

both results being compatible with that assuming no Q^2-dependence: $-0.0028 \pm 0.0009(stat.)$. All integrals are again evaluated in the measured region: $1.4 \cdot 10^{-4} < x_{Bj} < 0.66$.

For the carbon nucleus we may consider exploiting the better statistical significance of SLAC data for F_2^C/F_2^D at high x_{Bj} from ref. [90]. Since these data are given at a mean Q^2 of about 5 GeV^2/c^2, and no slopes are quoted, we may only evaluate the integral at this value of Q^2. However, this is not a problem now, since we shall be using data from this work only in the range: $1.4 \cdot 10^{-4} < x_{Bj} < 0.17$, and the SLAC data for $0.205 < x_{Bj} < 0.8$. The integral thus obtained is:

$$I^{C-D}(Q^2 = 5\ \mathrm{GeV}^2/c^2)|^{0.8}_{0.00014} = -0.0012 \pm 0.0006(stat.) \pm 0.0011(syst.),$$

for the interval $1.4 \cdot 10^{-4} < x_{Bj} < 0.8$.

We notice that such an integral has a better statistical error, but a poorer systematic one, due primarily to a quoted 1% overall normalization uncertainty on the SLAC data

(compared to an 0.3% normalization error in the present work). "It always comes down to these ... densities" [115].

In conclusion we might say that the value of the integrals of the F_2 differences are all compatible with zero with varying significance depending on Q^2 and the data used. At 30 GeV^2/c^2, the present data give the following constraints at the 95% confidence level:

$$\begin{aligned} -0.0040 < \; & I^{Li-D}|_{0.00014}^{0.66}(Q^2 = 30\ \mathrm{GeV}^2/c^2) \; < 0.0004 \\ -0.0047 < \; & I^{C-D}|_{0.00014}^{0.66}(Q^2 = 30\ \mathrm{GeV}^2/c^2) \; < 0.0005 \end{aligned}$$

However it is difficult to draw far reaching conclusions from these results: whereas we may assume that the contribution to the integral in the region $x_{Bj} < 0.00014$ is negligible, this not true for the contribution in the region $x_{Bj} > 0.66$, where the ratio rises very steeply. It is therefore not possible to give a statement about a global change of the momentum fraction carried by quarks in a bound nucleon.

Chapter 6

A glimpse at hadron physics

Apart from structure function ratios, the main subject of this work, many other physics results may be extracted from these data. Unfortunately, time has lacked to go into detailed analysis, but some preliminary results can be mentioned here.

In our inclusive analysis we have completely ignored hadrons seen in our detector. In the semi-inclusive measurement we have only used them to tag deep inelastic events.

6.1 Jets in deep inelastic muon scattering

It is possible to extract useful information about the structure of nucleons from the information the hadrons carry. One potentially powerful tool in that sense is the **jet topology** of the deep inelastic event.

Figure 6.1 illustrates lowest order processes of the one photon exchange graph (fig 1.1). Here only the struck parton is shown – the quark or the gluon. We see that if the topology of the event shows only one forward jet (and the additional "target remnant", or "spectator" jet, going backwards in the center-of-mass system), it means our virtual photon just "kicked out" one of the quarks which then hadronizes as in fig. 4.15. This means such events are only sensitive to the quark distribution in the nucleon. If, on the contrary, the hit parton is a gluon, then the interaction proceeds via photon-gluon fusion which gives a $q\overline{q}$ pair. The q hadronizes and forms one forward jet, but so does the $\overline{q}$ and forms a second jet. The target remnant forms the backward jet. However, the same 1+2 jet topology may originate from so-called gluon bremsstrahlung: a quark is struck by the virtual photon, and subsequently radiates a gluon. Both quark and gluon form distinct jets. 1+2-jet events are order-α_S processes.

This means that information about the gluons may be extracted from 2+1-jet events, but is "diluted" in the sense that some of the events with the same topology stem from events where the quark is the struck parton.

The next difficulty to be faced is the definition of a jet. We see hadrons in our detector with a certain topology and are trying to figure which ones stem from which parton at the origin. Intuitively, we imagine a jet as a narrow stream of hadrons "close" to each other. A measure of this "closeness" is given by the invariant mass of pairs of hadrons, normalized by the invariant mass of the whole hadronic system (W). We must then choose a scale (called *yscale* in the following) such that if the invariant mass normalized by W is smaller than this scale, we consider the two hadrons as belonging to the same jet:

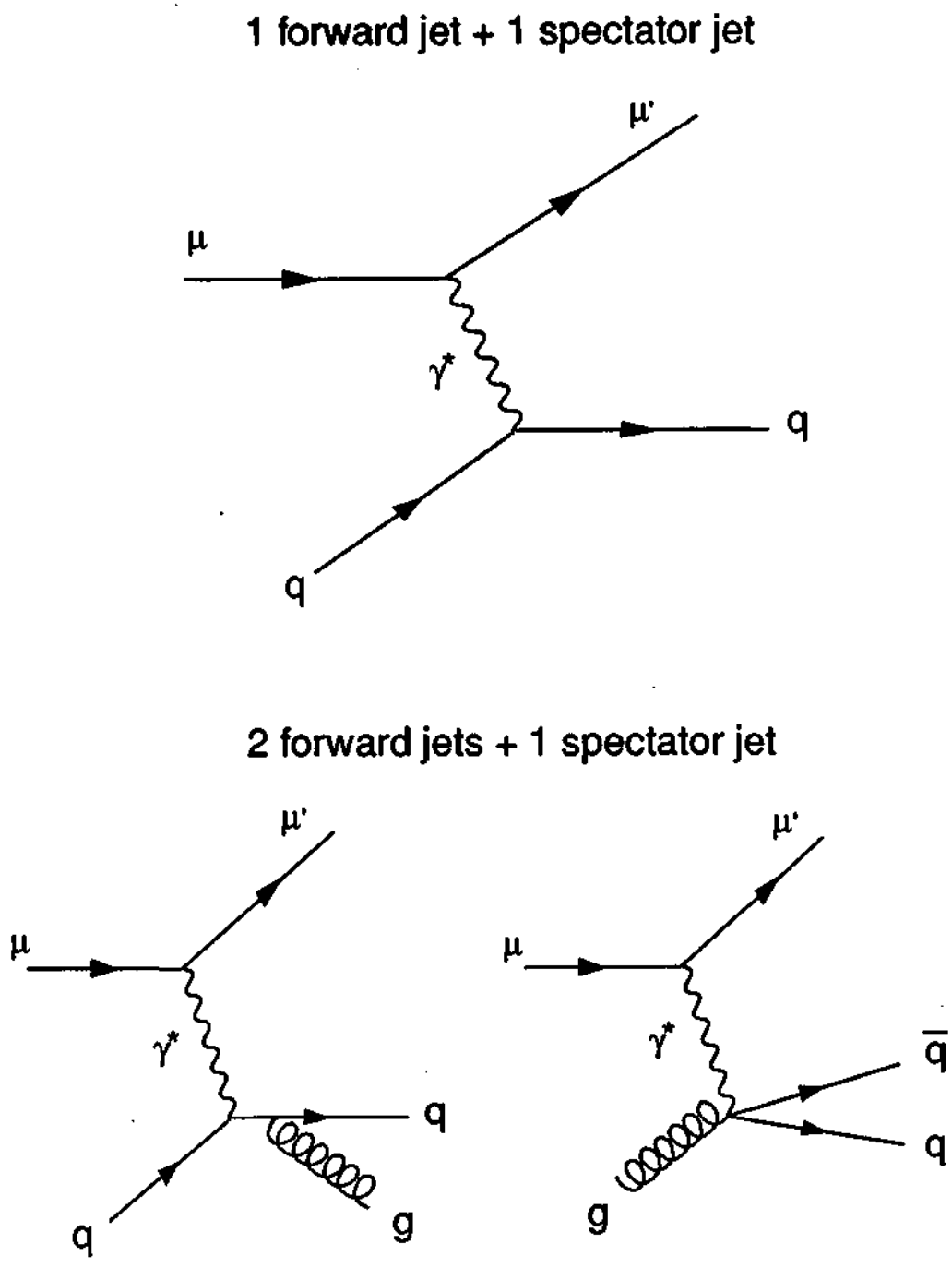

Figure 6.1: The leading order contribution (O(1)) gives a 1+1-jet event and is only sensitive to the quark distribution (above). The next to leading order contributions ($O(\alpha_S)$) give 1+2 jet topologies: gluon bremsstrahlung (below left) depends on the quark distribution; photon-gluon fusion (below right) depends on the glue

$$\frac{m_{ij}^2}{W^2} < yscale \Rightarrow i,j \text{ belong to the same jet,} \tag{6.1}$$

where the invariant mass is calculated as:

$$m_{ij} \approx 2E_iE_j(1-\cos\theta_{ij})$$

θ_{ij} being the angle between the two hadron tracks [1].

We start with two hadrons, check by the above criterion if they belong to the same jet; if they do, we add their four-momenta (to get the four-momentum of the jet) and restart with another hadron. This procedure is repeated until all remaining jets fail test 6.1. Then we count the jets.

The algorithm explained above is known as the JADE algorithm after the collaboration that introduced it for studying jet topologies of e^+e^- annihilation [116]. It contains an arbitrary parameter, *yscale*. If *yscale* is chosen very small, almost no pairs shall be matched and we shall have a majority of 1+3 or more-jet events (1+3-jet events do exist at the few percent level as order α_S^2 QCD processes [119]). Going to higher scales, the number of multijet events decreases to give place to 1+2 and 1+1 jet events.

Figure 6.2 illustrates a typical 1+1-jet and a typical 1+2-jet event, in three views; notice the greater $p_\perp$ (transverse momentum with respect to the virtual photon direction) of the 1+2-jet event. Only the forward jets are visible, no information is available for the backward hemisphere in the hadronic system center of mass system. The low average multiplicity means that we often have a single hadron representing a jet. Fig. 6.3 shows the evolution of the jet rates with *yscale*. A reasonable choice for *yscale* seems to be 0.08, where the 1+3-jet class is reduced to a small fraction. This corresponds to the choice of 0.04 in ref. [118] (because they normalize with W/2, not W).

How do we now use this information? Well, for a serious analysis one would need a complete MonteCarlo simulation with QCD predictions on the parton level, and hadronization models to follow (for instance the LUND MonteCarlo). Such studies would permit e.g. the extraction of α_S [117].

However, some information can again be extracted without any simulation. We may look at double ratios of the form:

$$\mathcal{R}^A_{1+2/1+1} = \frac{\frac{\sigma(\mu A \to \mu+1+2jets)}{\sigma(\mu A \to \mu+1+1jet)}}{\frac{\sigma(\mu D \to \mu+1+2jets)}{\sigma(\mu D \to \mu+1+1jet)}} \tag{6.2}$$

With the same arguments as for the simple structure function ratio, the complementary target setup should make all systematic effects cancel, thus yielding results directly from the data.

A preliminary result for these double ratios vs. *yscale* is shown in fig. 6.4 for T1 data. Only events with multiplicity greater than three are used, and a low W cut of 13 GeV is applied. Other cuts include the cuts on EMAGF and the two-dimensional cut as in 4.16 and kinematic cuts on $\theta > 10$ mrad, $\nu > 20$ GeV, and $y_{Bj} < 0.85$. We see that the result depends on *yscale*, but for the C/D double ratio it is consistently below unity.

This result confirms recent findings of the E665 collaboration [120], that 1+2-jet events are more shadowed than 1+1-jet ones. In view of fig. 6.1, this could mean that the gluon distribution in nuclei is more shadowed than the quark one.

[1] This is an expression neglecting the hadron rest masses – we anyway don't know what mass to assign since we have no particle identification

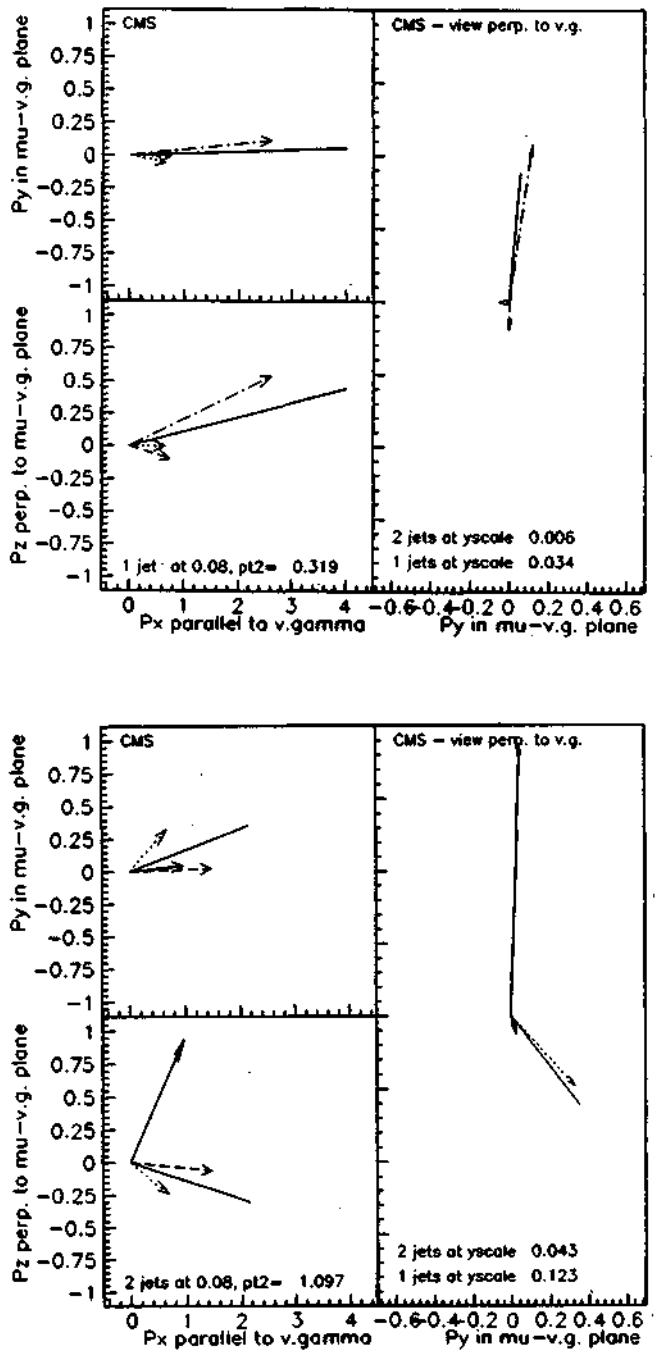

Figure 6.2: A typical 1+1 (above) and 1+2 jet event (below) in tbree views of the γ^*–nucleon center of mass frame: the scattering plane containing the scattered μ and *gamma** vectors (upper left corner), the plane containing the *gamma** vector and perpendicular to the scattered μ vector (lower left), and the plane perpendicular to tbe *gamma** (right). All units are GeV/c. The full lines with no arrows indicate jets as obtained hy summing one or more hadron vectors (dashed, dotted, dash-dotted arrows). Also indicated are the values of $p_\perp^2$, the jet multiplicity at *yscale* = 0.08, and the minimal values of yscale for the event to be declared a 1+2- respectively a 1+1-jet event

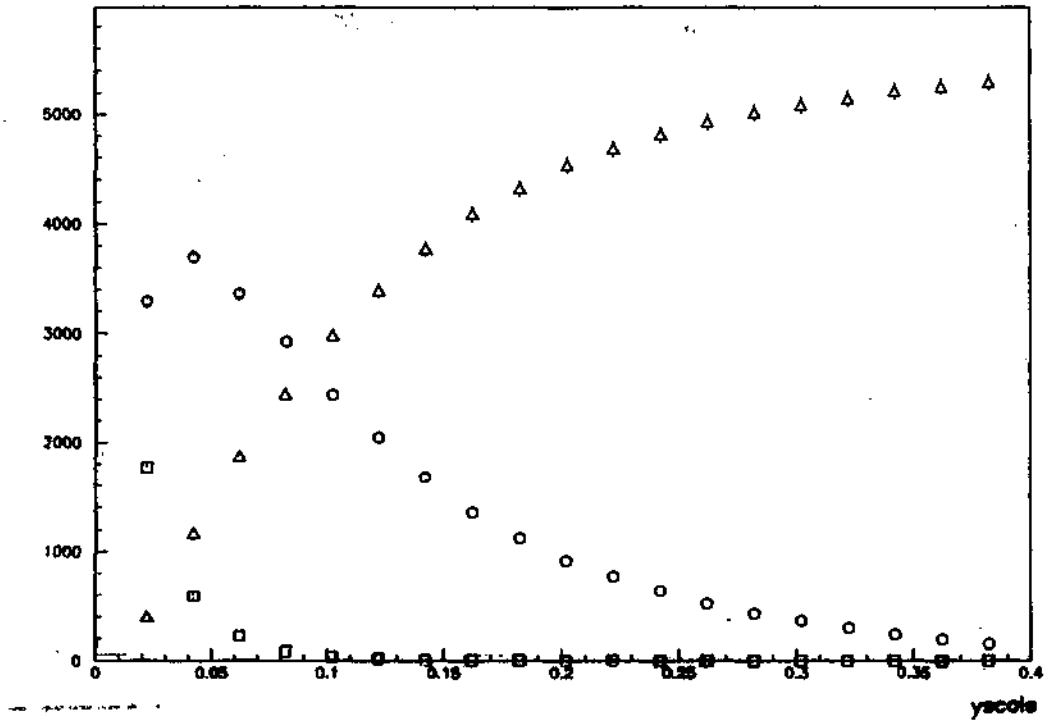

Figure 6.3: Evolution of jet rates with *yscale*: boxes indicate 1+3 (or more) jet events, open points are 1+2-jet events, while triangles designate 1+1-jet events.

However, as mentioned above, these results are preliminary in the sense that e.g. effects of secondary interactions of hadrons have not been investigated as this was done in sec. 4.2.2 for the semi-inclusive measurement of the simple ratio. We also cannot present any kinematic dependence of the double ratio, since the flux ratios present kinematic dependence themselves.

6.2 Pion interferometry

Another way to look at the hadrons is the Bose-Einstein correlation of like-charged pions. Pions obey Bose-Einstein, rather than simple Poisson statistics, because of the symmetrization of the two-particle wave function. The consequence of this is that pions are subject to a "bunching" effect, i.e. they have an enhanced probability of overlapping in phase space [123].

This effect is well-known in optics (photon bunching, see e.g. [121, 122]), and has been exploited by Hanbury-Brown and Twiss [125] to measure angular sizes of stars: two parabolic mirrors with detectors placed on a circular rail track were used to make different light rays of the same star interfere. Observing the largest baseline (distance between the detectors) for which a quantum correlation took place, they could conclude on the size of the phase space cell and thus on the angular size of the star.

Analogously to the Hanbury-Brown and Twiss (HBT) experiment it has been proposed by Kopylov, Podgoretskii and Cocconi [124] to measure the space-time structure of particle production in collisions. Pion interferometry is now a well-exploited tool in high-energy

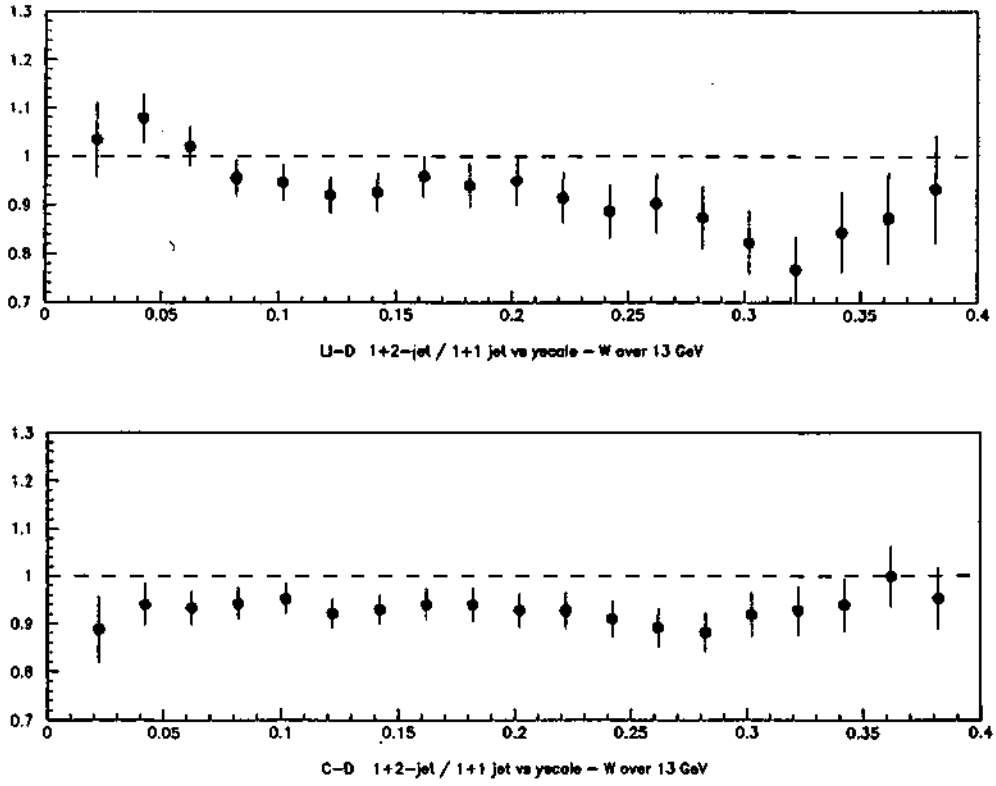

Figure 6.4: Double ratios $\mathcal{R}^{Li}_{1+2/1+1}$ (above) and $\mathcal{R}^{C}_{1+2/1+1}$ (above) vs. *yscale*

pbysics.

We proceed as follows: selecting like-cbarge hadrons (opposite charge hadrons are grouped by Coulomb attraction), we compute the Lorentz-invariant quantity:

$$Q_{inv} = \sqrt{-(p_1 - p_2)^2} = \sqrt{M_{\pi\pi}^2 - 4m_\pi^2} \tag{6.3}$$

where p_1 and p_2 are the momenta of the two hadrons, $M_{\pi\pi}$ is the effective pion pair mass and m_π is the pion mass.

Pairing pions inside the same event, we expect to see the enhancement effect. However, to see this effect, we need a reference distribution with the same kinematic dependence (save for the interference effect we want to measure, of course!). This reference distribution is obtained by pairing hadrons from *different* events. Such pairs are completely uncorrelated, while kinematically equally distributed. Dividing the two distributions, we get the correlation effect (fig. 6.5). The distribution is corrected for Coulomb repulsion by the nonrelativistic Gamow correction [126]:

$$G = \frac{2\pi m_\pi \alpha}{Q_{inv}\left(e^{\frac{2\pi m_{pi}\alpha}{Q_{inv}}} - 1\right)} \tag{6.4}$$

The ratio of the correlated to the uncorrelated is fitted by the usual Gaussian parametrization:

$$R(Q_{inv}) = N(1 + \lambda e^{-r^2 Q_{inv}^2}), \tag{6.5}$$

where N is a normalization factor, λ is the size of the enhancement (for a chaotic source it should be equal to 1, meaning a 100% overlap for $Q_{inv} = 0$), and r is a measure of the radius from which pions with similar momenta are produced.

We get a preliminary result:

$$\begin{aligned} \lambda &= 0.923 \pm 0.031 \\ r &= 0.304 \pm 0.014\text{fm} \end{aligned}$$

However, if one assumes a different shape of the fit, allowing for a slope in the baseline (this gives a better χ^2 of the fit), we get:

$$\begin{aligned} \lambda &= 0.638 \pm 0.065 \\ r &= 0.373 \pm 0.029\text{fm} \end{aligned}$$

This result is no measurement yet. Firstly, our sample is contaminated with protons, antiprotons (fermions), kaons (wrong mass assumed), etc. Secondly, the contributions of resonances would have to be corrected for. Again a detailed LUND MonteCarlo would be necessary. Apart from that, the source is not spherical, so a three-dimensional fit to the distribution would be needed to describe the source.

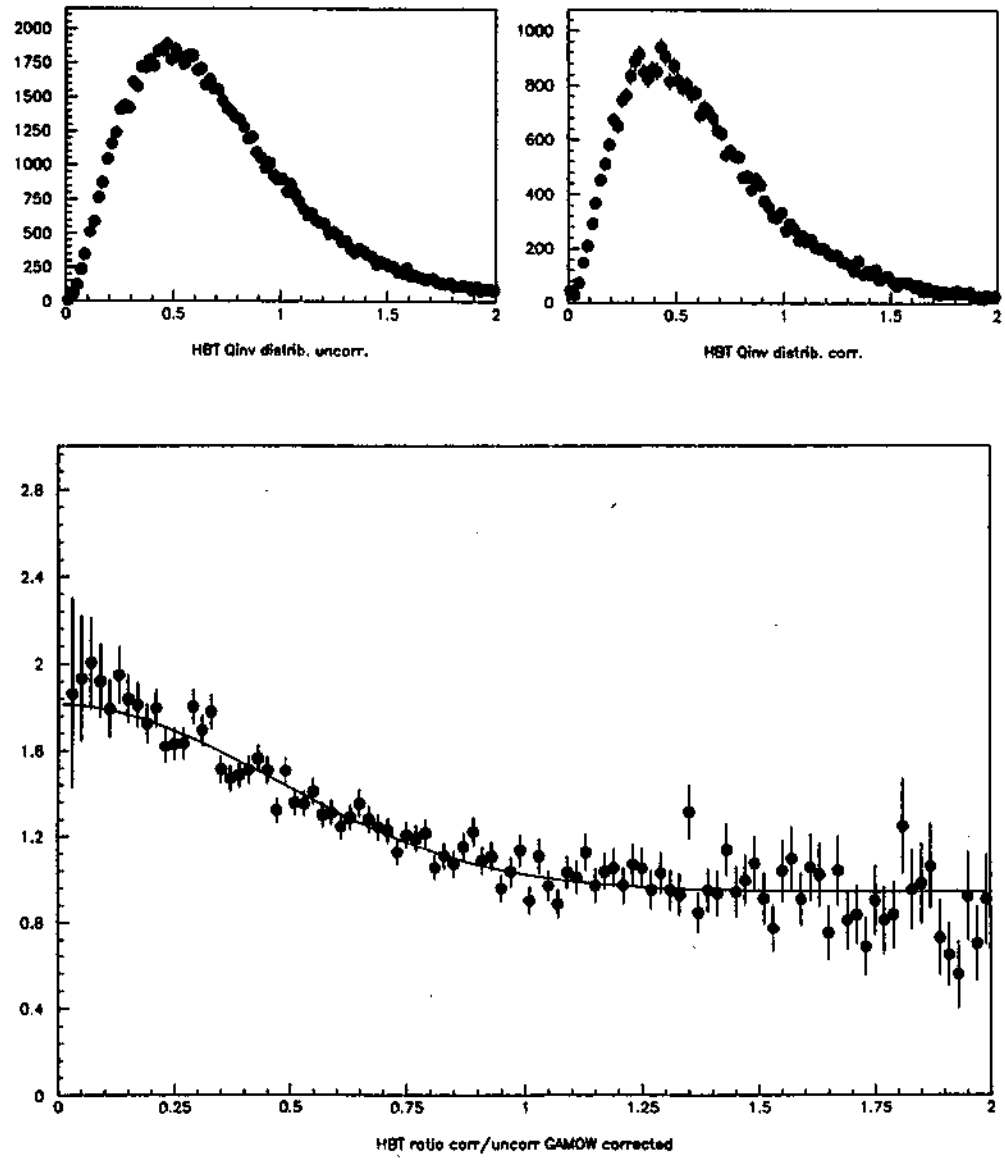

Figure 6.5: Bose-Einstein correlations of pions. The uncorrelated distribution (top left) is obtained by taking hadron pairs from different events. The correlated one (top right) is obtained by taking pairs from the same event. The correlation (down) is obtained by dividing the two distributions, after correcting for Coulomb repulsion (see text). Units are GeV/c.

Chapter 7

Conclusion

We have extracted the structure function ratios F_2^{Li}/F_2^D and F_2^C/F_2^D, presented in chapter 5. The F_2^C/F_2^D ratio confirms previous measurements for the same ratio, extending the kinematic region by more than an order of magnitude, and showing first evidence for saturation of shadowing for the carbon nucleus at a value of

$$0.851 \pm 0.014(stat.) \pm 0.029(syst.).$$

This value is compatible with the cross section ratio from photoabsorption experiments [127][1]:

$$\left(\frac{\sigma(\gamma C \to X)}{\sigma(\gamma D \to X)}\right)_{E_\gamma=60\text{GeV}} = 0.832 \pm 0.010$$

The F_2^{Li}/F_2^D ratio provides the first direct measurement of this ratio. Compared to the previous indirect measurement, it extends the kinematic region by almost two orders of magnitude, and shows evidence for saturation of shadowing below $x_{Bj} = 0.002$ at a value of:

$$0.890 \pm 0.010(stat.) \pm 0.021(syst.)$$

Unfortunately, no measurement is available for this ratio from photoabsorption experiments, but an interpolation in the A-dependence can be done, assuming shadowing follows a power law [128]:

$$\frac{\sigma(\gamma A \to X)}{\sigma(\gamma D \to X)} = \frac{A^{eff}/2}{A/2} = \frac{(A/2)^\alpha}{A/2},$$

where we divide A by 2 in order to normalize to deuterium as we do in our experiment (the assumption of no shadowing in deuterium). The power α would be equal to 1 if there were no shadowing, and 2/3 if there was maximal shadowing (i.e. the photon can only "see" the nucleons on the surface). Using the data from [127] on C, Cu and Pb at incident photon energy of 60 GeV we find

$$\alpha = 0.899 \pm 0.006.$$

This enables us to estimate shadowing in ^{6}Li for photoabsorption at:

[1] the authors don't give a number, this value is read off fig. 4. in the paper

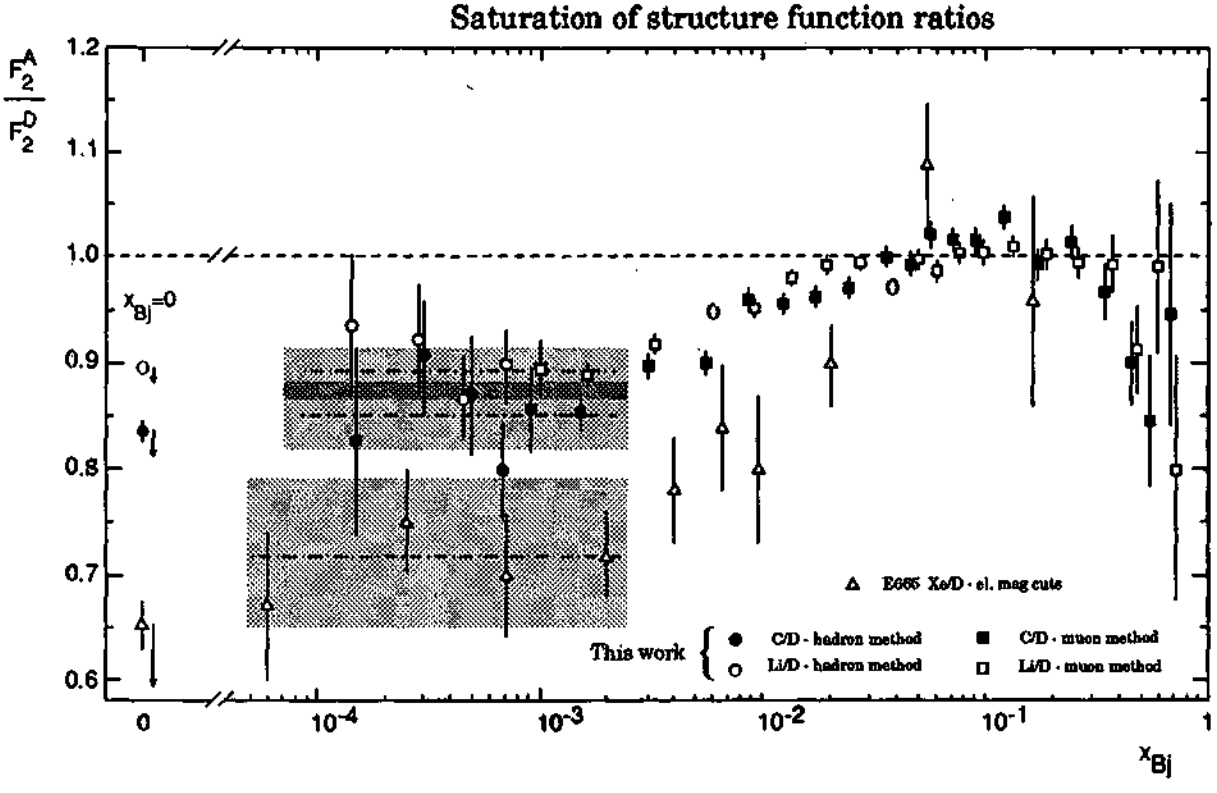

Figure 7.1: F_2^{Li}/F_2^D and F_2^C/F_2^D from the present work, shown with data on F_2^{Xe}/F_2^D from the E665 experiment and, at $x_{Bj} = 0$ the ratio $\sigma(\gamma^6 Li \to X)/\sigma(\gamma D \to X)$ from photoabsorption experiments at $E_\gamma = 60$ GeV. The arrows indicate by how much these points would move under some energy dependence assumptions to make E_γ correspond to the mean ν of the DIS data (see text). Dash-dotted lines indicate the saturation values, the shaded area corresponding to their errors. The errors on the DIS data points are statistical only; the satnration bands include statistical and systematic errors added in quadrature.

$$\left(\frac{\sigma(\gamma^6 Li \to X)}{\sigma(\gamma D \to X)}\right)_{E_\gamma=60\mathrm{GeV}} = 0.895 \pm 0.006,$$

showing remarkable agreement with the valne of saturation in deep inelastic scattering that we measure!

Tbe summary of the experimental situation in this very low x_{Bj} region is given in fig. 7.1. Our two data sets are plotted together with the Xe/D ratio from the Fermilab E665 experiment [35] – the saturation value and the photoabsorption point are calculated analogously as for our data.

The photoabsorption or "real pboton" point is plotted at $x_{Bj} = 0$ since it corresponds to $Q^2 = 0$ at a finite ν. Tbe energy ($E_\gamma = 60$ GeV) does not correspond exactly to the mean ν of our data (100-150 GeV) and there may be some energy dependence of shadowing, as illustrated on tbe measurement of shadowing on copper in [127]. However, no measurement exists of this energy dependence for lighter nuclei and therefore we refrain from any adjustment of this ratio. Let us only mention tbat tbe copper sbadowing effect ($1 - A^{eff}/A$) would seem to increase by abont one sixtb between 60 and 125 GeV. This means that a similar behaviour for lighter nuclei would imply a shift of the real photon points downward hy about 0.015 for Li/D and hy about 0.025 for tbe C/D point. Tbe Xe/D ratio has a mean ν of about 150 GeV – its shadowing may tbus increase by about one fifth bringing the real pboton Xe/D ratio down to about 0.59. The arrows in tbe picture indicate these guesstimates.

We may conclnde tbat the saturation value of deep inelastic shadowing in tbe limit of small x_{Bj} and Q^2 is consistent within the errors witb tbe shadowing observed with real pbotons. We must remember that we are bere in a region of very small Q^2 as well, so our virtual photon is here almost a real one!

Physics is continuous from $x_{Bj} = 0$ to 1.

Bibliography

[1] E.D. Bloom *et al.*, Phys. Rev. Lett. **23** (1969) 930; M. Breidenbach *et al.*, Phys. Rev. Lett. **23** (1969) 935

[2] F. Halzen, A.D. Martin, "Quarks and Leptons: An Introductory Course in Modern Particle Pbysics", John Wiley and Sons New York 1984 p.177-8

[3] F. Halzen, A.D. Martin, "Quarks and Leptons: An Introductory Course in Modern Particle Physics", John Wiley and Sons New York 1984 p.180

[4] F. Halzen, A.D. Martin, "Quarks and Leptons: An Introductory Course in Modern Particle Physics", Jobn Wiley and Sons New York 1984 p.188

[5] L.W. Whitlow et al., Pbys. Lett. **B** (1990) 193 (includes data from SLAC, EMC, CDHSW and BCDMS)

[6] V.N. Gribov and L.N. Lipatov, Sov. J. Nucl. Phys. **15** (1972) 438, 675; L.N. Lipatov, Sov. J. Nucl. Pbys. **20** (1974) 94; G. Altarelli and G. Parisi, Nucl. Pbys. **B 126** (1977) 298; Yu.L. Dokshitzer, Sov. Phys. – JETP **46** (1977) 641

[7] T. Sloan et al., Phys. Rep. **179** (1969) 156

[8] L. Whitlow *et. al.*, Phys. Lett. **B 282** (1992) 475

[9] EMC-NA2 Collab., J.J. Aubert *et. al.*, Nucl. Phys. **B 259** (1985) 189

[10] EMC-NA2 Collab., J.J. Aubert *et. al.*, Nucl. Phys. **B 293** (1987) 740

[11] BCDMS Collab., A.C. Benvenuti *et. al.*, Phys. Lett. **B 223** (1989) 485

[12] BCDMS Collab., A.C. Benvenuti *et. al.*, Phys. Lett. **B 237** (1990) 592

[13] NM Collab., P. Amaudruz *et. al.*, Phys. Lett. **B 295** (1992) 159

[14] NM Collab., M. Arneodo *et. al.*, Phys. Lett. **B 309** (1993) 222

[15] G.K. Mallot, Proceedings XIII Particles and Nuclei International Conference, Perugia, Italy, July 1993.

[16] V. Barone et al. Phys. Lett. **B 268** (1991) 279

[17] W. Zbu and L. Qian, Phys. Rev. **C 45** (1992) 1397

[18] R. Seitz, Ph.D. thesis, University of Mainz, 1994

[19] B. Badelek and J. Kwieciński Phys. Lett. **B 370** (1992) 278

[20] W. Melnitchouk, A.W. Thomas: Preprint ADP-92-192/T120, Preprint ADP-92-214/T132, Phys. Rev. **D 47** (1993) 3783

[21] V.R. Zoller Preprint ITEF 91-58, ITEF 91-102, Z. Phys. **C 54** (1992) 425, Phys. Lett. **B 279** (1992) 145

[22] D.O.Caldwell et al., Phys.Rev.Lett. **42** (1979) 553

[23] M. Arneodo, CERN-PPE/92-113, to appear in Phys. Rep.

[24] A. Witzmann, Ph.D. thesis, University of Freiburg-i.-B., 1993

[25] C. Scholz, Ph.D. thesis, University of Heidelberg, 1989

[26] R. Rieger, Ph.D. thesis, University of Mainz, 1990

[27] C. Broggini, Ph.D. thesis, University of Neuchatel, 1990

[28] NMC, P. Amaudruz et al., Phys. Lett. **B 294** (1992) 120; E140, S. Dasu et al., Phys. Rev. Lett. 60 (1988) 2591

[29] CERN NA2/EMC, J.J. Aubert et al., Phys. Lett. **B 123** (1983) 275

[30] SLAC E139, R. G. Arnold et al., Phys. Rev. Lett. **52** (1984) 727; SLAC E139, R. G. Arnold et al., SLAC-PUB-3257 (1983); CERN NA4/BCDMS, G. Bari et al., Phys. Lett. **B 163** (1985) 282; CERN NA4/BCDMS, A. C. Benvenuti et al., Phys. Lett. **B 169** (1987) 483; CERN NA2'/EMC, J. Ashman et al., Phys. Lett. **B 202** (1988) 603

[31] CERN NA28/EMC, M. Arneodo et al., Phys. Lett. **B 211** (1988) 493; CERN NA28/EMC, M. Arneodo et al., Nucl. Phys. **B 333** (1990) 1

[32] NMC, P. Amaudruz et al., Z. Phys. **C 53** (1992) 73

[33] NMC, P. Amaudruz et al., Z. Phys. **C 51** (1991) 387

[34] J. Gomez et al., SLAC-PUB-5813 (1993)

[35] FNAL E665, M.R. Adams et al., Phys.Rev.Lett. **66** (1992) 387

[36] N.N. Nikolaev and V.I. Zakharov, Phys. Lett. **55B** (1975) 397

[37] A.H. Mueller and J. Qiu, Nucl.Phys. **B266** (1986) 427

[38] G.L. Li, K.F. Liu and G.E. Brown, Phys.Lett. **B 213** (1988) 531

[39] V. Barone, M. Genovese, N.N. Nikolaev, E. Predazzi and B.G. Zakharov, KFA-IKP(TH)-1992-13

[40] G.L. Li, J.P. Shen, and M.J. Yu, BIHEP-TH-93-17

[41] B. Badelek, K. Charchula, M. Krawczyk and J. Kwiecinski, Rev. Mod. Phys. **64** (1992) 927

[42] F.E. Close, R.L. Jaffe, R.G. Roberts and G.G. Ross, Phys. Rev. **D 31** (1985) 1004

[43] D. Allasia et al., proposal CERN/SPSC 85-18

[44] EMC, O.C. Allkofer et al., Nucl. Instr. Meth. **179** (1981) 445

[45] EMC, J.J. Aubert et al., Nucl. Instr. Meth. **B 259** (1985) 189

[46] D. Sanders, Ph.D. thesis, University of Houston, 1993

[47] A. Dyring, TSL/ISV-93-0083, Licentiate thesis, Uppsala University, 1993

[48] G. Baum, private communication

[49] J. Zmeskal of Paul Scherrer Institute, private communication via R. Rieger, all of this being quoted from C. Scholz, NMC internal note NMC/90/21

[50] R.J. Tapper, N1RL/R/95, Rutherford 1965

[51] R. Prydz, National Bureau of Standards Report NBS-9276, Boulder, Colorado, 1967

[52] H.J. Hoge and R.D. Arnold, J.Res.Nat.Bur.Stand. **47** (1951) 63

[53] A. Milsom, NMC internal note NMC/90/6

[54] C. Scholz, NMC internal note NMC/90/21

[55] S. J. Wimpenny, Ph. D. thesis, University of Sheffield 1981, HEP/T/90

[56] M. Arneodo, Ph.D. dissertation, Princeton University, 1992

[57] M. Arneodo, private communication May 8, 1991

[58] H. Wind, Nucl. Instr. Meth. 115 (1974) 431

[59] D. von Harrach, private communication

[60] F. Bourgeois, private communication

[61] I. G. Bird, private communication: "There's no way you can use the information"

[62] *Mathematica* version 2.2, from Wolfram Research, Inc.

[63] Particle Properties Data Booklet, Phys. Rev. **D** Part 2 (June 1992)

[64] R. G. Roberts, "The structure of the proton", Cambridge University Press 1990

[65] L. W. Mo and Y. S. Tsai, Rev. Mod. Phys. 41, 205 (1969); Y. S. Tsai, SLAC Pub. 848(1971)

[66] A. A. Akhundov et al., Sov. J. Nucl. Phys. 44 (1986) 988

[67] EMC, J. J. Aubert et al., Z. Phys. **C 22** (1984) 341

[68] B. Badelek, D. Bardin, K. Kurek and C. Scholz, TSL/ISV-94-092

[69] W. Lohmann and A. A. Akhundov, Zeuthen HEP Institute preprint PHE 90-32

[70] A. Brüll, Ph. D. thesis, Freiburg 1993.

[71] A. A. Akhundov, D. Yu. Bardin and N. M. Shumeiko, JINR preprint E2-10205 (1976)

[72] A. A. Akhundov, private communication.

[73] G. K. Mallot, NMC internal report NMC/89/2

[74] T. A. Shibata, NMC internal report NMC/90/12 contains T1 and T2 resolutions

[75] A. Dyring was kind enough to provide me with the T14 resolutions

[76] E. Gabathuler et al., EMC internal report EMC/78/15

[77] J. H. Cobb et al., EMC internal report EMC/79/5

[78] J. Gillies, EMC internal report EMC/87/11

[79] A. Staiano, Ph.D. thesis University of Heidelberg, 1989

[80] N. N. Nikolaev, private communication

[81] A. Sandacz, private communication

[82] EMC, J. Ashman et al., Z. Phys. **C 52** (1991) 1

[83] S. P. Denisov et al., Nucl. Phys **B 61** (1973) 62

[84] S. P. Denisov et al., Nucl. Phys **B 65** (1973) 1

[85] A. S. Carroll et al., Phys. Lett. **61 B** (1976) 303

[86] A. S. Carroll et al., Phys. Lett. **80 B** (1979) 319

[87] B. Badełek and J. Kwieciński, Phys. Lett. **B 295** (1992) 263; Z. Phys. **C 43** (1989) 251

[88] A. Donnachie, P. V. Landshoff, Phys. Lett. **B 296** (1992) 227; A. Donnachie, P. V. Landshoff, Preprint M/C-TH 93/11

[89] NMC, P. Amaudruz et al., Nucl. Phys. **B 371** (1992) 3

[90] J. Gomez et al., SLAC-PUB-5813 (1993)

[91] M. Gari and W. Krümpelmann, Z. Phys. **A 322** (1985) 689

[92] W. B. Atwood, Ph. D. Thesis, Stanford University (1975); SLAC report 185

[93] A. Švarc and M. P. Locher, Fizika **22** (1990) 549

[94] S. Stein et al., Phys. Rev. **D 12** (1975) 1885

[95] W. Fabian and H. Arenhövel, Nucl. Phys., Nucl. Phys. **A 314** (1979) 253; W. Leidermann and H. Arenhövel, Nucl. Phys., Nucl. Phys. **A 381** (1982) 362;

[96] E. J. Moniz, Phys. Rev. **164** (1969) 1154

[97] J. Bernabeu and P. Pascual, Nuovo Cim. **10 A** (1972) 61; J. Bernabeu, Nucl. Phys. **B 49** (1972) 186

[98] Li et al., Nucl. Pbys. **A 162** (1971) 583

[99] I. Sick, Phys. Lett. **116 B** (1982) 212

[100] J. A. Jansen et al., Nucl. Pbys. **A 188** (1972) 337

[101] A. Brüll and C. Scholz, to appear as an NMC internal report in '94.,

[102] NMC, P. Amaudruz et al., Z.Phys. **C53** (1992) 77

[103] NMC, P. Amaudruz et al., Z.Pbys. **C51** (1991) 387

[104] N. N. Nikolaev, private communication.

[105] E665, T. J. Carroll, XXVIII Rencontres de Moriond 1993, preprint FERMILAB-Conf-93/166-E

[106] S. A. Kulagin, G. Piller and W. Weise, TPR-94-02, ADP-94-1/T144

[107] S. J. Brodsky and H. J. Lu, Phys. Rev. Lett. **64** (1990) 1342

[108] P. Castorina and A. Donnachie, Phys. Lett. **B 215** (1988) 589

[109] P. Castorina and A. Donnachie, Z. Phys. **C 45** (1989) 141

[110] W. Zhu and J. G. Shen, Pbys. Lett. **B 219** (1989) 107

[111] S. Kumano, preprint Indiana University IU/NTC 92-20

[112] A. D. Martin, R. G. Roberts and W. J. Stirling, Phys. Rev. **D 37** (1988) 1161

[113] C. Scholz, NMC internal note NMC/91/2

[114] O. Nachtmann, Nucl. Phys. **B 78** (1974) 455

[115] A. Brüll, private communication.

[116] JADE Collaboration, W. Bartel et al., Z. Phys. **C 33** (1986) 23

[117] E665 Collaboration, M. R. Adams et al., FNAL PUB 93/17, submitted to Pbys. Rev. Lett.

[118] E665 Collaboration, M. R. Adams et al., Phys. Rev. Lett. **69** (1992) 1026

[119] J. G. Körner, E. Mirkes, and G. A. Schuler, Int. J. Mod. Pbys. **A 4** (1989) 1781

[120] H. L. Melanson for tbe E665 Collaboration, FERMILAB-Conf-93/165-E, talk presented at XXVIIIth Rencontres de Moriond, Les Arcs, France, March 20-27, 1993

[121] Arecchi, Gatti and Sona, Pbys. Lett. **20** (1966) 27

[122] Morgan and Mandel, Phys. Rev. Lett. **16** (1966) 1012

[123] D. Ferenc, Ph. D. thesis, University of Zagreb, 1992

[124] G. I. Kopylov and M. I. Podgoretskii, Sov. J. Nucl. Phys. **15** (1972) 219; G. I. Kopylov, Phys. Lett. **B 50** (1974) 472; G. Cocconi, Phys. Lett. **B 49** (1974) 459

[125] R. Hanbury-Brown and R.Q. Twiss, Philos. Mag. **45** (1954) 663; Nature **178** (1956) 1449

[126] M. Gyulassy et al., Phys. Rev. **C 20** (1979) 2267

[127] D. O. Caldwell et al., Phys. Rev. Lett. 42 (1979) 553

[128] D. O. Caldwell et al., Phys. Rev. **D 7** (1973) 1362